AERODYNAMIC EFFECTS OF HIGH SPEED TRAINS IN CONFINED SPACES

by

TIMOTHY GILBERT

A thesis submitted to

the University of Birmingham

for the degree of

DOCTOR OF PHILOSOPHY

School of Civil Engineering

University of Birmingham

August 2013

Abstract

This research aims to describe the effect which changing the geometry of confining structures has on transient aerodynamic effects induced by passing high-speed trains. Experiments were undertaken at the 'TRAIN Rig' moving-model facility, which is owned and operated by the University of Birmingham. A moving-model high-speed train was fired past walls, partially-enclosed tunnels, and single-track tunnels. A control experiment was carried out in the open air. The model was a simplified 1/25 scale four-carriage ICE2 train, travelling at 32m/s. The three-dimensional air velocity components and static pressure coefficient were measured inside the structures. Data for the open air, wall and tunnel cases were compared directly with existing datasets, and close agreement was found in some cases. A reliability study found that the results were repeatable.

The main findings are as follows. The durations and magnitudes of the pressure loads and maximum air velocities were found to be dependent on: the lateral separation of the walls; whether walls on both sides of the tracks are placed symmetrically or asymmetrically; the longitudinal positioning of the sensor in relation to the length of the tunnel; the cross-sectional area of the tunnel; the tunnel's length in relation to the train's length; and, finally, the size of an opening in the cross-section of a tunnel in relation to the tunnel's internal perimeter. The reasons for these relationships were discussed. Observations were made on the three-dimensionality of the flow by comparing the results at different sensor positions. Maximum velocities were affected by confinement as a result of changes to the following flow structures: helical vortices in the wake; durations and magnitudes of the pressure fluctuation around the tail; the piston effect in tunnels; the boundary layer shape; and secondary flows induced by pressure gradients in the tunnel cross-section caused by vents.

“Coming back to where you started is not the same as never leaving.”

(Terry Pratchett, A Hat Full of Sky)

Acknowledgements

I am grateful to the School of Civil Engineering at the University of Birmingham for providing me with financial support throughout my PhD. I am thankful to my supervisors, Prof. Chris Baker and Dr. Andrew Quinn, for their excellent feedback and constant support. I have benefitted greatly from their expertise in the field of vehicle aerodynamics, their constructive criticism of all aspects of my work, and the many opportunities to gain experience of academic work beyond PhD level which they have given to me. Regarding the final point, I also gratefully acknowledge Prof. Lawrence Coates, Prof. Michael Ward, Dr. Mark Ward, Sally Tottenham, Helen Booth, Janet Roberts, Jayne Sharples and Prof. Roy Johnston, for their support in gaining further experience, skills and opportunities which have already proven invaluable for my future. I am sincerely grateful to my external examiner Prof. Mark Sterling; his advice, encouragement and support throughout my studies at the University of Birmingham inspired me to pursue a PhD, and helped me to keep things in perspective when faced with challenges which initially seemed to be overwhelmingly complex. I am also grateful to Terry Johnson for kindly sharing his industry insight and helping me to understand the context and potential applications of my research.

I am really grateful for Dr. Hassan Hemida, as well as Prof. Sinisa Krajnovic, Nainesh Patel, Dominic Flynn and Matthew Haines, all of whom helped me to develop skills in computational fluid dynamics. It was great to work with Jochem Straathof, and help him with his CFD validation study which formed part of his M.Sc project on pedestrian comfort and wind in train stations. I am grateful to him for sharing his data which I was able to use in my thesis, for collaborating with me on a conference paper, and for giving me the opportunity to contribute to further research in his area.

I would like to acknowledge my colleagues who provided invaluable help at all stages of my PhD, including Dr. Francesco Dorigatti, Dr. Sarah Jordan, David Soper, Martin Gallagher and Justin Morden, as well as Clive Pope. I am very grateful to my colleagues for working beyond their obligations at the TRAIN Rig in order to help me to meet a very demanding testing schedule and conduct extra experiments. I am grateful to Mike Vanderstam and the technicians of the Civil Engineering Laboratory of the University of Birmingham for guiding me on the designs of my structures, and helping me to solve logistical issues. I am grateful to Derwent Patterns Ltd for producing an excellent train model and ensuring that it always performed as well as it could.

On a personal level, I am deeply grateful for the love and support of my family (and unwavering adulation of our pet birds, despite the many late nights I have inflicted on them). I could not find the words to express how, or why, until I first listened to a commencement speech, delivered by an author who my wife studies as part of her Literature degree. I thank them all for their emotional and practical support throughout this learning process, and most of all for helping me to remember that:

> The really important kind of freedom involves attention, and awareness, and discipline, and effort, and being able truly to care about other people and to sacrifice for them, over and over, in myriad petty little unsexy ways, every day. That is real freedom. The alternative is unconsciousness, the default setting, the "rat race" - the constant gnawing sense of having had and lost some infinite thing. (David Foster Wallace, This is Water).

Contents

List of Figures

List of Tables

List of symbols

A	Area.
a_1, a_2, a_3	Constants in a function describing the time-averaged resultant velocity in the far-wake region.
A_{tr}	Cross-sectional area of train.
A_{tun}	Cross-sectional area of tunnel.
B	Constant in a function describing the ensemble-averaged resultant velocity in the near-wake region (Jordan et al., 2009).
C_1, C_2	Constants in a function describing the velocity distribution in the boundary layer region (Jordan et al., 2009).
C_f	Skin friction coefficient.
C_n, C_t	Model constants used in Iida et al. (2005).
C_P	Static pressure coefficient.
C_{P1}	Predicted maximum peak-to-peak static pressure coefficient on a vertical wall (BSI, 2005).
C_{P2}	Predicted maximum peak-to-peak static pressure coefficient on a horizontal ceiling above the tracks (BSI, 2005).
ΔC_P	Peak-to-peak static pressure coefficient.
$\Delta C_{P,tail}$	Peak-to-peak static pressure coefficient around the train's tail.
c	Speed of sound in air.
c_1, c_2, c_3	Pressure transducer calibration coefficients.
E	Voltage measured by pressure transducers, after elimination of offset.
E_{raw}	Voltage measured by pressure transducers, before elimination of offset.
F_{jk}	Potential flow function (Iida et al., 2005).
f	Frequency.
f_c	Frequency at cutoff for model-scale data.
$f_{c,fs}$	Frequency at cutoff for full-scale data.
f_s	Sampling frequency.
G_0	Gain of a Butterworth filter at zero frequency.
g	Peak scaling factor.
H	Boundary layer shape factor.
j	Denotes a complex number.
K_1, K_2	Constants in a function describing the rate of decay of the peak-to-peak static pressure coefficient with increasing lateral distance.
k	Pole of a Butterworth filter.
k_1	Shape coefficient of the train used in formulae predicting the pressure loads on surfaces (BSI, 2005).
k_N	Nose pressure loss coefficient (Vardy, 1996).
k_T	Tail pressure loss coefficient (Vardy, 1996).
L	Length of structure.
l_{ab}	Separation distance between two light gate beams.
l_{gap}	Gap width.
l_{nose}	Length of train nose.
l_{per}	Internal perimeter length of the tunnel cross-section.
M	Mach number.
m	Power law decay exponent (Barrow and Pope, 1987).
N	Number of test repeats, i.e. the ensemble size.
N_n	Number of samples in a time history.
n	Sample number in a time history.
n_a, n_b	Sample numbers of the rising or falling edges of the light gate time history data.
n_m	Middle point of a moving-average window.
n_{nose}	Sample number when the train nose passes the sensor.
n_w	Number of elements in a moving-average window applied to model-scale data.
$n_{w,fs}$	Number of elements in a moving-average window applied to full-scale data.
Δn	Index locator for resampling velocity data.
o	Order of a Butterworth filter.
P	Static pressure.
P_{atm}	Atmospheric pressure.
p	Probability value.
ΔP	Peak-to-peak static pressure.
q	Source term in potential flow equation (Howe, 1998).
Re	Reynolds number.
s	Complex frequency of a Butterworth filter.
s_h, s_k	Transfer functions of a Butterworth filter.
T	Temperature.

t	Time.
t_{fs}	Time interval in full-scale data.
t_{ms}	Time interval in model-scale data.
U	Resultant air velocity.
$U_{2\sigma}$	95% confidence limit of the maximum resultant velocity (TSI, 2008).
U_{max}	Velocity at the circumference of a vortex (Jordan et al., 2009).
U_{∞}	Free stream air velocity.
u	Longitudinal air velocity.
u_R	Radial velocity.
u_{τ}	Friction velocity.
u_w	Speed of a wavefront.
V	Desired constant train speed.
V_0	Train speed.
v	Lateral air velocity.
w	Vertical air velocity.
X	Maximum length of train.
x	Longitudinal axis originating from train nose.
x_1, x_2, x_3	Rectangular axes taken in the plane of the tunnel mouth, used in Howe (1998) and Iida et al. (2005).
Δx_n, Δx_t	Starting points of the pressure rise ahead of the train's nose and tail respectively in a partially-enclosed tunnel. Used in Iida et al. (2005).
x_P	Longitudinal axis relative to structure entrance.
x_{tail}	Longitudinal axis originating from the train tail.
Y	Maximum width of train.
Y_{wall}	Lateral separation of vertical wall from the track centreline.
$Y_{wall\text{-}to\text{-}wall}$	Lateral separation of vertical walls from each other.
y	Lateral axis originating from track centreline.
y_1	Longitudinal axis outside a tunnel, used in Iida et al. (2005).
Z	Maximum height of train above the top of the rail.
Z_{ceil}	Height of horizontal ceiling above the top of the rail.
z	Vertical axis originating from the top of the rail.

List of Greek symbols

α	Opening ratio (expressed as %).
α_R	Model constant (Iida et al., 2005).
β	Blockage ratio = A_{tr}/A_{tun}.
β_d, β_0, β_1	Geometric parameter for partially-enclosed tunnels (Iida et al., 2005).
δ	Boundary layer thickness.
δ^*	Boundary layer displacement thickness.
θ	Boundary layer momentum thickness.
κ	Von-Kármán constant.
μ	Dynamic viscosity.
ν	Kinematic viscosity.
ξ	Flow contraction coefficient (Iida et al., 2005).
ρ	Air density.
σ	Standard deviation.
τ_w	Wall shear stress.
φ	Velocity potential.
ω_c	Cutoff angular frequency of a Butterworth filter.

List of subscripts

atm	Atmospheric value.
e	Error.
fs	Full-scale.
lg1-4	Light gate beams 1 to 4.
ms	Model-scale.
nose	Nose of train.
0	Raw value (unprocessed).
per	Internal cross-section perimeter length.
pr	Sensor (a.k.a. probe).
run	The data from one run (one train pass).
tr	Train.
tun	Tunnel.

List of abbreviations

AeroTRAIN	Aerodynamics Total Regulatory Acceptance for the Interoperable Network (project).
BSI	British Standards Institute.
CFD	Computational Fluid Dynamics
DB	Deutsche Bahn.
DES	Detached Eddy Simulation.
EUK	Eisenbahn-Unfallkasse.
ERRI	European Rail Research Institute.
FFT	Fast-Fourier Transform.
GC	A railway loading gauge geometry.
HS2	High Speed Two.
ICE 1/2/3	Inter-City Express 1/2/3.
LES	Large Eddy Simulation.
LHS	Left-hand side.
OA	Open air.
PDF	Probability density function.
RANS	Reynolds-Averaged Navier-Stokes.
RHS	Right-hand side.
RSSB	Rail Safety and Standards Board.
RTRI	Railway Technical Research Institute.
T1, T2, T3, T4	Tunnels used in the experiments.
TFI	Turbulent Flow Instrumentation Ltd.
TRAIN Rig	Transient Railway Aerodynamic Investigations Rig.
TSI	Technical Specifications for Interoperability.
W1S, W2S, W3S	Single-wall structures used in the experiments.
W1D, W2D, W3D	Double-wall structures used in the experiments.

Chapter 1

Introduction

1.1 Outline of studies

This thesis reports on an experimental investigation into the transient aerodynamic effects of high-speed trains operating in confined spaces. Two journal articles also investigate the experimental data. They are included in Appendix C:

- A journal article published in the Journal of Wind Engineering and Industrial Aerodynamics (Gilbert et al., 2013b);
- A journal article published in the Proceedings of the Institution of Mechanical Engineers Journal of Rail and Rapid Transit (Gilbert et al., 2013a);

Several conference papers were delivered:

- Two conference papers which make reference to the full results. These were presented at the 2013 International Workshop on Railway Aerodynamics (Gilbert et al., 2013c), and the 2013 European and African Conference on Wind Engineering (Gilbert and Straathof, 2013). The latter paper is included in Appendix C.
- Two conference papers which make reference to preliminary results. These were presented at the 7th International Colloquium on Bluff Body Aerodynamics and

Applications (Gilbert et al., 2012), and the 10th UK Conference on Wind Engineering (Gilbert, 2012).

The author assisted in two experimental studies which were complementary to- but outside of the context of the main research, and helped to inform the methodology adopted in the thesis:

- Assessment of the transient aerodynamic pressures and forces on trackside and overhead structures due to passing trains, which was undertaken as part of RSSB-funded project T750 (Baker et al., 2012).
- Assessment of the pressure transients due to passing trains in tunnels with different entrance designs, which was undertaken as part of the EU-funded AeroTRAIN project (Work package 4.2). The findings are unpublished at the time of writing.

1.2 Engineering problems caused by transient slipstream gusts

The air velocity transients which are induced by passing trains impose dynamic pressure loads ('gust loads') on trackside workers and trackside furniture. These air velocity transients are created by the train's slipstream and wake. Issues related to slipstream safety have been investigated in the UK since the 1970's - see for example Gawthorpe (1978). Concerns have been raised that the continual increase in the operating speeds of passenger trains will lead to stronger airflows which will further increase the safety risks and reductions in the serviceable life of trackside furniture (Sterling et al., 2008). Increases in train speeds cause the slipstream gust loads to increase. Particularly large jumps in maximum and operating speeds have been observed in the high-speed rail sector over recent decades (Raghunathan et al., 2002). The UK is also preparing for a new 'High Speed Two' (HS2) high speed rail network, in which the design speed of 400kph is double that of current mainline speeds (Department for Transport, 2012).

Figure 1.1 shows a generic illustration of the air velocity caused by a passing train in the open air. A fluctuation occurs as the nose of the train passes the observer, followed by a region of increasing velocity, and then a larger fluctuation around the train's tail.

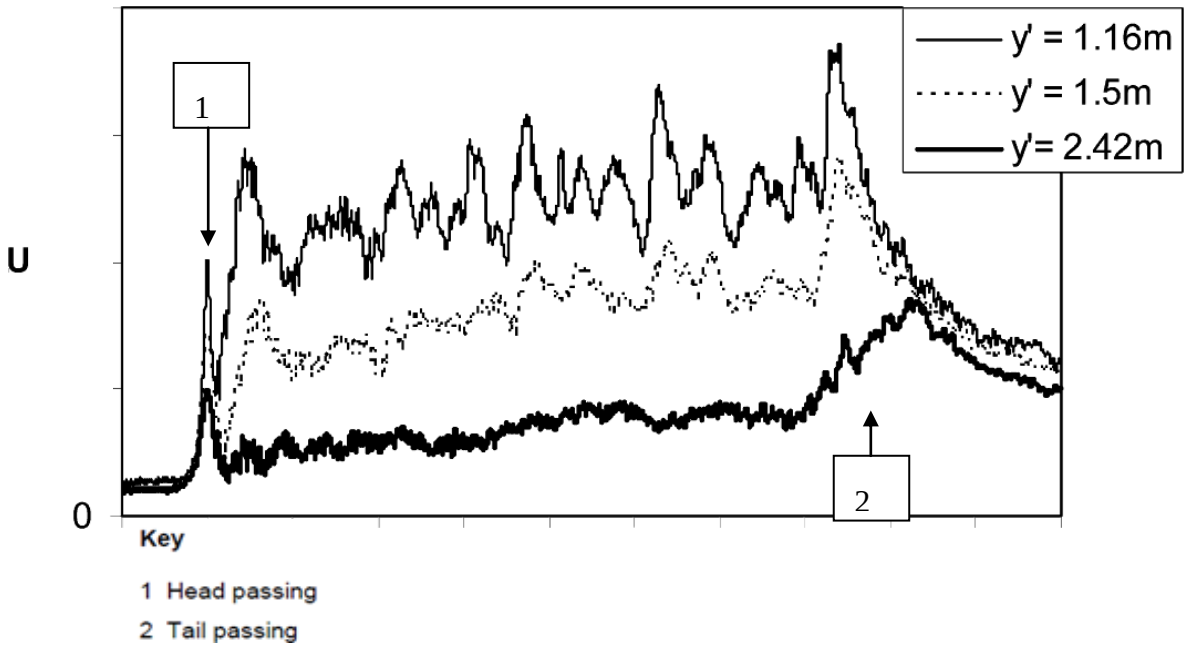

Figure 1.1: Typical transient air velocity time history caused by a passing train (Sterling et al., 2008). *U* is the normalised velocity, and *t* is time. Measurements were made at a height of 0.5m above the rail, and at various lateral distances *y'* from the rail edge.

Codes of practice require that the maximum transient gust load generated by a passing train is treated as a design load. An EU-wide 'Technical Specifications for Interoperability' (TSI) code for high-speed trains (TSI, 2008) imposes limit criteria on the slipstream loads acting on trackside workers. The limit criteria must be met by all high-speed rolling stock operating across national borders under interoperability legislation. A methodology is defined in the TSI code (referred to henceforth as the 'TSI methodology') for assessing safety and risk against limit criteria, but it stipulates open air operation only so there is no guidance for confined spaces. BSI (2005) includes similar guidance for routes outside the scope of the TSI, as well as additional guidance for assessing the gust loads on objects.

Until now, little attention has been devoted to assessing transient slipstream velocity gusts in 'confined spaces'. These include tunnels (defined as 20m or longer by code of practice BSI, 2006), partially-enclosed tunnels which are slightly open to the atmosphere, and vertical surfaces running parallel to the tracks such as noise barriers. BSI (2003) provides a summary of the factors affecting slipstreams in tunnels - 'the induced flow velocity depends on the train speed, the blockage ratio [the train area divided by the tunnel area], the length of the train, and of the tunnel respectively, the roughnesses [sic] of the train and the tunnel wall respectively, and on the initial air speed in the tunnel'. BSI (2003) stated that an upcoming code of practice would explore these issues further, but this has not yet been produced.

Figure 1.2 shows a generic illustration of the air velocity in a tunnel caused by a passing train. The air velocity begins to increase a long time before the train's nose ('head') passes the observer, due to a 'piston effect' which moves the internal air column. Fluctuations occur as the train's nose and tail pass the observer, and localised reversals of the flow direction may occur.

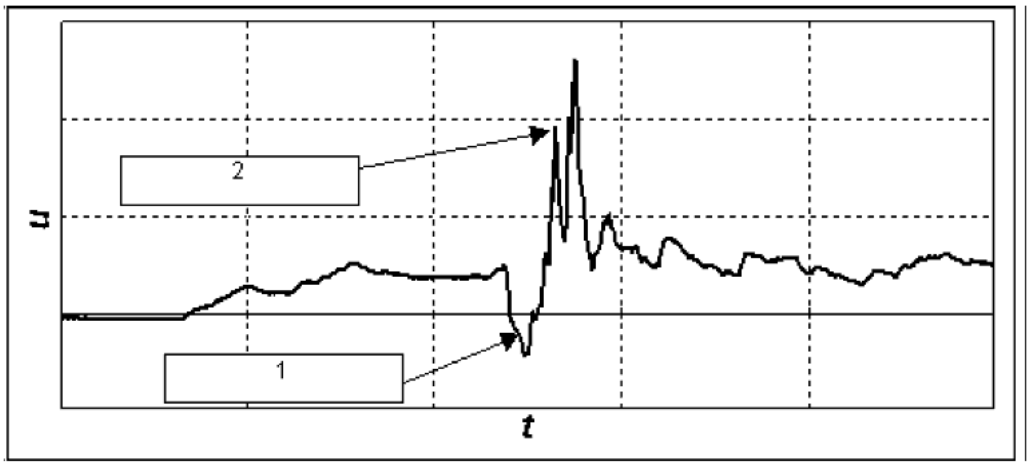

Key

1 Head passing

2 Tail passing

Figure 1.2: Typical transient air velocity time history in a tunnel caused by a passing train (© BSI, 2003). *u* is the velocity, and *t* is time.

1.3 Engineering problems caused by transient pressure loads

High-speed trains generate transient static pressure fluctuations which impose loads on surfaces close to the tracks. Some progress towards understanding the fundamental nature of these loads has been made in recent years (Sanz-Andrés et al., 2003; Baker et al., 2012). Aerodynamic effects in tunnels present unique challenges, which have been identified as being particularly important in the high-speed rail sector (Johnson, 2012). These issues require careful consideration at the design stage of new routes such as HS2 (Arup, 2012).

In the open air, the passage of the train nose is marked by a positive static pressure peak followed by a negative (suction) peak. The passage of the train tail is marked by a suction peak followed by a positive peak. The form of the 'loading pattern' is illustrated in Figure 1.3.

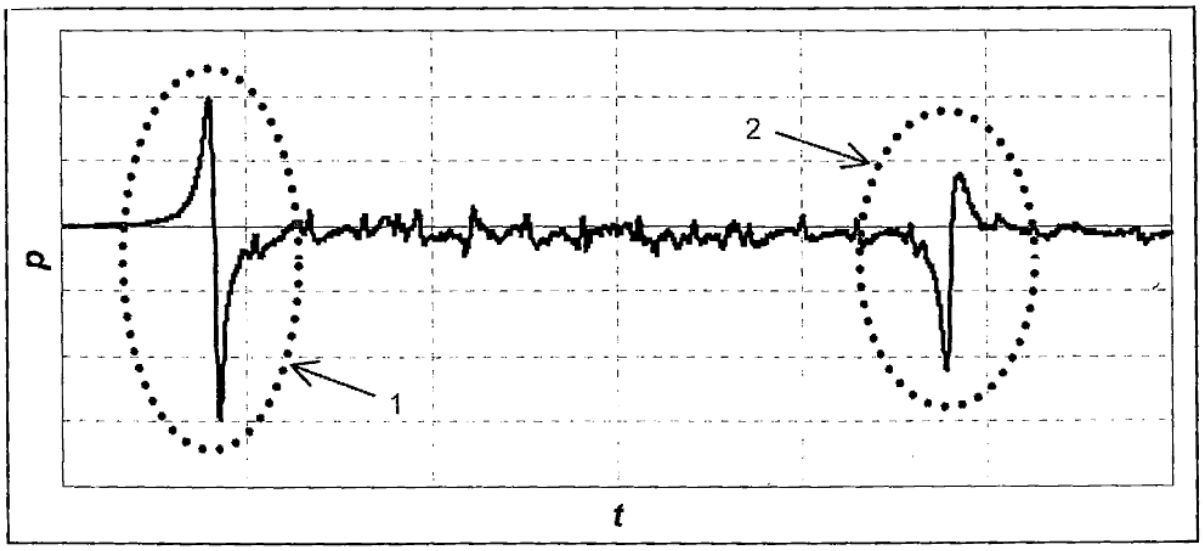

Figure 1.3: Typical transient static pressure time history caused by a passing train, from EN 14067-4 (© BSI, 2005)

In codes of practice, the highest loads are assumed to occur around the train's nose, so nose loads form the basis for assessing pressure loading amplitudes on trackside and overhead structures. European codes include EN 1991-2 (BSI, 2003) and a railway-specific standard EN 14067-4 (BSI, 2005). These codes were developed from experimental and theoretical work carried out for ERRI (1994). EN 14067-4 includes methodologies for experimental or numerical assessment of loads, and shortcut predictive formulae for assessing loads on a limited range of structures. The predictive formulae may be applied to vertical walls, horizontal surfaces, mixed surfaces including inclined sections, and tunnels shorter than 20m (formed by vertical walls and a horizontal surface).

Baker et al. (2012) recommended that further experiments are carried out at the TRAIN Rig on 'continental gauge' trains with the aim of replacing 'the less reliable data' on which the predictive formulae in EN 14067-4 are based. Gilbert et al. (2012) reported on preliminary data from the experiments which were carried out for this thesis. It described the experiments as ideal in addressing the research gap, because the test parameters represent somewhat of a 'worst case'. It found that the pressure loads and predicted loads closely corresponded to each

other at positions far from the train, but the formulae over-predicted the loads at positions close to the train. The more extensive experimental dataset reported in this thesis will help to further address this research gap. For example, the predictive formulae for vertical walls only apply to walls on one side of the tracks, and this thesis includes commentary on the difference between single walls and walls on both sides of the tracks. Symmetrical and asymmetrical configurations are compared for walls on both sides of the tracks. The predictive formulae also assume that the load is linear along the wall's height. This thesis comments on how the loads on vertical walls vary depending on the height at which measurements are taken.

The predictive formula for a short tunnel in EN 14067-4 defines the tunnel as a 'closed structure enveloping the tracks', and amplification factors are simply applied to the formulae for vertical walls and horizontal surfaces above the tracks, which are based on the assumed loading pattern shown in Figure 1.3. This thesis questions whether this loading pattern is an acceptable assumption for a short tunnel of 20m length, and explores how it varies as the length of the tunnel increases. This thesis comments on how the load on ceiling varies depending on the lateral position of the sensor.

Any tunnel longer than 20m is considered in the code of practice EN 14067-5 (BSI, 2006). As a train enters a tunnel, the air ahead of the train nose is compressed, causing compression and expansion wavefronts to propagate through the tunnel at the speed of sound, and reflect from the entrance and exit portals. The overall 'pressure wave' pattern is complex. Figure 1.4 shows an example of a wave pattern measured by a trackside probe, for a tunnel significantly longer than the train's length. The probe detects the nose-entry compression wave at (1), the tail-entry expansion wave at (2); reflecting pressure waves at (3), (4) and (6); and the passage of the train's nose and tail at (7) and (8) respectively. The events at (5) are only relevant to an observer on the train.

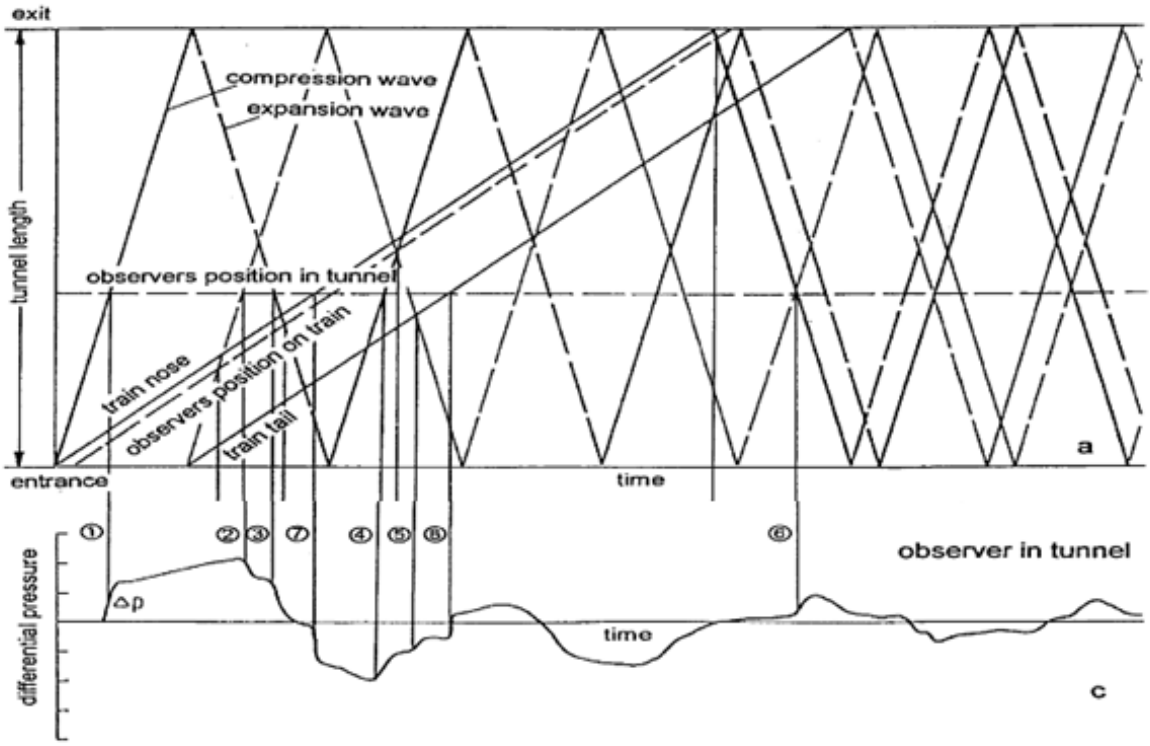

Figure 1.4: Typical transient static pressure time history caused by a passing train in a tunnel, from EN 14067-5 (© BSI, 2006). A wave diagram is used to indicate the propagation of compressible flows through the tunnel.

The wave pattern superimposes onto the pressure field around the train at positions along the tunnel which are specific to a particular train speed and tunnel length. As the tunnel length decreases, the wave pattern seen by a stationary observer tends towards a sinusoidal shape which is superimposed onto the pressure field around the train, as was found in experiments reported in Schultz (1990). This thesis examines whether the loading pattern for a 20m long single-track tunnel is more similar to that in Figure 1.3 or Figure 1.4, in other words exploring why this length represents the boundary between the two aforementioned codes of practice. This thesis also examines how the loading pattern is influenced by changing either the tunnel length, or the longitudinal positioning of sensors.

EN 14067-5 sets out methodologies for assessing the 'train-tunnel-pressure signature' using trackside instrumentation, in order to assess how closely the worst-case total pressure change

conforms to criteria for medical health. Full-scale tests, numerical simulations or reduced-scale tests may be used. The minimum tunnel length for carrying out the tests must be 250m (full-scale length), with additional adjustments accounting for the length and speed of the train, so the 'pressure signature' (loading pattern) is of the required form. The guidance ensures that the sensor is sited at a location where the tail-entry expansion wave (indicated by a dashed line in Figure 1.4) occurs before the train nose passes the sensor, and the first reflected expansion wave occurs after the train nose passage. This thesis investigates the relationship between the tunnel's length and the pressure loading pattern. This thesis also queries the assumption that the pressure loading pattern is one-dimensional (and therefore identical at any point within the tunnel cross-section); it is known that pressure waves are three-dimensional at the point of formation and may actually remain three-dimensional in short tunnels.

Neither of the aforementioned codes of practice addresses partially-enclosed spaces, which are formed by longitudinal openings in what would otherwise be tunnels. Moving-model tests undertaken by Takei et al. (2008) for RTRI found that the form of the loading pattern around the train in a partially-enclosed space is unique, and not like either of the standard patterns in Figure 1.3 or Figure 1.4. Figure 1.5 shows a typical static pressure time history for a partially-enclosed tunnel, in which the ratio of the size of the tunnel's opening to its cross-section perimeter length (i.e. the opening ratio) - is 1% (when expressed as a percentage).

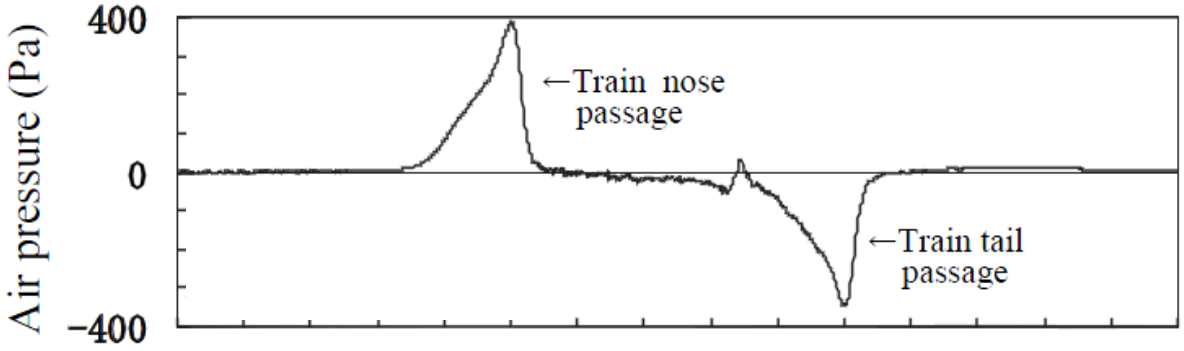

Figure 1.5: Typical transient static pressure time history caused by a passing train in a partially-enclosed space.

The time history shows that a positive load occurs around the train nose, and a suction load occurs around the tail. The study showed that the loading pattern changes as this 'opening ratio' changes. This thesis considers how the loading pattern evolves from that expected in a tunnel to a 'partially-enclosed tunnel' as the opening ratio increases, and investigates the geometric parameters affecting the loading patterns for partially-enclosed tunnels.

In this thesis, pressure fluctuations will be correlated with maximum slipstream velocities, in order to gain a better understanding of the flow structures which drive the critical engineering loads. The pressure loading patterns in a variety of confining structures will be compared with the three patterns described above, and the relationships between loading patterns and maximum slipstream velocities will be assessed.

1.4 Aims and objectives

The main aim of this research is to describe how changing the geometry of confining structures affects the flow patterns and transient velocity and pressure loads which are induced by passing high-speed trains.

In order to accomplish the aim, a parametric experimental study has been undertaken at the 'TRAIN Rig' moving-model facility in Derby (UK), which is owned and operated by the

University of Birmingham. In order to explore the transition from unconfined to confined spaces, experimental cases included the open air, single and double vertical walls (in symmetrical and asymmetrical configurations), partially-enclosed spaces, short single-track tunnels, and a longer tunnel.

The objectives of this research are as follows:

1. Develop a test methodology for undertaking TRAIN Rig moving model experiments and measuring the slipstream velocity and static pressure. The methodology should conform to codes of practice where their requirements do not inhibit the ability of the study to meet the other objectives.
2. Undertake moving-model experiments in the open air, in order to validate the results against existing data, check the reliability of the methodology, and provide open air reference data against which to compare data for confined spaces.
3. Undertake moving-model experiments on a variety of structures including single and double vertical walls, partially-enclosed tunnels, and single-track tunnels.
4. Describe how changing the structure geometry, including the surfaces of the confined spaces and the positions of sensors, affects the flow patterns, maximum gusts and pressure fluctuations.
5. Comment on how the observations in Objective 4 challenge the validity of the guidance in codes of practice.
6. Provide a dataset of experimental data for third party use, which may for example be used as a benchmark for prediction models or CFD simulations.

The aim and objectives will be recapped in Chapter 6, which presents the main conclusions and recommendations for further work. The section includes an explanation of what has been done to address the aim and objectives.

1.5 Structure of the thesis

The contents of the following sections are organised as follows:

- In Chapter 2, the research carried out in this thesis is placed in context by exploring the state of the art concerning aerodynamic effects of high-speed trains in the open air and confined spaces. The main aim of the chapter is firstly to highlight the various assumptions which are commonly made about velocity and pressure transients in the open air and in tunnels, and secondly to highlight the current level of understanding of the relationships between geometric parameters and velocity and pressure transients (Objective 4). The chapter will show that the flow patterns differ greatly between the open air and tunnel environments, and that mathematical models describing the flow in both types of environment differ greatly in their assumptions. It will also show that there is a need to understand the range of geometric variables over which the assumptions are valid, in order to make it easier to determine the suitability of different prediction models.

- Chapter 3 describes the experimental methodology and how it fulfils the requirements of Objectives 1, 2 and 3. The TRAIN Rig facility is described. The train model is described. The experimental variables and coordinate systems are described. The velocity and pressure sensors are described. The test cases and structures are defined, as well as the positions of the sensors in each test case. The test speed is explained. The post-processing techniques are explained. The uncertainty of the results is

assessed. Finally, the extent to which the methodology conforms to requirements in codes of practice is appraised.

- Chapter 4 presents and discusses the experimental static pressure results within the framework of Objectives 4 and 5. The discussion focuses on time histories of the pressure, the maximum pressure change, and the engineering loads.
- Chapter 5 presents and discusses the experimental slipstream velocity results within the framework of Objectives 4 and 5. The discussion focuses on time histories of the average velocity and the turbulence level, the maximum gust loads, and the engineering loads. Correlations are sought between pressure fluctuations and maximum gust loads.
- In Chapter 6, the main outcomes of the research are summarised within the framework of the aim and Objectives 1-6, and further work is recommended.

Chapter 2

Aerodynamics of high-speed trains in the open air and confined spaces

In this section, the research carried out in this thesis is placed in context by exploring the state of the art concerning aerodynamic effects of high-speed trains in the open air and confined spaces. The main aim of this section is firstly to highlight the various assumptions which are commonly made about velocity and pressure transients in the open air, tunnels and partially-enclosed tunnels, and secondly to highlight the current level of understanding of the relationships between geometric parameters and velocity and pressure transients (Objective 4).

The first sub-section (Section 2.1) describes the equations of fluid motion. The following sub-sections describe theories relating to the velocity and pressure fields around high-speed trains. Research by Sterling et al. (2008) into the fundamentals of transient slipstreams of high-speed trains found that the flow field in the open air can be defined by four regions, including: an upstream/nose region in which inviscid velocity fluctuations occur; a boundary layer region in which a turbulent and highly three-dimensional boundary layer develops along the length of the train on all sides; a near-wake region which is dominated by large scale unsteady flow structures; and a far wake region in which the velocity decays gradually. These region names are reflected in the titles of the following sub-sections: the ‘Upstream and Nose Region’ in Section 2.2, the ‘Boundary Layer Region’ in Section 2.3, and the ‘Tail and Wake Region’ in Section 2.4.

2.1 Equations of fluid motion

The incompressible Navier-Stokes equations are commonly applied to simulations of the flow around a train in cases where compressible effects may be ignored, such as the open air, spaces next to walls, and special cases inside tunnels (e.g. the time interval between the passage of compression or expansion wavefronts).

Inside tunnels, compressible effects cannot be ignored due to pressure waves (described in Section 1.3). The flow is often assumed to be compressible, but one-dimensional and inviscid. Linear models are often used to predict the flow inside tunnels. They are based on the continuity, momentum and Bernoulli equations. Second order terms may be included in order to improve the accuracy of the prediction (e.g. Howe et al., 2000), and the entry of the train into the tunnel has been modelled using potential flow theory in Howe (1998). The main flow structures of interest are substantially one-dimensional: a movement of the internal air column driven by the 'piston effect' of the train; and the compression or expansion wavefronts generated at the entrance and exit portals.

Vardy (1996) developed linear models describing the flow around significant discontinuities such as pressure wavefronts and changes in the tunnel cross-section. The propagation of a wavefront may be described by:

$$\frac{\rho_2}{c} + \frac{\rho_1}{(u_2 - u_w)} = 0 \qquad 2.1$$

$$p_2 - p_1 = \rho_1 c(u_2 - u_1) \qquad 2.2$$

in which u_w is the speed of the wavefront, p is the static pressure, c is the speed of sound, u_1 and u_2 are the air velocities in the tunnel downstream and upstream of the wavefront,

respectively, and ρ_1 and ρ_2 are the air densities downstream and upstream of the wavefront, respectively.

Vardy (1996) describes the continuous flow (between significant discontinuities) using a one-dimensional simplification of the Euler equations. The Euler equations are a simplified form of the Navier-Stokes equations in which the flow is assumed to be inviscid. This assumption is valid when the effect of fluid viscosity on the flow structures being investigated is negligible.

$$\frac{\partial}{\partial t}(\rho A) + \frac{\partial}{\partial x}(\rho A u) = 0 \tag{2.3}$$

$$\frac{\partial}{\partial x}(pA) + \frac{\partial}{\partial t}(\rho A u) + \frac{\partial}{\partial x}(\rho A u^2) = \mathrm{T} \tag{2.4}$$

$$-\frac{\partial}{\partial t}(pA) + \rho A\left(\frac{\partial}{\partial t} + u\frac{\partial}{\partial x}\right)\left(h + \frac{1}{2}u^2\right) = E \tag{2.5}$$

u is longitudinal velocity, p is pressure, t is time, ρ is density, x is the longitudinal axis, A is the area of the tunnel, T represents shear stresses, E represents the internal energy, and h is the specific enthalpy. One-dimensional approximations generally only hold for long tunnels. In short tunnels, the highly three-dimensional flow fields must be accounted for at tunnel portals, and around train noses and tails. One way in which this has been addressed is by modelling the change in flow area inside the tunnel with time (Schultz and Sockel, 1991). The models for tunnel flows are also compromised by an incomplete understanding of how to accurately approximate the shear stresses induced by unsteady friction effects, which are dependent on the air viscosity and three-dimensional flow structures. This thesis discusses how changing the geometric parameters of confined spaces affects the accuracy of assumptions of one-dimensional and inviscid flow.

2.2 Upstream and nose region

The velocity in the upstream and nose region is assumed to be inviscid. Sanz-Andrés et al. (2003) presented an analytical solution to the velocity around the vehicle nose using potential flow theory for a simple Rankine half-body (or moving-source). The Rankine half-body assumption is a poor approximation of the nose shape of a real vehicle, particularly a high-speed train. Potential flow theory dictates that the flow is inviscid and irrotational. Such assumptions would only be accurate for train noses around which flow separation does not occur. The longitudinal (u) and radial (u_R) velocities measured by a stationary observer are:

$$u = -\frac{VA_{tr}}{4\pi}\frac{x}{(x^2+y^2+z^2)^{3/2}} \tag{2.6}$$

$$u_R = \frac{VA_{tr}}{4\pi}\frac{\sqrt{(y^2+z^2)}}{(x^2+y^2+z^2)^{3/2}} \tag{2.7}$$

in which: x, y and z are the axes corresponding to longitudinal (u,V), lateral (v) and vertical (w) motion respectively; V is the speed of the train; and A_{tr} is its cross-sectional area. The static pressure coefficient (C_P) is the static pressure (p) divided by the dynamic pressure ($0.5\rho U^2$), where U is the resultant velocity. The static pressure coefficient in the nose region may be derived using an unsteady potential flow approximation:

$$C_P = -\left(\frac{U}{V}\right)^2 - \frac{2}{V^2}\frac{\partial\varphi}{\partial t} \tag{2.8}$$

in which φ is a velocity potential function. Analytical formulae based on the above models have been adapted to predict forces on: pedestrians; signs at various orientations; and continuous parallel walls. Baker et al. (2012) studied the inviscid velocity and pressure fluctuation around the nose of a passing train in the open air, and applied Bernoulli's equation to relate the pressure coefficient to the air velocity:

$$C_P = 1 - (1-u)^2 - v^2 - w^2 \quad (2.9)$$

From experimental results it was found that *w* was small and could be neglected, while *u* and *v* were sufficiently similar to validate the following simplification:

$$C_P \approx 2u \quad (2.10)$$

If the effect of a wall next to the tracks is considered using potential flow theory, the pressure coefficient can be represented simply by an 'image' source on the other side of the wall. Consequently the pressure coefficient on the wall is double that in the open air:

$$C_P \approx 4u \quad (2.11)$$

This provides a simple prediction of the effect of the confinement of a single wall on the static pressure.

Maximum static pressure loads tend to occur in the upstream and nose region. Section 1.3 showed that guidance in codes of practice relating to maximum static pressure fluctuations focuses on this region, for both open air and tunnel operation. It was also stated that the flow in this region is effectively inviscid. Three-dimensional velocity fluctuations occur in conjunction with the passage of the train's nose past the observer. A 'piston effect' causes compression of the air ahead of the train's nose and expansion behind the train's tail. This forces the internal air column of the tunnel to move, which induces a steady wind inside the tunnel. The wind velocity is related to the ratio of the cross-sectional area of the train to that of the tunnel (blockage ratio). These fluctuations are seldom critical because they are overshadowed by the peaks in the wake (Baker et al., 2013a). This thesis investigates the effect of changing geometric parameters of confined spaces on the flow in the upstream and nose region, including maximum pressure loads.

In tunnels, simple models for the change in air pressure assume that the flow is inviscid and steady, as with the open air. The pressure inside the tunnel is assumed to be one-dimensional. Analytical equations have been derived (outside the scope of this thesis) which predict the pressure fluctuations in the upstream and nose region (Sockel, 2003; Vardy, 1996), and the maximum pressure (Howe et al., 2000).

The most complex effects which need to be accounted for in commonly used numerical models of the flow inside tunnels include the unsteady and highly three-dimensional frictional forces along the tunnel wall and train (Adami and Kaltenbach, 2008). Friction forces affect all flows inside the tunnel. Quasi-steady and one-dimensional assumptions may be necessary in order to obtain friction coefficients; these assumptions would only apply to long tunnels.

The flow in the nose region from a position upstream of the train nose to behind the nose has been described in a semi-empirical model from Vardy (1996), which takes the extended Bernoulli equation as:

$$\left(p_1 + \frac{1}{2}\rho u_1^2\right) - \left(p_2 + \frac{1}{2}\rho u_2^2\right) = k_N \frac{1}{2}\rho u_2^2 \qquad 2.12$$

in which subscript 1 represents a measurement upstream of the train's nose, and subscript 2 represents a measurement made a certain distance downstream of the nose, and k_N is a nose pressure loss coefficient.

Howe (1998) modelled the compression wave generated by a train entering a circular cross-section tunnel by modelling the train as a continuous distribution of monopole sources with strengths determined by the train nose profile. This potential flow model had the advantage of accounting for three-dimensional effects which are neglected from other tunnel flow models. It is better suited to predicting the compression wave. The source term *q(x)* is as follows:

$$q(x) = V\frac{\partial A_{tr}}{\partial x_1}(x_1)\delta(x_2)\delta(x_3) \qquad 2.13$$

in which (x_1,x_2,x_3) are the rectangular axes taken in the plane of the tunnel mouth (Figure 2.1), and the train travels in the -x_1 direction. The derivative $\partial A_{tr}/\partial x$ describes the rate of change of the cross-sectional area of the non-axisymmetric train nose, which is an essential term due to the sensitivity of the tunnel compression wave to the shape of the train nose. Nevertheless, the assumption of inviscid and irrotational flow limits the validity of A_{tr} to streamlined nose shapes around which separation would not occur.

An analytical model for partially-enclosed tunnels was developed in Iida et al. (2005). The model captures the velocity and pressure pulse upstream of the train's nose, and the pulse of opposite magnitude downstream of the train's tail, as shown in Figure 1.5. This was done in two stages. Firstly the potential flow model by Howe (1998) in Equation 2.13 was modified and extended in order to describe the pressure induced by a train travelling through a rectangular cylinder:

$$p(\mathbf{x},t) = -\frac{\rho V^2}{4\pi}\sum_{J=-\infty}^{\infty}\sum_{K=-\infty}^{\infty} \times \int_{-\infty}^{\infty}(x_1 - y_1)F_{JK}(\mathbf{x},y_1)\frac{\partial A_{tr}}{\partial y_1}(y_1 + Vt)dy_1 \qquad 2.14$$

$$\begin{aligned} F_{JK}(\boldsymbol{x},y_1) = {} & \frac{1}{|\boldsymbol{x} - (y_1, y_t + 2JZ_{ceil}, z_t + 2KY_{wall-to-wall})|^3} \\ & + \frac{1}{|\boldsymbol{x} - (y_1, -y_t + 2(J+1)Z_{ceil}, z_t + 2KY_{wall-to-wall})|^3} \\ & + \frac{1}{|\boldsymbol{x} - (y_1, y_t + 2JZ_{ceil}, -z_t + 2(K+1)Y_{wall-to-wall})|^3} \\ & + \frac{1}{|\boldsymbol{x} - (y_1, -y_t + 2(J+1)Z_{ceil}, -z_t + 2(K+1)Y_{wall-to-wall})|^3} \end{aligned} \qquad 2.15$$

in which F_{jk} is a source term function, y_1 is the longitudinal axis outside the tunnel (the train travels in the direction -y_1), and the geometric constants of the train and tunnel are Z_{ceil}, $Y_{wall\text{-}to\text{-}wall}$, y_t, and z_t, all of which are defined in Figure 2.1.

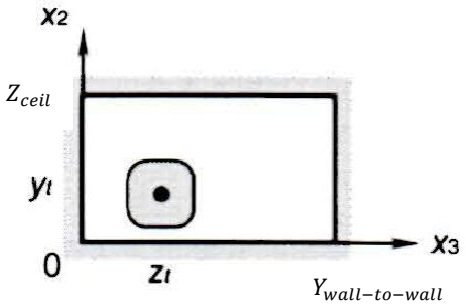

Figure 2.1: Coordinate system used in Iida et al. (2005).

The train does not have to be positioned symmetrically in the cross-section, so the prediction applies to both single-track and double-track operation.

The second stage involves an analytical description of the flow in a partially-enclosed space by adopting a similar approach to Vardy (1996) (Equation 2.12). This involves modelling the train as a discontinuity and describing the flow around the train's nose and tail using Bernoulli's equation. The geometric parameter β_d accounts for the tunnel geometry and opening ratio:

$$\beta_d = \begin{cases} \dfrac{\zeta \alpha l_{per}}{A_{tun}}, & (d = 0) \\ \dfrac{\zeta \alpha l_{per}}{(1-\beta) A_{tun}}, & (d = 1) \end{cases} \qquad 2.16$$

in which d=0 upstream of the train nose and downstream of the tail, otherwise d=1. ζ is a flow contraction coefficient, α is the opening ratio, l_{per} is the internal cross-sectional perimeter length, A_{tun} is the area of the tunnel, and β is the blockage ratio. The air velocity and pressure upstream of the train's nose is:

$$u(x) = \begin{cases} V, & (x \le -\Delta x_n, 0 \le x) \\ V\sin(-\beta_0 x + C_n), & (-\Delta x_n < x < 0) \end{cases}$$

$$p(x) = \begin{cases} 0, & (x \le -\Delta x_n, 0 \le x) \\ \frac{1}{4}\rho V^2\{1 + \cos 2(-\beta_0 x + C_n)\}, & (-\Delta x_n < x < 0) \end{cases} \qquad 2.17$$

in which β_0 is defined in Equation 2.16, and:

$$C_n = \sin^{-1}(1-\beta), \qquad \Delta x_n = \frac{\cos^{-1}(1-\beta)}{\beta_0} \qquad 2.18$$

in which C_n is a constant, and Δx_n is used to define the starting point of the pressure rise. The velocity and static pressure gradually build up starting from $-\Delta x_n$, both reaching a peak at the location of the train nose (at x=0), then sharply 'stepping' back to free-stream velocity V and zero static pressure (hence the use of step-type indicator functions). This flow pattern is illustrated in Figure 2.2(a). Similar equations for the flow around the tail are defined in Section 2.4. The two parts (Equations 2.14 and 2.17) are combined in order to account for the true shape of the train rather than the less accurate 'discontinuity' model. This produces a smoother time history which is illustrated in Figure 2.2(b) for different opening ratios.

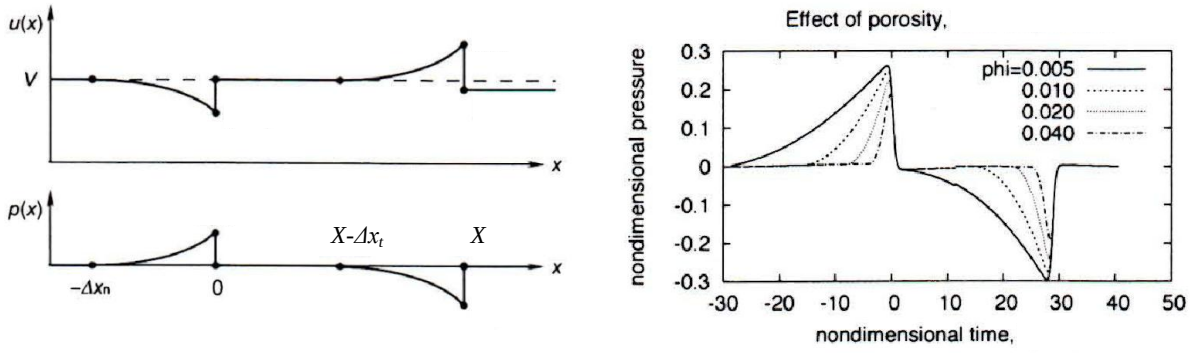

Figure 2.2: Velocity and pressure distribution in a partially-enclosed tunnel (adapted from Iida et al., 2005): (a) pressure for a one-dimensional model with train ends modelled as discontinuities; (b) predicted pressure when combined with a potential flow model, for different opening ratios ('phi').

The model was calibrated against moving-model experiments of an axisymmetric train running through a rectangular cylinder (Figure 2.1), and later with full-scale experiments of

real trains running through partially-enclosed train stations (Muraki et al., 2010). In both cases an excellent level of agreement was obtained. However, there are some cases which the model may not predict accurately. In tunnels of finite length and relatively high blockage ratio, the pressure wave reflection phenomenon would cause oscillations to be superimposed onto the data, which would affect the magnitudes and durations of peak pressures. Moreover in more confined spaces the effect of air viscosity and rotationality on the flow around the train may be important, particularly for bluff-nosed trains which induce flow separation. Other models such as Equation 2.12 from Vardy (1996) include a nose loss coefficient k_N to account for this, and it appears to have been ignored in this model. The model has not been tested against realistic high-speed train shapes in relatively confined cases (compared to the partially-enclosed train stations), and tunnels of finite length in which there are pressure wave reflections.

This thesis discusses the extent to which changing the geometric parameters of confined spaces affects the assumptions made by models relating to the upstream and nose region, for example: a specific type of loading pattern occurs for a certain 'type' of structure; pressure wave reflections are ignored and the tunnel is presumed to have infinite length; the three-dimensional components of the flow are negligible; and the effect of air viscosity and rotationality may be ignored. From this thesis it is hoped that ranges of geometric parameters for which such assumptions would be valid can be derived.

2.3 Boundary layer region

A boundary layer grows between the nose and tail of the train. Its thickness is related to the number of carriages, the shape of the train's nose (Baker et al., 2013a), the surface roughness and any surface features such as inter-carriage gaps. The flow in the boundary layer is highly

turbulent and three-dimensional, and features pressure gradients around changes in the train's cross-sectional area. CFD simulations have shown that the main points of turbulence generation include bogies (Sakuma et al., 2010), inter-carriage gaps (Hemida et al., 2012) and upper body corners (Diedrichs et al., 2004). Most of the turbulence is generated at around bogie height due to the rough underbody equipment (Suzuki et al., 2008). Consequently most of the boundary layer energy starts at low heights and moves up the train side, leading to observations of flow travelling up the train side and impinging on the train roof (as described in Brockie and Baker, 1990).

Pressure gradients occur in the boundary layer region near the train's nose and tail due to the pressure fluctuations described in Section 1.3. As demonstrated in Schlichting (1979), turbulent three-dimensional boundary layers in pressure gradients are difficult to characterise accurately. Empirical information is generally needed to capture the boundary layer properties. An integration approach for characterising the boundary layer is used. The concept of the integration approach is illustrated in Figure 2.3, which shows that a 'displacement thickness' parameter δ^* may be derived to describe the distance to which the boundary is displaced to yield the same mean flow rate in the absence of the boundary layer, which has a thickness of δ. The coordinate system is also shown.

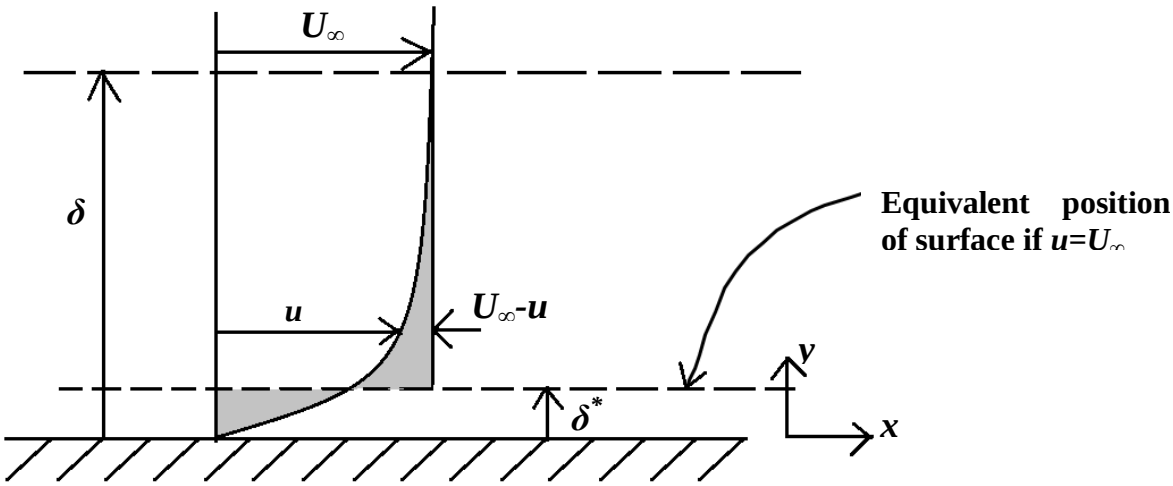

Figure 2.3: A diagram illustrating the concept of boundary layer displacement thickness.

The Von-Kármán momentum integral equation is capable of characterising two-dimensional and incompressible turbulent boundary layers:

$$\frac{d}{dx}[\theta] + (\delta^* + 2\theta)\frac{1}{U_\infty}\frac{dU_\infty}{dx} = \frac{C_f}{2} \qquad 2.19$$

U_∞ is the velocity outside the boundary layer, C_f is the skin friction coefficient, δ^* is the displacement thickness, and θ is the momentum thickness:

$$C_f = \left(\frac{\tau}{\frac{1}{2}\rho U_\infty^2}\right) \qquad 2.20$$

$$\delta^* = \int_0^\delta \left(1 - \frac{u}{U_\infty}\right) dy \qquad 2.21$$

$$\theta = \int_0^\delta \frac{u}{U_\infty}\left(1 - \frac{u}{U_\infty}\right) dy \qquad 2.22$$

where τ is shear stress and U_∞ is the free-stream velocity outside the boundary layer. The momentum thickness is referred to in a semi-empirical model of the high-speed train boundary layer (Jordan et al., 2009), and is shown later in the thesis to correlate with flows in

the wake region. The presence of pressure gradients in the boundary layer may be revealed using the shape factor (*H*) parameter:

$$H = \frac{\delta^*}{\theta} \tag{2.23}$$

This is useful as pressure gradients exist in the boundary layer region close to the nose and tail of the train. The momentum thickness and shape factor in particular have been referred to in past characterisations of the boundary layer of a high-speed train (Baker et al., 2001; Brockie and Baker, 1990), and even related to flow structures in the wake (Muld, 2012). It has been shown in numerous studies (summarised in Baker, 2010) that this approach will not provide accurate estimations of sensitive parameters such as the skin friction coefficient, as it is only truly applicable to two-dimensional equilibrium boundary layers. However, useful information can still be derived about the flow.

Jordan et al. (2009) modelled the boundary layer flow for open air operation by combining a power law velocity distribution with the momentum integral equation. The power law velocity distribution was as follows:

$$\frac{u}{u_\tau} = C_1 \left(\frac{y u_\tau}{\nu}\right)^{1/C_2} \tag{2.24}$$

in which C_1 and C_2 are constants for a given velocity distribution and u_τ is the friction velocity. The momentum integral equation was applied for this distribution, but the pressure gradient term was removed for simplification (dU_∞/dx=0), yielding:

$$\frac{d\theta}{dx} = \frac{\tau_w}{\rho V^2} \tag{2.25}$$

in which τ_w is the wall shear stress. Therefore this rule only applies to areas which are away from the train's nose and tail and geometric features which might introduce significant pressure gradients. The velocity distribution relative to the boundary layer was given by:

$$\frac{V-u}{u_\tau}=\frac{V}{u_\tau}\left[1-\left(\frac{y-\frac{Y}{2}}{\delta}\right)^{\frac{1}{C_2}}\right] \tag{2.26}$$

in which Y is the train's width. The boundary layer resultant velocity was:

$$U=1-\left(\frac{tV}{X}\right)^{-\frac{(C_2+1)}{C_2(C_2+3)}}\left(\left(\frac{y}{X}\right)-\frac{(Y/X)}{2}\right)^{\frac{1}{C_2}}\left[\frac{(C_2+2)(C_2+3)}{C}C_1^{\frac{-2C_2}{(C_2+1)}}\right]^{-\frac{(C_2+1)}{C_2(C_2+3)}}\left(\frac{Vx}{\nu}\right)^{\frac{2}{C_2(C_2+3)}} \tag{2.27}$$

in which X is the train's length. The model was calibrated against experimental data collected at full-scale in open air operation.

In tunnels, a Couette-type flow occurs in the boundary layer region due to the movement of the train relative to the tunnel wall. The analytical velocity profile in a steady two-dimensional Couette flow is of the following form:

$$u(y)=\frac{1}{2\mu}\frac{dp}{dx}y(y-h)+\frac{\nu y}{h} \tag{2.28}$$

in which h is the width of the annulus between the train boundary and the wall boundary, and μ is the dynamic viscosity. It is fundamentally a pressure-gradient-dependent velocity profile superimposed onto a linear profile. This profile type differs considerably from those encountered in open air operation in which log-law and power-law profiles are common. In tunnels, high pressure gradients occur due to the modified fluctuations around the train's nose and tail, and the passage of compression and expansion waves. Therefore the velocity profile is highly disrupted. The velocity profile is based on turbulent flow and unsteady friction generated by the rough train surface and tunnel wall. An algorithm for calculating velocity

profiles was developed specifically for one-dimensional models of trains in tunnels by Barrow and Pope (1987). The velocity profiles adjacent to the train side and tunnel wall were assumed to follow power law distributions:

$$\left(\frac{u}{u_\infty}\right) = \left(\frac{y}{\delta}\right)^{1/m} \qquad 2.29$$

m is an exponent. The train side was considered to be rougher than the tunnel wall, so *m*=7 for the smoother tunnel wall, and *m*=4 for the rougher train side. The application of these exponent values to smooth and rough surfaces is empirically sound (Schlichting, 1979). The two velocity profiles were matched by iteration using a simplified form of the momentum integral equation which took into account the train and wall shear stresses and the pressure gradient.

Experimental measurements of the boundary layer along the train side in tunnels were presented in Sakuma et al. (2010). The experiments were carried out at full-scale in the open air and in double-track tunnels, on Japanese A- and B-series Shinkansen trains. Pitot tubes were mounted to the train side in order to measure the air velocity. A power law distribution identical to Equation 2.29 was found to provide the best fit to the data. The exponent varied from *m*=8 to 10, which is much higher than the value of *m*=4 suggested by Barrow and Pope (1987). The boundary layer was thinner in tunnels compared to the open air. This would be expected as a Couette-type profile would occur.

In Sakuma et al. (2010), a number of trackside anemometers were installed in order to measure the transient air velocity. The results showed that boundary layer grew between the nose and tail of the train. The flow in the narrowest part of the annulus was predominantly longitudinal in the direction of train motion. Flow reversals were detected in the wider part of the annulus.

This thesis discusses the extent to which the simple one-dimensional and inviscid flow assumptions are valid for predicting velocity and pressure loads in the boundary layer region as the geometric parameters of confined spaces are changed. This thesis uses integral parameter analysis techniques to determine how the boundary layer is affected by confinement, and how the boundary layer characteristics affect the flow in the wake. From this thesis, it is hoped that a better understanding may be obtained on when simplifying assumptions may be appropriate for modelling the flow.

2.4 Tail and wake region

The highest transient velocity gusts tend to occur in this region (Baker et al., 2013a), imposing dynamic loads on people and trackside objects. This region is therefore the focus of much research (Muld, 2012). A static pressure fluctuation also occurs around the train's tail, which is generally lower in magnitude than that around the nose due to flow separation, but which may induce fatigue cycles on trackside structures. The static pressure fluctuation is generally ignored in the literature for trains operating in the open air, as the fluctuation around the nose is often higher. This thesis investigates the effect of changing geometric parameters of confined spaces on the flow in the tail and wake region, including maximum gust loads.

The dominant flow structures influencing the maximum trackside gusts vary considerably with the shape of the train's tail (Baker et al., 2013a). The general wake patterns have been assessed in numerous studies of high-speed trains operating in the open air. Baker (2001) found by analysing the Strouhal number (a dimensionless eddy shedding frequency $St=f\ Y/V$) that there are certain flow structures in the near-wake which apply broadly to streamlined high-speed trains. These include separated shear layers caused by detachment of the boundary layer, and longitudinal helical vortices which are shed from the left and right sides of the

train's tail with a characteristic frequency. The helical vortices decay rapidly so that lower frequency flow oscillations remain in the far wake. These oscillations may be characteristic of the entire wake. The dominant flow structures influencing the wake patterns vary with the properties of the boundary layer. For example, an experimental study of the flow over a flat plate with a blunt trailing edge (Rowe et al., 2000) found that *St* varied with the boundary layer momentum thickness. This finding was replicated for high-speed trains by Muld (2012).

An empirical fitting function was developed in Jordan et al. (2009), describing the time averaged resultant velocity between the boundary layer region and near wake region (from the train's tail to ten train heights into the boundary layer):

$$\frac{U}{V} = \frac{U_{max}}{V} \exp\left(-B\sqrt{x_V^2 + y_V^2} - r\right) \qquad 2.30$$

In this function, B is a fitting constant, U_{max} is the slipstream velocity at the circumference of the vortex, r is the normalised radius of the vortex, and x_V and y_V are the normalised longitudinal and lateral distances from the centre of the vortex respectively. It is considered valid for streamlined train tails, behind which longitudinal helical vortices occur.

Baker et al. (2013a) fitted a power law function to open air full-scale measurements of the decaying air velocity in the far-wake region, in order to compare the far-wake flows between different vehicles. It is of the following form:

$$U = a_1(x_{tail})^{a_2} \qquad 2.31$$

in which x_{tail} is the distance from the train's tail, and a_1 and a_2 are constants. It was found to provide a more accurate description of the far-wake flow than other previously accepted functions.

For operation in tunnels, numerous studies have found that a particularly high maximum velocity is reached in the wake (Liu et al., 2010; Sakuma et al., 2010). This high gust affects whether track workers should be granted access to tunnels, as was found in Liu et al. (2010). A German national regulation (Deutsche Bahn, 2003) includes a relationship between the maximum air velocity in tunnels, the train speed, and the ratio of the cross-sectional areas of the train and tunnel. However, its derivation is unclear, and a comparison between prediction and experiment (Busslinger et al., 2009) found that its use may lead to over-predictions of air velocity. Simple models for the change in air pressure rely on an assumption of inviscid steady one-dimensional flow. These models would be inaccurate for the wake region due to the effects of large scale unsteadiness and highly three-dimensional flow structures (vortices or separation bubbles), unless their influence on the essential flow structures could be deemed negligible.

The 'piston effect' described in Section 2.2 is also characterised by a movement of the air column behind the train's tail due to expansion. This is related to the ratio of the cross-sectional area of the train to that of the tunnel (blockage ratio). It can be a dominant flow phenomenon in tunnels. One simplified semi-empirical model from Vardy (1996) takes the extended Bernoulli equation as:

$$\left(p_3 - \frac{1}{2}\rho u_3^2\right) - \left(p_4 + \frac{1}{2}\rho u_4^2\right) = k_T \frac{1}{2}\rho u_3^2 \qquad 2.32$$

in which subscript 3 represents a measurement upstream of the train's tail, and subscript 4 represents a measurement a certain distance downstream of the tail (one or two train diameters downstream of the tail), and k_T is a tail pressure loss coefficient. Further assumptions may regard the conditions as analogous to a flow through a sudden expansion. The expansion assumption would be less accurate for streamlined train tail shapes.

In partially-enclosed tunnels, the analytical model developed by Iida et al. (2005) predicts the flow around the tail of the train in the same manner as around the nose. The 3D potential flow equation (Equation 2.14) is combined with the Bernoulli model of the flow around the discontinuity representing the train's tail:

$$u(x) = \begin{cases} V, & (x \le X - \Delta x_t) \\ \frac{V}{2}\left\{\cosh\left(\sqrt{2}\beta_1 x + C_t\right) + 1\right\}, & (X - \Delta x_t < x < X) \\ \frac{(1-\beta)V}{\alpha_R}, & (X \le x) \end{cases} \qquad 2.33$$

$$p(x) = \begin{cases} 0, & (x \le X - \Delta x_t, X \le x) \\ -\frac{1}{8}\rho V^2\left\{\cosh 2\left(\sqrt{2}\beta_1 x + C_t\right) - 1\right\}, & (X - \Delta x_t < x < X) \end{cases}$$

β_1 is defined in Equation 2.16, and:

$$C_t = \cosh^{-1}\frac{(2-\alpha_R)}{\alpha_R} - \sqrt{2}\beta_1 X, \qquad \Delta x_t = \frac{1}{\sqrt{2}\beta_1}\cosh^{-1}\frac{(2-\alpha_R)}{\alpha_R}, \qquad \alpha_R = \frac{2 - 2\beta + \beta^2 + \mathrm{k_T}\beta^2}{2} \qquad 2.34$$

C_t and α_R are constants, Δx_t is used to define the starting point of the pressure rise, and k_T is the tail loss coefficient. The velocity and static pressure gradually build up starting from point X-Δx_t, then both reach a peak at the location of the train tail (at x=X) before sharply 'stepping' back to free-stream velocity V and zero static pressure respectively. This is illustrated in Figure 2.2(a). Its combination with the 3D potential flow equation provides the smoother results around the tail illustrated in Figure 2.2(b) for different opening ratios. The inclusion of the tail loss coefficient k_T is essential for modelling the effect of flow separation on the results, which is not otherwise modelled due to the potential flow assumption of irrotational and inviscid flow which prevents flow separation. However its value must be derived from experiment or further assumptions.

This thesis discusses the extent to which changing the geometric parameters of confined spaces affects the assumptions made by models relating to the tail and wake region, for example: a specific type of loading pattern occurs for a certain ‘type’ of structure; pressure wave reflections are ignored and the tunnel is presumed to have infinite length; the three-dimensional components of the flow are negligible; and the effect of air viscosity and rotationality may be ignored. From this thesis it is hoped that the ranges of geometric parameters for which such assumptions would be valid can inform the modelling procedure.

Chapter 3

Methodology

This chapter describes the experimental methodology and how it fulfils the requirements of Objectives 1, 2 and 3 of this thesis. It is described in eleven sub-sections. The TRAIN Rig facility is described in Section 3.1. The train model is described in Section 3.2. The experimental variables and coordinate systems are described in Section 3.3. The velocity and pressure sensors are described in Section 3.4. The test cases and structures are defined in Section 3.5, as well as the positions of the sensors in each test case in Section 3.6. The test speed is explained in Section 3.7. The ensemble analysis technique is explained in Section 3.8. The low-pass filtering approaches for smoothing the data are defined in Section 3.9. The uncertainty of the results is assessed in Section 3.10. Finally, the extent to which the methodology conforms to requirements in codes of practice is appraised in Section 3.11.

3.1 TRAIN Rig facility

This section describes the TRAIN Rig experimental facility and explains its advantages and disadvantages relative to alternative facilities and test methods.

Reduced-scale model vehicles are propelled along a straight track past stationary sensors and structures. The track is divided into three 50m long sections: an ‘accelerating section’; a ‘test section’; and a ‘braking section’. A Kevlar rope sling attached to the underside of the vehicle catapults the vehicle along the acceleration section to a speed as close as possible to its desired velocity. The desired velocity is achieved by adjusting the catapult force. The vehicle is released from the sling at the start of the test section, causing it to free-wheel through the test section whilst naturally decelerating. When the vehicle reaches the brake section, a hook on its underside catches a Kevlar rope which pulls a piston through a tightly fitting tube in order to dissipate the kinetic energy of the vehicle.

The time interval between train passages is approximately 10 minutes due to the need to reset the apparatus between each test. Figure 3.1 is a schematic representation of the TRAIN Rig showing the layout of the three track sections, the catapult and the braking mechanism. Figure 3.2 is a photograph of the test section taken from the end of the accelerating section. The experiments were carried out on the track on the left side of the photograph. The track enters a circular tunnel which is visible in the background. The presence of the tunnel meant that 10m of the test section was available for carrying out the experiments.

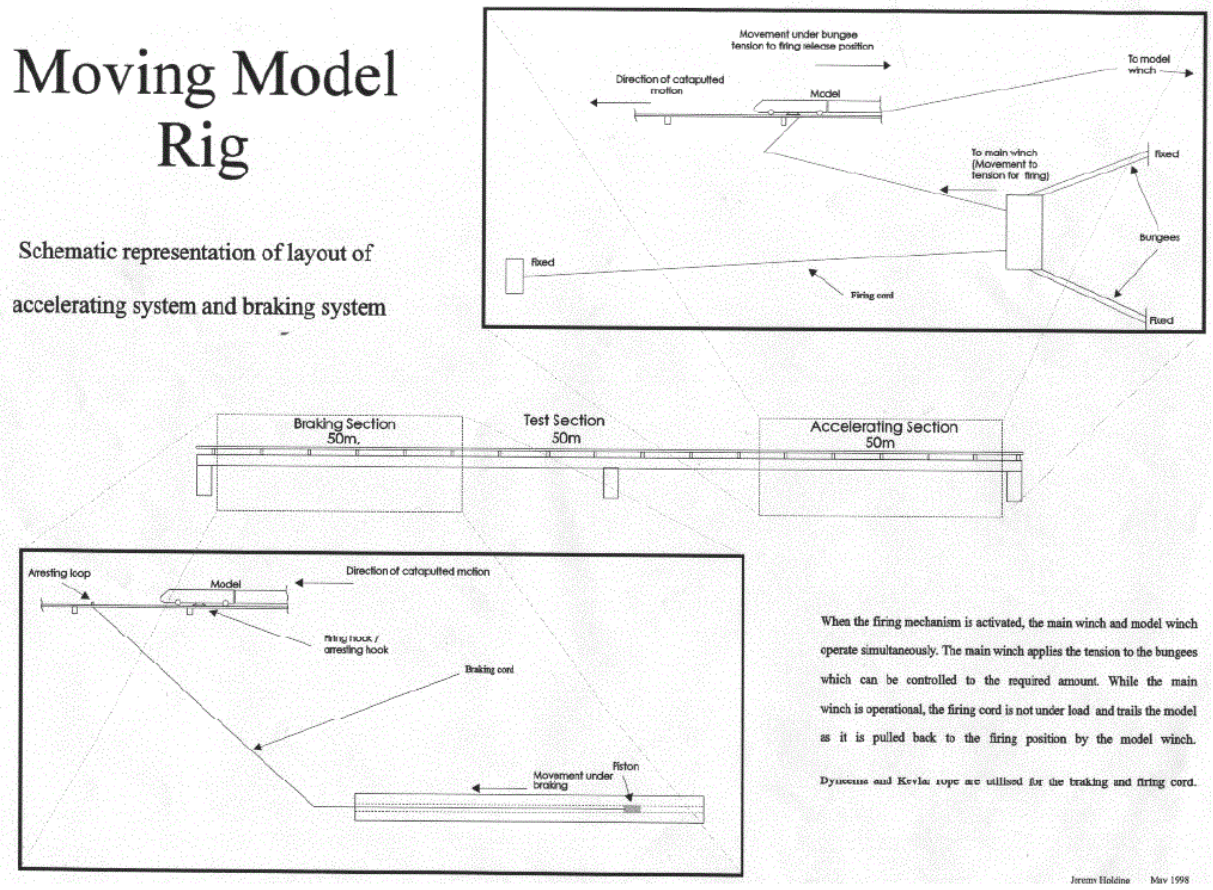

Figure 3.1: Schematic of the TRAIN Rig (Baker et al., 2001).

Figure 3.2: Photograph of the TRAIN Rig's test section.

The track bed arrangement was aerodynamically similar to a 'slab-track' system. It was flat and smooth, so its aerodynamic surface roughness was lower than what would be expected on a ballasted track. This track bed profile has been used in past moving-model studies including Baker et al. (2001) and Temple and Dalley (2001). Aerodynamic data collected using this track bed profile has previously been compared directly with data from full-scale experiments in which the track was ballasted and featured ballast shoulders on either side of the tracks (Temple and Dalley, 2001; Sterling et al., 2008). The sensors in the moving-model study were higher above the ground, due to the relatively lower ground level of the slab-track configuration. The uncertainty associated with this was deemed to be secondary to other sources of uncertainty. Nevertheless, slab-track configurations are increasingly preferred in planned high-speed lines for reasons relating to maintenance and loads (Johnson, 2012). This makes the choice of track bed arrangement for these tests increasingly relevant as slab track becomes a dominant configuration for high-speed rail.

Alternative testing methodologies include full-scale tests, wind tunnels, moving-model tests on circular tracks, and CFD simulations. Their advantages and disadvantages are described in what follows.

Full-scale tests provide results which are least susceptible to Reynolds number scale effects. However, these tests would require costly and time-consuming construction work to erect the confining structures. Moreover, uncontrollable variations in environmental conditions and the speeds of passing trains would compromise the accuracy of the results. For example, Quinn et al. (2011) showed a correlation between natural wind, at a range of low yaw angles ($\pm 2^{o}$), and the magnitudes of slipstream velocity gust peaks. The yaw angle is the orientation of the natural wind with respect to the direction of train travel.

Wind tunnel tests may be used to collect a large volume of data in a short time. However, these tests are unable to capture the full-scale Reynolds number or the relative motion between the train and structure surfaces, both of which affect the characteristics of the flow (evidenced in Chapter 2).

Moving model tests may be undertaken in order to capture the relative motion correctly, by using either straight-track facilities such as the TRAIN Rig or circular track facilities such as the one used in Del Valle (2012). If a large number of train passes is needed within tight time constraints, circular tracks provide an advantage compared to other methods because the time interval between vehicle passes is of the order of seconds rather than the 10 minutes which are required in the TRAIN Rig. However, the centrifugal effect of the circumferentially moving train on the slipstream reduces the accuracy of the results. Whilst this has been addressed in Del Valle (2012) for open air tests, significant work outside the scope of this thesis is needed in order to determine the accuracy of this method when confining structures are used.

CFD simulations can capture the relative motion between the train and structure surfaces, and allow the entire flow field around the train to be visualised. In order to satisfy Objective 4, a Large-Eddy Simulation (LES) approach would be necessary to accurately model the flow patterns and maximum gusts (Hemida et al., 2010), or a Detached Eddy Simulation approach (DES) (Muld, 2012). Muld's DES approach was tailored to provide a saving in computational time compared to LES, but the computational time was reportedly 500 hours on at least 64 processor cores. This time could be longer in tunnel cases where compressible effects would need to be accounted for. By contrast an experiment at the TRAIN Rig could be completed in between two hours and two days. Overall, the TRAIN Rig represented a satisfactory compromise between accuracy and the number of train passes and test cases desired.

3.2 Train model

A TRAIN Rig-compatible train model was constructed. The decision to use only one train model was taken in order to focus on testing the maximum number of structure variations within the available time. The model was based on a DB-operated ICE2 high-speed train, an example of which is shown in Figure 3.3

Figure 3.3: Photograph of an ICE2 train (© Sebastian Terfloth, Wikimedia Commons).

A comparison study was necessary in order to validate the methodology, due to the original nature of this research. This meant that data had to exist for the same model and at least one of the cases considered in this research. The ICE2 shape met this criteria because it has previously been used in tests conducted using various different experimental techniques (Baker et al., 2001; Temple and Dalley, 2001; Baker et al., 2013b; Schultz, 1990; and Del Valle, 2012).

A photograph of the model is shown in Figure 3.4. A general arrangement of the model is shown in Figure 3.5.

Figure 3.4: Photograph of the ICE2 model.

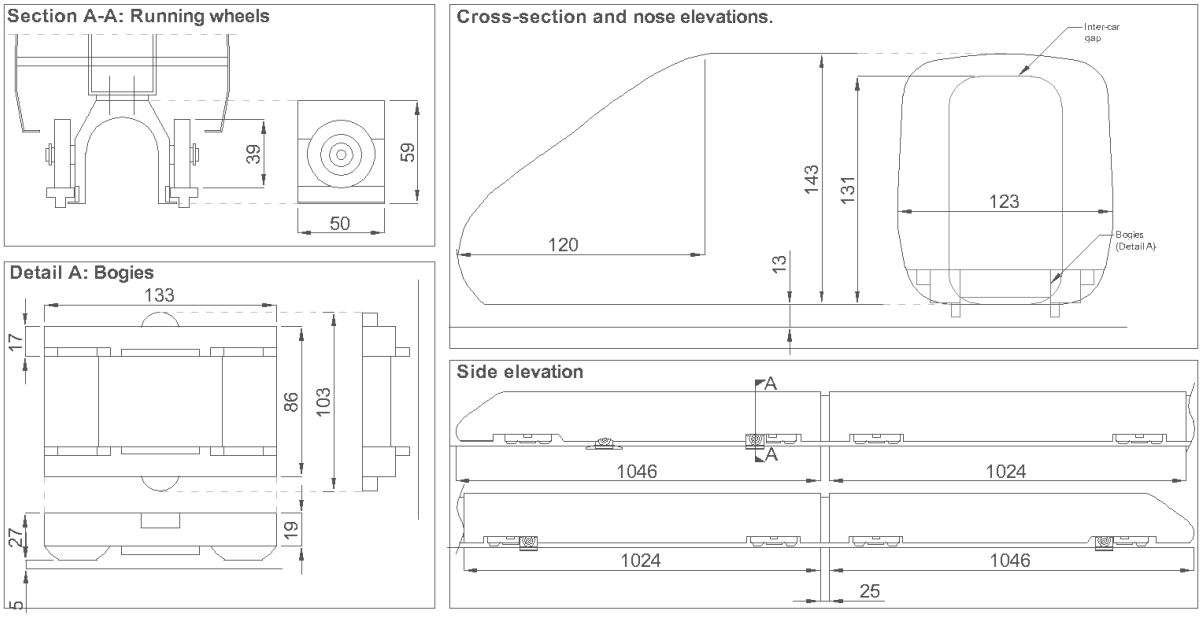

Figure 3.5: Elevations of the ICE2 model, with key dimensions shown in mm (1/25 scale).

The model geometry was simplified compared to the full-scale train, which therefore altered its aerodynamic shape. The model featured four carriages - this is fewer than the full-scale train which operates in eight- or sixteen-carriage consists. A pantograph was not added to the model roof. The model was fitted with wooden bogies which were similar to typical bogies used on the ICE2 but simpler in shape. Dummy wheels were added which did not make contact with the rails. Figure 3.6 shows a photograph of a bogie-wheel arrangement alongside an illustration of a typical full-scale bogie-wheel arrangement.

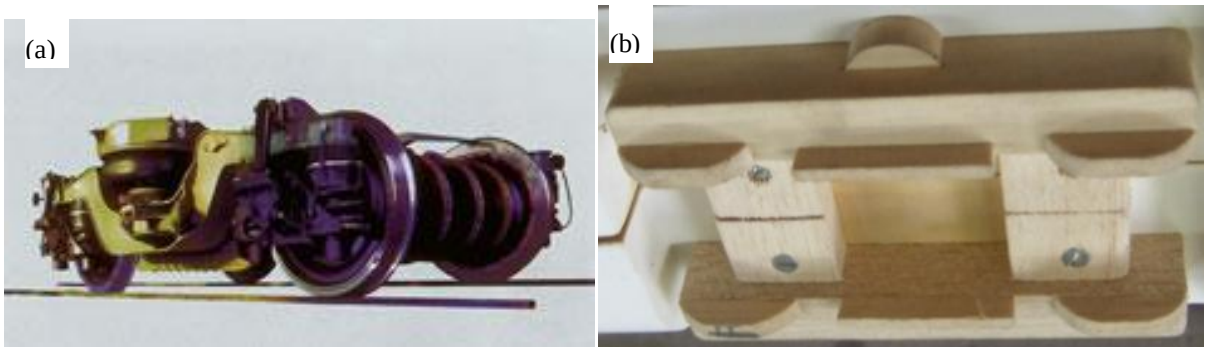

Figure 3.6: (a) Bogies used on operational ICE2 trains (© Transtec Vetschau GmbH); (b) Bogies used on model ICE2.

An arrestor hook was added to the underside of the model in order to provide an attachment point for the catapult and braking ropes of the TRAIN Rig. Steel running wheels were added to the first, third and fourth carriages in order to allow the model to roll along the tracks. At the design stage it was found that the running wheels overlapped with the locations of the wooden bogies at three points, so the wooden bogies had to be modified in order to accommodate the running wheels. The attachments are visible in Figure 3.5.

The decision to test only one train model means that further work is needed in order to establish how far the discoveries made in this thesis can be applied to trains with different aerodynamic shapes. It is pertinent to consider which aspects of the train's aerodynamic shape are important. Baker (2010; 2012) described the common and unique flow characteristics of different high-speed trains. The train's nose and tail shape have the greatest effect on the airflow, because they affect the magnitudes and durations of pressure and velocity fluctuations around the nose and tail. The train's tail affects the flow structures in the wake due to the influence of its shape on the points of flow separation. The cross-sectional area and nose shape of the train affects the magnitudes of the pressure waves seen in tunnels. The unique features of the ICE2 include a lower and wider body cross-section than most high-speed trains, and a wedge-shaped nose which is relatively 'bluff' compared to more up-to-date streamlined high-speed trains such as the ICE3. The ICE2 is 50mm wider than the ICE1

at full-scale, but is otherwise aerodynamically very similar. Therefore these research findings might also apply to an ICE1 train.

3.3 Definitions of experimental variables

Figure 3.7 shows the origins of the Cartesian coordinate systems and geometric variables, showing key full-scale equivalent dimensions. They can be divided by 25 to obtain the 'as-built' dimensions. The left and right directions are defined relative to the train's direction of motion.

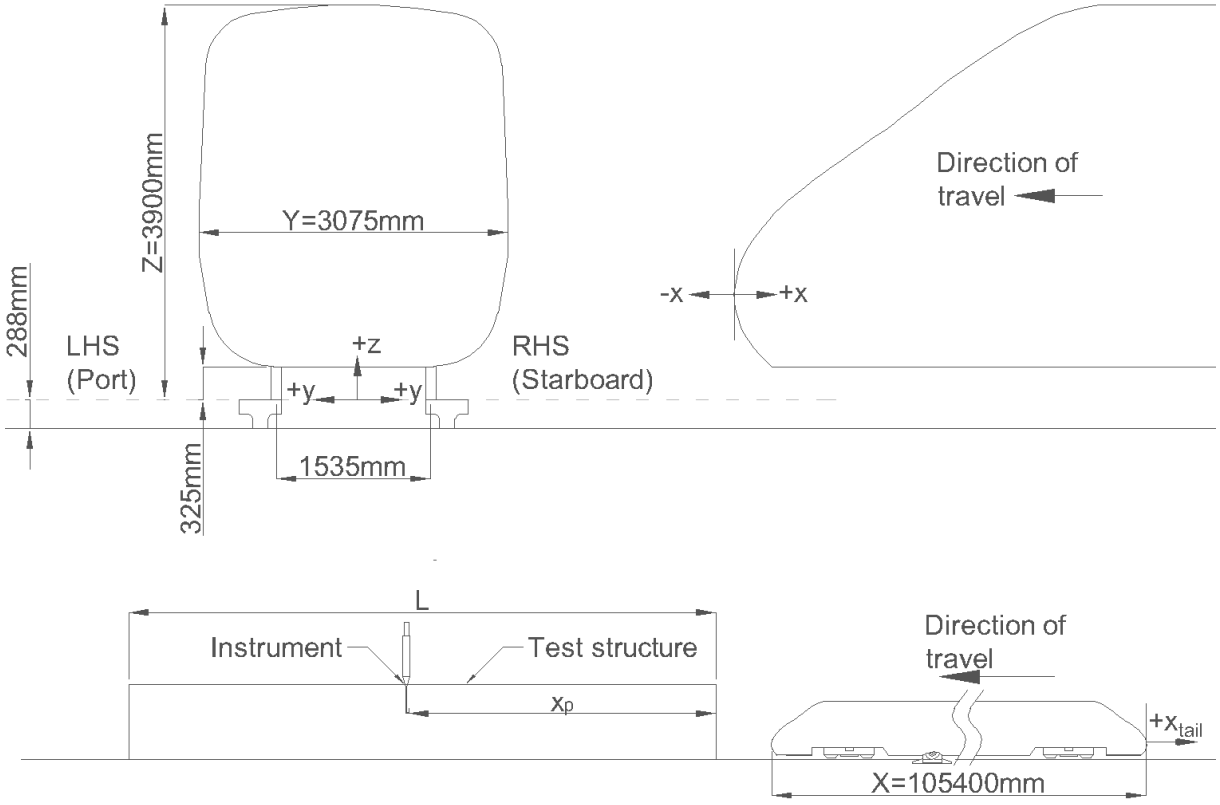

Figure 3.7: Coordinate systems, with full-scale equivalent dimensions shown.

The spatial terms are all normalised by the train's height (Z), and are defined herein: x is the longitudinal axis which originates from the tip of the train nose; X is the length of the train; y is the lateral axis which is measured as an absolute distance from the track centre; Y is the width of the train; Y_{wall} is the position of a vertical wall on the y-axis; z is the vertical axis

which originates from the railhead; Z_{ceil} is the position of a flat ceiling on the *z*-axis; L is the length of a structure; x_P is the distance of the sensor from the tunnel entrance (it is normalised by the tunnel's length in some circumstances); x_{tail} is the *x*-axis re-aligned to the train's tail.

The blockage ratio (β) is the ratio of the cross-sectional areas of the train (A_{tr}) and tunnel (A_{tun}), expressed as a percentage or decimal. The opening ratio (α) is the ratio of the length of a gap in the cross-section of a tunnel (l_{gap}) to the total internal perimeter of a tunnel (l_{per}), expressed as a percentage. This parameter has been used in a past study (Takei et al., 2008). The dimensionless spatial parameters are:

$$\left(\frac{x}{Z}\right)\left(\frac{y}{Z}\right)\left(\frac{z}{Z}\right)\left(\frac{X}{Z}\right)\left(\frac{Y}{Z}\right)\left(\frac{Z}{Z}\right)\left(\frac{Y_{wall}}{Z}\right)\left(\frac{Z_{ceil}}{Z}\right)\left(\frac{L}{Z}\right)\left(\frac{x_{tail}}{Z}\right)\left(\frac{x_P}{Z}\right)\left(\frac{x_P}{L}\right)\left(\frac{A_{tr}}{A_{tun}}\right)\left(\frac{l_{gap}}{l_{per}}\right) \quad 3.1$$

The time history sample axis has been converted to dimensionless distance along the *x*-axis (*x/Z*), in order to represent the distance of the train nose from the sensor at each sample:

$$\frac{x}{Z} = \frac{25Vn}{f_s Z} \quad 3.2$$

$$\{n \in \mathbb{Z} | -n_{nose} \leq n < N_n - n_{nose}\} \quad 3.3$$

n is the sample number relative to the train nose, n_{nose} is the sample number when the train nose passes the sensor, N_n is the number of samples in the time history, f_s is the sampling frequency, and V is a constant value of 32m/s. A constant value has been assigned rather than the recorded speed of the train, because the data have been resampled to align them to a common *x*-axis (see Section 3.8).

Flow velocities are expressed in the longitudinal (u), lateral (v), and vertical (w) directions, and a resultant (U) is calculated. More specifically: u occurs in the direction of the train's 'longitudinal' motion along the +ve *x*-axis; v occurs in the direction away from the train along the +ve *y*-axis; w occurs in the upwards direction along the +ve *z*-axis; and U occurs in the

direction calculated by the angle of the resultant velocity vector. The velocity terms are normalised by the recorded speed of the train (V_0) in order to create dimensionless groups. The data are then resampled in order to account for the variation in train speed (see Section 3.8), meaning that the final flow velocities are expressed in relation to a constant value of train speed (V=32m/s):

$$\left(\frac{u}{\mathrm{V}}\right)\left(\frac{v}{\mathrm{V}}\right)\left(\frac{w}{\mathrm{V}}\right)\left(\frac{U}{\mathrm{V}}\right) \tag{3.4}$$

The resultant velocity is defined as:

$$\frac{U}{\mathrm{V}} = \sqrt{\left(\frac{u}{\mathrm{V}}\right)^2 + \left(\frac{v}{\mathrm{V}}\right)^2 + \left(\frac{w}{\mathrm{V}}\right)^2} \tag{3.5}$$

The static pressure (P) is converted to a dimensionless static pressure coefficient (C_P) by normalizing the static pressure by the reference dynamic pressure. The dynamic pressure is referenced to the recorded speed of the train (V_0). The data are resampled in order to account for the variation in train speed, meaning that the static pressure coefficient is expressed in relation to a constant value of train speed (V=32m/s):

$$C_P = \frac{P}{0.5\rho \mathrm{V}^2} \tag{3.6}$$

where ρ is the ideal gas density of air. Pressure changes are represented by a differential pressure coefficient - the overall peak-to-peak pressure change is the differential between the maximum positive and suction pressures:

$$\Delta C_P = \max(C_P) - \min(C_P) \tag{3.7}$$

3.4 Sensors

This section describes all of the sensors used in the experiments, focusing on their performance and calibrations, and the data acquisition methods. The in-flow velocity and static pressure were measured by Cobra probes (Section 3.4.1). The static pressure on surfaces was measured using pressure tappings connected to Sensortechnics HCLA-type pressure transducers (Section 3.4.2). The train speed was measured using light-gates (Section 3.4.3).

3.4.1 Cobra probes

Cobra probes were manufactured by Turbulent Flow Instrumentation (TFI). They are a type of 'multi-hole pressure probe', and are capable of measuring the static pressure and air velocity along three orthogonal axes. They are described in TFI (n.d., 2007). Figure 3.8 shows the geometric details of the Cobra probes, and zoomed-in elevations of a sensing head. The sensing heads are 2.6mm wide at their widest points, so the disturbances to the flow caused by the sensing heads and stems are small. The sensing head features four 0.5mm diameter pressure tappings on faceted faces. The tappings are each connected to pressure transducers in the probe bodies. The transducers measure the phase- and amplitude- corrected pressure field. A calibration surface is used to calculate the dynamic pressure in three orthogonal directions, as well as the yaw and pitch angles. The velocity vectors and static pressure are then calculated.

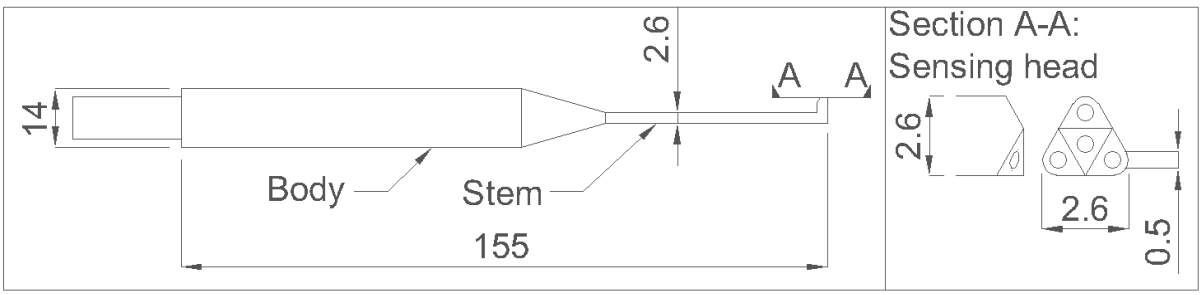

Figure 3.8: Cobra probe, with dimensions shown in mm.

The performance of the Cobra probes will be discussed using information from TFI (n.d.). Apparently they work well with air as the gas medium and do not need to be recalibrated regularly (calibrations were undertaken by the manufacturer). The frequency response is of the same order of magnitude as that achievable using hot-wire anemometry, so small-scale flow fluctuations can be measured. The Cobra probes came from two batches. The maximum calibrated frequency response was 650Hz for one batch and 2000Hz for the other. The issues relating to their different frequency responses are discussed in Section 3.9. The manufacturer claims that Cobra probes are capable of measuring flow accurately for turbulence intensities exceeding 30%. The uncertainty of the velocity and pressure is discussed in greater detail in Appendix A2 and is summarised in Section 3.10.

Reference pressure ports on the Cobra probes were connected to silicone tubes, the vents of which were used to measure the atmospheric pressure. The vents were sited far away from the flow disturbances caused by the passing train and other sources of air movement. The vents were located underneath the elevated concrete deck which contained the tracks (seen in Figure 3.1), at a section in which the tracks were completely in a permanent tunnel.

Cobra probes have a flow angle of receptivity of $<45^{o}$ of the total flow angle relative to the longitudinal velocity axis (the +ve *x*-axis). This limits their range of detection. When the angle of receptivity is exceeded, the data for each affected sample is replaced with a null value. Null values cause gaps in the time history data ('dropouts'). Many of the dropouts were compensated for by undertaking numerous repeats and using the ensemble averaging technique explained in Section 3.8. Nevertheless, some visible gaps appeared in the time histories in regions where the flow angle regularly exceeded the angle of receptivity, such as around the train's nose.

The data were sampled by an interface supplied by TFI. The sampling rate was set to a frequency of 5kHz. The Cobra probes were ‘zeroed’ between every run, which aligned their zero ordinates to the ambient air.

Circular holes were drilled into the walls of the test structures in order to accommodate the probe bodies. The annular gaps between the probe bodies and structures were sealed with masking tape on both the inner and outer sides of the walls. It was not possible to use a higher performance seal as the Cobra probes needed to be removed and replaced once every day.

3.4.2 Pressure transducers

The pressure transducers came from the Sensortechnics HCLA 12X5PB series. They are described in Sensortechnics (2010; 2013a; 2013b). The frequency response is 2kHz and the measuring range is ±1250Pa which was sufficient to avoid clipping. The sensors inside the transducers constitute piezoresistive Wheatstone bridges embedded into silicon-based diaphragms. The transducer circuits perform digital signal conditioning but the output signal is analogue. The signal conditioning corrects for error sources including offset, span, temperature effects, non-linearity and hysteresis. The output signal is single-ended, which would make it more susceptible to electromagnetic interference in transmission. However, the effect of interference is reduced because the transducer circuits amplify the output signals. The transducers have very low position sensitivity, so mechanical vibrations transmitted from the TRAIN rig to the transducers caused minimal oscillations in the recorded data.

The pressure transducers were connected to tappings on the structure surfaces. The diameters of the tappings were 1.8mm. The tappings were drilled into surfaces which were oriented along the direction of train motion.

The connections between the tappings and the transducers were made by silicone tubes with internal diameters of 1.8mm and lengths of 30mm±5mm. The chosen lengths of the silicone tubes between the tappings and the transducers ensured that the first acoustic resonant node frequency was 2.75 kHz, which was higher than the calibrated frequency response of the pressure transducers. Therefore, resonance did not affect the pressure measurements within the calibrated frequency range.

Reference pressure ports on the transducers were connected to silicone tubes which were vented to the same location as the Cobra probe reference tubes.

The output signals of the pressure transducers were recorded to a 16-bit Measurement Computing LGR-5325 data logger. The logger's sampling rate was 5kHz to match that used for the Cobra probes. The output signal corresponds to the differential pressure between the pressure tapping and reference tube.

Steps were taken in order to reduce electromagnetic interference effects in the 15m long cables carrying the signals from the transducers to the data logger. The cables carrying the supply voltage were not shared with the cables carrying the output and ground signals. Moreover, the four-core cable carrying the output and ground signals used two cores per-signal rather than one. The cables were also screened by a shield carrying the ground signal.

Dorigatti (2013) provided calibration data for the pressure transducers. Linear voltage-pressure scaling was found to be inaccurate. A cubic polynomial function was found to be at least twice as accurate as linear scaling. It is of the form:

$$P = c_3E^3 + c_2E^2 + c_1E \qquad 3.8$$

in which c_1-c_3 are coefficients which are given in Table 3.1, and E is the voltage measured by the transducers after a formula was used to align 0V to 0Pa by subtracting the average voltage over 5500 samples ahead of the train nose (n_{nose}) from the raw voltage (E_{raw}):

$$E = \left(E_{raw} - \frac{1}{5500} \sum_{n=n_{nose}-9000}^{n_{nose}-3501} E_{raw}[n] \right) \quad 3.9$$

The cubic polynomial was shown to improve the calibration accuracy compared to a linear pressure-voltage scaling. Table 3.1 references the calibration constants with the ID numbers that were written on the transducers. The database described in Appendix B may be used to match the results to a particular transducer ID.

Table 3.1: List of transducer calibration coefficients.

Coefficients	Transducer ID										
	2	**3**	**4**	**5**	**6**	**7**	**8**	**9**	**10**	**11**	**12**
c_3	1.413	1.489	1.534	2.507	2.121	1.44	1.087	1.328	2.159	1.499	1.558
c_2	-0.139	0.217	0.077	-0.533	-1.159	-0.701	0.003	-0.209	-0.081	-0.468	0.088
c_1	614.41	615.42	614.31	612.27	601.99	617.11	618.95	614.93	612.19	614.85	613.95

Environmental readings were collected in order to estimate the air density for each run which was needed in order to calculate the static pressure in Equation 3.6. The pressure was measured with a GBP3300 Digital Barometer. The temperature and humidity were measured by an Oregon Scientific BAR208HGA weather station. The temperature varied from 1 to 15.1 Celcius over the course of the tests. The humidity varied from 63 to 88 percent. The uncertainty of the air density measurement is discussed in Section 3.10.

3.4.3 Light gates

Four pairs of 'Sick WS250-D142' photoelectric transmitters and receivers were installed in the test section of the TRAIN Rig. A 5V DC signal was produced when the beam between the transmitter and receiver was blocked by the passage of the train between them. Each

transmitter-receiver pair formed a 'light gate', and two light gates were needed in order to produce one train speed estimate. Light gate pairs were stationed at the beginning and end of the test section in the TRAIN Rig (9.125m apart), and the beams in each pair were spaced apart by 1m so that a 1m-averaged speed reading could be obtained. The output signals were sent to a bespoke interface unit which automatically calculated the 1m-averaged train speed for each light gate pair. The output signals were also recorded to the Measurement Computing LGR-5325 data logger in order to assist with the alignment of multiple train passes and the verification of train speed calculations.

3.5 Test cases and structures

Section 3.5.1 describes and illustrates the test cases and their geometric parameters, and Sections 3.5.2 to 3.5.5 explain the choices of geometric parameters for each type of test case.

3.5.1 Overview of test cases

The structures transitioned from unconfined to fully enclosed spaces, and only one parameter was changed at a time. The list below describes the test cases and parametric changes:

- The least confined case was the open air (OA: Figure 3.9(a));
- Figure 3.9(b,c,d): A vertical wall was installed with a height of z/Z=1.79 and a length of L/Z=51. The lateral separation of the 'Single Wall' from the tracks was changed, so that Y_{wall}/Z=0.84 (W1S: Figure 3.9(b)), Y_{wall}/Z=0.71 (W2S: Figure 3.9(c)), and Y_{wall}/Z=0.58 (W3S: Figure 3.9(d));
- An additional wall was placed on the opposite side of the track to form a 'Double wall' case. The separations of the 'Double Walls' from the tracks were changed (W1D, W2D, W3D). The right wall positions matched those of the single walls. The

left wall positions matched those of the single walls in cases W1D (Figure 3.9(b)) and W2D (Figure 3.9(c)), making these two cases symmetrical about the *z*-axis. However case W3D (Figure 3.9(d)) was asymmetrical because the left wall was placed further away at Y_{wall}/Z=0.84 while the right wall was placed at Y_{wall}/Z=0.58.

- An enclosed 'tunnel' was created by placing a ceiling over 'Double Walls' case W1D (T2, T3, T4). Tunnel T2 (Figure 3.9(f)) was the same length as the wall cases (L/Z=51). Tunnel T3 (Figure 3.9(g)) was shorter at L/Z=13, and T4 (Figure 3.9(h)) was the shortest at L/Z=5. A longer tunnel was tested (T1: Figure 3.9(e)) with L/Z=147, and its cross-section was circular because it was an existing structure at the TRAIN Rig. The blockage ratio was β=0.23 in all cases.

- 'Partially-enclosed tunnels' were formed by one or more openings which ran along the lengths of various tunnels. The widths of the openings were changed in order to control the opening ratio (α). For T2 (β=0.3) (Figure 3.9(i)), the opening ratios are $\alpha\approx$0.4% and α=1%. For T3 (β=0.23) (Figure 3.9(g)), the opening ratios are α=0.2%, 0.4%, 1.4% and 4.3%. For T2 (β=0.23) (Figure 3.9(f)), the opening ratio is $\alpha\approx$0.4%.

- The tunnel ceiling was lowered to Z_{ceil}/Z=1.36 in order to raise the blockage ratio, for T2 ($\alpha\approx$0.4%) (Figure 3.9(i)) and T3 ($\alpha\approx$0.4%) (Figure 3.9(i)).

Cross-section views and structure geometries are shown in Figure 3.9 and Table 3.2. A database accompanying this thesis, described in Appendix B, also includes the full geometries of each test case, and details of the sensors used in each test case.

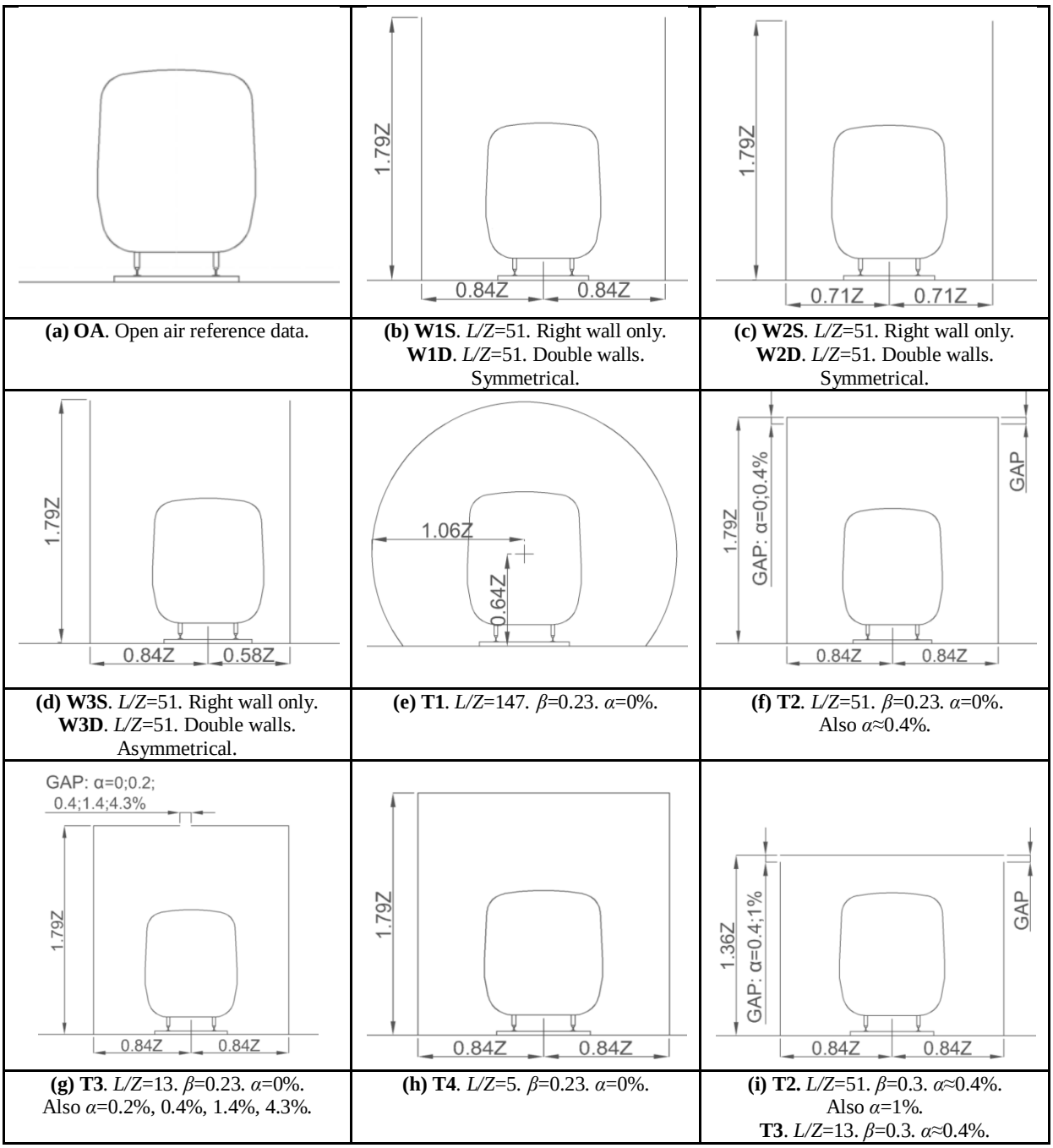

(a) OA. Open air reference data.

(b) W1S. *L/Z*=51. Right wall only. **W1D**. *L/Z*=51. Double walls. Symmetrical.

(c) W2S. *L/Z*=51. Right wall only. **W2D**. *L/Z*=51. Double walls. Symmetrical.

(d) W3S. *L/Z*=51. Right wall only. **W3D**. *L/Z*=51. Double walls. Asymmetrical.

(e) T1. *L/Z*=147. β=0.23. α=0%.

(f) T2. *L/Z*=51. β=0.23. α=0%. Also $\alpha\approx$0.4%.

(g) T3. *L/Z*=13. β=0.23. α=0%. Also α=0.2%, 0.4%, 1.4%, 4.3%.

(h) T4. *L/Z*=5. β=0.23. α=0%.

(i) T2. *L/Z*=51. β=0.3. $\alpha\approx$0.4%. Also α=1%. **T3**. *L/Z*=13. β=0.3. $\alpha\approx$0.4%.

Figure 3.9: Cross-section views and geometric details of all test cases.

Table 3.2: Geometric details of all test cases.

Structure geometry:		**OA**	**W1S**	**W2S**	**W3S**	**W1D**	**W2D**	**W3D**	**T1[1]**	**T2**	**T2**	**T2**	**T2**	**T3**	**T3**	**T3**	**T3**	**T3**	**T3**	**T4**
Length	*L/Z*		51	51	51	51	51	51	147	51	51	51	51	13	13	13	13	13	13	5
Left wall separation	*y/Z*					0.84	0.71	0.84		0.84	0.84	0.84	0.84	0.84	0.84	0.84	0.84	0.84	0.84	0.84
Right wall separation	*y/Z*		0.84	0.71	0.58	0.84	0.71	0.58		0.84	0.84	0.84	0.84	0.84	0.84	0.84	0.84	0.84	0.84	0.84
Height	*z/Z*		1.79	1.79	1.79	1.79	1.79	1.79		1.79	1.79	1.36	1.36	1.79	1.79	1.79	1.79	1.79	1.36	1.79
Opening ratio	α (%)					24	24	24	0	0	≈0.4[2]	≈0.4[2]	1	0	0.2	0.4	1.4	4.3	≈0.4[2]	0
Blockage ratio	β								23	23	23	30	30	23	23	23	23	23	30	23

Notes: [1] See Figure 3.9 for the geometry of T1. [2] See Section 3.5.4 for explanation.

All structures apart from T1 were constructed from medium density fibreboard. T1 was constructed from fibreglass. The internal surfaces were made hydraulically smooth by countersinking then taping over all fixings. All contact edges between the walls, ground and ceilings were sealed with silicone to prevent air leakage.

3.5.2 Open air

Open air tests were undertaken in order to provide reference 'least confined' data for all Cobra probe positions. The results were compared with those from previous studies in order to validate the methodology.

3.5.3 Walls

In the 'Single Wall' tests, a wall was placed on the right side of the tracks ('RHS' in Figure 3.7). A photograph is shown in Figure 3.10(a). The end of the wall is separated from the entrance to the tunnel by x/Z=8. Three lateral wall separations were included with equal increments of y/Z=0.13 in order to determine the effects of wall proximity on the flow.

The furthest wall separation was Y_{wall}/Z=0.84 in case W1S. Various codes of practice permit a continuous walkway running alongside the tracks (at full-scale) for this wall separation. Worker access would therefore be permitted during train operation, for operating train speeds

of 200km/h in the UK (RSSB, 2011) or 160km/h in Germany (EUK, 1999). Closer wall separations were included, including W2S, at Y_{wall}/Z=0.71, and W3S, at Y_{wall}/Z=0.58. The latter separation is the minimum allowed in EN 14067-4 (BSI, 2005) for applying predictive formulae describing the aerodynamic pressures on flat vertical structures parallel to the tracks. The wall heights were z/Z=1.79 in order to match the heights of the ceilings used in the rectangular cross-section tunnels for which the blockage ratio was β=0.23. The wall lengths were L/Z=51 in order to match the length of tunnel T2.

In the 'Double Wall' tests, walls were placed on the opposite side of the track ('LHS' according to Figure 3.7), in addition to the single walls mentioned in the previous paragraph. A photograph is shown in Figure 3.10(b). The left-wall separations in cases W1D and W2D were identical to those used in W1S (Y_{wall}/Z=0.84) and W2S (Y_{wall}/Z=0.71), so the configurations were symmetrical about the z-axis. It was possible to transition from wall case W1D to tunnel case T2 (β=0.23) by adding a flat ceiling only. Therefore it was possible to examine the transition from walls to tunnels. The configuration of W3D was asymmetrical (left wall: Y_{wall}/Z=0.84; right wall: Y_{wall}/Z=0.58), in order for the effect of asymmetry on the results to be assessed.

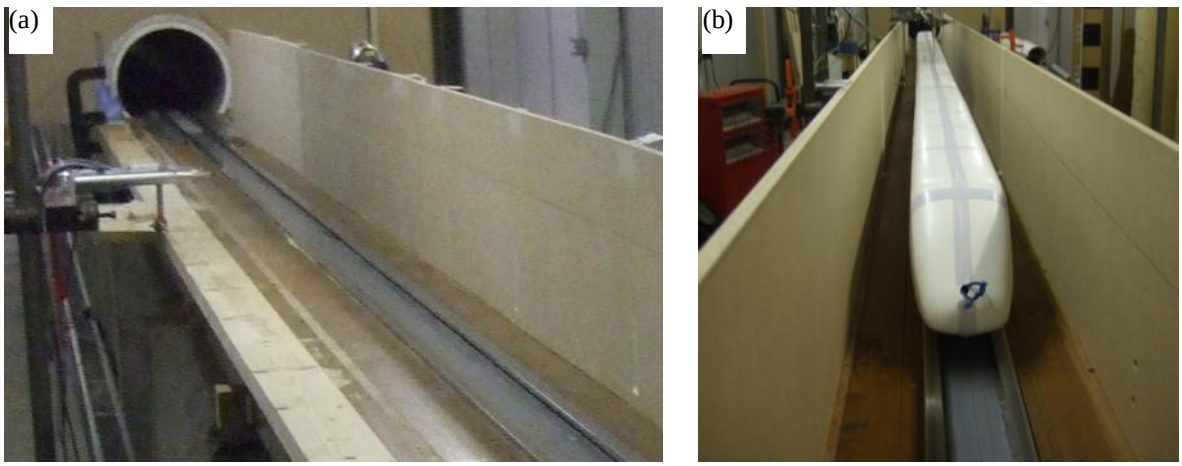

Figure 3.10: Photographs of wall structures: (a) Single Wall (W2S); (b) Double Walls (W1D).

3.5.4 Tunnels

Enclosed tunnels were built with lengths of L/Z=147 (T1 - Figure 3.11(a)), 51 (T2), 13 (T3) and 5 (T4 - Figure 3.11(b)).

(a)  (b) 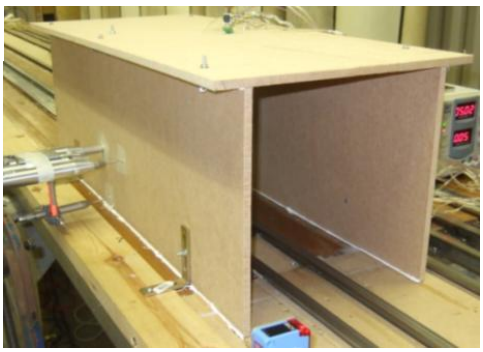

Figure 3.11: Photographs of tunnels (β=0.23, α=0%): (a) T1; (b) T4.

The blockage ratio was β=0.23 in all four tunnels. The lateral separation of the vertical tunnel walls was Y_{wall}/Z=0.84 in all cases in order to match W1D. Single-track tunnels were chosen for this study because they are increasingly favoured for future high-speed lines (Johnson, 2012). Further work is needed in order to establish whether the discoveries made in this thesis may be applied to double track tunnels which have asymmetrical cross-sections relative to the z-axis of the running line.

The longest tunnel (T1) was an existing structure at the TRAIN Rig and featured a circular cross-section. Issues relating to its different cross-section shape are discussed later in this section. The shortest tunnel (T4) was equivalent in length to a 20m long tunnel at full-scale, making it by definition the minimum length to be considered a tunnel in EN 14067-5 (BSI, 2006), and also the maximum length to be considered an 'enclosed structure' in EN 14067-4 (BSI, 2005).

Tunnels with a higher blockage ratio of β=0.3 were included, with lengths of L/Z=51 (T2) and 13 (T3). This blockage ratio was chosen because it represented the smallest possible single track tunnel that could accommodate a 'GC' loading gauge (Arup, 2010). However, there

were anomalies in the results for both of the higher-blockage-ratio tunnels (and a third case) which are investigated in Appendix A5. The cases are T2 (β=0.23 and 0.3) and T3 (β=0.3). It was found that the tunnels were not fully sealed. The seals of subsequent tunnels were improved, and one of the affected tunnels (T2, β=0.23) was re-tested. A thorough statistical analysis was carried out in order to determine the effect of the leakage on the results, and to suggest which sections of the data were not affected by the imperfect seal. From this analysis the opening ratios of the imperfectly sealed tunnels were determined to be $\alpha \approx 0.4\%$. It was found that only the velocity data in the wake region ($x/Z \geq 27$) could be regarded as $\alpha \approx 0\%$ for tunnel T2. All other data were discarded. The '≈' symbols have been used consistently in the results sections.

The tunnel cross-sections were rectangular for two reasons. Firstly, it was possible to transition from vertical walls to tunnels by just installing a ceiling, therefore ensuring that one geometric variable was changed at a time. Secondly, the guidance in EN 14067-4 (BSI, 2005) relating to predictive formulae defines a structure enclosing the tracks as being formed by combined horizontal and vertical surfaces. The structures were built according to this definition, so the results for T4 could be compared with prediction. Various geometric parameters needed to be matched in order to ensure that the circular cross-section tunnel (T1) could be considered alongside the rectangular cross-section tunnels, with the tunnel's length (L) as the only variable being changed. Therefore the cross-sectional area of the tunnel (A_{tun}) and its cross-sectional perimeter length (l_{per}) had to match between every structure. Since T1 was an existing structure which could not be modified, the rectangular tunnel geometries were adapted to match the geometric parameters. When the wall separation was fixed at the furthest wall position (W1D and W1S), giving a wall-to-wall full-scale-equivalent width of 6.535m

($Y_{wall\text{-}to\text{-}wall}$), the required tunnel ceiling height (Z_{ceil}) needed to satisfy the following formulae for A_{tun} and l_{per}:

$$A_{tun} = Y_{wall-to-wall} Z_{ceil} T_z = 45.918, \qquad l_{per} = 2(Y_{wall-to-wall} + Z_{ceil}) = 24.87 \tag{3.10}$$

If $Y_{wall\text{-}to\text{-}wall}$=6.535m was used, it was impossible for one value of Z_{ceil} to satisfy both formulae. In order to find a compromise value of Z_{ceil}, it was decided that it was more important to satisfy the formula for A_{tun}. This was because simple analytical models predicting the peak-to-peak pressure inside a tunnel (e.g. Howe et al., 2000) rely on A_{tun} but negate l_{per}. This gave Z_{ceil}=7m. This meant that l_{per} was 8.8% higher in the rectangular tunnels.

Tunnels T1, T2 and T3 featured vertical walls which were oriented perpendicular to the direction of train motion and located at the entrance and exit portals. These 'portal walls' were used in order to match the approach used in past investigations (Schultz, 1990; Straathof, 2013) which are cited as part of a comparison study (Sections 4.1 and 5.1). Experiments were undertaken for T3 (L/Z=13, β=0.23, α=0%) in order to investigate the effect of removing the portal walls on the static pressure results. The portal walls were found to increase the maximum static pressure by 2.5%±0.3%. Tunnel T4 did not feature portal walls as it came under the EN 14067-4 (BSI, 2005) code definition of a 'closed structure enveloping the tracks over a limited length up to 20m', which does not require portal walls.

3.5.5 Partially-enclosed tunnels

Partially-enclosed variations of T3 and T2 were included. Photographs are shown in Figure 3.12. A continuous slit was cut along the length of the ceiling of T3 in the x-axis at y=0. Brackets held the two halves of the ceiling together in order to retain its stiffness and prevent mechanical oscillations due to aerodynamic loads. The width of the slit was adjustable, so four opening ratios were included: α=0.2% (shown in Figure 3.12(a)), 0.4%, 1.4% and 4.3%

(shown in Figure 3.12(b)). The static pressure loading pattern was most sensitive to changes in the opening ratio when it was low. Therefore, the increments of opening ratio were initially small. The highest opening ratio was limited by the maximum extendibility of the brackets. However, two 'extreme' opening ratios were also possible by considering the double-wall case W1D and the enclosed tunnel T3, in which α=24% and 0% respectively.

The opening size was increased by sliding the left portion of the ceiling away from the immovable right side which contained the pressure tappings. Consequently the tappings maintained constant lateral positions relative to the track centreline. Therefore, when the gap was at its widest (α=4.3%), the eccentricity of the gap centreline from y/Z=0 was 0.15.

T3 was shorter than the train, so it was not known whether the observations would also apply to tunnels longer than the train. T2 was longer than the train, and a partially-enclosed version existed, with $\alpha\approx$0.4%. This potentially allowed the effect of the length of partially-enclosed tunnels to be assessed. However the accuracy of the assessment was hindered by geometric differences: firstly the opening ratio was not precisely α=0.4% along the length of the tunnel; and second of all the slits in the longer tunnel ran along the eaves rather than the ceiling centreline. These differences had an unquantified effect on the results, and this is acknowledged in their analysis.

As mentioned in Section 3.5.4, the imperfect sealing of some tunnels meant that partially-enclosed variations were available. For T2 (β=0.23) the opening ratio was $\alpha\approx$0.4, and for T2 (β=0.3) the opening ratio was $\alpha\approx$0.4%. In the latter case the opening ratio was (deliberately) increased to an exact value of α=1%. (Figure 3.12(d)). For T3 the opening ratio was $\alpha\approx$0.4%.

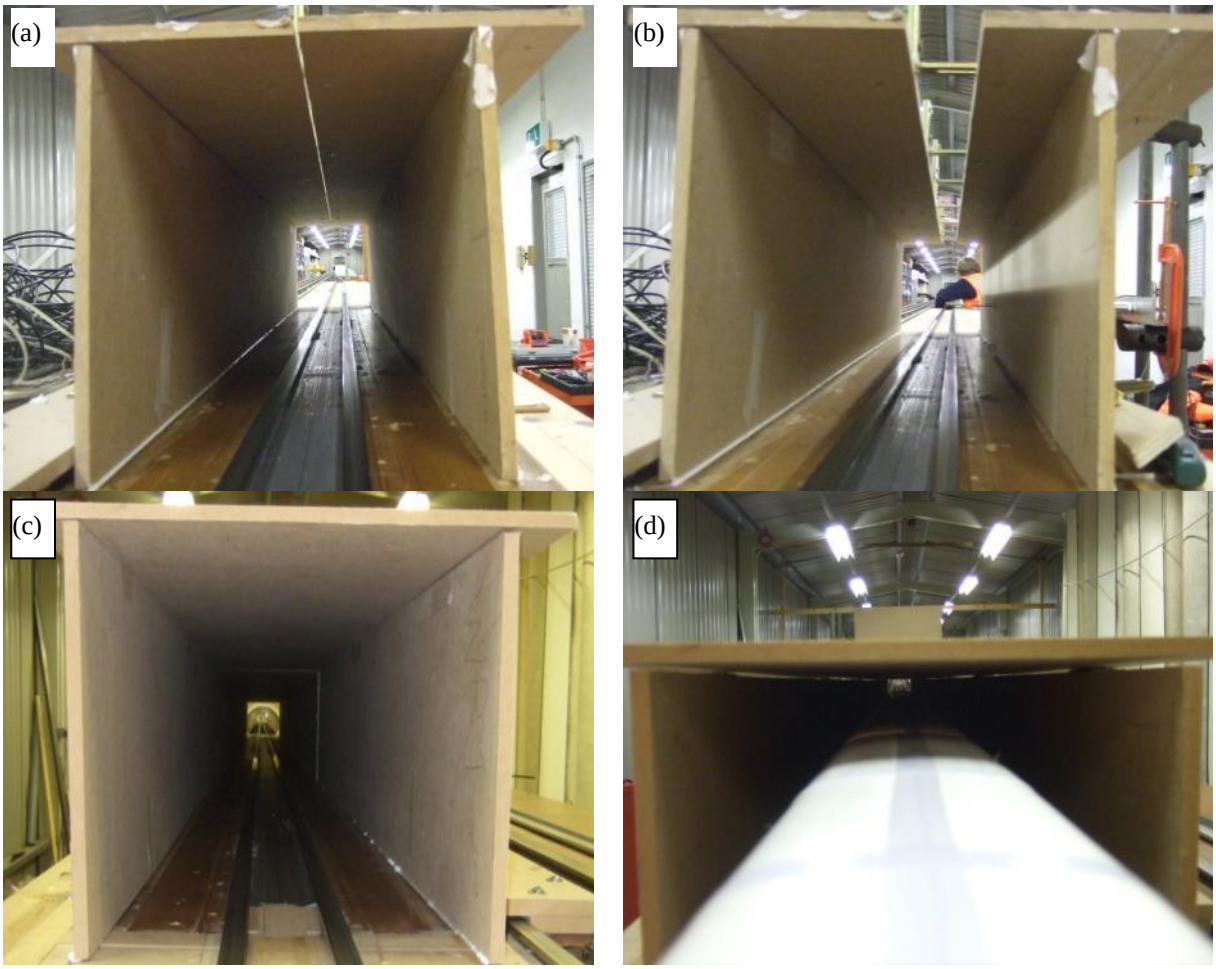

Figure 3.12: Photographs of partially-enclosed tunnels: (a) T3 (L/Z=13, β=0.23, α=0.2%); (b) T3 (L/Z=13, β=0.23, α=4.3%); (c) T2 (L/Z=51, β=0.23, α≈0.4%); (d) T2 (L/Z=51, β=0.3, α=1%).

The partially-enclosed tunnels did not feature portal walls, as portal walls are only used to represent a train entering a fully-enclosed (underground) space. Moreover, portal walls have not been used in past studies of the flow inside partially-enclosed stations (Iida et al., 2005; Muraki et al., 2010; Takei et al., 2008).

3.6 Positions of sensors in each test case

This section describes the sensor positions used in every test case, and explains the rationale for the chosen positions. The discussion is split into Cobra probes (Section 3.6.1) and Pressure tappings (Section 3.6.2).

3.6.1 Cobra probes

The Cobra probes were arranged in a way similar to that shown in Figure 3.13, on the left hand side relative to the direction of train motion. Their precise locations varied between test cases so the dimensions are not shown in the figure. The number of train passes per test case also varied between Cobra probes. Table 3.3 therefore shows a full list of Cobra probe positions as well as the number of train passes for each test case.

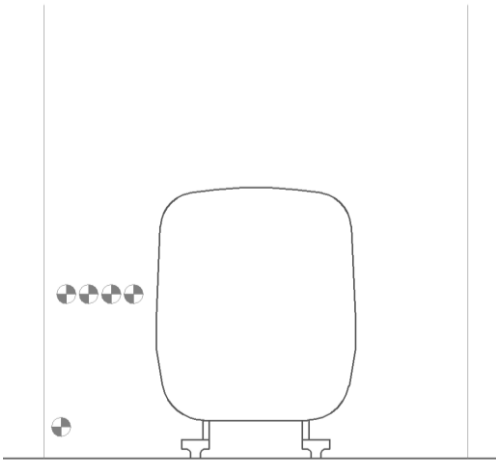

Figure 3.13: General arrangement of Cobra probes in a generic test case.

Table 3.3: Positions of Cobra probes and number of train passes (ensemble repeats).

Test cases:													
Structure geometry:		**OA**	**W1D**	**W2D**	**W3D**	**T2**	**T2**	**T2**	**T2**	**T3**	**T3**	**T3**	**T4**
Length	*L/Z*		51	51	51	51	51	51	51	13	13	13	5
Left wall separation	*y/Z*		0.84	0.71	0.84	0.84	0.84	0.84	0.84	0.84	0.84	0.84	0.84
Right wall separation	*y/Z*		0.84	0.71	0.58	0.84	0.84	0.84	0.84	0.84	0.84	0.84	0.84
Height	*z/Z*		1.79	1.79	1.79	1.79	1.79	1.36	1.36	1.79	1.79	1.36	1.79
Opening ratio	α (%)		24	24	24	0	≈0	≈0	1	0	4.3	≈0.4	0
Blockage ratio	β					0.23	0.23	0.3	0.3	0.23	0.23	0.3	0.23
y/Z	***z/Z***	**Longitudinal position (x_P/Z) and Ensemble repeats (N):**											
0.46	0.58	x_P/Z			31								
		(N)	(25)		(25)								
0.48	0.58	x_P/Z		31	31	31	31	31	31	6	6	6	3
		(N)	(60)	(25)	(25)	(25)	(15)	(25)	(25)	(25)	(16)	(16)	(23)	(15)
0.52	0.58	x_P/Z			31								
		(N)	(25)		(25)								
0.57	0.58	x_P/Z		31		31		31	31	31			5	
		(N)	(25)	(25)		(25)		(25)	(25)	(25)			(23)	
0.58	0.58	x_P/Z			34									
		(N)	(25)		(25)									
0.65	0.58	x_P/Z			31									
		(N)	(25)		(25)									
0.66	0.58	x_P/Z		34		34			34				8	
		(N)		(25)		(25)			(25)				23	
0.75	0.58	x_P/Z		31		31	31	31	31	31	5	5	5	3
		(N)	(25)	(25)		(25)	(15)	(13)	(25)	(25)	(15)	(16)	(23)	(15)
0.77	0.05	x_P/Z		32/35		32/35	31	31	35	31	6	6	9	3
		(N)	(50)/(12)	(25)/(25)		(25)/(25)	(15)	(25)	(25)	(25)	(16)	(15)	(23)	(15)
0.58	0.13	x_P/Z			32/35									
		(N)	(18)		(25)/(25)									
0.64	0.38	x_P/Z												
		(N)	(25)											
0.64	0.85	x_P/Z												
		(N)	(12)											

A horizontal line of Cobra probes extended outwards from the train side in the lateral direction, at height *z*/Z=0.58. The number of Cobra probes placed along this line varied between two and six, depending on the test case. This height was chosen so that some of the open air data could be compared directly with results from Baker et al. (2001) in a comparison study reported in Section 5.1.1. This height corresponds to the half-height of the train body. Their lateral positions were based on equal one-fifth increments of the distance between the side of the train at its widest point and the surface of the wall, so that when the walls were moved the Cobra probes could also move to fill the space. The Cobra probes were spaced by

y/Z=0.09 for the cases where the left wall was at Y_{wall}/Z=0.84. The probes were spaced by y/Z=0.06 for the case where the left wall was at Y_{wall}/Z=0.71.

The aerodynamic loads (peak velocities) on trackside workers are assessed in a way which conforms to some of the requirements set out in TSI codes of practice (TSI, 2008), which includes a specified measurement position. It is taken out of context in this research as its main requirements are for experiments to be carried out at full-scale. A trackside Cobra probe was installed in the 'TSI position', at y/Z=0.77 and z/Z=0.05 (equivalent to y=3m and z=0.2m at full-scale). This was only possible in cases where the wall separation was sufficient to accommodate the Cobra probe. The Cobra probe was moved closer to the train and slightly higher when the wall was moved closer to Y_{wall}/Z=0.71, to a position previously used in (Temple and Dalley, 2002): y/Z=0.58 and z/Z=0.13 (y=2.27m and z=0.5m at full-scale). Both of these positions are relevant to the study of aerodynamic loads on trackside workers (Section 5.3.3) as well as a comparison study (Section 5.1.2).

In the open air tests, Cobra probes were placed at the lowest and highest of seven available TSI pressure measurement positions. These positions were y/Z=0.64, and z/Z=0.38 and 0.84 (equivalent to y=2.5m, and z=1.5m and 3.3m, at full-scale). The peak-to-peak static pressure coefficient is compared directly with results from a full-scale study that formed part of the 'AeroTRAIN' project (Sima et al., 2011).

The positions of the Cobra probes in the longitudinal axis (x_P) were determined so that they were closer to the exit portal than the entrance in the longest tunnel in which they were installed (T2). This was due to the need to increase the 'fetch' from the entrance in order to allow the boundary layer and wake flow patterns to transition fully from the open air behaviour to the tunnel behaviour - highly localised flows near the entrance and exit were not desired. The longitudinal positions in the shorter tunnel (T3) were determined by design

constraints. The Cobra probes were installed approximately half-way along the length of the shortest tunnel (T4).

The Cobra probes had to be staggered slightly along the longitudinal axis in all cases due to the designs of the stands that held them in place. In some cases, Cobra probes were placed further downstream of the others at the same lateral and vertical positions in order to collect double measurements. This made it possible to perform useful studies (Appendix A4.3), including the effects on the results of: changing longitudinal positions; merging datasets of staggered Cobra probes; or replacing erroneous data from a Cobra probe. The analysis in Appendix A4.3 led to the conclusion that data from staggered probes could be merged with upstream probes or replace erroneous data. All of the data from the position at y/Z=0.66 and z/Z=0.58 was deemed unusual, so from that point onward a staggered Cobra probe was installed downstream of that position. The data for the upstream probe was later discarded, so the downstream probe provided all of the data for that position. Two Cobra probes staggered along the x-axis measured the velocity at a low-height position in many test cases, so their datasets were merged in order to increase the number of repeats and therefore reduce the uncertainty of a statistical analysis of maximum gusts which is carried out later in the thesis.

3.6.2 Pressure tappings

Figure 3.14 shows a cross-section of a typical tunnel case, with a large group of surface tappings shown on the right hand side relative to the direction of train motion. Their precise locations varied between test cases so the dimensions are not shown in the figure.

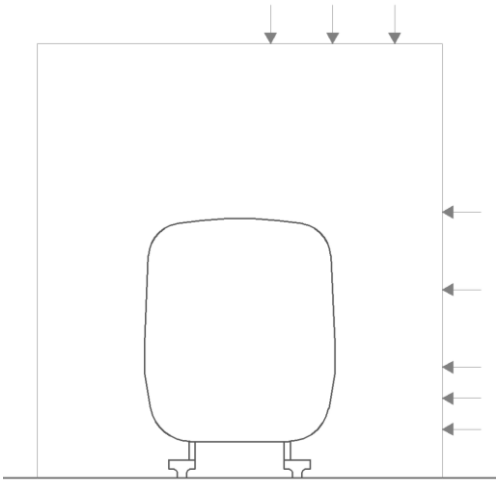

Figure 3.14: General arrangement of pressure tappings in a generic test case.

Table 3.4 shows a full list of surface tapping positions and ensemble repeats for each test case.

Table 3.4: Positions of pressure tappings and number of ensemble repeats.

Test cases																				
Structure geometry:		**OA**	**W1S**	**W2S**	**W3S**	**W1D**	**W2D**	**W3D**	**T1[1]**	**T2**	**T2**	**T2**	**T2**	**T3**	**T3**	**T3**	**T3**	**T3**	**T3**	**T4**
Length	*L/Z*		51	51	51	51	51	51	147	51	51	51	51	13	13	13	13	13	13	5
Left wall separation	*y/Z*					0.84	0.71	0.84		0.84	0.84	0.84	0.84	0.84	0.84	0.84	0.84	0.84	0.84	0.84
Right wall separation	*y/Z*		0.84	0.71	0.58	0.84	0.71	0.58		0.84	0.84	0.84	0.84	0.84	0.84	0.84	0.84	0.84	0.84	0.84
Height	*z/Z*		1.79	1.79	1.79	1.79	1.79	1.79		1.79	1.79	1.36	1.36	1.79	1.79	1.79	1.79	1.79	1.36	1.79
Opening ratio	α (%)					24	24	24	0	0	≈0.4	≈0.4	1	0	0.2	0.4	1.4	4.3	≈0.4	0
Blockage ratio	β								23	23	23	30	30	23	23	23	23	23	30	23
Right wall, middle:																				
z/Z	***x_P/Z***		**31**	**31**	**31**	**31**	**31**	**31**		**31**	**31**	**31**	**31**	**6**	**6**	**6**	**6**	**6**	**6**	**3**
0.12	*N*		2	5	2	25	25	25		15	25	25	24	5	5	4	5	9	23	9
0.26	*N*		2	5	2	25	25	25		15	25	25	24	5	5	4	5	9	23	9
0.38	*N*		2	5	2	25	25	25		15	25	25	24	5	5	4	5	9	23	9
0.71	*N*		2	5	2	25	25	25		15	25	25	24	5	5	4	5	9	23	9
1.03	*N*		2	5	2	25	25	25		15	25	25	24	5	5	4	5	9	23	9
Right wall, near entrance:																				
z/Z	***x_P/Z***								**31**	**6/28**				**3**	**3**	**3**	**3**	**3**		
0.26	*N*								25	15/15				5	5	4	5	9		
Right wall, near exit:																				
z/Z	***x_P/Z***									**33**				**10**	**10**	**10**	**10**	**10**		
0.26	*N*									15				5	5	4	5	9		
Ceiling, right hand side (z/Z=Height):																				
y/Z	***x_P/Z***									**31**	**31**	**31**	**31**	**6**	**6**	**6**	**6**	**6**	**6**	**3**
0.13	*N*									15	25	25	24	5	5	4	5	9	23	9
0.38	*N*									15	25	25	24	5	5	4	5	9	23	9
0.64	*N*									15	25	25	24	5	5	4	5	9	23	9

Notes: [1] See Figure 3.9 for the geometry of T1.

A line of five pressure tappings extended along the *z*-axis on the right wall (see 'Right wall, middle' in Table 3.4). This line of tappings was included in all test cases apart from the open air. The *z*-axis tapping positions were *z/Z*=0.13, 0.26, 0.38, 0.71 and 1.03. The lowest three positions matched those used in 'hoarding' pressure tests in reported in Baker et al. (2012). The highest two positions were spaced with increments of *z/Z*=0.32 between each other and the lowest ceiling (which was at *z/Z*=1.36).

A line of three pressure tappings extended along the *y*-axis on the right side of the ceiling, which featured in the tunnel and partially-enclosed tunnel cases (see 'Ceiling, right hand side' in Table 3.4). This line of tappings extended from the centreline (*y/Z*=0) laterally to the eaves. The tapping positions were *y/Z*=0.13, 0.38 and 0.64, which matched those used in 'overbridge' pressure tests reported in Baker et al. (2012). The tappings in the partially-enclosed tests maintained these exact positions relative to the track centre, even while the two halves of the ceiling were slid apart to increase the opening ratio. This was because the gap in the ceiling opened eccentrically with the left side sliding away from the stationary (tapped) right side.

The lines of wall and ceiling tappings mentioned above formed half a ring around the cross-sections of the tunnel and partially-enclosed tunnel cases. In the symmetrically arranged structures, all of the results are presumably symmetrical about *y/Z*=0, based on past measurements of the pressure conducted at the TRAIN Rig on the soffits of 'overbridges' (Baker et al., 2012). The 'ring of tappings' was positioned at a similar *x*-axis position to the Cobra probes, in order to accurately compare in-flow and surface pressure measurements.

In tunnels T2 and T3, a third line of pressure tappings was installed along the longitudinal *x*-axis of the vertical walls, at a uniform height of *z/Z*=0.26 (see 'Right wall, near entrance' and

'Right wall, near exit' in Table 3.4). This line intercepts the one of the tappings in the 'ring'. This allows a number of studies to be undertaken:

- The effect of position within a tunnel was studied, by changing x_P for a constant L. Small and large increments of x_P/L were included. In T2, two tappings were placed short distances downstream and upstream of the ring of tappings, so the evolution of the pressure wave was studied for small increments of x_P/L. In T3, the increments of x_P/L were large, so the near-entrance and near-exit results could be compared with those near the centre.
- The effect of tunnel length was studied by changing L for constant x_P. This was used to link T1 with T2, T2 with T3, and T3 with T4. Therefore, four values of L may be assessed.

In Tunnel T1 just one tapping was installed at height z/Z=0.26 and position x_P/L=31. The y-axis separation of the tapping from the train was different from that of the equivalent tapping used in the rectangular cross-section tunnels, due to the circular cross-section shape of the tunnel. The resulting uncertainty was deemed to be negligible as preliminary experiments revealed that the pressure waves were nearly one-dimensional at the chosen distance from the entrance.

3.7 Reynolds number

The test Reynolds number is denoted by:

$$Re = \frac{VZ}{\nu} \qquad 3.11$$

which is based on the height of the train (Z=156mm at 1/25th scale) and the desired constant train speed (V=32m/s). Therefore Re=333,000. Although higher speeds were possible at the TRAIN Rig, the selected Reynolds number matched that used in past studies by Baker et al. (2001) and Schultz (1990). EN 14067-4 (BSI, 2005) requires that the Reynolds number based on the train height must exceed Re=250,000 for moving-model testing. The requirement was exceeded in these experiments. TSI (2008) requires testing at full operational speed (280km/h), but this requirement was ignored in favour of conducting the open air tests at the same speed as that used in Baker et al. (2001) and Schultz (1990) for the benefit of the comparison study. EN 14067-4 (BSI, 2005) allows train speed variations of ±3%, but this was only achieved in 93% of the runs. Section 3.8 explains a resampling algorithm which was designed to reduce inaccuracy in the alignment of ensembles due to speed variations.

The model speed was measured by light gate pairs (Section 3.4.3) stationed at the entrance (light gates 1 and 2) and exit (light gates 3 and 4) of the test section. The 1m-averaged train speed reading at the entrance and exit of the test section was calculated by a bespoke interface unit, which timed the delay between the signals indicating the passage of the train's nose.

The train speed decreased between the entrance and exit of the test section, and the sensors were mostly placed somewhere in the middle of the test section. Therefore the train speed past the sensors was estimated by interpolating the entrance and exit readings. The interpolated speed was calculated individually for each sensor to account for their staggered positions in the x-direction. The following function was used to calculate the raw train speed, based on the assumption of linear deceleration between the light gates:

$$V_0 = \frac{V_{0,lg3lg4}\left(x_{pr:lg1lg2}\right) + V_{0,lg1lg2}\left(x_{pr:lg3lg4}\right)}{x_{pr:lg1lg2} + x_{pr:lg3lg4}} \qquad 3.12$$

The beams of the light gates are denoted by *lg1-lg4*, where *lg1lg2* represents the positions of the light gates at the entrance of the test section, and *lg3lg4* represents the positions of the light gates at the exit of the test section. The terms $x_{pr:lg1lg2}$ and $x_{pr:lg3lg4}$ represent the distance from the sensor to the mid-point of the light gate pair (i.e. distance to the nearest beam plus half a metre).

3.7.1 Reynolds number independence

A Reynolds number sensitivity study was not carried out as part of the experiments due to time constraints. However, studies have been already undertaken in other research projects for this train model and similar train models. This section refers to the outcomes of existing studies to determine whether the requirements in codes of practice for Reynolds number independence are likely to have been met, for the static pressure (Section 3.7.1.1) and slipstream velocity (Section 3.7.1.2).

3.7.1.1 Static pressure

EN 14067-4 (BSI, 2005) regards structures enclosing the tracks which are shorter than 20m, and also surfaces close to the tracks. It permits the use of moving-model tests for assessing train-induced pressure changes causing loading on objects. The experiments should demonstrate that the peak-to-peak static pressure coefficient is independent of Reynolds number for train speeds between 60% and 100% of the test Reynolds number (Re_{max}), and the variation in the results must be no greater than ±3%.

Johnson and Dalley (2002) reported on moving-model experiments which investigated the pressure changes caused by passing high-speed trains. This included a study in which the Reynolds number was varied from approximately 40% (Re=211,200) of the maximum Reynolds number to Re_{max}=528,000. Pressure tappings were installed on the side of a

stationary train which was passed by a moving model train, both in the open air and inside a tunnel. In both cases a linear relationship was found between ΔC_P and the train speed squared, so the EN 14067-4 requirements would probably have been met. It was suggested that the 'simulation of actual train speeds is not important' for 1/25 scale tests.

Schultz (1990) reported on moving-model experiments of pressure changes on flat vertical plates at the trackside caused by a passing ICE2 model. This included a study in which the Reynolds number was varied from approximately 63% (Re=217,000) of the maximum Reynolds number to Re_{max}=347,000. The lateral separation of the plate from the train was varied three times. Further analysis of the results reveals that out of the measurements from nine pressure tappings, ΔC_P was 2.5% lower at the reduced Reynolds number. The EN 14067-4 criterion was met in this case, suggesting that the results for flat vertical plates may be extrapolated to full-scale.

EN 14067-5 (BSI, 2006) regards tunnels. It permits the use of moving-model tests for assessing train-induced pressure changes in tunnels in order to meet medical health criterion, provided the experiments match the full-scale train Mach number (M) which was not achieved in these tests. Mach number scaling is important. Pressure waves (explained in Section 1.3) propagate through the tunnel at the speed of sound (M=1), and they cause fluctuations in the transient static pressure data for a stationary sensor position. The pattern of superimposed fluctuations is only repeatable at full-scale if the train traverses the tunnel at its expected operating speed - i.e. the operational Mach number is conserved as well as the Reynolds number. In what follows, existing experimental data is analysed in order to reveal the effect of changing the combined Reynolds number and Mach number on the peak pressures.

The moving-model data from Schultz (1990) included results for a train passing through tunnels. An ICE2 shaped train passed through tunnels with lengths of L/Z=13, 31 and 51, and

blockage ratios of β=0.115 and 0.15. The results have been reanalysed in order to examine the sensitivity of the pressure magnitudes to Reynolds number. The peak-to-peak static pressure was the absolute difference between the maximum positive pressure ahead of the train nose, and the maximum suction pressure at any point in the time history - this ensured that the peaks were caused by the same main flow phenomena in all cases (in some cases sharp positive pressure peaks occurred in the wake). The peak-to-peak static pressure coefficient was measured by 22 pressure tappings in tunnels of three different lengths. It was 12% lower on average for the slower tests. Therefore the tunnel experiments failed to meet the EN 14067-4 requirement of a ±3% variation in the peak-to-peak static pressure, and the results cannot be extrapolated to full-scale.

In conclusion, the only static pressure results which may be considered independent of Reynolds number are the open air or wall test cases.

3.7.1.2 Slipstream velocity

EN 14067-4 (BSI, 2005) requires that moving-model experiments of train-induced airflow changes causing loading on objects should demonstrate that the peak slipstream velocity is independent of Reynolds number for train speeds between 60% and 100% of the test Reynolds number, with the variation in values being no more than ±3%.

Del Valle (2012) carried out moving model experiments of the slipstream velocity caused by a passing train in the open air. The data have been re-analysed in order to highlight the relationship between the peak slipstream velocity and Reynolds number. A 1/25 scale ICE2-shaped train travelled radially on a circular rotating track past stationary trackside Cobra probes. Velocity data were analysed for Reynolds numbers of 60% (Re=44,100) of the maximum Reynolds number and Re_{max}=77,000. Further analysis of the results reveals that the peak velocity in the wake region was 7% lower on average for the slower tests. Therefore, the

experiments failed to meet the EN 14067-4 requirement of a ±3% variation in U/V, and the results could not be extrapolated to full-scale. However the experiments were performed at a Reynolds number four times lower than that used in these tests; it is known that the relationship between Reynolds number and various flow phenomena is nonlinear. Further analysis of the results for four different Reynolds numbers reveals that the results for the second highest speed had converged with the results for the highest speed. This suggests that the results had converged by Re=77,000. Nevertheless, the study concluded that the mismatch of Reynolds numbers between model-scale and full-scale testing is an issue which is yet to be addressed satisfactorily for the assessment of slipstream velocities.

Baker et al. (2001) carried out moving-model experiments of the slipstream velocity caused by a passing train in the open air. The train model and facility were identical to those used in this study. Single-film hot-wire anemometers measured the air velocities at height z/Z=0.58, which is the same height as many of the Cobra probes used in this study. The train speed was V=32m/s which is the same as the speed used in this study. The track and ground detailing was the same as that used in this study. Velocity data were analysed for Reynolds numbers of 60% (Re=333,000) of the maximum Reynolds number to Re_{max}=520,000. The effect of model speed on the boundary layer velocity profiles was found to be small, although it was acknowledged that Reynolds effects may have been disguised by experimental scatter.

In a CFD study, Muld (2012) examined the effect of the number of carriages of an ICE2-shaped train on the boundary layer momentum thickness along the tail carriage. This can be reinterpreted as a study on the longitudinal Reynolds number (the reference length originates from x=0 at the train's nose). The momentum thickness affects separation around the tail and hence the wake flow structures. The results were compared with those for full-scale trains. The Reynolds number in the CFD study was Re=60,000, but the momentum thickness

corresponded to a full-scale train with 12 carriages and a Reynolds number approximately 200 times higher. This suggests that despite the relatively short length of this train and the low Reynolds number of reduced scale testing, some aspects of the wake flow structures are comparable to those seen in full-scale open air operation. This suggestion is investigated further in a comparison study in Section 5.1.

3.8 Ensemble analysis

It was important to repeat each experiment and adopt the ensemble averaging technique for slipstream velocity. It has been employed in many previous studies, with Del Valle (2012) and Baker et al. (2013a, 2013b) examining the effect of the technique on results. Velocity time histories from individual runs are highly turbulent, so run-to-run variation must be accounted for using this technique to avoid over- or under- predictions. Although principally used in the study of air velocities, this technique has also been used to assess the static pressure. The tests were repeated '*N*' times to form 'ensembles' of *N* 'runs'. Taking the longitudinal velocity *u* as an example, the ensemble average is defined by:

$$\langle u[n] \rangle = \lim_{N \to \infty} \frac{1}{N} \sum_{run=1}^{N} u^{(run)}[n] \qquad 3.13$$

The ensemble average tends towards the true average for an infinite number of test repeats. Although chevrons are used above to denote the average, their use is not deemed necessary for the rest of the thesis as written explanation offers greater clarity.

The ensembles were aligned to a common point at the train nose. The alignment method is described later in this section. The data were resampled to prevent run-to-run drifting far from the nose alignment point, using an algorithm described later in this section. Cobra probe dropouts (null values) were excluded from ensemble averaging. The ensembles formed arrays

aligned to the x-axis. The ensemble average was obtained by averaging the samples at each sample increment. The uncertainty of the ensemble average is discussed in Appendix A2.4. The uncertainty for the Cobra probes was reduced by only taking into account the velocity results provided that $N \geq 5$ at a sample increment after dropouts were removed, and the static pressure coefficient provided that $N \geq 3$ at a sample increment after dropouts were removed. This improved the reliability of the ensemble average in regions of high dropouts.

Analysis of the uncertainty of the ensemble average in Appendix A2.4 reveals that the variation in air velocity between runs was very high, so 15 to 25 repeats were needed in order to increase the accuracy of the ensemble average. The true number of ensemble repeats for each Cobra probe and test case is shown in Table 3.3. The variation of static pressure between runs was lower, so fewer repeats were needed. The true number of ensemble repeats for each pressure tapping and test case is shown in Table 3.4.

The time histories were aligned to samples corresponding to the passage of the tip of the train nose passing the sensor (n_{nose}). It was deemed impossible to locate this point from the light gate data. This was because they were sited too far from the sensors for the uncertainties associated with the deceleration of the train to be negligible. Instead, the time histories were aligned to a specific flow fluctuation around the train's nose. It is known from the potential flow approximations described in Section 2.2 that the static pressure coefficient is zero when the tip of a Rankine half-body (moving-source) passes the sensor. Therefore, the ensemble data has been aligned with $x/Z=0$ corresponding to the zero-crossing point of the static pressure coefficient.

Small variations in the train speed between runs caused the time histories to go increasingly out of alignment with growing distance from the alignment point. This caused coherent fluctuations in the data to be smoothed out in ensemble averaging. The time histories were

resampled before ensemble averaging, using an algorithm which stretched or compressed the time histories for each run, simulating a standard train speed of 32m/s. The resampling involved changing the value of each data sample $u[n]$ with $u[n+\Delta n]$, where Δn represents an adjustment in the location of the data sample within the time history. The adjustment Δn placed the sample into the location in the time history where it would be expected had the train been travelling at 32m/s. The adjustment Δn was rounded 'half-down' to an integer so data was retrieved from (and placed into) existing index locations, without interpolating between neighbouring samples. Interpolation did not provide any visible improvements in accuracy and did not work adjacent to dropouts (null values), at the expense of a significantly higher computational cost. The locator was calculated using the following equation:

$$\Delta n = \left\lfloor n \left(\frac{V}{V_0} - 1\right)\right\rceil \tag{3.14}$$

for a time history with N_n elements, each element denoted by n, and:

$$\{n \in \mathbb{Z} | -n_{nose} \leq n < N_n - n_{nose}\} \tag{3.15}$$

The following function replaced the data at n with data from $n+\Delta n$, unless $n+\Delta n$ was outside the bounds of the array:

$$\mathrm{u[n]} = \begin{cases} \mathrm{u[n + \Delta n]} & \text{if } 1 \leq (n + \Delta n) \leq N_n \\ 0 & \text{if } (n + \Delta n) > N_n \text{ or } (n + \Delta n) < 1 \end{cases} \tag{3.16}$$

$u[n]$ was replaced with zero if the desired index location was outside the boundaries of the array (only when $V>V_0$). This equation is presumed to account for some of the uncertainty caused by relaxing the EN 14067-4 (BSI, 2005) requirement of $0.97 \leq V/V_0 \leq 1.03$, although Reynolds number scale effects still affect the accuracy of the results.

Figure 3.15 demonstrates the effectiveness of the algorithm at aligning the data. Figure 3.15(a) shows a typical ensemble of static pressure on a wall caused by the passage of the train tail, before the application of the algorithm. Figure 3.15(b) shows the data after the application of the algorithm. When the algorithm was applied, ΔC_P at the train tail increased by 4.4%.

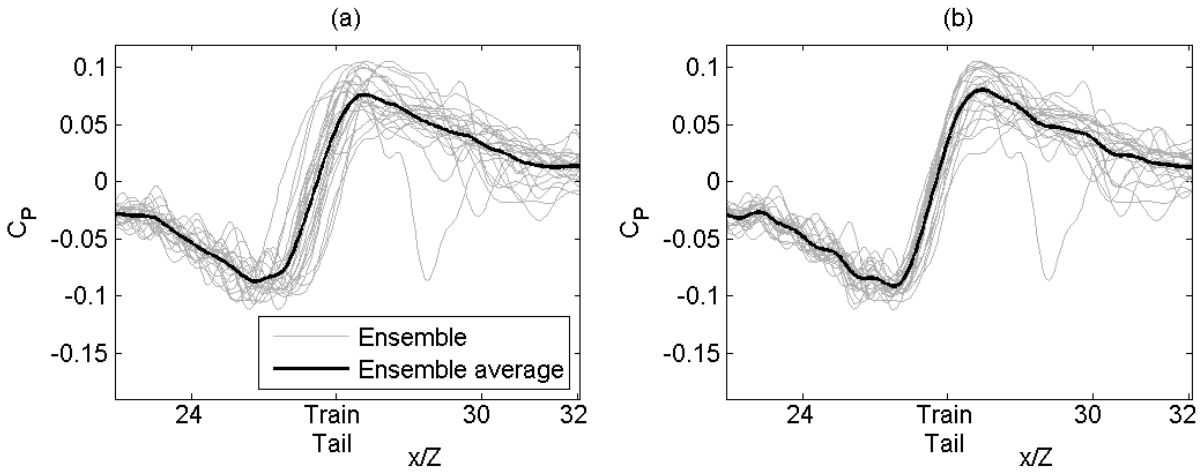

Figure 3.15: Effect of the resampling algorithm on the static pressure fluctuation around the train's tail: (a) Original data; (b) Resampled data.

3.9 Low-pass filters

Some forms of analysis which are presented in this thesis involve low-pass filtering the data to a code-specified cutoff frequency. Butterworth or moving-average methods were used. They are defined in Section 3.9.1. Issues regarding the scaling of filtered maximum velocities and static pressure coefficients are discussed in Section 3.9.2. A low-pass pre-filter was also applied to all of the data. It was optimised to reduce the effect of mechanical vibrations on the accuracy of the data. It is discussed in Section 3.9.3.

3.9.1 Types of filter used in this work

The Butterworth filter kernel is defined by the following transfer function:

$$H(s) = \frac{G_0}{\prod_{k=1}^{n}(s - s_k)/\omega_c} \quad 3.17$$

in which G_0 is the gain at zero frequency, s is the complex frequency, s_k is a transfer function, and ω_c is the angular frequency at cutoff. The poles of the transfer function are:

$$s_k = \omega_c \exp\left(\frac{j(2k + o - 1)\pi}{2o}\right), \qquad k = 1,2,3, \dots, o \quad 3.18$$

in which j denotes a complex number, o is the filter order, and k is the pole. The Butterworth filter was applied forwards and backwards to prevent phase-shifting, using MATLAB's 'filtfilt' function. The cutoff frequency therefore represents the -6dB point.

A moving-average is carried out in the time domain:

$$x[n] = \frac{1}{n_m} \sum_{i=-n_m}^{n_w - n_m - 1} x[n + i] \quad 3.19$$

n_m is the middle point of the moving-average window, and n_w is the number of elements in the window. Therefore:

$$n_m = \left\lfloor \frac{n_w}{2} \right\rfloor \quad 3.20$$

The centre value is rounded down, so for odd values of n_w there is a small (and insignificant) offset to the data.

Both filter types suffer from rippling in the time domain. As mentioned in Section 3.4, the Cobra probe time history data contained randomly distributed zeros due to dropouts, which acted as impulses on the filter. Both filters introduced severe rippling to the data near the dropouts which reduced the accuracy of the results considerably. It was therefore necessary to temporarily interpolate the gaps in the data. After filtering, the interpolated lines were

removed and the gaps were reintroduced. This approach was deemed valid as the filters introduced zero phase-shift.

3.9.2 Scaling issues relating to velocity peaks

Maximum gusts and pressure fluctuations are attenuated when a low-pass filter is applied to model-scale data. The level of peak-attenuation is dependent on the time scale (duration) of the peak gust or pressure fluctuation in relation to the size of the moving-average window or the filter cutoff frequency, as was observed in Gilbert et al. (2013b). The filter parameters must be adjusted accordingly in order for a model-scale transient to occur over a specified 'full-scale-equivalent' duration. The appropriate filter parameters are the focus of this section.

There is a growing body of research publishing aerodynamic rolling stock homologation test results, in which aerodynamic loads (peak velocities) on track workers at the lineside have been calculated in accordance with requirements in the TSI code of practice (TSI, 2008). An analysis of 'TSI velocities' is carried out later in the thesis. The mean ($\overline{u}$) and standard deviation (σ) of the maximum one-second gusts for individual runs must be calculated, of which there were N for each test case. The 95% confidence limit is represented by $U_{2\sigma}/V$:

$$\frac{U_{2\sigma}}{\mathrm{V}} = \frac{\overline{\max\,(U)} + 2\sigma(\max(U))}{\mathrm{V}} \qquad 3.21$$

The loads are obtained by applying a moving-average to velocity data, with a window size that needs to be equivalent to one second at full-scale (the code requires that tests are carried out at full-scale, but this is ignored in the later analysis). A scaling equation is used in order to obtain a one-second equivalent filter window:

$$t_{ms} = g \cdot t_{fs}\left(\frac{l_{ms}}{l_{fs}}\right)\left(\frac{V_{fs}}{V}\right) \qquad 3.22$$

in which l_{ms}/l_{fs} is the length scale factor, g is a peak scaling factor, and V_{fs} is the operating speed of the train which is divided by the test speed (V) in order to obtain a speed scale factor. The relationship between time, cutoff frequency and samples is $n_w=t_{ms}.f_c$ and $n_{w,fs}=t_{fs}.f_{c,fs}$. The reduced length of the model train puts the length scale factor into question; it may be 1/25 when considering the width (Y_{ms}/Y_{fs}) and height (Z_{ms}/Z_{fs}) of the train, but 1/50 or 1/100 when considering the length of the train (X_{ms}/X_{fs}). This is because the length of the model is four-carriages, which is half or a quarter of the number of carriages used in full-scale operation. Reynolds effects mean that the window size is unlikely to be directly proportional to the length and speed scale factors. The scaling depends on how the duration of the gust and the resulting peak-attenuation are affected by all of the above parameters. As a result, the peak scaling factor (g) has been added in order to account for these uncertainties.

In what follows, the peak scaling factor will be calculated by fitting the open air results from the 'TSI position' onto those from past studies. Baker et al. (2013b) reported full-scale experimental TSI measurements of sixteen carriage ICE2 trains and a gust of $U_{2\sigma}/V$=0.27-0.28 was found. Bell et al. (2013) reported 1:10 scale wind tunnel TSI measurements on an ICE2 train. The measurements in the latter study were fitted to (unreported) moving-model results and a gust of $U_{2\sigma}/V$=0.29 was found. Figure 3.16 shows how the peak scaling factor affects $U_{2\sigma}/V$, and includes lines representing the empirical values. The methodologies in the past experiments are very different to that used in this thesis, but together they predict the TSI velocity reliably to within $U_{2\sigma}/V$=0.28±0.1. The peak scaling factor is therefore fitted to produce $U_{2\sigma}/V$=0.28.

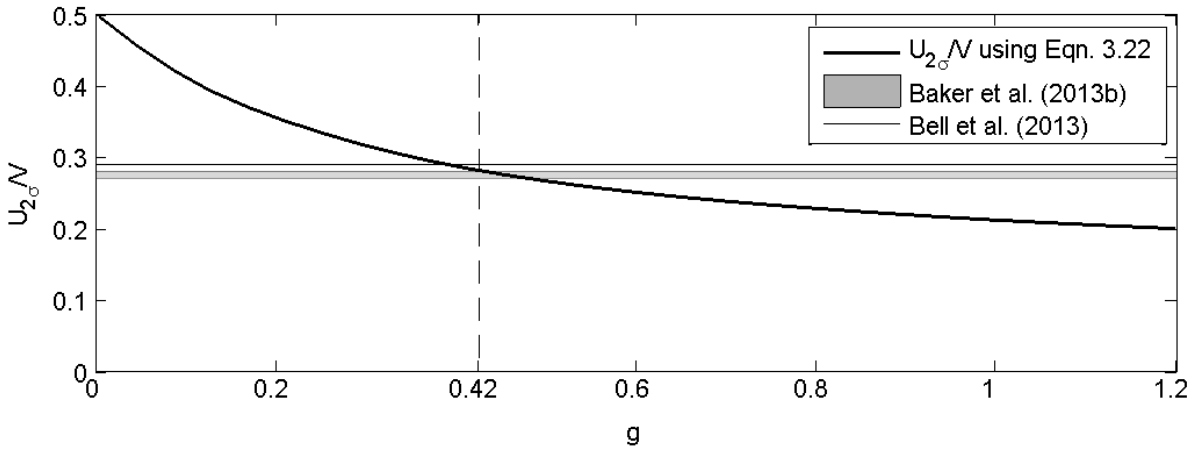

Figure 3.16: Relationship between the maximum TSI velocity ($U_{2\sigma}/V$) and the peak scaling factor (g).

A peak scaling factor of g=0.42±0.03 ensures that the TSI velocity lies within the empirical range. For a peak scaling factor of unity, the TSI velocity is 25% lower than the mean empirical range. This proves that scaling uncertainties are significant, and suggests that the velocity peaks encountered at model scale are too narrow and are therefore over-attenuated. A comparison study in Section 5.1.2 confirms that the gusts are too narrow. The comparison study uses an 'integral breadth' method to determine the 'narrowness' of the peaks. From this, a peak scaling factor is calculated independently which is g=0.49±0.05. This independent estimation gives further confidence that the chosen value of g=0.42 is accurate at least to within one decimal place of its true value for accurate peak scaling.

Reference is often made in the results chapters to peaks occurring over specified 'full-scale-equivalent' durations (t_{fs}), after low-pass filters have been applied to the data. Equation 3.22 is used to calculate t_{fs}, using a peak scaling factor of g=0.42.

3.9.3 Preliminary filtering of the data

This section describes the low-pass filtering approach for noise reduction. Figure 3.17 demonstrates two low-pass filters which were used to smooth the Cobra probe velocity data to a cutoff frequency of f_c=325Hz (calculated using Equation 3.22). The moving-average filter

does not have a well-defined cutoff frequency. A mathematical description of the Fourier transform of a rectangular pulse reveals that the -3dB cutoff frequency of a moving-average filter is $f_c=0.443f_s/n_w$. Therefore $n_w=7$ for $f_c=325$Hz.

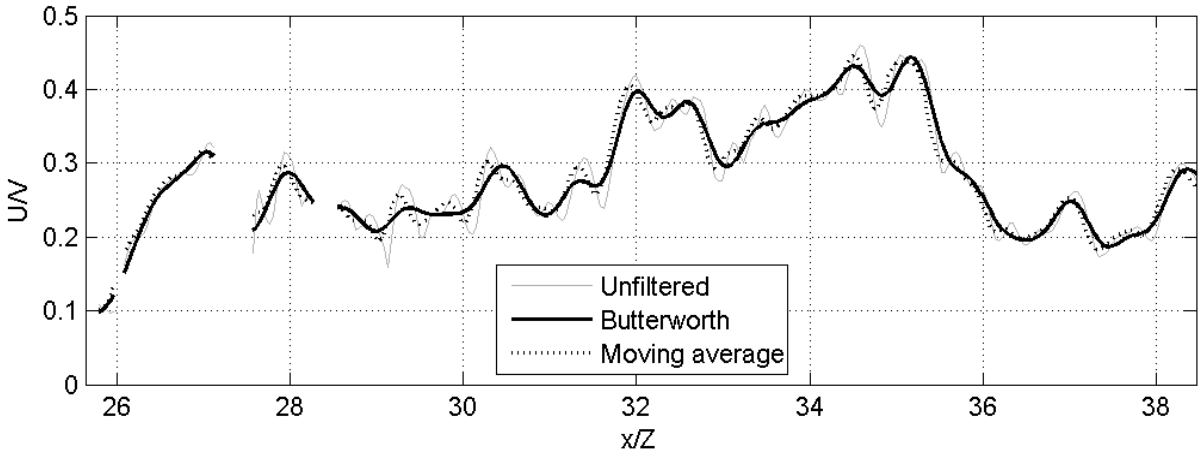

Figure 3.17: A fifth order Butterworth low-pass filter compared to a seven-period moving-average filter, when applied to ensemble average resultant velocity data.

The results show that the Butterworth filter performs similarly to the moving-average filter. However, the Butterworth filter offers a greater degree of control over the frequency roll-off. Therefore the Butterworth filter was chosen as the pre-filter.

In order to achieve maximal noise reduction and minimal peak attenuation, it was necessary to determine an appropriate cutoff frequency and filter order. The background noise level increased in the time histories for all sensor types after the train was fired (catapulted) but long before it reached the sensors. This was due to mechanical vibrations which travelled through the track bed and into the sensors - particularly the sensors on track-mounted stands rather than floor mounted stands. The background noise before and after the firing of the train was compared so that the cutoff frequency could be set to a frequency below which mechanical vibrations did not affect the data, but not low enough to over-smooth the data. The comparison was made based on Figure 3.18. It shows the FFT spectra of the pre- and post-firing background noise in the static pressure time histories for one run. It also shows PDFs of

the post-firing background noise, with and without low-pass filtering. Data for three sets of sensors are included: firstly, Cobra probes with a manufacturer's calibrated frequency response of 650Hz, all of which shared a floor-mounted stand; secondly, Cobra probes with a frequency response of 2kHz, which were on attached to various trackside-mounted stands; and finally, pressure transducers with frequency responses of 2kHz, which were attached to tubes connected to pressure tappings.

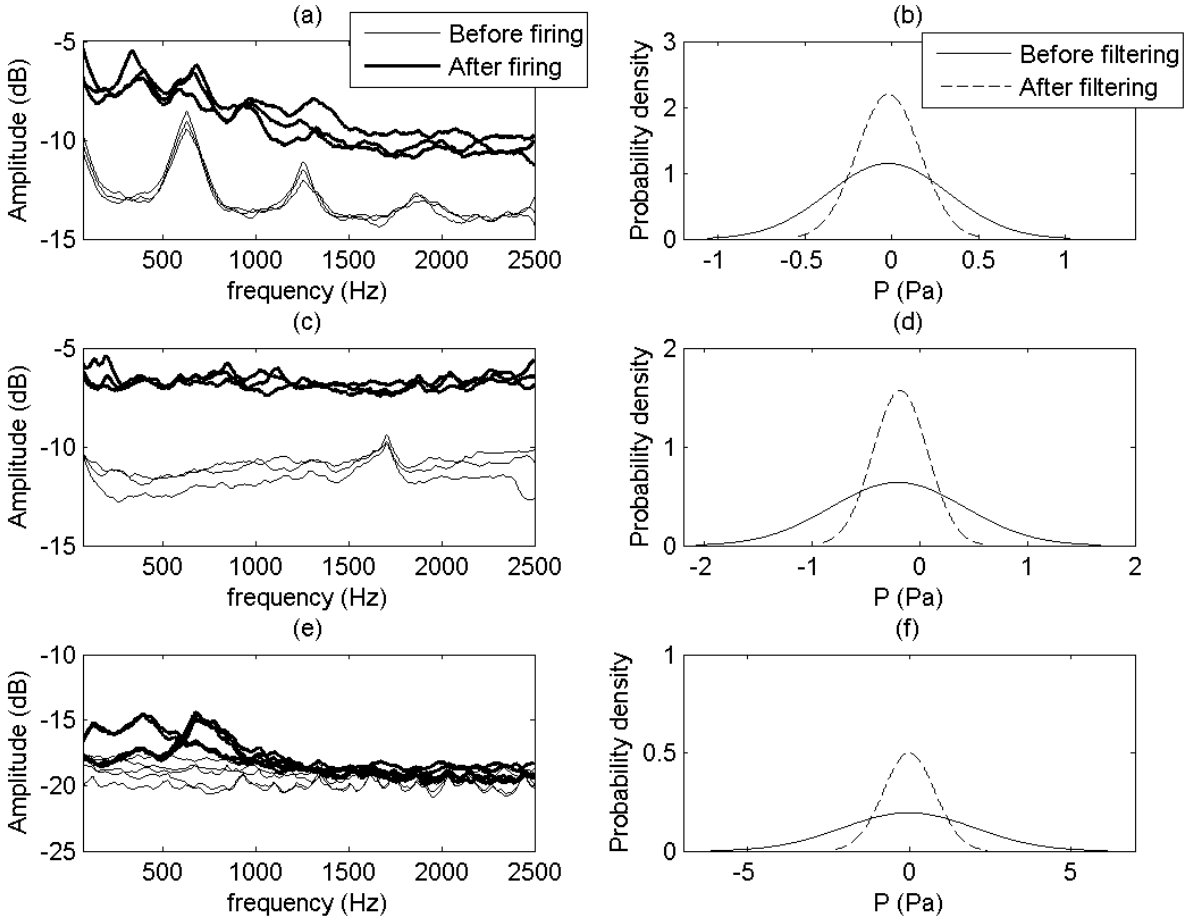

Figure 3.18: FFT power spectra of the background static pressure before and after train firing and before it reached the sensors, and Gaussian PDFs of the data before and after smoothing by low-pass filtering, from measurements by different sensors: (a-b) '650Hz' Cobra probes; (c-d) '2kHz' Cobra probes; (e-f)'2kHz' Pressure transducers.

The FFT spectra calculated before and after the firing of the train show that the Fourier power increased across the frequency range after the train was fired. Peaks in power appeared after

the firing at frequencies between 300Hz and 750Hz. These were detected by the floor-mounted '650Hz' Cobra probes and the pressure transducers. The likely cause of the spikes in power are mechanical vibrations transferred into the sensors from the track bed and floor.

A Butterworth low-pass filter was applied to reduce the noise associated with the vibrations. The cutoff frequency was set to 325Hz. This not only corresponded to the folding frequency of the 650Hz Cobra probes, but it also halved the standard deviation of the noise in the background data after the train had been fired. This is illustrated in the PDFs which compare normal distributions of the background noise before and after a low-pass filter was applied. The pre-filter introduced some peak attenuation to the data: the peak-to-peak static pressure coefficient was reduced by 5% on average for the Cobra probes, and by 7% for the pressure transducers. However, this was deemed to be valid as the background noise was superimposed onto the peaks.

3.10 Uncertainty analysis

The detailed calculations of uncertainty are included in Appendix A2. Table 3.5 summarises the uncertainty of the measured values.

Table 3.5: Summary of uncertainty of key variables.

Variable		Uncertainty	Appendix section
V	Train speed	0.71%	Appendix A, Section A2.1
U/V	Resultant air velocity	5.2%[1]	Appendix A, Section A2.2
ΔC_P	Peak-to-peak static pressure coefficient	1.6%[1]	Appendix A, Section A2.3
	Ensemble average	U: 2.6% C_P: 0.7%	Appendix A, Section A2.4
	5% probability maximum gust	$U_{2\sigma}$: *<7%*	Appendix A, Section A2.5
x=0	Train nose passes sensor	0.05m	Appendix A, Section A2.7

[1] Approximately 5% of the runs exceeded this uncertainty.

Appendix A3 explains why some sections of time history flow data were removed. They were affected by problems including mechanical vibrations, and pressure fluctuations caused by an arrestor hook under the train.

3.11 Conformance to codes of practice

Objective 1 states that the methodology should conform to codes of practice where their requirements do not inhibit the ability of the study to meet the other objectives. This section assesses how closely the methodologies prescribed in three relevant codes of practice have been followed by this methodology. The code requirements are compared to the relevant aspects of the methodology on a clause-by-clause basis in a tabular format, to check the level of conformance. Repeated clauses refer back to their first instances by means of reference IDs.

Table 3.6 lists the relevant clauses from EN 14067-4 (BSI, 2005), and specifies whether each clause was met. The code sets out requirements and test procedures for measurement of pressure and slipstream velocity loads on various structures (excluding tunnels) or trackside workers.

Table 3.6: Conformance of the methodology to clauses in EN 14067-4 (BSI, 2005).

ID	Section	Clause	Clause met?
	5.4.3: Dynamic pressure loads	*Note: Moving-model tests may be used.*	
A1		The tests should consist of at least 10 independent and comparable test samples.	Not always
A2		Models of the test train should accurately represent the train head and tail, and a good representation of bogies, inter-carriage gaps and exterior surface features [sic].	Yes
A3		The Reynolds number has to be at least Re=250,000.	Yes
A4		$\Delta C_{P,2\sigma}$ [1] is independent of Reynolds number for train speeds between $0.6Re_{max}$ to Re_{max} within ±3%.	Not always
A5		The chosen scale has to be applied to the whole model configuration.	Yes
A6		The basic shape of the train body should be modelled in width and height to a tolerance of ±0.02m full-scale from the true shape.	Yes
A7		The smoothness of the exterior surfaces shall be hydraulically comparable.	Yes
A8		The test rig parameters and ambient air conditions, i.e. temperature, pressure and humidity, have to be recorded at the time of the tests.	Yes
A9		Variability of speeds between test runs is allowable during testing (±3%).	93% of runs
A10		Data is sampled at a rate of at least $10V/(l_{nose} * 1/25) \approx 2.67$kHz.	Yes
A11		The sensors used should be capable of measuring the pressure with a minimum resolution of the data sampling rate.	No
A12		The pressure sensors shall be calibrated prior to use over the expected pressure range.	Yes
A13		The measurement error shall be less than 2% of the expected range.	Yes
A14		The uncertainty of the train speed measurement shall be determined and may not exceed ±1%.	Yes
	6.4: Train induced airflow loads	*Previous clauses: A2, A3, A5, A6, A7, A8, A9.* *Note: Moving-model tests may be used.*	
A15		The tests should consist of at least 20 independent and comparable test samples.	Not always
A16		$U_{2\sigma}$ [2] is independent of Reynolds number for train speeds between $0.6Re_{max}$ to Re_{max} within ±3%.	No
A17		Data is sampled at a rate of at least 10 / (1/25) Hz = 250Hz.	Yes
A18		The measurement error should be less than 1% of the expected range.	No
A19		The anemometers shall have a valid calibration.	Yes
	8.4: Train induced loading on trackside workers	*Previous clauses: A2, A3, A5, A6, A7, A8, A9, A15, A16, A17, A18, A19.* *Note: Moving-model tests may be used.*	

[1] $\Delta C_{P,2\sigma}$ is the characteristic pressure difference, calculated using equation 12 in the code. It is not used in this thesis.
[2] $U_{2\sigma}$ is the characteristic airflow, calculated using equation 17 in the code.

Table 3.7 lists the relevant clauses in EN 14067-5 (BSI, 2006), and specifies whether each clause was met. The code sets out requirements and test procedures for pressure measurement at a stationary position in tunnels.

Table 3.7: Conformance of the methodology to clauses in EN 14067-5 (BSI, 2006).

ID	Section	Clause	Clause met?
	4: Pressure changes, medical health criterion.	*Previous clauses: A12, A14, A18.* *Note: Moving-model tests may be used.*	
B1		The tunnel should have constant cross-section.	Yes
B2		The tunnel should have no airshafts.	Yes
B3		The tunnel should have no residual pressure waves.	Yes
B4		There should be no initial airflow in the tunnel.	Yes
B5		The speed of the train should be constant during the entry into the tunnel within 1%.	57% of runs
B6		Data should be sampled at a rate of at least $5V/(l_{nose})$ Hz. *(N.B. 1.33kHz at model-scale)*	Yes
B7		The distance x_p between the entrance portal and the measuring position is given by equation 1 [sic]. *(N.B. equation 1 gives model-scale equivalent value of 8.7m).*	No
B8		The minimum tunnel length is given by equation 2 or 3 [sic]. *(N.B. equation 2 gives approximately 36.4m, equation 3 gives approximately 55m).*	No

Table 3.8 lists the relevant clauses in TSI (2008), and specifies whether each clause was met. The code sets out requirements and test procedures for assessing aerodynamic loads on track workers at the lineside. It is taken out of context in this research as its main requirements are for experiments to be carried out at full-scale, and for the test speeds to be close to full-operational speeds.

Table 3.8: Conformance of the methodology to clauses in TSI (2008).

ID	Section	Clause	Clause met?
	4.2.6.2.1: loads on track workers	*Previous clauses: A14, A15.*	
C1		Only full-scale tests may be used.	No
C2		The train is full length.	No
C3		Assessment is carried out at y=3m, and z=0.2m	Yes
C4		Tests shall be undertaken on ballasted track.	No
C5		Tests shall be undertaken on straight track.	Yes
C6		The vertical distance between the top of the rail and the surrounding ground level is 0.75m ± 0.25m.	No
C7		The ambient wind speed is ≤2m/s.	Yes
C8		At least 50% of the measurements shall be within ±5%, and 100% of the measurements within ±10%, of the maximum train speed (280km/h).	No
C9		The track shall have no obstacles such as bridges or tunnels nearer than 500m ahead or 100m after the sensors in the longitudinal direction.	No
C10		Groups of sensors must be placed 20m apart from each other.	No
C11		The sampling rate of the sensor shall be at least 10Hz. *(N.B. assumed to be equivalent to 250Hz at model-scale).*	Yes
C12		The uncertainty in the air speed measurements shall be determined and may not exceed ±3%.	Yes

Chapter 4

Static pressure

This chapter describes the static pressure results within the framework of Objectives 4 and 5 of this thesis. This chapter expands considerably on the discussion in Gilbert et al. (2013a). Relationships between pressure fluctuations and slipstream velocity transients are sought in Chapter 5 which discusses slipstream velocities, and not in this chapter.

There are four parts to this chapter: a comparison of results with existing data in Section 4.1; analysis of the time history results in Section 4.2; analysis of characteristic loads on objects in Section 4.3; and concluding remarks in Section 4.4.

4.1 Comparison of results with existing data

The static pressure results have been compared with those from previous studies in order to assess the adequacy of the methodology in capturing the correct pressure changes. Open air pressure measurements were undertaken recently as part of the AeroTRAIN project (summarised in Sima et al. (2011)), using a full-scale ICE2 train travelling in the open air at high speed. Open air tests were undertaken in this study with in-flow Cobra probes stationed in two positions matching those used in the full-scale experiments, equivalent to y=2.5m, and z=1.5m and 3.3m. The results from both datasets are shown in Figure 4.1.

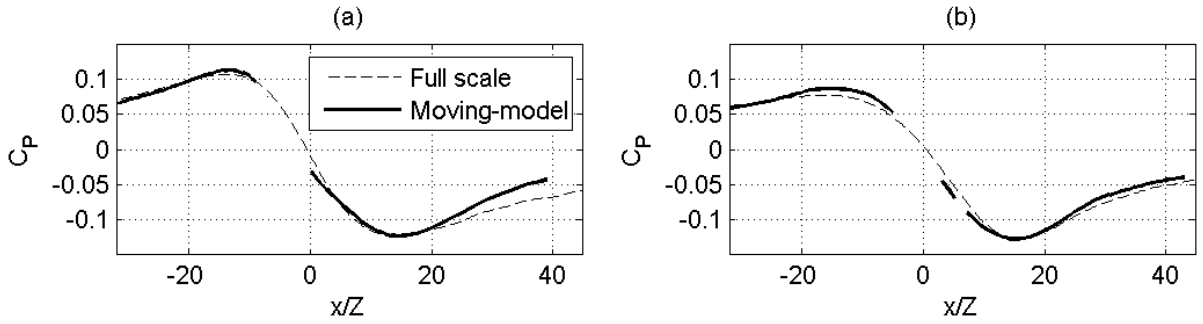

Figure 4.1: Comparison of static pressure around the train's nose in the open air (OA) with full-scale data (Sima et al., 2011), at position y/Z=0.64 and: (a) z/Z=0.38; (b) z/Z=0.85.

The differences in the peak-to-peak pressure changes between the full-scale and model-scale results at the lower and higher positions are 0.8% and 4.2% respectively. The moving-model tests produce higher pressures in both cases. The shape of the pressure fluctuation is similar to that in the full-scale experiment. This methodology appears to yield accurate results in the open air case.

The surface static pressure on a movable vertical wall has previously been measured as part of a doctoral investigation into the pressure field around an ICE1 train (Schultz, 1990). The ICE1 is geometrically similar to the ICE2, as explained in Section 3.2, with the only major difference being the ICE2's 50mm increase in full-scale width. The moving-model technique

was used. Individual runs were undertaken at approximately 32m/s, and data from two to five runs were averaged in both cases. The peak-to-peak static pressure coefficients have been extracted and averaged over three different tapping heights on the wall. The single wall results from these experiments (W1S, W2S, and W3S) have also been averaged over all five surface tapping positions. Figure 4.2 shows the relationship between the peak pressures with the lateral separation of the wall from the train's side.

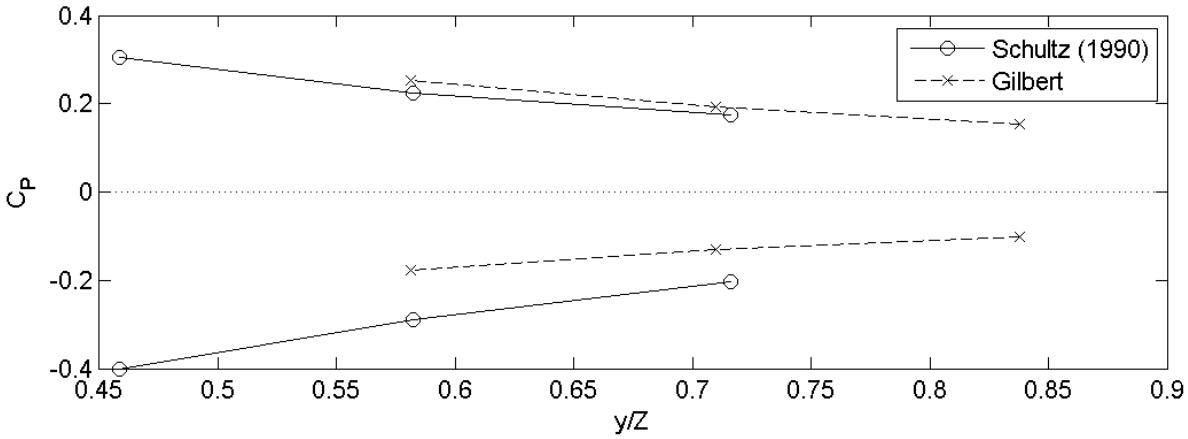

Figure 4.2: Comparison of the static pressure on a movable vertical wall with moving-model data from Schultz (1990).

The difference between the positive peaks is smaller than for the suction peaks. Whilst the positive peak is consistently higher than the measurement by Schultz (1990), the suction peak is consistently lower. The disagreement might arise from a combination of several differences in experimental procedure: the ICE1 train on which the model was based is 50mm wider at full-scale than the ICE2; any differences in the construction of the nose geometries is unknown (e.g. curvature of the nose, or friction of the surface material); and differences in the construction of the vertical wall may have had an impact (e.g. the plate was shorter and taller, the three tappings were spaced at a greater range of heights, or vibrations had a greater effect on the transducer measurements). Further, the data from Schultz were obtained by averaging data from just two or three individual runs, each of which were carried out at different speeds.

Therefore the data may at least have contained larger fluctuations that affected the peak pressures. The fluctuations would have been smoothed out in these experiments.

It is not possible to compare the results for tunnels with existing datasets, as none of the existing datasets which included tunnel pressure measurements for the ICE2 (e.g. Schultz, 1990; Diedrichs et al. 2004) had methodologies which were deemed to be similar enough to allow direct comparison of results. It is likely that the results in tunnels would not be directly scalable, due to the influence of pressure waves on the results. Pressure waves propagate through the tunnel at the speed of sound, and they superimpose fluctuations onto the static pressure data. The pressure signature is only repeatable at full-scale if the train traverses the tunnel at its expected operating speed - i.e. the operational Mach number is conserved as well as the Reynolds number, and if the length of the tunnel matches that of the full-scale tunnel. These parameters did not match those used in previous datasets.

This section has established that this methodology is acceptable in relation to previous accepted methodologies for reduced-Reynolds number testing in the open air, and that this methodology can provide results which are close to results from full-scale tests. However, this section has not proven that the results in confined spaces are analogous to results from full-scale tests. The superimposition effect of pressure waves in tunnels means that the results are not scalable unless the Mach number (M) is matched to full-scale operation. The flow physics are likely to be correct, based on an upcoming comparison between the experimental loading patterns presented in Section 4.2.1 and the illustrated loading patterns from Section 1.3. These findings do not hinder the ability of the thesis to meet the aims and objectives which focus on comparative rather than quantitative debate.

4.2 Time history results

The effect of changing geometric parameters on the pressure loading patterns is discussed in this section, using time histories and peak positive and suction pressure data. All of the data have been filtered to a cutoff frequency of f_c=325Hz (calculated from Equation 3.22). The full-scale-equivalent gust duration for this cutoff frequency is t_{fs}=0.08 seconds. Three fundamental types of pressure loading patterns are introduced in sub-section 4.2.1. Then results for each type of loading pattern are discussed: open air and wall cases in sub-section 4.2.2; the tunnel cases in sub-section 4.2.3; and the partially-enclosed tunnel cases in Section 4.2.4.

4.2.1 Pressure loading patterns

In Section 1.3, three fundamental 'pressure loading patterns' were introduced: pressure loads in the open air and on single surfaces; pressure loads inside tunnels; and pressure loads in partially-enclosed tunnels. The three patterns are used in this research as generic benchmarks, and the results are compared with these benchmarks (and each other) as the geometric parameters are varied. This section recaps and elaborates on the essential features of each loading pattern using experimental data from test cases representative of the open air, vertical walls, a tunnel, and a partially-enclosed tunnel.

The basic characteristics of the loading patterns are defined in this section. A pressure loading pattern is characterised using the visible static pressure fluctuations in a time history. Particular attention is paid to shapes and locations of the maxima-causing fluctuations (maximum positive and suction pressure, and peak-to-peak pressure).

The static pressure loading pattern in the open air is characterised by two pressure transients, each occurring around the train's nose and tail. They are separated by a region of $C_P \approx 0$. The

passage of the train's nose is marked by a positive peak followed by a suction peak. The passage of the train's tail is marked by a suction peak followed by a positive peak. Figure 4.3 shows the loading pattern for both the open air and symmetrical double wall case W2D.

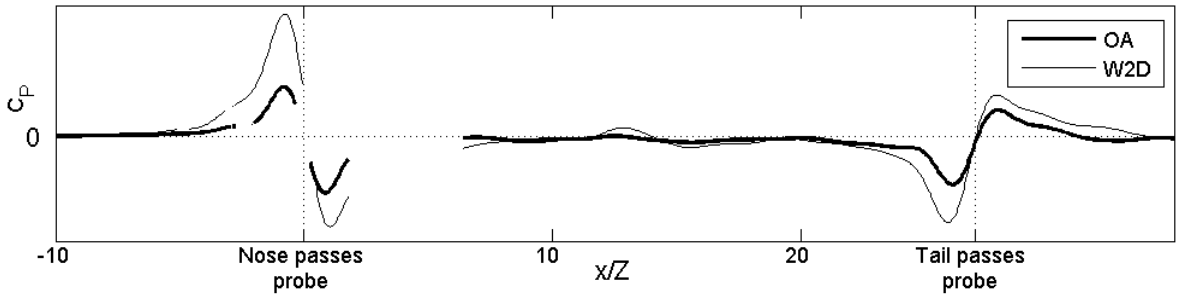

Figure 4.3: 'Pressure loading pattern' in a typical open air (OA) and double wall (W2D) case, at position y/Z=0.64 and z/Z=0.58.

The results show that the loading pattern in the double wall case is identical to that in the open air (i.e. the shapes and locations of the maxima-causing fluctuations are identical). It will be shown in Section 4.2.2 that the same loading pattern occurs in all wall cases. The walls only increase the magnitudes and durations of the maximum pressures.

The loading pattern changes significantly in tunnels. As a train enters a tunnel, a 'pressure wave' propagates at the speed of sound towards the tunnel's exit portal. Upon reaching the exit, a lower magnitude expansion wave is reflected back towards the entrance, starting a complex decaying sinusoidal pressure wave pattern inside the tunnel. Figure 4.4 shows the loading pattern for tunnel T1, with the causes of fluctuations in the time history linked to particular events on a wave diagram.

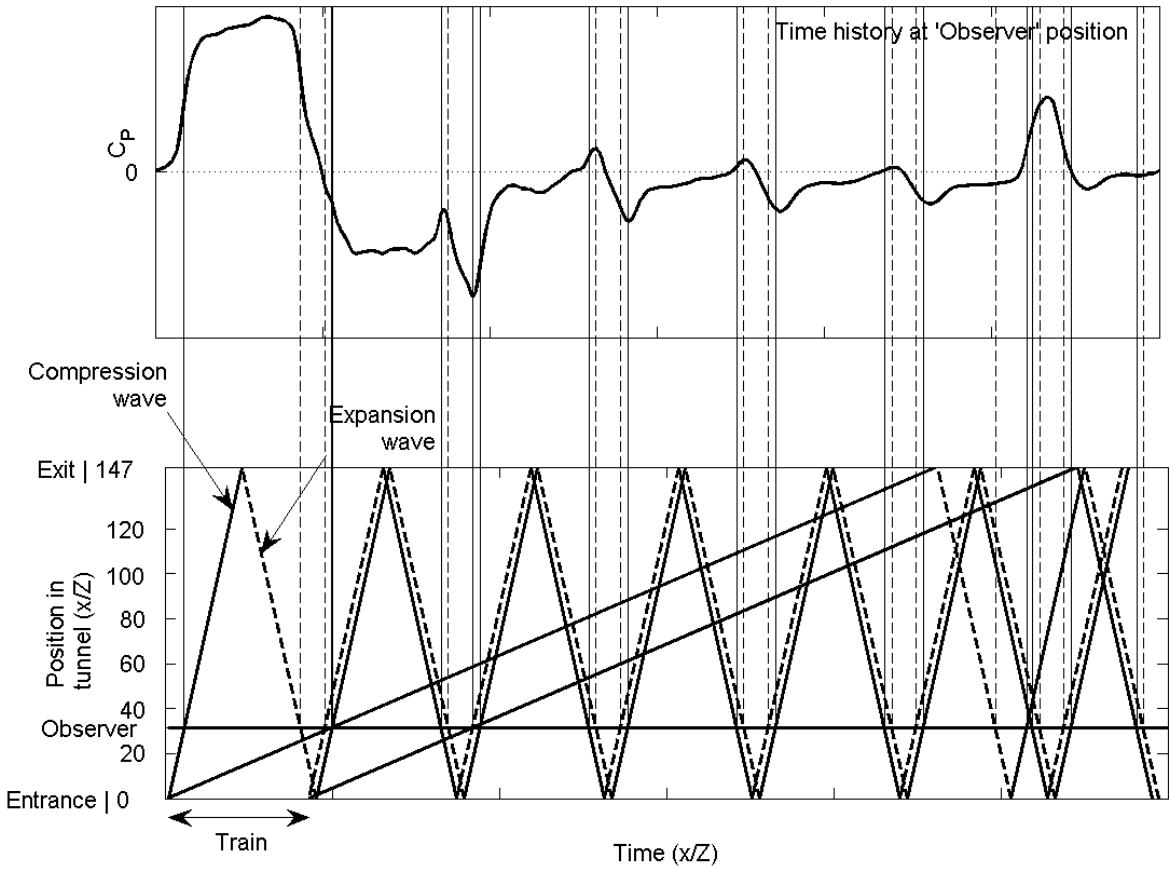

Figure 4.4: 'Pressure loading pattern' in a typical tunnel (T1: L/Z=147, β=0.23, α=0%), including a wave diagram showing the causes of the pressure fluctuations in the time history.

The initial steep pressure gradient is due to the 'nose-entry compression wave' generated as the train's nose enters the tunnel. The gradual pressure rise is an effect of 'friction pressure rise' as the train body enters the tunnel. The drop in pressure to suction is a result of the 'first reflected expansion wave' propagating from the tunnel exit, then a 'tail-entry expansion wave' caused by the train's tail entering the tunnel, and then the pressure fluctuation associated with the 'nose passage' past the sensor (i.e. Figure 4.3 is superimposed onto Figure 4.4). This is followed by a compression wave which is the second reflection of the original nose-entry compression wave. The pressure remains in suction until the next succession of fluctuations occurs due to reflections of the original nose-entry and tail-entry pressure waves, followed closely by the 'tail passage' past the sensor (i.e. Figure 4.3 is superimposed onto Figure 4.4). Following this, decaying reflections of the original nose-entry and tail-entry

pressure waves occur. A ‘nose-exit expansion wave’ is released when the train’s nose reaches the exit. A ‘tail-exit compression wave’ is released when the train’s tail reaches the exit. For the remainder of the time history, multiple pressure wave-fronts reflect inside the tunnel and gradually decay. It will be shown in Section 4.2.3 that not all results will follow the pattern of Figure 4.4, because the pressure loading pattern is related to the train speed, the longitudinal (x-axis) position of the sensor, and the tunnel’s length.

The loading pattern changes significantly in partially-enclosed tunnels due to the equalisation of pressure with the external atmospheric pressure via an opening in the tunnel’s cross-section. This equalisation damps pressure differentials between the tunnel interior and the external atmosphere at a rate controlled by the size of the opening. For a tunnel made from a flat ceiling placed on top of the double walls, the loading pattern must transition from the double wall loading pattern seen in Figure 4.3 (for an opening a large as the ceiling) to the tunnel loading pattern seen in Figure 4.4 (for no opening). The way in which the loading pattern evolves with the opening ratio is of interest. Figure 4.5 illustrates the basic characteristics of the loading pattern in a partially-enclosed version of T2 (L/Z=51, β=0.3, α=1%).

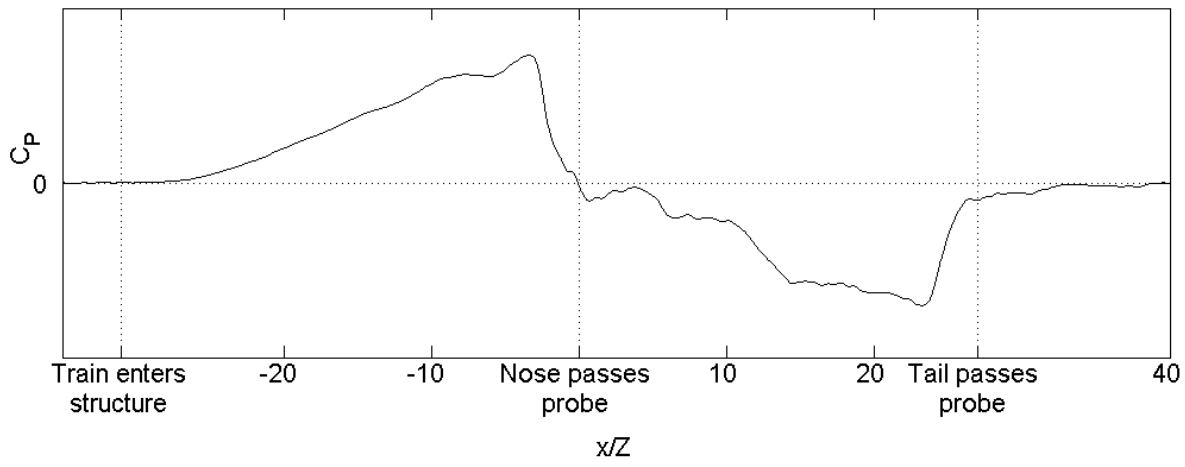

Figure 4.5: ‘Pressure loading pattern’ in a typical partially-enclosed tunnel (T2, L/Z=51, β=0.3, α=1%), at sensor position x_P/L=62%.

The loading pattern is consistent with that seen in experiments reported in Takei et al. (2008) (Figure 1.5) and analytical predictions reported in Iida et al. (2005) (Figure 2.2(b)). It is a simple 'sawtooth' shape characterised by a positive peak around the nose and a suction peak around the tail. The rising edges occur over long durations whilst the falling edges occur over short durations. The gradient of the initial compression wavefront is significantly shallower than in the tunnel loading pattern. There is no easily discernible superimposition from reflecting pressure waves as would be expected in the tunnel loading pattern. It will be shown in Section 4.2.4 that the loading pattern is dependent on the opening ratio (α) and blockage ratio (β) as predicted by the analytical formulation (Equation 2.16). It will also be shown that for low opening ratios it is also dependent on the longitudinal position of the sensor and the tunnel's length.

The experimental loading patterns presented in this section closely correspond to the illustrated loading patterns from Section 1.3. This means that it is likely that the flow physics have been captured correctly in these experiments.

4.2.2 Open air and Walls

The results for the open air and wall cases are analysed in this section, with a focus on the effect of sensor placement. The loading pattern has been defined in Section 4.2.1 (Figure 4.3). Details of the relevant wall test cases are recapped in Figure 4.6, and the reasons for choosing the geometric parameters are given in Section 3.5.3.

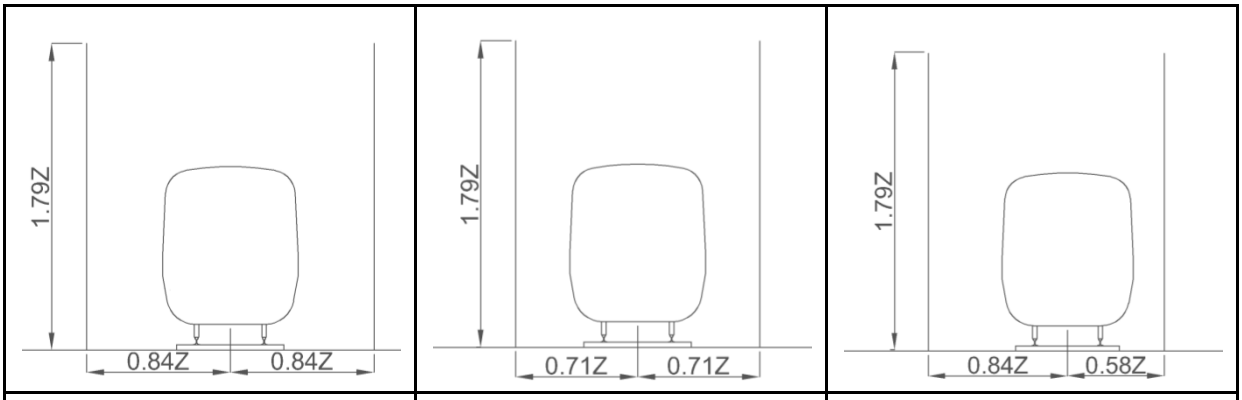

W1S. *L/Z*=51. Right wall only. **W1D.** *L/Z*=51. Double walls. Symmetrical.	**W2S**. *L/Z*=51. Right wall only. **W2D**. *L/Z*=51. Double walls. Symmetrical.	**W3S**. *L/Z*=51. Right wall only. **W3D**. *L/Z*=51. Double walls. Asymmetrical.

Figure 4.6: Cross-section views and geometric details of the open air and wall test cases (recap).

The lateral variation of the maximum positive and suction static pressure and the peak-to-peak pressure around the train's nose is shown in Figure 4.7(a) and (b) respectively. Cases include the open air (OA) and two symmetrical double wall cases W1D and W2D. The pressure was measured by Cobra probes at multiple *y*-axis positions and height *z*/*Z*=0.58. The data were extended to the wall surfaces. Wall tappings were not installed at the height *z*/*Z*=0.58 so the results for two neighbouring tappings were linearly interpolated. The graphs include vertical lines showing the wall positions. In all cases the Cobra probe data was only used if there were no dropouts hiding the maximum positive and suction pressures. A power-law function may be fitted to describe the rate of decay of the peak-to-peak pressure with increasing lateral distance:

$$\Delta C_P = K_1 \cdot \left(\frac{y}{Z}\right)^{K_2} \qquad 4.1$$

in which K_1 is a constant and K_2 is an exponent. The exponents are shown in Figure 4.7(b).

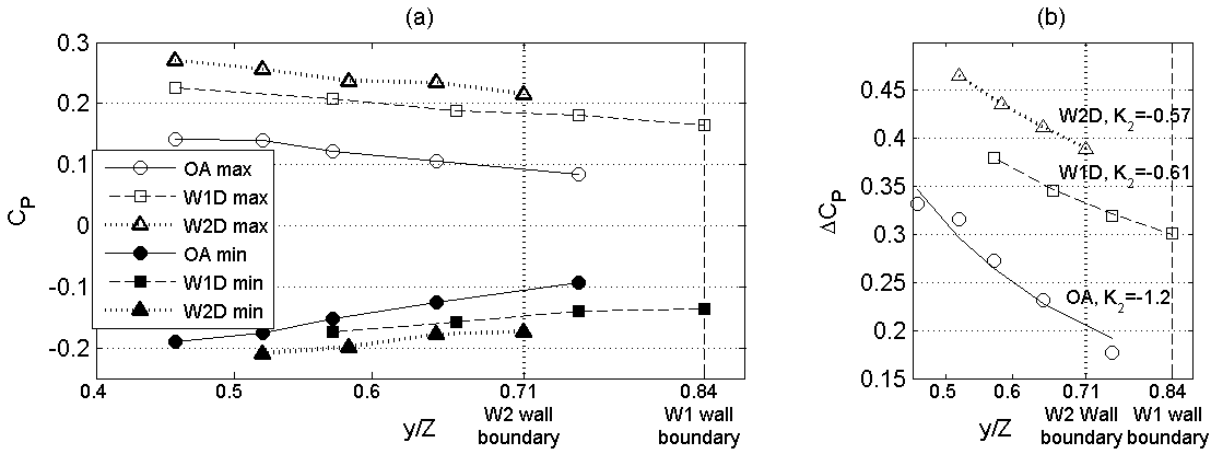

Figure 4.7: Maximum static pressure fluctuation around the train's nose at increasing lateral (*y*-axis) positions and height *z/Z*=0.58, for the open air (OA) and wall cases (W1D, W2D): (a) Maximum positive and suction pressure; (b) Peak-to-peak pressure, with inverse-power curves fitted to the data and labelled with their exponents (K_2).

The results show that both of the double wall cases cause the peak pressures to increase relative to the open air at all *y*-axis positions. The peak-to-peak pressure on the surface of wall W2D is C_P=0.4, which is nearly double (195%) that at the equivalent position in the open air (C_P=0.2). This matches the prediction of Baker et al. (2012), shown in Equations 2.8 to 2.10 in Section 2.2, which uses potential flow theory and a simplification of the Bernoulli equation to predict that the pressure coefficient on a wall is double that in the open air at the same position.

The closer walls W2D cause higher pressures than the further walls W1D at all positions. The positive peaks increase more than the suction peaks.

Quinn et al. (2001) found that the pressure around a vehicle's nose in the open air decays proportionally to the inverse square of the separation distance (K_2=-2). Johnson and Dalley (2002) investigated the effect of track spacing on the peak-to-peak pressure on the side of a stationary train passed by a moving-model train, using three different train noses. In each case, an inverse-square relationship was fitted to the data; a lower exponent of K_2=-1.6 might have been more appropriate. The results in Figure 4.7 show that an exponent of K_2=-1.2

provides the best fit for open air data. This is substantially lower than in the past experiments. However, the ICE2 has a significantly larger cross-sectional area than the vehicles used in the past experiments, and this may be related to the decay exponent. The results for the wall cases show that the exponent halves to K_2=-0.6 because the pressure decays at a lower rate than in the open air. This may cause higher pressure loads on objects wherever they are located in the cross-section of the structure.

Figure 4.8 shows the vertical variation of the pressure fluctuation around the train's nose along the line of surface tappings for all wall cases.

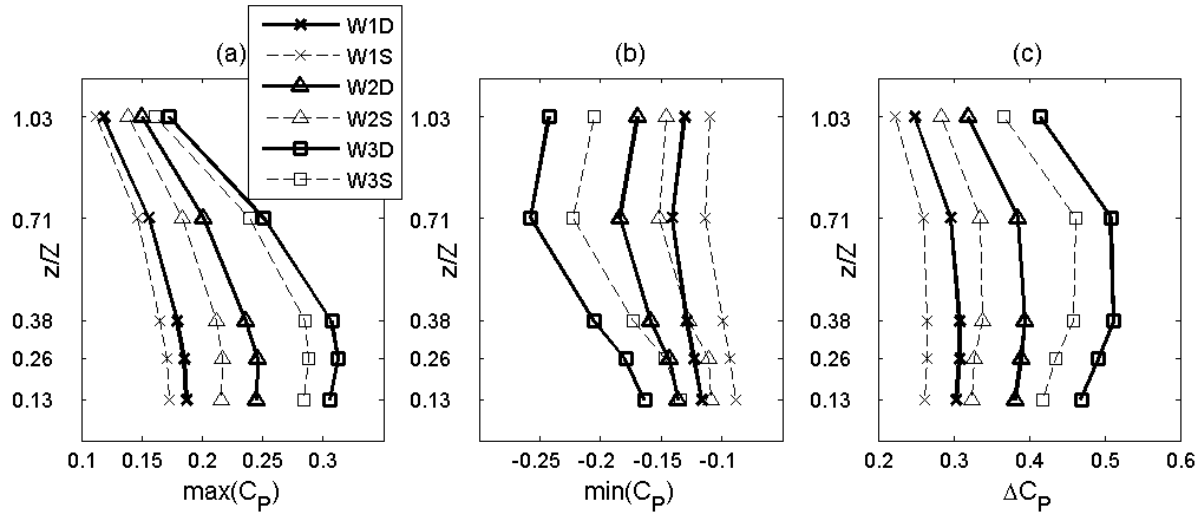

Figure 4.8: Maximum static pressure fluctuation around the train's nose at increasing vertical (*z*-axis) positions along the wall surface, for six wall configurations. (a) Maximum positive pressure; (b) maximum suction pressure; (c) peak-to-peak pressure.

The results show that the pressure fluctuation varies with height. The maximum suction pressure reduces with increasing height whilst the maximum positive pressure increases. The two effects clearly do not cancel each other out as the peak-to-peak results vary with height. A maximum peak-to-peak pressure occurs in the range of 40-60% of the train body height, and a minimum occurs close to the ground and the train's roof. As a rough measure of the variation of peak-to-peak pressure with height, the first standard deviation of the peak-to-peak pressure

divided by the mean for all five wall tappings has been calculated: $\sigma(\Delta C_P)/mean(\Delta C_P)$=0.08 for the single walls and 0.08 for the double walls.

An 'edge effect' caused by the top of the wall is not deemed to play a significant part in the reduction of peak pressure with increasing height, as the top edge of the wall (z/Z=1.79) is much higher than the train's roof (z/Z=1) and the highest tapping (z/Z=1.03). Rather, this observation is attributed solely to the aerodynamic shape of the train. A similar variation in pressure with height has also been observed in Schultz (1990), which reported measurements of the surface static pressure on flat vertical trackside plates caused by a passing moving-model 1/25 scale ICE1. The peak-to-peak pressure at the centre tapping was considerably higher than at the upper and lower tapping positions.

The results also show that the mean increase in ΔC_P caused by the symmetrical double walls compared to the single walls is 17% and 16% for W1 and W2 respectively. The mean increase caused by the asymmetrical double walls (W3D) is less, at 12%; the wall opposite the instrumented wall was further away from the tracks than the W3S position, so its presence caused a smaller increase on the single wall case.

4.2.3 Tunnels

The results for tunnels are analysed in this section. The loading pattern has been defined in Section 4.2.1 (Figure 4.4). The first sub-section (Section 4.2.3.1) examines how the loading patterns and maximum pressures are affected by the placement of the surface tapping along the *x*-axis (longitudinally), the length of the tunnel, and the train's speed. The second sub-section (Section 4.2.3.2) examines how the maximum pressure change varies at different lateral and vertical surface tapping positions.

Details of the relevant test cases are recapped in Figure 4.9, and the reasons for choosing the geometric parameters are given in Section 3.5.4.

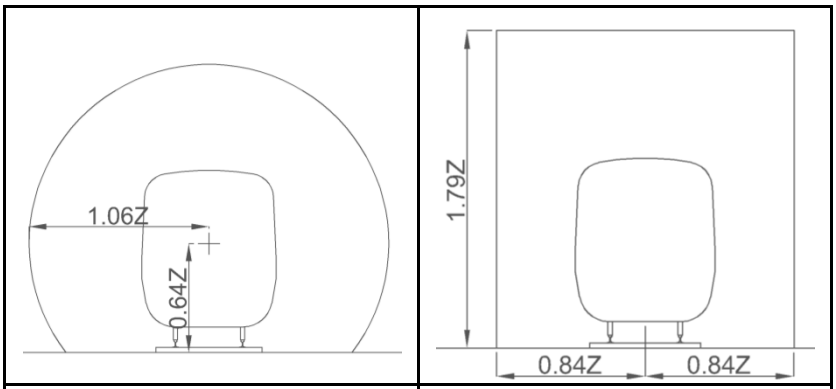

T1. *L/Z*=147. *β*=0.23. *α*=0%.

T2. *L/Z*=51. ***T3.*** *L/Z=15.* ***T4.*** *L/Z=5.* In all cases *β*=0.23. *α*=0%.

Figure 4.9: Cross-section views and geometric details of the tunnel test cases (recap).

4.2.3.1 Effect of tunnel length, sensor position and train speed

Figure 4.10 shows how the loading pattern varies based on a surface tapping's *x*-axis position, while the tunnel length and train speed are constant. In Figure 4.10(a), two positions are shown for T2 (length *L/Z*=51), and in Figure 4.10(b), three positions are shown for T3 (length *L/Z*=13).

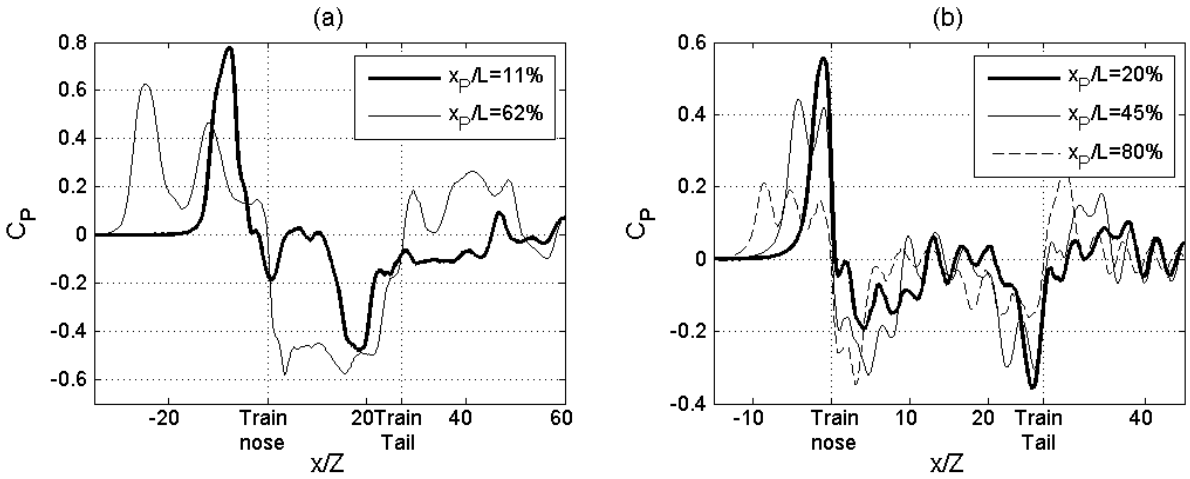

Figure 4.10: Effect of longitudinal (*x*-axis) position in a tunnel on the pressure loading pattern, for *α*=0% and *β*=0.23, measured by a wall surface tapping at *z/Z*=0.26. Tunnels: (a) T2; (b) T3.

The results show that increasing the distance from the tunnel's entrance causes the following changes to the pressure loading pattern: Firstly, the peak positive pressure ahead of the train's nose decreases; Then the peak suction pressure just behind the nose increases; Then the peak suction pressure just ahead of the tail increases; and finally, the peak positive pressure behind the tail decreases. All of this can be explained in relation to the terminology and description of the general loading pattern for a long tunnel in Section 4.2.1.

The peak positive pressure is caused by the nose-entry compression wave and friction pressure rise, and occurs just ahead of the train's nose. Dissipation of the compression wave explains some of the reduction of the peak positive pressure with distance from the entrance. If the sensor is placed far enough into the tunnel (which it was in this case), the peak reduces greatly as the first reflected expansion wave superimposes onto the friction pressure rise region before the peak is reached. Subsequent reflected waves may reduce the peak further if the sensor is placed further from the entrance - the results in Figure 4.10(b) for x_P/L=80% show that three wave periods occur before the train's nose reaches the sensor. The peak suction pressure just behind the train's nose increases with proximity to the exit due to the nose-exit expansion wave.

The peak suction pressure around the train's tail is analogous to the above description of the positive pressure region ahead of the nose, but it is generated by the tail-entry expansion wave (rather than nose-entry), and therefore the pressure has an opposite sign. The peak positive pressure behind the train's tail is analogous to the above description of the suction pressure region just behind the nose, but it is generated by the tail-exit compression wave (rather than nose-exit), and therefore the pressure has an opposite sign.

The results suggest that the pressure remains in suction between the train's nose and tail if the tunnel is longer than the train, and returns to atmospheric ($C_P \approx 0$) if the tunnel is shorter than the train.

Figure 4.11 shows how the loading pattern varies with the length of the tunnel, whilst the surface tapping's x-axis position and train speed are constant.

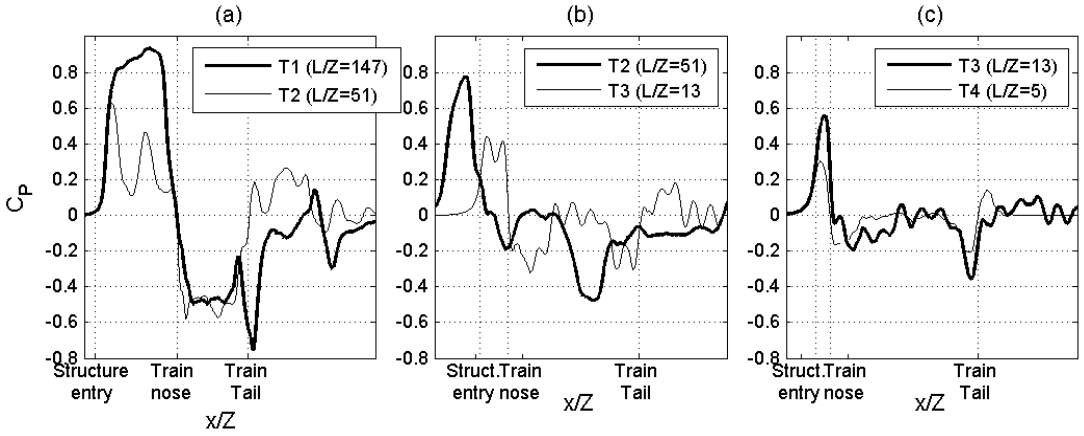

Figure 4.11: Effect of tunnel length (L/Z) on the pressure loading pattern, for α=0% and β=0.23, measured by a wall surface tapping at z/Z=0.26 and: (a) x_P/Z=31; (b) x_P/Z=6; (c) x_P/Z=2.6.

The results suggest that the length of the tunnel greatly affects the peak pressure magnitudes. This behaviour is related to the distance of the tunnel's exit from the measuring point, as this controls the superimposition of the pressure waves onto the underlying flow. The results show that the peak positive pressure at x_P decreases as L reduces because the first reflected expansion wave cancels out the friction pressure rise before the peak is reached.

The above investigations of x_P for constant L, and L for constant x_P, show that the peak positive pressure ahead of the nose is affected by the combination of x_P and L. The relationship is best described using an analytical equation which splits the tunnel into two regions. The regions are bounded by the location in the tunnel where the first reflected expansion wave, and the train's nose pass the sensor simultaneously. The length of the tunnel does not affect the peak positive pressure if the train's nose passes the sensor before the first

reflected expansion wave. Equation 4.2 assumes that the time taken for the nose-entry compression wave to travel from the entrance portal to the exit at the speed of sound, and then for the first reflected expansion wave to travel from the exit to back to x_P, is the same as the time taken for the selected point on the train to travel from the tunnel entrance to x_P+x at speed V.

$$\frac{x_P}{L} = \frac{2M - \frac{x}{L}}{M + 1} \qquad 4.2$$

x_P/L is the dimensionless position within the tunnel, and M is the Mach number of the train.

The equation represents the boundary between two regions:

1. When LHS>RHS, a change in tunnel length affects the loading pattern.
2. When LHS<RHS, a change in tunnel length does not affect the loading pattern.

Figure 4.12 shows the boundary between the two regions. As $L\rightarrow\infty$, or $x\rightarrow 0$, the x/L term may be neglected, so the equation reduces to a generic form in which the tunnel length does not need to be known initially.

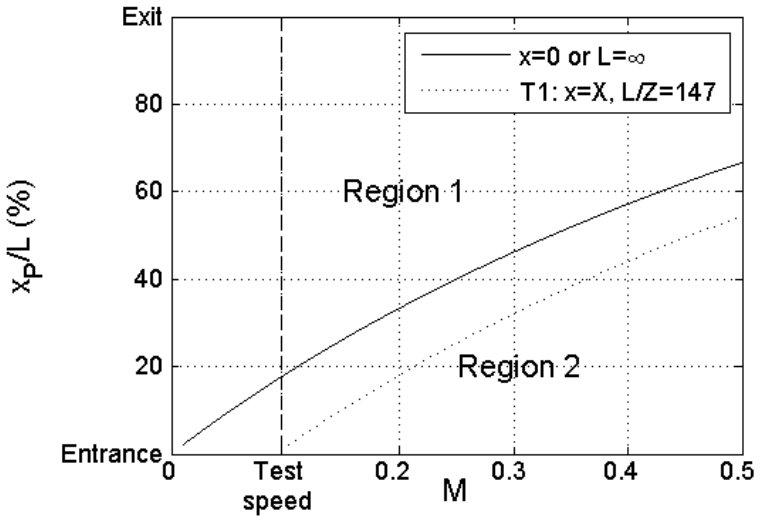

Figure 4.12: Positions in a tunnel (x_P/L) where the pressure loading pattern is in Region 1 (affected by tunnel length up to a given point relative to the train nose), or Region 2 (not affected by tunnel length).

It is clear that Region 1 fills the majority of the tunnel even with the extreme values and the highest Mach numbers. An example for T1 (L/Z=147, β=0.23, α=0%) is also shown in Figure 4.12, with x=X. All of the results from these experiments were clearly confined to Region 1.

Further analysis of Figure 4.11(c) reveals that the loading pattern for T4 (L/Z=5, β=0.23, α=0%) is more similar to that for open air and wall cases than tunnels, based on the shapes and locations of the maxima-producing fluctuations, and the absence of reflecting pressure waves. The durations of the positive and suction peaks are substantially longer than the wall cases, which may affect the maximum loads on structures.

4.2.3.2 Effect of lateral and vertical position

In this section the variation of the peak positive and suction pressure is assessed around the cross-section of a tunnel, for tunnels of three lengths and constant blockage ratio β=0.23. The cross-section contains the ring of surface tappings and the Cobra probes. The sensors are assumed to have been placed at identical x-axis positions so the results apply to a two-dimensional y-z plane, although in reality the Cobra probes were staggered by x_P/Z<0.7

relative to each other and the surface tappings. Figure 4.13 shows the peak positive and suction pressure, and Figure 4.14 shows the peak-to-peak pressure.

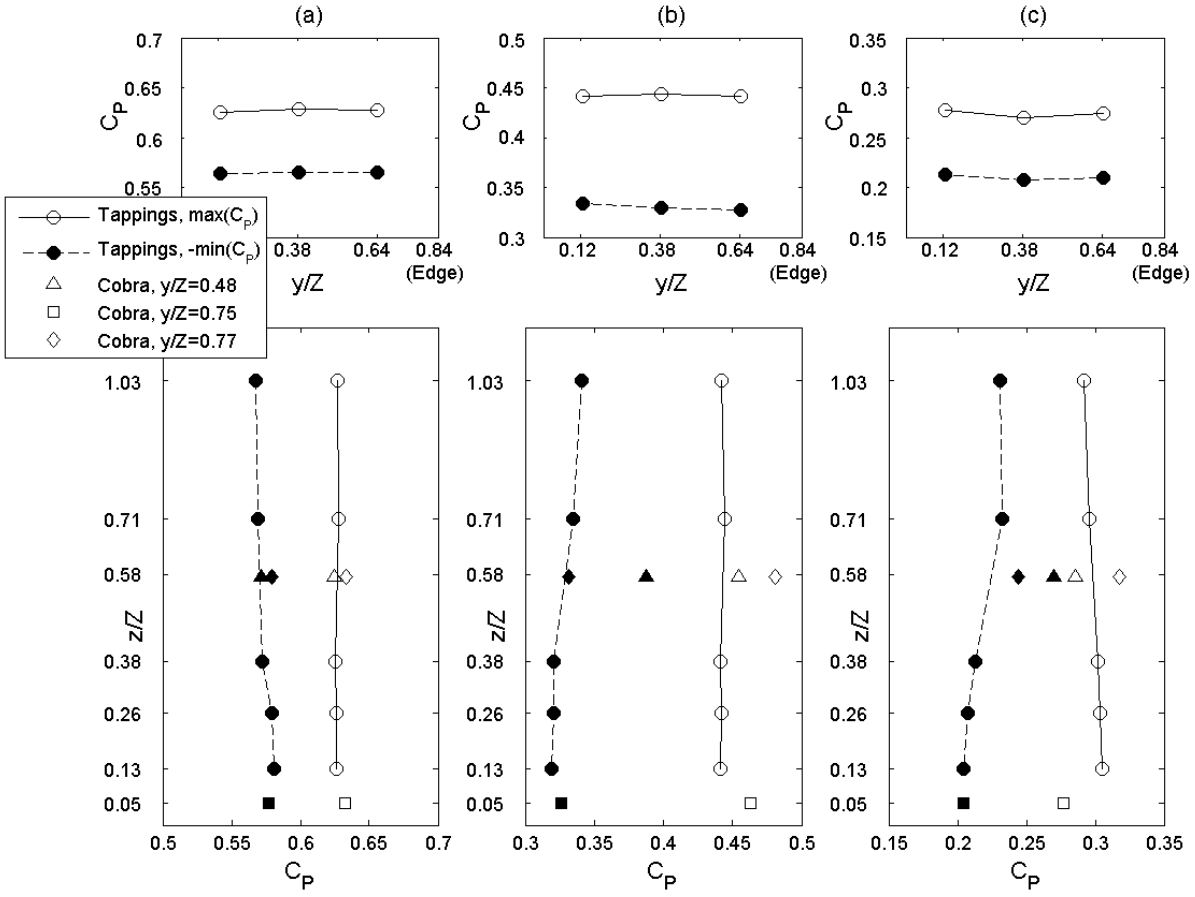

Figure 4.13: Maximum positive and suction pressure along tunnel walls and ceilings and in the annulus, for α=0%, β=0.23 and: (a) T2 (L/Z=51, x_P/L≈62%); (b) T3 (L/Z=13, x_P/L≈45%); (c) T4 (L/Z=5, x_P/L≈50%)

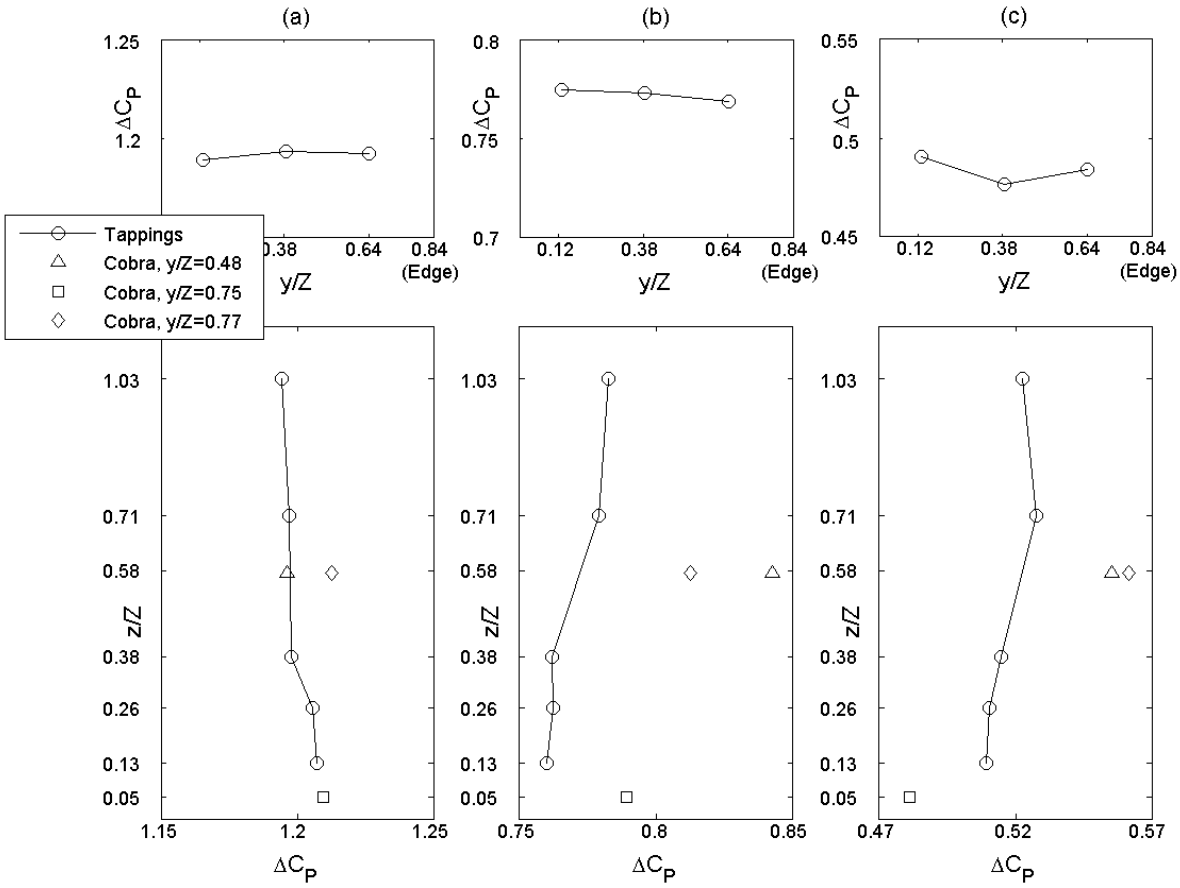

Figure 4.14: Peak-to-peak pressure along tunnel walls and ceilings and in the annulus, for α=0%, β=0.23, and: (a) T2 (L/Z=51, x_P/L≈62%); (b) T3 (L/Z=13, x_P/L≈45%); (c) T4 (L/Z=5, x_P/L≈50%).

The peak-to-peak pressure change along the wall tappings is higher than in the wall cases. The results are not linear, and the relative difference between the highest and lowest peak-to-peak pressures is not substantially different from that seen in the wall test cases (Figure 4.8). The positive pressure peaks are more linear than the suction pressure peaks, particularly for the longer tunnels. The positive peaks are caused by the nose-entry compression wave, which becomes near-one-dimensional a short distance from the tunnel entrance before reaching the sensor. Conversely, the suction peaks occur between the first carriage and tail of the train, which is a region in which the three-dimensionality of the flow is greater due to flow fluctuations around the nose and tail of the train, as well as the boundary layer.

The results for shorter tunnels T3 (L/Z=13) and T4 (L/Z=5) show similarities to each other. The ceiling peak-to-peak pressure increases slightly as y decreases. This has also been found

in moving-model tests measuring the pressure on the soffits of 'overbridges', presented in Baker et al. (2012). Moreover, the peak-to-peak pressure increases as height increases in both cases, which contrasts with the findings for the walls. The opposite occurs in longer tunnel T2: ΔC_P increases as y increases and z decreases. The differences are very small in comparison to the overall magnitudes - the results are closer to one-dimensional than in the wall cases.

The in-flow Cobra probe measurements at the two near-wall positions (y/Z=0.75, z/Z=0.58 and y/Z=0.77, z/Z=0.05) are increasingly dissimilar to those measured on the surface tappings as the tunnel length decreases. The lateral variation of the pressure fluctuation does not match that seen in the wall cases (Figure 4.7). Moreover, the peak positive pressure is higher close to the wall (y/Z=0.77) than close to the train (y/Z=0.48) in T2 and T4, which is the opposite of what would be expected based on the open air and wall results (Figure 4.7). Further analysis reveals that this may be due to the slightly staggered positions of the Cobra probes along the x-axis, which means that they detect superimposed pressure waves which are 'out of phase' compared to the rest of the sensors. This appears to have altered the peak pressures.

It appears that as L and x_P decrease, the three-dimensionality of the peak-to-peak pressure tends towards that seen for wall cases. As a rough measure of the variation of peak-to-peak pressure with height, the first standard deviation of the peak-to-peak pressure divided by the mean for all five wall tappings and three ceiling tappings has been calculated: $\sigma(\Delta C_P)/mean(\Delta C_P)$=0.005 for T2, 0.01 for T3, 0.04 for T4, and 0.08 on average for the single and double wall cases. Therefore the three-dimensionality of the peak-to-peak pressure tends towards that seen for wall cases as L and x_P decrease.

4.2.4 Partially-enclosed tunnels

The results for partially-enclosed tunnels are analysed in this section. The loading pattern has been defined in Section 4.2.1 (Figure 4.5). The first sub-section (Section 4.2.4.1) examines how the loading patterns and maximum pressures are affected by: the opening ratio; the placement of the surface tapping along the *x*-axis (longitudinally); and the length of the tunnel. The second sub-section (Section 4.2.4.2) examines how the maximum pressure change varies at different lateral and vertical positions. Details of the relevant test cases are recapped in Figure 4.15, and the reasons for choosing the geometric parameters are given in Section 3.5.5.

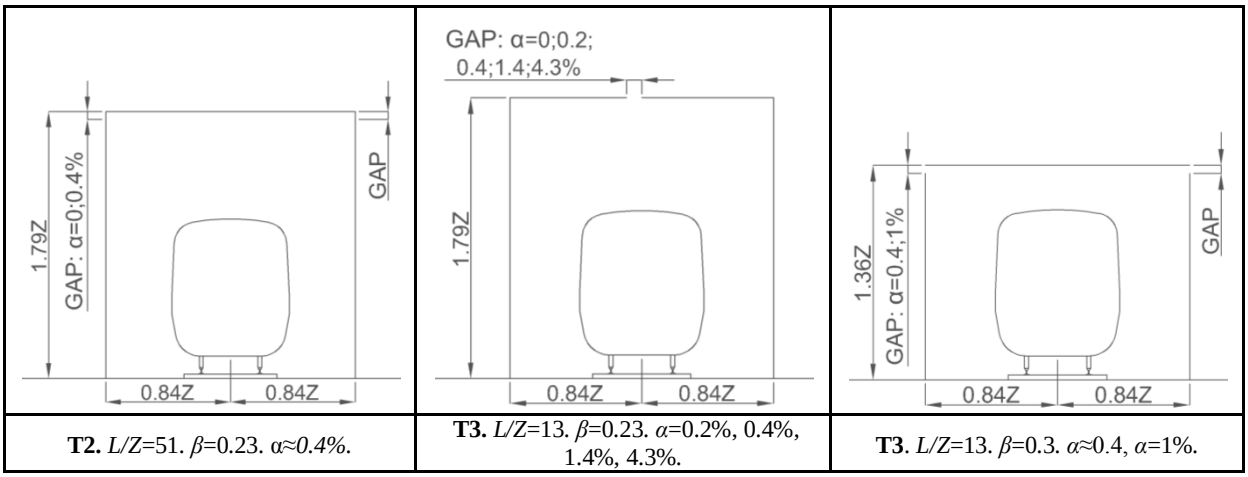

T2. *L*/*Z*=51. β=0.23. $\alpha \approx 0.4\%$.	**T3.** *L*/*Z*=13. β=0.23. α=0.2%, 0.4%, 1.4%, 4.3%.	**T3**. *L*/*Z*=13. β=0.3. $\alpha \approx 0.4$, α=1%.

Figure 4.15: Cross-section views and geometric details of the partially-enclosed tunnels (recap).

4.2.4.1 Effect of opening ratio, sensor position and tunnel length

Figure 4.16 shows time histories near the entrance, middle, and exit of T3 (β=0.23) for six values of opening ratio (α), including results for α=0% and α=24% (case W1D) to represent extreme values. In case W1D, data is only available for one sensor position (x_P/L=45%).

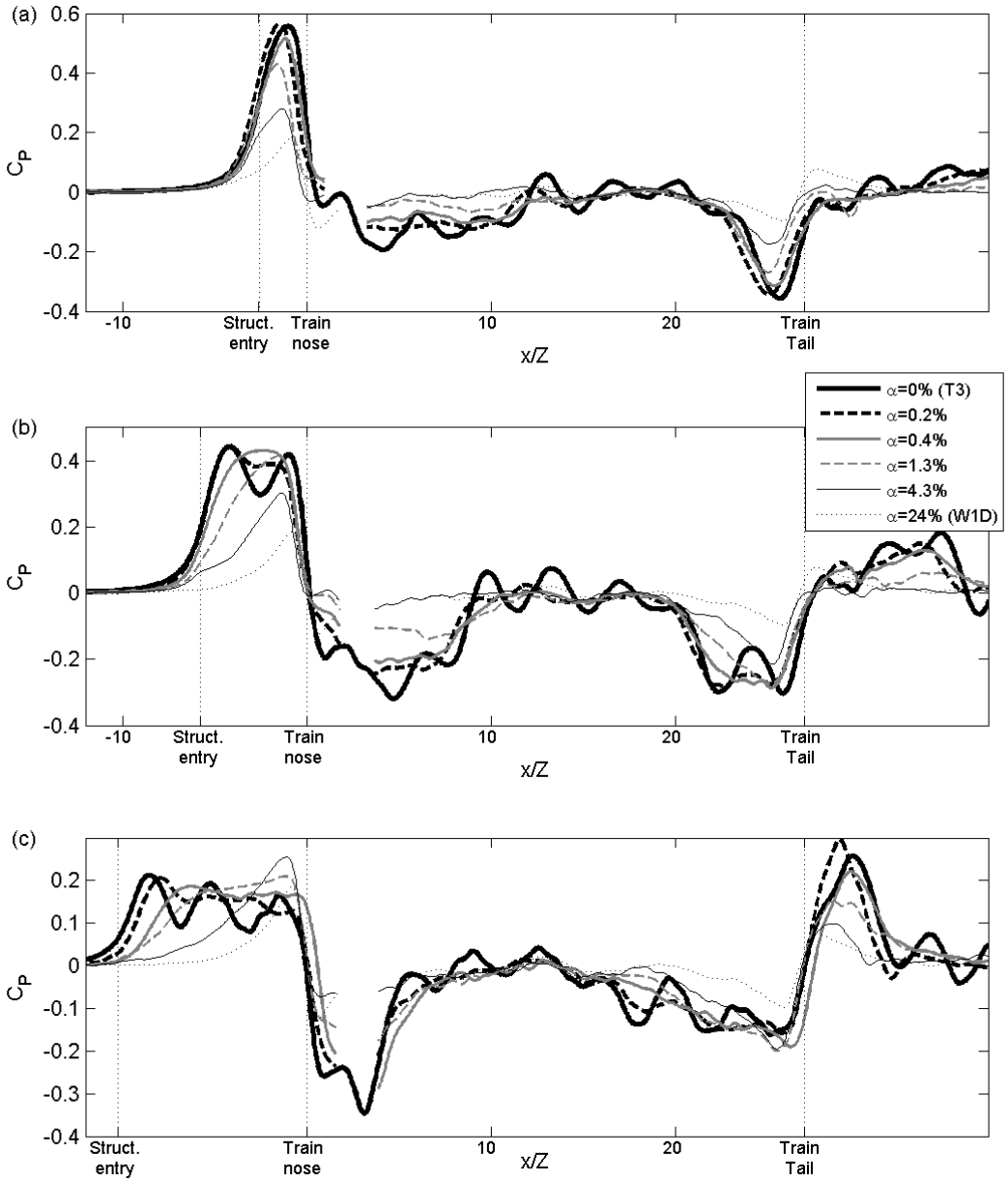

Figure 4.16: Effect of changing opening ratio (α) on the pressure loading pattern, for T3 (L/Z=13, β=0.23), measured by a wall surface tapping at z/Z=0.26 and: (a) x_P/L=20%; (b) x_P/L=45%; (c) x_P/L=80%.

The results show that a clear transition occurs between the three loading patterns as the opening ratio changes. The generic loading pattern for partially-enclosed tunnels (Figure 4.5) occurs for opening ratios of $\alpha \geq 0.4\%$ and sensor positions of x_P/L=20% and 45% (the generic loading pattern is characterised by a single positive pressure peak around the train's nose followed by a single suction peak around the tail). This represents a range of geometric parameters over which the predictions made by the analytical model by Iida et al. (2005)

would be most accurate. There must, however, be an upper bound of the opening ratio as the results clearly tend towards the generic 'open air and walls' loading pattern while the opening ratio increases. The upper bound must lie somewhere within the untested range 4.3%<α<24%.

The loading patterns for $\alpha \leq 0.2\%$ and $x_P/L=80\%$ are similar to those seen in enclosed tunnels. The durations and relative magnitudes of the fluctuations immediately upstream of the train's nose and tail (and ignoring those just downstream) for different opening ratios agree very closely with Iida's predictions (illustrated in Figure 2.2(b)) - as α decreases the durations and magnitudes of the two pressure fluctuations decrease whilst maintaining the same sharp drops immediately around the train's nose and tail.

The magnitudes of the peak pressures change as the opening ratio and sensor position vary. Figure 4.17 illustrates the relationship between the peak positive and suction pressure and x_P/L. The positive pressure is calculated around the train's nose, and the suction pressure around the tail.

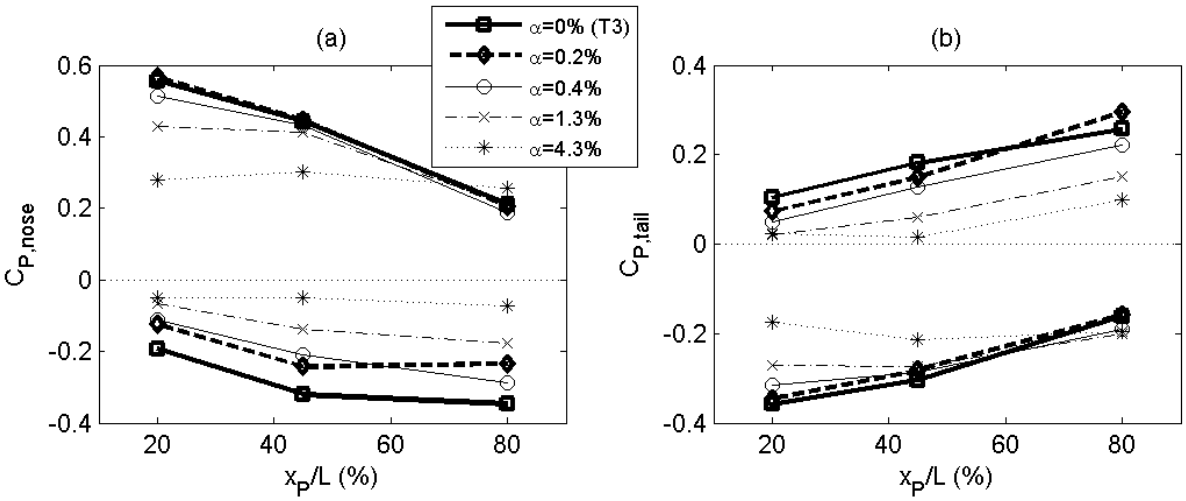

Figure 4.17: Effect of longitudinal position (x_P/L) on the peak positive and suction pressure, for different opening ratios (α), in T3 (L/Z=13, β=0.23), measured by wall surface tappings at z/Z=0.26, around the train's: (a) nose; (b) tail.

The effect of changing x_P and L on the results is similar to that seen in Section 4.2.3.1 for low opening ratios. The nose-entry and tail-exit compression waves, and the nose-exit and tail-

entry expansion waves, play a dominant role in the results. However the compression and expansion wavefronts have less of an effect on the results as the opening ratio increases, due to their dissipation. Therefore the peak pressures tend towards becoming invariant of the sensor position within the tunnel.

Figure 4.18 illustrates the relationship between the peak pressures and the opening ratio.

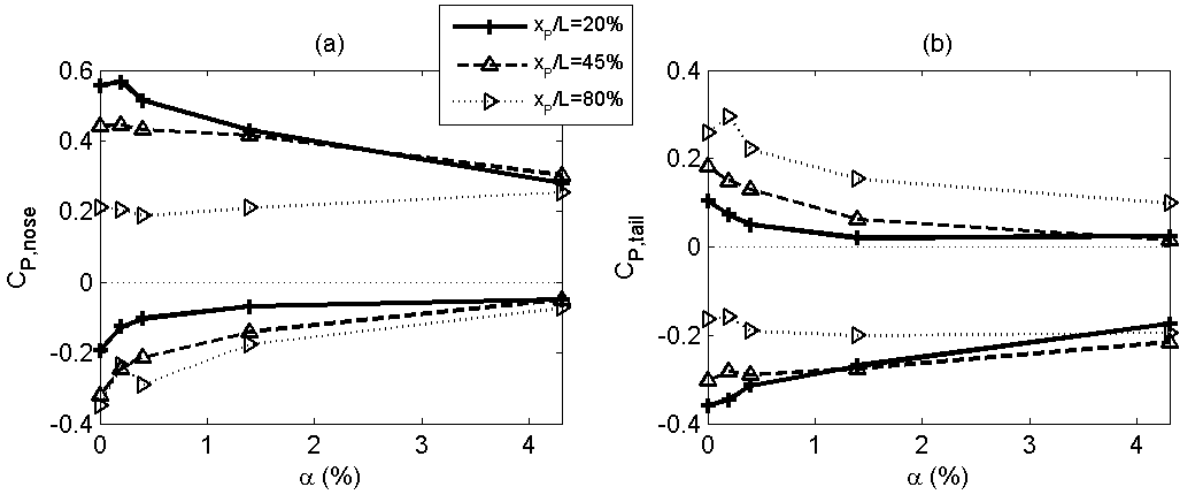

Figure 4.18: Effect of opening ratio (α) on the peak positive and suction pressure, for different longitudinal positions (x_P/L), in T3, measured by wall surface tappings at z/Z=0.26, around the train's: (a) nose; (b) tail.

The dissipative effect of air leakage on the compression and expansion waves can also be seen in Figure 4.18, which shows some level of convergence of the peak pressures with sensor position as the opening ratio increases. The nose suction peak and the tail positive peak decay most rapidly, showing an exponential decay. These are associated with the dissipation of the nose-exit expansion wave and tail-exit compression wave respectively. The nose positive peak and tail suction peak decrease linearly at the two upstream positions (x_P/L=20% and 45%), and increase linearly at the position closest to the exit (x_P/L=80%). These are associated with the dissipation of the nose-entry compression wave and tail-entry expansion wave respectively. The increase suggests that the peak-to-peak pressure change can be higher in a partially-enclosed tunnel with a large opening than in a fully enclosed tunnel. The reason for

the increase is evident from Figure 4.16(c): the pressure reaches a higher value because it is not suppressed by the superimposition of pressure waves.

Further analysis of the peak-to-peak pressure results reveals that ΔC_P decreases linearly with increasing opening ratio, with a linear gradient of -5.3 (when α is expressed as a percentage). A similar study was carried out by Muraki et al. (2010), in which it was found that for full-scale Shinkansen trains passing through partially-enclosed train stations (with very large areas hence low blockage ratios), the gradient was between -1.9 and -2, over the range α=0.8% to 2.5%. The different gradients may result from differences in the blockage ratio. It is known from Equation 2.16 that the opening ratio and blockage ratio both affect the magnitude of the pressure, thereby altering the gradient.

Figure 4.19(a) shows time histories for a longer tunnel (T2, L/Z=51, β=0.23) at sensor position x_P/L=62%, for two opening ratios (α). The fully-enclosed case (α=0%) is shown alongside the partially-enclosed case (α≈0.4%) for comparison. In Figure 4.19(b), data for a higher blockage ratio of β=0.3 are included, and results for two opening ratios are shown. The accuracy of any comparisons made between T2 (α≈0.4%) and T3 (α=0.4%) is hindered by geometric differences between the structures: firstly the opening ratio was not precisely α=0.4% along the length of T2 (discussed in Section 3.5.4); and second of all the slits in T2 ran along the eaves rather than the ceiling centreline (shown in Section 3.5.5 - Figure 3.12).

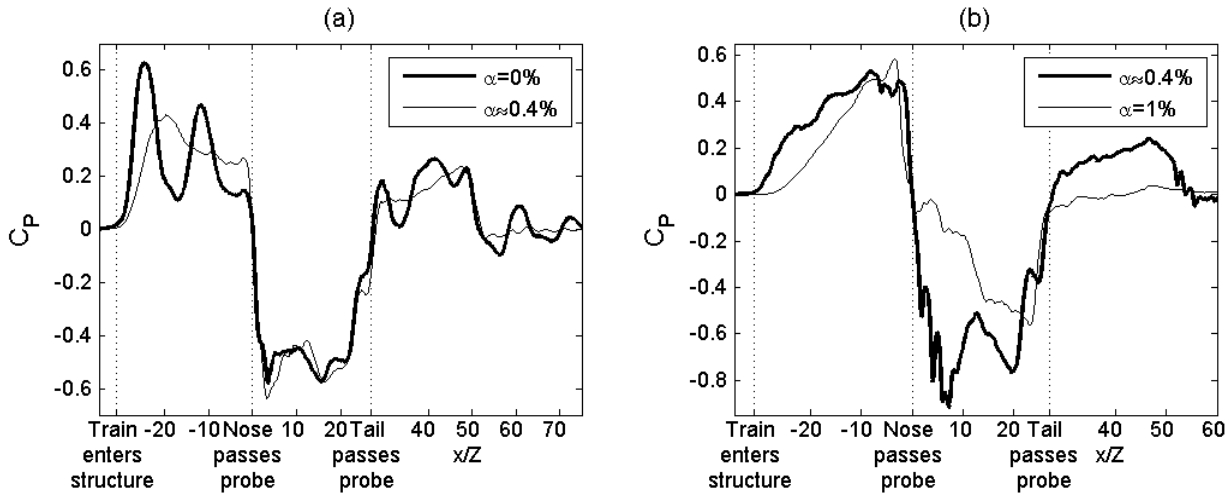

Figure 4.19: Effect of opening ratio (α) in T2 (L/Z=51) on the pressure loading pattern, for a wall tapping at z/Z=0.26, x_P/L=62%, and blockage ratios of: (a) β=0.23; (b) β=0.3.

The time history for T2 (α≈0.4%) exhibits the same qualitative characteristics as that found in the past research (Takei et al., 2008; Muraki et al., 2010; Iida et al., 2005) . It most closely fits the 'sawtooth' generic loading pattern which forms the basis of the analytical model from Section 2.2.

Comparison of the results for T2 with the earlier results for T3 (β=0.23) suggests that the changes to the loading pattern can be attributed to the same geometric variables: as the opening ratio increases from α=0% to 0.4%, dissipation caused by air leakage removes the sinusoidal pressure wave pattern but does not appear to attenuate the 'underlying' ensemble average.

4.2.4.2 Effect of lateral and vertical position

In this section the variation of peak positive and suction pressure is assessed around the cross-section of a partially-enclosed version of T3 (L/Z=13, β=0.23) with four opening ratios. The cross-section contains the ring of surface tappings and the Cobra probes. The results for opening ratios of α=0% (T2) and α=24% (W1D) have already been plotted (Figure 4.14 for T3, Figure 4.7 and Figure 4.8 for W1D), and their results will be taken into account in the

analysis for this section. The sensors are assumed to have been placed at identical *x*-axis positions so the results apply to a two-dimensional *y*-*z* plane, although in reality the Cobra probes were staggered by up to $x_P/Z<0.7$ relative to each other and the surface tappings. Figure 4.20 shows the peak positive and suction pressure, and Figure 4.21 shows the peak-to-peak pressure.

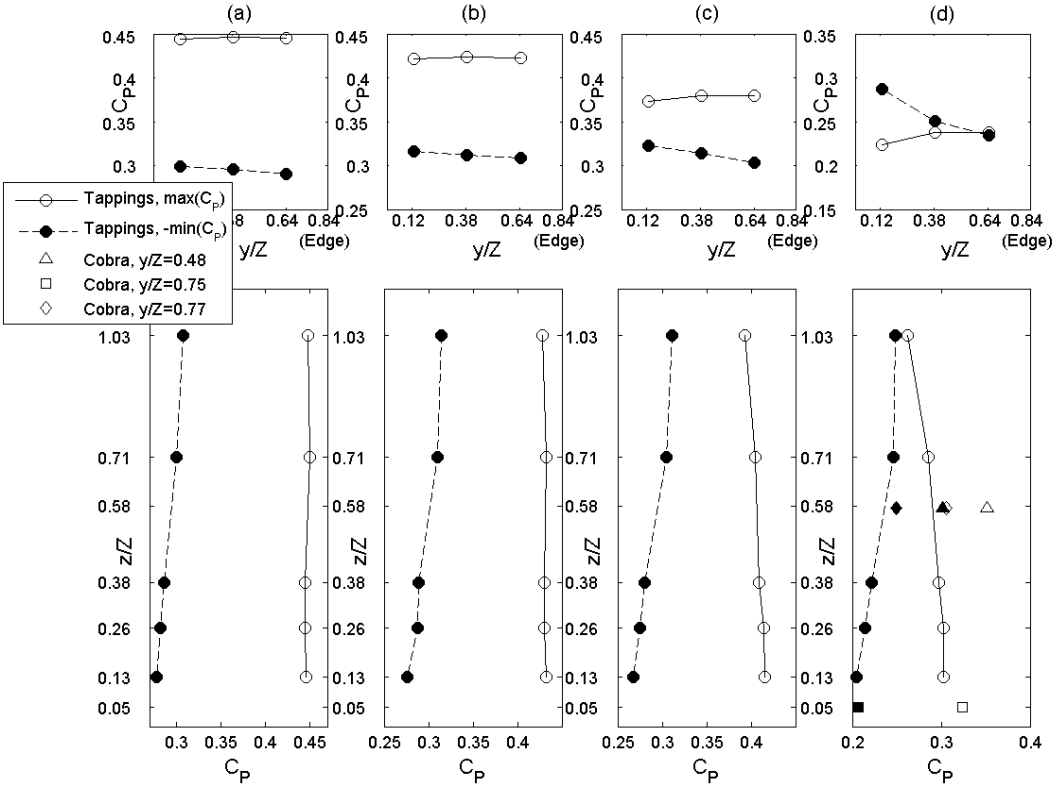

Figure 4.20: Maximum positive and suction pressure along the walls and ceilings and in the annulus of partially-enclosed tunnel T3 (L/Z=13, β=0.23, x_P/L=45%), for opening ratios of: (a) α=0.2%; (b) α=0.4%; (c) α=1.4%; (d) α=4.3%.

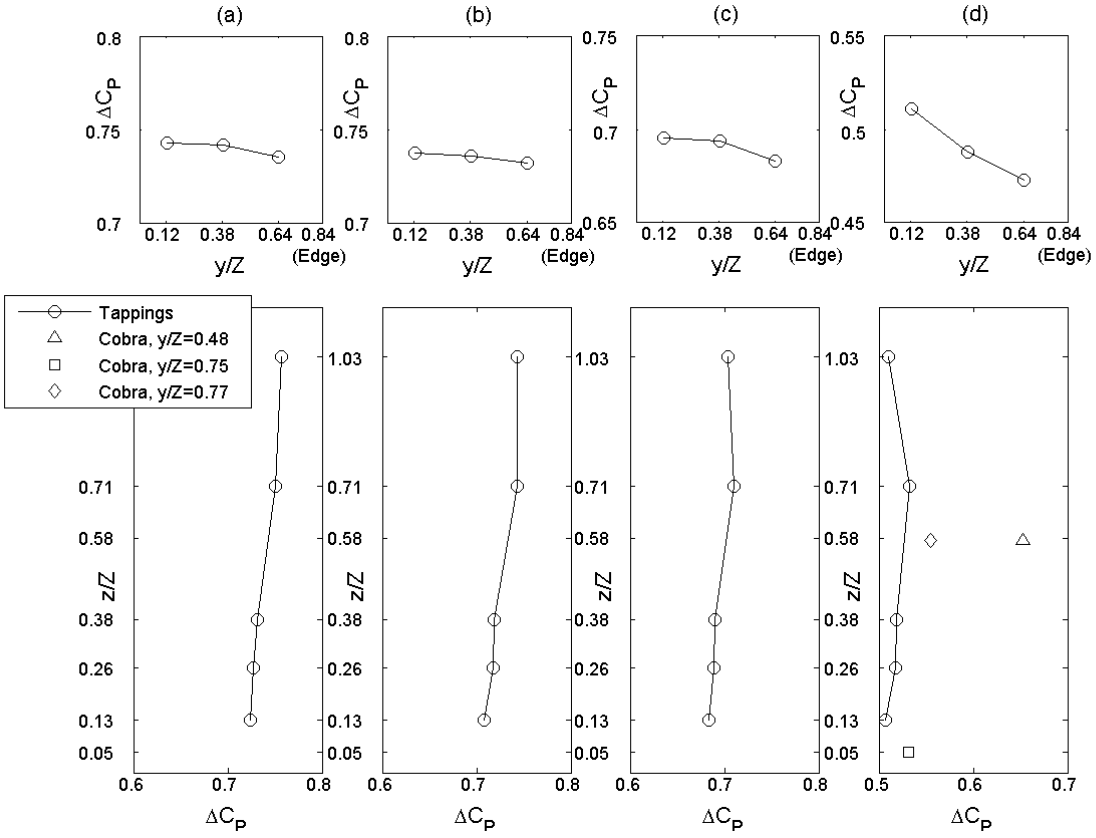

Figure 4.21: Peak-to-peak pressure along the walls and ceilings and in the annulus of partially-enclosed tunnel T3 (L/Z=13, β=0.23, x_P/L=45%), for opening ratios of: (a) α=0.2%; (b) α=0.4%; (c) α=1.4%; (d) α=4.3%.

In all cases, the results show that the peak-to-peak pressure magnitudes are greater than in the walls and open air, but lower than in the short tunnels. The results are not linear, and the variation between the highest and lowest peak-to-peak tapping pressures is not substantially different from the variations seen in T2 or W1D. The positive peak is more linear than the suction peak, particularly for the lower opening ratios. This was also observed in the enclosed tunnels (Section 4.2.3.2).

As α decreases, the three-dimensionality of the peak-to-peak pressure tends towards that seen for wall cases. As a rough measure of the variation of peak-to-peak pressure with height, the first standard deviation of the peak-to-peak pressure divided by the mean for all five wall tappings and three ceiling tappings has been calculated: $\sigma(\Delta C_P)/mean(\Delta C_P)$=0.01 for α=0%, 0.015 for α=0.2%, 0.018 for α=0.4%, 0.014 for α=1.4%, and 0.037 for α=4.3%. Apart from

the one anomaly (α=1.4%), this parameter increases as the opening ratio increases, thus showing that the three-dimensionality of the peak-to-peak pressure tends towards that for seen in the wall cases.

For the three lower opening ratios, the peak-to-peak pressure rises with increasing height on the wall and decreasing lateral separation on the ceiling. The same pattern was found for the enclosed tunnels (Figure 4.14). A bulge of peak-to-peak pressure occurs in the range of 60-80% of the train's body height for the two higher opening ratios of α=1.4% and 4.3%. A similar pattern occurs for the walls (W1D, Figure 4.8). The peak-to-peak pressure becomes increasingly linear along the ceiling as the opening ratio increases. Overall, it may be said that as the opening ratio increases, the pattern of pressure variation around the cross-section transitions from tunnel- to wall-type behaviour, starting from an opening ratio around α=1.4%. The in-flow and surface pressure measurements correspond more closely to each other than in the short tunnels (in the one case where in-flow Cobra probes were used: α=4.3%).

On the ceiling, the opening has an effect on the observations. The positive pressure falls with increasing proximity to the opening while the suction pressure increases, causing the peak-to-peak pressure to rise. The effect becomes more pronounced as the opening ratio increases. This was not seen to the same extent in the enclosed tunnels. In the case of a flow through an orifice, the positive pressure on the plate surrounding the orifice reduces at close proximity to the orifice, and the suction pressure on the lee-side increases. Evidence of this pressure distribution near the opening would suggest two things: firstly that the opening is analogous to an orifice on a flat plate; and secondly that a flow is induced through the opening by pressure differentials between the tunnel interior and the exterior. The peak positive pressure reduces with increasing proximity to the opening, as would be expected for a flow exiting the

tunnel. The peak suction pressure grows with increasing proximity to the opening, as would be expected for a flow entering the tunnel. This suggests that the opening is analogous to an orifice on a flat plate.

4.3 Characteristic load analysis

In this section, two important engineering load types are considered: fatigue loads and maximum loads. In sub-section 4.3.1, the characteristic loads for assessing fatigue damage to structures have been calculated. In sub-section 4.3.2, the maximum loads have been calculated and compared with predictive formulae from codes of practice, within the framework of Objective 5 of this thesis.

4.3.1 Maximum pressure change over a characteristic duration

This section presents analysis of the maximum pressure changes at different characteristic durations. Friedl et al. (2011) assumes that the time separation between the maximum and minimum loads is half the wavelength of a periodic function. The characteristic frequency and duration may be derived from this. The load at a characteristic frequency may be compared with the natural resonance frequency of the structure to determine the risk of accelerated fatigue failure.

The peak-to-peak pressure has been calculated within a moving fixed-size window. The size of the window corresponds to half the wavelength of the characteristic frequency. The characteristic duration is the inverse of this frequency. This method produces the same values of peak-to-peak pressure as those calculated in Friedl et al. (2011) for open air and wall cases.

Figure 4.22 shows the peak-to-peak pressure calculated along the whole time history and the peak-to-peak pressure at three characteristic durations: 1s (1Hz); 0.33s (3Hz); and 0.2s (5Hz),

which have been determined according to Equation 3.22. The durations have been chosen to reflect the range of natural frequencies associated with noise barrier systems listed in Reiterer and Altay, (2009).

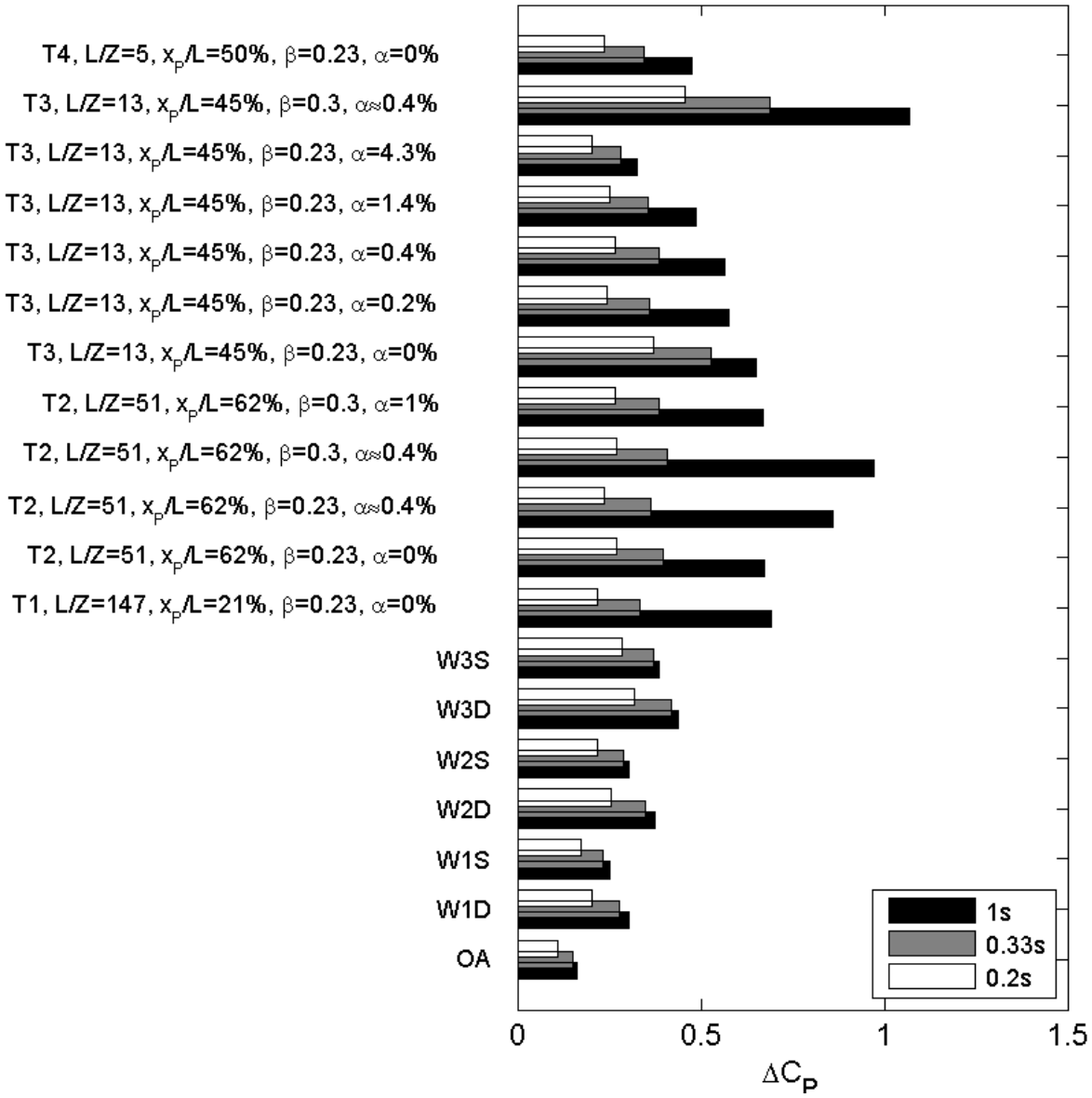

Figure 4.22: Peak-to-peak pressure measured over different characteristic durations for all test cases, by a wall tapping at *z*/*Z*=0.26.

All of the results show that the peak-to-peak pressure reduces with decreasing durations. This would be expected as the size of the window becomes smaller than that required to calculate the worst case pressure change. The rate of change of peak pressure with the characteristic duration varies. In the longest tunnels and partially-enclosed tunnels ($L/Z \geq 51$), the peak-to-

peak pressure decreases more rapidly compared to the open air and walls, as well as the shorter tunnels and partially-enclosed tunnels. This is because the peak positive and suction pressures tend to occur at widely spaced intervals in the long structures.

4.3.2 Comparison with predictive formulae in codes of practice

This section presents a comparison of the experimental peak-to-peak pressures with those calculated using predictive formulae in EN 14067-4 (BSI, 2005). The predictive formulae originated from CFD 'Panel method' simulations reported in ERRI (1994). In Section 1.3, some issues were raised by Baker et al. (2012) regarding the predictive formulae. It was recommended that experiments are carried out at the TRAIN Rig on continental gauge trains to replace 'the less reliable data in the current code'. Gilbert et al. (2012) reported on preliminary data from the double-wall experiments described in this thesis. The study found that the pressure loads and predicted loads closely corresponded to each other at positions far from the train, but the formulae over-predicted the loads at positions close to the train. The more extensive experimental dataset reported in this section will help to further address this research gap.

All of the single and double wall cases are included in this analysis, as their results may be compared with the predictive formulae for flat vertical structures parallel to the tracks. The guidance does not discuss the application of the formula to walls on both sides of the tracks, but the double-wall data will be compared with prediction nonetheless. Data for tunnels T3 and T4 (β=0.23, α=0%) are also included, which have lengths of L/Z=13 and 5 respectively. The results for T4 may be compared with the predictive formulae for a closed structure enveloping the tracks over a limited length up to 20m, as the full-scale equivalent length of T4 is 20m. The results for T3 are included to test the limit of applicability of the prediction as the

length of the tunnel increases. The rectangular tunnel cross-section shape is ideal for comparison as the predictive formulae are based on combined vertical and horizontal surfaces.

The analysis has been carried out using a method previously adopted in Baker et al. (2012). It involves obtaining the maximum positive and suction pressures by averaging the pressure 5m (x/Z=1.28) in front of and behind the location in the time history where the pressure coefficient crosses zero due to the passage of the train's nose. The mean wall pressure has been calculated by measuring the bending moment (M) about the base of the structure using the maximum 5m-averaged positive and suction pressures at each of the five tapping positions. Then the bending moment equation for a cantilever has been rearranged so that $\omega=2M/L^2$, in which L is the distance to the highest tapping (z/Z=1.03), so L=4m (full-scale equivalent), and ω is the dimensionless uniformly distributed load (C_P per unit length). This 'moment method' predicts slightly higher loads than a 'normal' integration of pressure tappings, but the results for both methods agree to within one decimal place. The mean ceiling pressure has been calculated from the simple arithmetic mean of the 5m averaged positive and suction pressures measured at each tapping, in accordance with Baker et al.'s methodology. In all cases, the 5m averaging window may not produce the worst-case pressure, so the maximum possible pressure has also been calculated by changing the size of the averaging window for the positive and suction peaks independently until the maximum load occurs.

The predictive formulae are defined. They are all multiplied by a prescribed factor of k_1=0.6 which corresponds to the aerodynamic shape of the train. The predictive formula for a flat vertical structure parallel to the tracks, separated by distance y, is used for comparison with surface pressures from the wall test cases:

$$C_{P1} = k_1\left[\frac{2.5}{(y+0.25)^2}+0.02\right] \qquad 4.3$$

In the code, this formula is constrained to $y \geq 2.3$m ($y/Z \geq 0.59$), which is very slightly further from the train's side than the wall-separation of W3D/W3S.

The predictive formulae for a closed structure enveloping the tracks over a limited length up to 20m are used for comparison with the tunnel structures T3 and T4 (enclosed, α=0%). In order to calculate the wall surface pressure, a modification factor of 2 is applied to C_{P1}. The ceiling surface pressure C_{P2} is modified by a factor of 2.5. The ceiling pressure is predicted by:

$$C_{P2} = k_1 \left[\frac{2}{(z - 3.1)^2} + 0.015 \right] \qquad 4.4$$

Table 4.1 compares experimentally derived dimensionless uniformly distributed loads with predictions that have been doubled in order to represent the peak-to-peak pressure. The 5m-averaged and 'maximum possible' pressures are included for the experimental results.

Table 4.1: Comparison between experimental pressure loads on structures with predictions from EN 14067-4 (BSI, 2005).

Test case	Surface type	x-axis position	Position (full-scale, m)	BSI prediction		Experimental observation	
				Parameter	Prediction	5m averaging	Maximum possible
W1D	Wall	x_P/L=62%	y=3.2675	C_{P1}	0.27	0.24	0.25
W1S	Wall	x_P/L=62%	y=3.2675	C_{P1}	0.27	0.21	0.22
W2D	Wall	x_P/L=62%	y=2.7675	C_{P1}	0.35	0.31	0.32
W2S	Wall	x_P/L=62%	y=2.7675	C_{P1}	0.35	0.26	0.26
W3D	Wall	x_P/L=62%	y=2.2675	C_{P1}	0.50	0.38	0.38
W3S	Wall	x_P/L=62%	y=2.2675	C_{P1}	0.50	0.33	0.33
T3 (L/Z=13, α=0%, β=0.23)	Wall	x_P/L=45%	y=3.2675	$2C_{P1}$	0.53	0.54	0.69
T3 (L/Z=13, α=0%, β=0.23)	Ceiling	x_P/L=45%	z=6.712	$2.5C_{P2}$	0.50	0.40	0.54
T4 (L/Z=5, α=0%, β=0.23)	Wall	x_P/L=50%	y=3.2675	$2C_{P1}$	0.53	0.35	0.45
T4 (L/Z=5, α=0%, β=0.23)	Ceiling	x_P/L=50%	z=6.712	$2.5C_{P2}$	0.50	0.24	0.35

For all cases apart from T3, the 5m-averaged and maximum possible experimental pressures are lower than predictions. The pressure on single walls is slightly lower than that on double walls, which is to be expected based on the findings in Section 4.2.2. The level of over-prediction increases for wall positions close to the train's side. It appears that EN 14067-4

(BSI, 2005) gives valid predictions of the pressure loads on walls at greater lateral distances, but the predictive formulae should be revised to reduce the over-prediction close to the train's side.

The difference between the 5m-averaged and maximum possible pressure for T4 is very large. This shows that the 5m averaging window is too small to capture the (extended duration) pressure fluctuation. Nevertheless, the maximum possible pressures are still below prediction. The 5m-averaged pressure on the walls in case T3 is slightly above prediction, whilst the pressure on the ceiling is below prediction. The maximum possible pressure exceeds prediction by a great margin. Overall, it is clear that the limiting tunnel length of L=20m specified in EN 14067-4 is sensible for ensuring that the measurements are below the maximum predictions.

4.4 Concluding remarks

The following conclusions can be drawn from the analysis carried out in this chapter:

(a) The static pressure data has been compared with existing data for the ICE2. Because the open air peak-to-peak pressure matches full-scale measurements, the methodology for static pressure measurement is deemed to be acceptable in relation to previous accepted methodologies for open air operation. However, this comparison study has not proven that the results in confined spaces match results from full-scale tests. The superimposition effect of pressure waves in tunnels means that the results are not scalable unless the Mach number (M) is matched to full-scale operation. Nevertheless, the flow physics are likely to be correct based on a comparison of loading patterns. These findings have not hindered the ability of the thesis to meet the aim and objectives 4 and 5 which focus on comparative rather than quantitative debate.

(b) Three loading pattern types have been considered. The first type is characterised by two fluctuations occurring around the train's nose and tail. These are respectively a positive followed by a suction peak, and then a suction followed by a positive peak. This is assumed in the literature to occur in the open air and on surfaces such as walls. The second type is characterised by: increased peak pressure magnitudes and durations caused by compression and expansion waves propagating from the tunnel entrance and exit portals; a region of suction or zero-pressure between the train's nose and tail; and an oscillatory 'pressure wave' pattern superimposed onto the underlying data which also affects peak load magnitudes and durations. This is assumed in the literature to occur in tunnels (longer than 20m at full-scale). The third type is characterised only by a positive peak around the train's nose, and a suction peak around the train's tail. This is assumed in the literature to occur in partially-enclosed tunnels.

(c) The tunnel loading pattern is altered in a number of ways by geometric parameters. The loading pattern is most strongly affected by: the position of the sensor; the tunnel's length; and the train speed. All of these factors control the time taken for the compression and expansion waves to reach the sensor from the entrance and exit portals, as well as the frequency of the oscillatory pressure wave pattern. The peak suction pressure decays towards atmospheric conditions between the train's nose and tail if the tunnel is shorter than the train.

(d) It is possible to transition between all three loading pattern types by varying the opening ratio in partially-enclosed tunnels. The opening ratio describes a continuous opening in a tunnel that allows pressure discontinuities to dissipate at a rate controlled by the size of the opening. As the opening ratio increases from α=0% to 0.4%, the oscillatory 'pressure wave' pattern disappears due to dissipation. As the opening ratio

increases further to 4.3%, the loading pattern transitions from its second to its third state. The position of the sensor and the length of the tunnel have less of an effect on the results as the opening ratio increases. Further increases of the opening ratio cause the loading pattern to transition to the first state. The relationship between the maximum pressure and opening ratio depends on both the opening ratio and blockage ratio (β) - this is supported by an analytical prediction model.

(e) In-flow pressure measurements were made by Cobra probes positioned in the air gap between the train and a vertical wall. The peak-to-peak pressure decays according to a power law with an exponent of -1.2 in the open air, and -0.6 in wall cases. The wall surface pressure is twice that which would be experienced at the equivalent position in the open air. Moreover, the wall surface pressure measurements fit the decay relationships closely. However, significant differences occur between in-flow and surface pressure measurements in tunnels and partially-enclosed tunnels. These differences increase with growing tunnel length and distance of the sensor from the entrance portal, and also with reducing opening ratio.

(f) Peak-to-peak pressure loads over characteristic durations have been calculated in order to test the effects that the different structure types and geometric variations have on engineering fatigue loads. Three characteristic durations between 0.2s and 1s (full-scale equivalent) have been tested using moving windows with widths corresponding to the required durations. Some of the tunnels and partially-enclosed tunnels which previously caused the highest peak-to-peak pressures are found to cause very low loads over short characteristic durations. This is because the size of the window is smaller than that required to envelop both the positive and suction peaks, so the worst

case pressure change is missed. By contrast, the worst-case pressure changes lie within the envelopes in wall cases.

(g) Peak-to-peak pressure loads have been calculated and compared with predictive formulae from codes of practice, for some qualifying test cases. The results for single vertical walls and a short tunnel were found to be significantly lower than the predictions. Even the loads for double wall configurations, which produced higher pressures than single walls, were lower than predictions. In the short tunnels, the method for calculating pressures failed to account for the increased load duration associated with the second loading pattern type. Had this been accounted for, the loads would be much higher and closer to the limits (and more relevant to operational conditions).

Some commentary has been made on the flow structures driving the observations. Relationships between pressure fluctuations and slipstream velocity transients are sought in the next section on slipstream velocities, Chapter 5, in order to obtain a more thorough understanding of the flow.

Chapter 5

Slipstream velocity

This chapter describes the slipstream velocity results within the framework of Objectives 4 and 5. This chapter expands considerably on the discussion in Gilbert et al. (2013b). The pressure data from Chapter 4 are taken into account in order to help with identifying the flow structures driving the observations.

This section is structured similarly to Chapter 4 - there are four parts: a comparison of results with existing data in Section 5.1; analysis of the time history results in Section 5.2; analysis of maximum velocities in individual runs Section 5.3; and concluding remarks in Section 5.4.

The test cases relevant to this chapter are illustrated in Figure 5.1. A full explanation of the test structures, chosen geometric changes, and sensors is included in Sections 3.5 and 3.6.

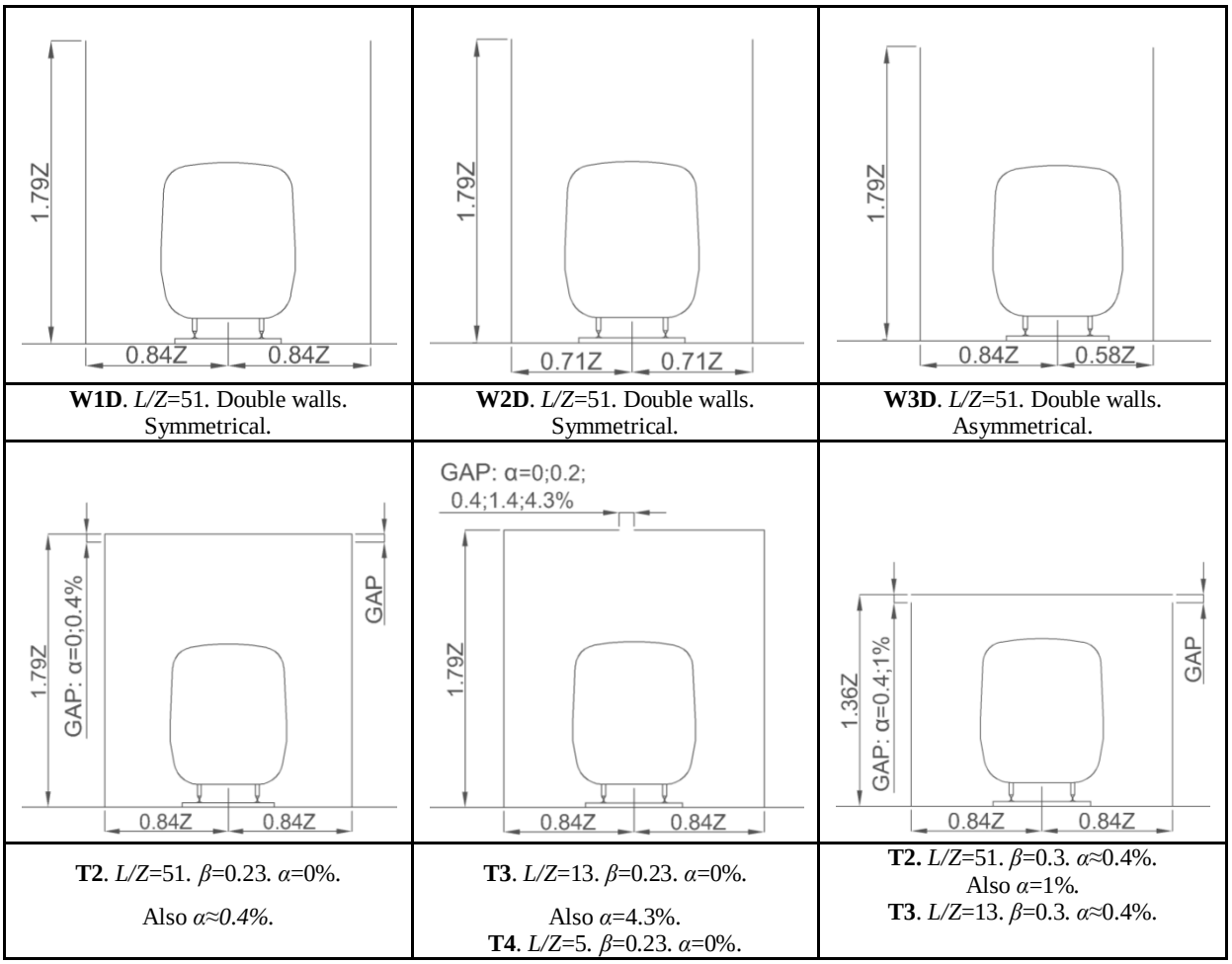

W1D. *L/Z*=51. Double walls. Symmetrical.	**W2D**. *L/Z*=51. Double walls. Symmetrical.	**W3D**. *L/Z*=51. Double walls. Asymmetrical.
T2. *L/Z*=51. *β*=0.23. *α*=0%. Also *α≈0.4%*.	**T3**. *L/Z*=13. *β*=0.23. *α*=0%. Also *α*=4.3%. **T4**. *L/Z*=5. *β*=0.23. *α*=0%.	**T2.** *L/Z*=51. *β*=0.3. *α*≈0.4%. Also *α*=1%. **T3**. *L/Z*=13. *β*=0.3. *α*≈0.4%.

Figure 5.1: Cross-section views and geometric details of all test cases (recap).

5.1 Comparison of results with existing data

The slipstream velocity results have been compared with those from previous studies in order to assess the adequacy of the methodology in capturing the correct flow structures. Section 5.1.1 considers results at mid-height positions near the train side. Section 5.1.2 considers results at low-height positions at the trackside.

5.1.1 Mid-height positions

This section considers the velocities measured at the mid-height position of z/Z=0.58. The ensemble average and maximum velocities from this study are compared directly with existing data for shared sensor positions. Del Valle (2012) and Baker et al. (2001) conducted moving-model experiments measuring the slipstream of an ICE2 in the open air. In the Del-Valle ('DV') study, a 1/50 scale curved model train was attached to a rotating rail rig. The maximum train speed was 16.5m/s. The experiments were repeated N=80 times to obtain very reliable ensemble averages. Cobra probes were placed at six y-axis positions to measure resultant air velocities. In the 'Baker' study, the train model and facility were identical to those used in this study. Single-film hot-wire anemometers were placed at eight y-axis positions to measure the air velocities. The train speed was V=32m/s. The track and ground profile was the same as that used in this study. The experiments were repeated N=20 times. In this study, Cobra probes were placed at six y-axis positions to measure the resultant air velocities. The experiments were repeated N=25 times.

Figure 5.2 shows contour plots which allow the results from the three studies to be compared. They were produced by interpolating and smoothing the data between the neighbouring positions. The boundary layer momentum thickness is also shown as a thick white line, which acts as a reference measure of the boundary layer properties (Refer to Section 2.3 for a description of integral parameters)

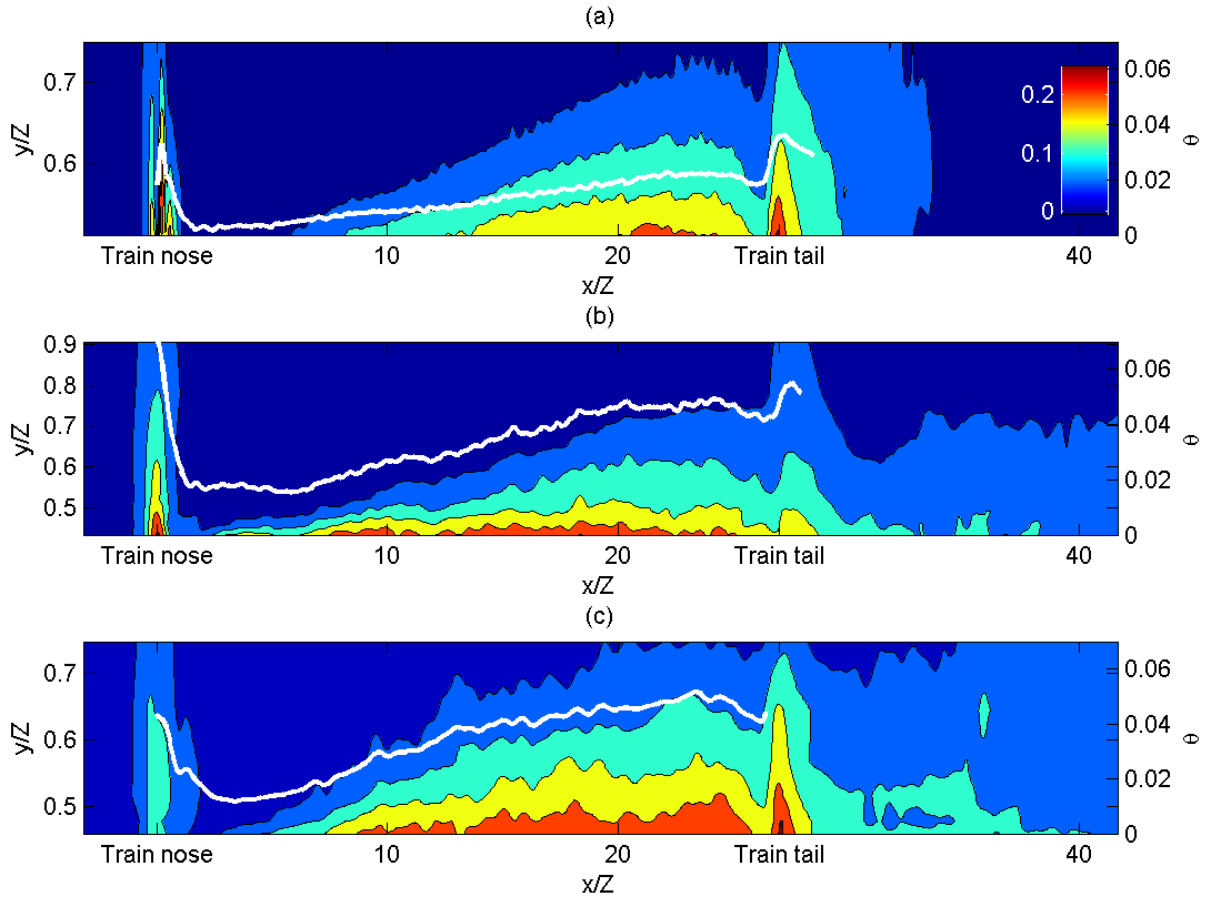

Figure 5.2: *x-y* plane contour plots of the dimensionless resultant air velocity at mid-height in the open air. Data from three studies are included: (a) Del Valle (2012); (b) Baker et al. (2001); (c) This study.

The 'Baker' and 'DV' results agree with results from this study in all regions apart from the nose region. The results in the nose region may be inaccurate.

The results will now be compared in the frequency domain. Baker (2001) identified a number of flow structures in the near-wake by analysing the Morlet wavelet spectra of the 'Baker' data. Spectral peaks were associated with Strouhal numbers of periodically separating shear layers. The spectra of the 'Baker' data have been recalculated, and are shown in Figure 5.3(a-b); they do not match those shown in Baker (2001) as the wavelet parameters are different. Wavelet power spectra of the data from this study are shown in Figure 5.3(c-d).

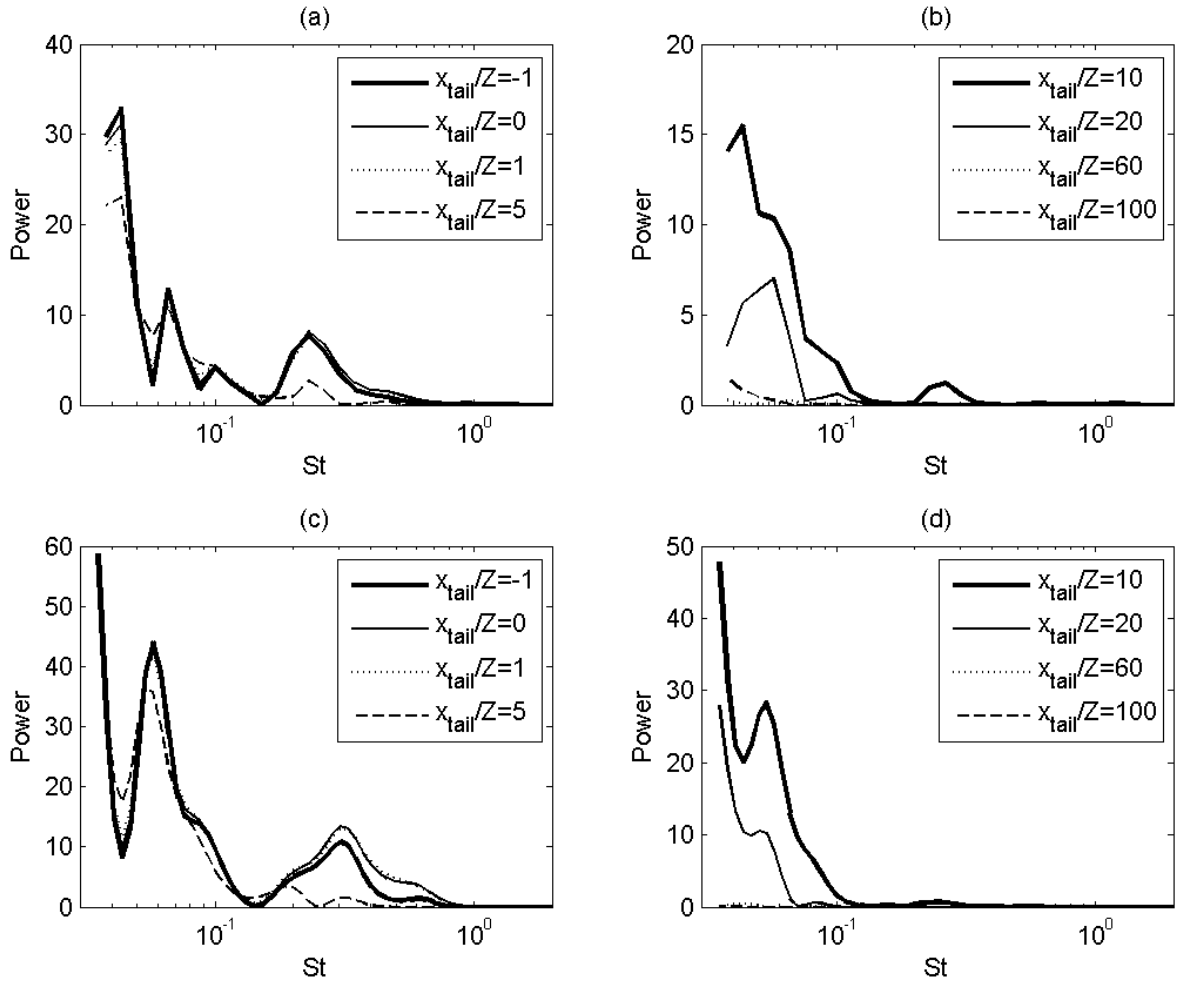

Figure 5.3: Wavelet power spectra of the ensemble average resultant velocity at different *x*-axis positions relative to the train's tail, at *y/Z*=0.09 and *z/Z*=0.58. Data from two studies are shown: (a-b) Baker et al. (2001); (c-d) this study.

In the Baker results, the peak at *St*=0.21 presumably corresponds to separated shear layers which the original study identified as occurring at *St*=0.5, whilst the peak at *St*=0.04-0.05 corresponds to an underlying wake pattern that exists a long distance into the wake which the original study identified as occurring at *St*=0.03-0.05.

The Baker results appear to be very similar to the results from this study. The spectral peak in these results at *St*=0.2-0.3 appears to correspond to the separated shear layers. A peak at *St*=0.06 aligns with a peak in the Baker data. The variation of the results between *x*-axis positions agrees between both studies.

Gilbert and Straathof (2013) compared the results of CFD simulations with the experimental data for two tunnel test cases. Figure 5.4 shows the comparison of the resultant velocity. Appendix A5 explains why there is no experimental data before the wake in Figure 5.4(a).

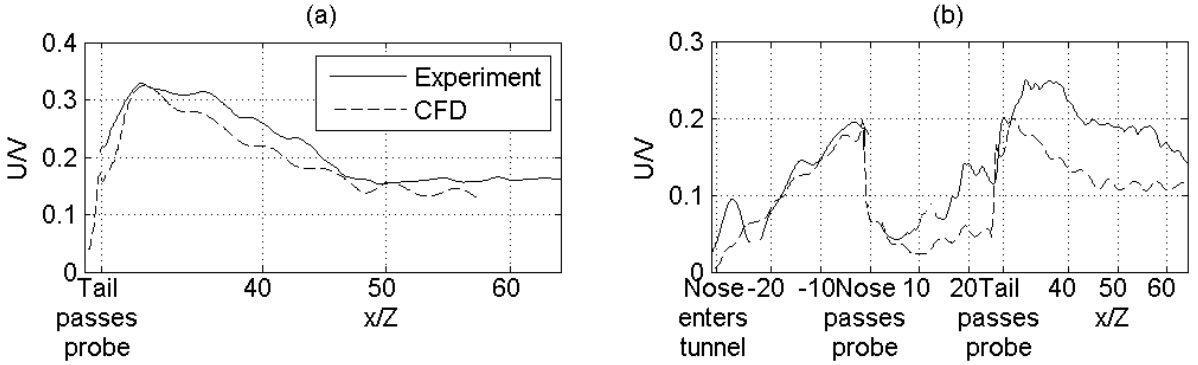

Figure 5.4: Comparison of CFD with experiment (Gilbert and Straathof, 2013), for the ensemble average resultant velocity at y/Z=0.48, z/Z=0.58, for tunnel T2 (L/Z=51), and: (a) $\alpha\approx$0%, β=0.3; (b) α=0%, β=0.23.

The results show that the maximum velocity from CFD for a higher blockage ratio of β=0.3 is within 1% of experiment. However it is 20% lower than experiment for a lower blockage ratio of β=0.23, although the maximum velocity around the train's nose is within 1% of experiment. This difference may be explained by the choice of a RANS-based 'Realizable k-ε' CFD turbulence model. It averages the Reynolds stresses in the Navier-Stokes equations by replacing them with two-equation models which assume that Reynolds stresses are proportional to the mean strain rate of the flow. Because the results at low heights are typically dominated by helical vortices, this turbulence model may produce inaccurate results in this region due to poor predictions of the separation points of the flow around the train's tail, and of the main wake flow structures. Nevertheless it is encouraging to see that the essential features of the flow have been reproduced by the CFD simulation - the velocity gradient matches at all points, and inflections occur at similar values of x/Z.

Overall, it appears that the velocity results from this study at mid-height positions are accurate for the boundary layer and wake regions and in the upstream and nose region in certain cases. The level of accuracy is acceptable for the aim and Objectives 4 and 5 to be met (they focus on comparative rather than quantitative debate), as the flow physics captured in the experiments are likely to be correct.

5.1.2 Low-height positions

This section considers the results for the low-height position of z/Z=0.05 and 0.13. The CFD study in Gilbert and Straathof (2013) included velocity results for a low-height position. Figure 5.5 compares the resultant velocity at a low-height position.

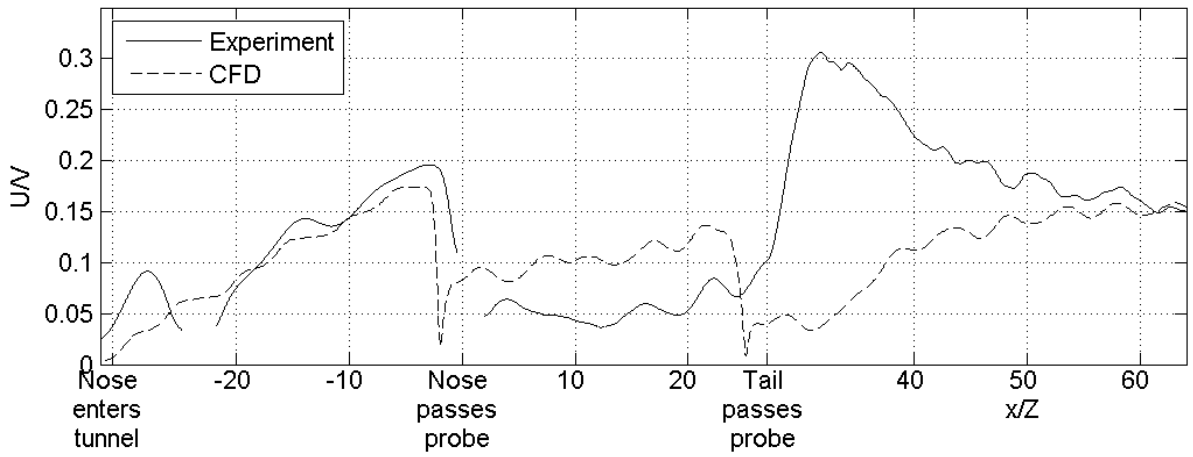

Figure 5.5: Comparison of CFD with experiment (Gilbert and Straathof, 2013) for the ensemble average resultant velocity, at position y/Z=0.77, z/Z=0.05. Tunnel T2 (L/Z=51, α=0%, β=0.23).

The results show that the agreement is close in the nose region, but the gust in the wake region does not occur. The gust has been observed in past experiments in tunnels (Schultz, 1990; Sakuma et al. 2010), so the disagreement is most likely due to the choice of CFD turbulence model (as has also been suggested in Section 5.1.1).

Temple and Dalley (2001) ('T&D') conducted open air moving-model and full-scale experiments measuring the slipstream of an ICE2. A common sensor position was shared

between these experiments. In the T&D moving-model experiment, a single-film hot-wire anemometer measured the resultant of the longitudinal and lateral air velocity components. The train model and facility were identical to those used in this study. The train speed varied from V=52 to 55m/s. The track and ground profiles matched those used in this study. In the full-scale experiment, a gust anemometer measured the air velocity around a 206m long eight-carriage ICE2 service train, travelling at speeds between 60 and 77.8m/s. The track bed featured a ballast shoulder. In both experiments, just N=7 repeats were undertaken, so the results are less reliable than those from this study for which N=46 repeats were undertaken. Figure 5.6(a) compares the ensemble average T&D results with those from this study.

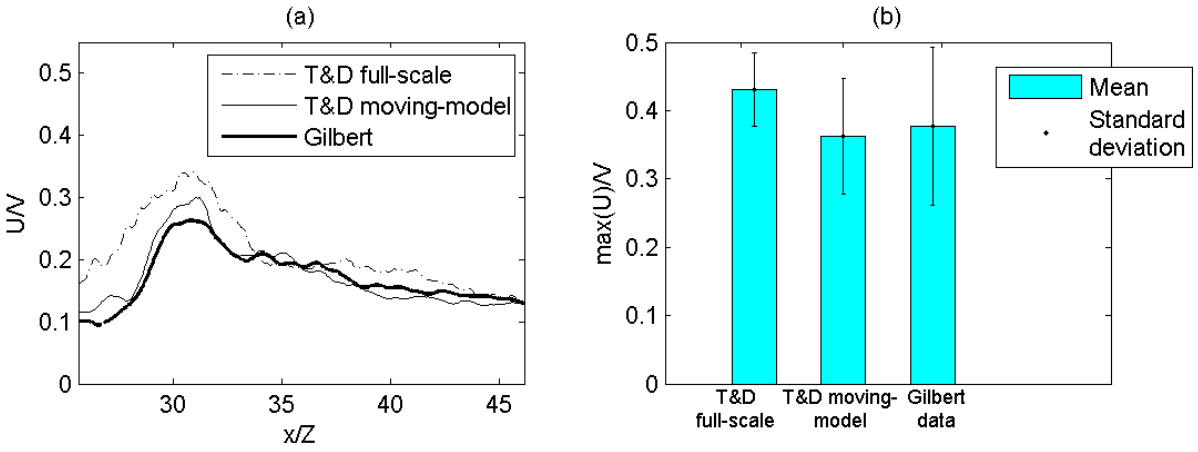

Figure 5.6: Comparison of experimental data with moving-model and full-scale resultant velocity data from Temple and Dalley (2001): (a) Ensemble average time histories; (b) Mean and standard deviation of peak gusts.

The results show that the peak velocity in the T&D full-scale data is higher. However, since ensemble averaging has the smoothing effect of a low-pass filter, the reduced peak attenuation caused by ensemble averaging just seven repeats rather than 46 may be responsible for this. If seven moving-model runs are chosen instead, there are many combinations which produce a higher mean than that observed. Figure 5.6(b) compares the peak gusts from individual runs. The mean velocity from this study is higher than the T&D moving-model results, but still less than the full-scale results. The standard deviation of the velocity from this study is much

higher than all of the T&D results. A two-sample t-test comparing the gust peaks from these experiments with the full-scale data reveals a *p*-value of 0.23. This means that the differences between the data are not statistically significant to the $p \leq 0.05$ level. This probability level is commonly used in codes of practice, e.g. TSI (2008) and BSI (2005), for assessing maximum aerodynamic loads.

The results in Figure 5.6(a) also suggest that the duration of the model-scale gust from these experiments is shorter than at full-scale. The durations of the gusts will be compared by calculating the integral breadth, which involves first integrating the velocity data over a fixed interval along the *x*-axis. The interval is centred on the peak and extends symmetrically either side of the peak. Secondly the integrated data is divided by the maximum velocity to obtain the integral breadth. The model-scale divided by the full-scale integral breadth is 2.05 on average, with a range of 0.5. This helps to explain the finding in Section 3.9.2 that a peak scaling factor of less than unity is necessary in order to account for scaling uncertainties. If the peak scaling factor was calculated based on the integral breadths, then its value would be between $g=0.49\pm0.05$.

Overall, it appears that the level of accuracy of the velocity results from this study at low-height positions is acceptable for the upstream and nose region and the boundary layer region, but inconclusive in the wake region. The level of accuracy is acceptable for the aim and Objectives 4 and 5 to be met (they focus on comparative rather than quantitative debate), as the flow physics captured in the experiments are likely to be correct.

5.2 Time history results

This section assesses the effect of changing geometric parameters on the general 'time history' patterns of slipstream velocity. Graphs showing all of the time history results are

included in Section 5.2.1. The following sub-sections investigate the flow in different regions separately. These regions are the same as was defined in Chapter 2: the upstream and nose region (Section 5.2.2); the boundary layer region (Section 5.2.3); and the wake region (Section 5.2.4). All of the data have been filtered to a cutoff frequency of f_c=100Hz (calculated from Equation 3.22). This is a full-scale-equivalent duration of t_{fs}=0.25 seconds.

5.2.1 Ensemble averages and standard deviations

This section presents the time histories of the resultant velocity (U/V) measurements for all test cases, including the ensemble averages ($\overline{U}/V$), and standard deviations (σ_U/V). Note that the standard deviation is aligned to the abscissa, and not added to or subtracted from the ensemble average. The standard deviation is an approximate measure of turbulence, representing the run-to-run variation of U. The results from three positions are included in five figures, each of which highlights the effects of changing particular geometric variables relative to the open air reference data:

- Figure 5.7: The effect of transitioning from the open air to symmetrical walls (W1D), and the effect of moving the wall on the right side closer to the train (W3D).
- Figure 5.8: The effect of transitioning from the open air to symmetrical walls close to the train (W2D).
- Figure 5.9: The effect of transitioning from the open air to tunnels, and the effect of changing the tunnel length (T2, T3 and T4).
- Figure 5.10: The effects of transitioning from the open air to tunnels of length L/Z=51 (T2), and the effects of increasing blockage ratio (β) (wake only) and opening ratio (α).

- Figure 5.11: The effects of transitioning from the open air to tunnels of length L/Z=13 (T3), and the effects of increasing blockage ratio (β) (wake only) and opening ratio (α).

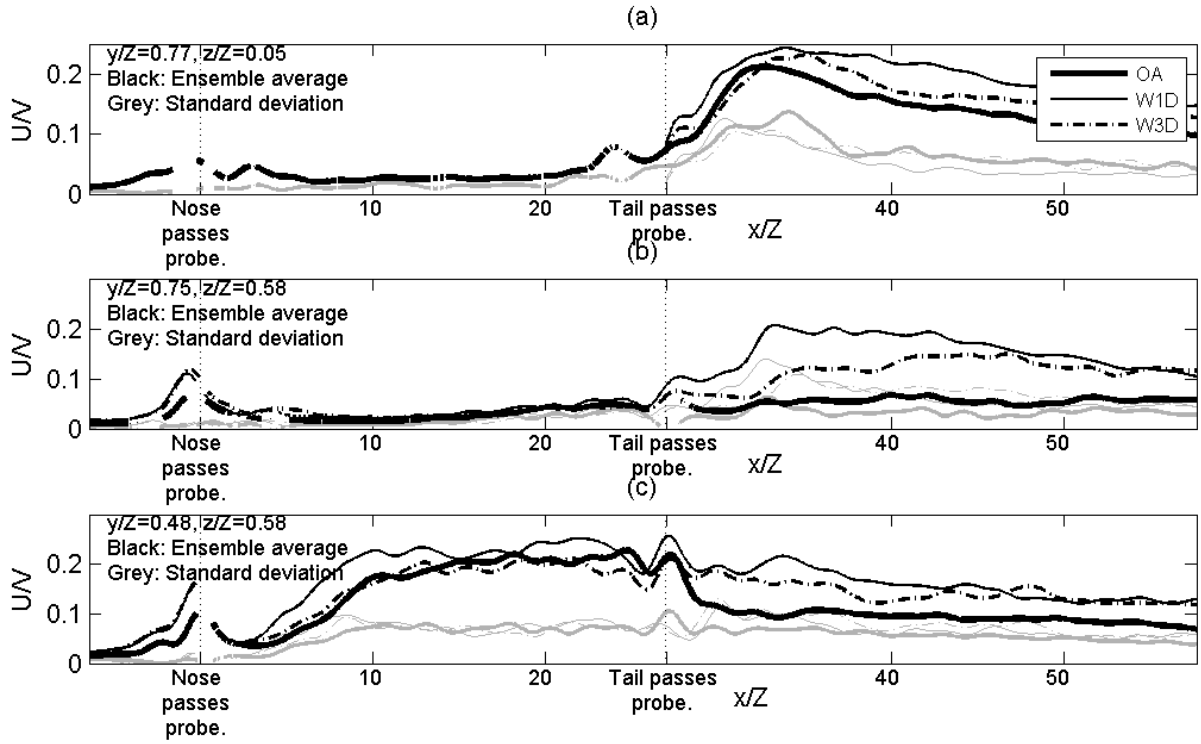

Figure 5.7: Ensemble average resultant velocity time histories at three positions for the open air (OA), and wall cases (W1D and W3D).

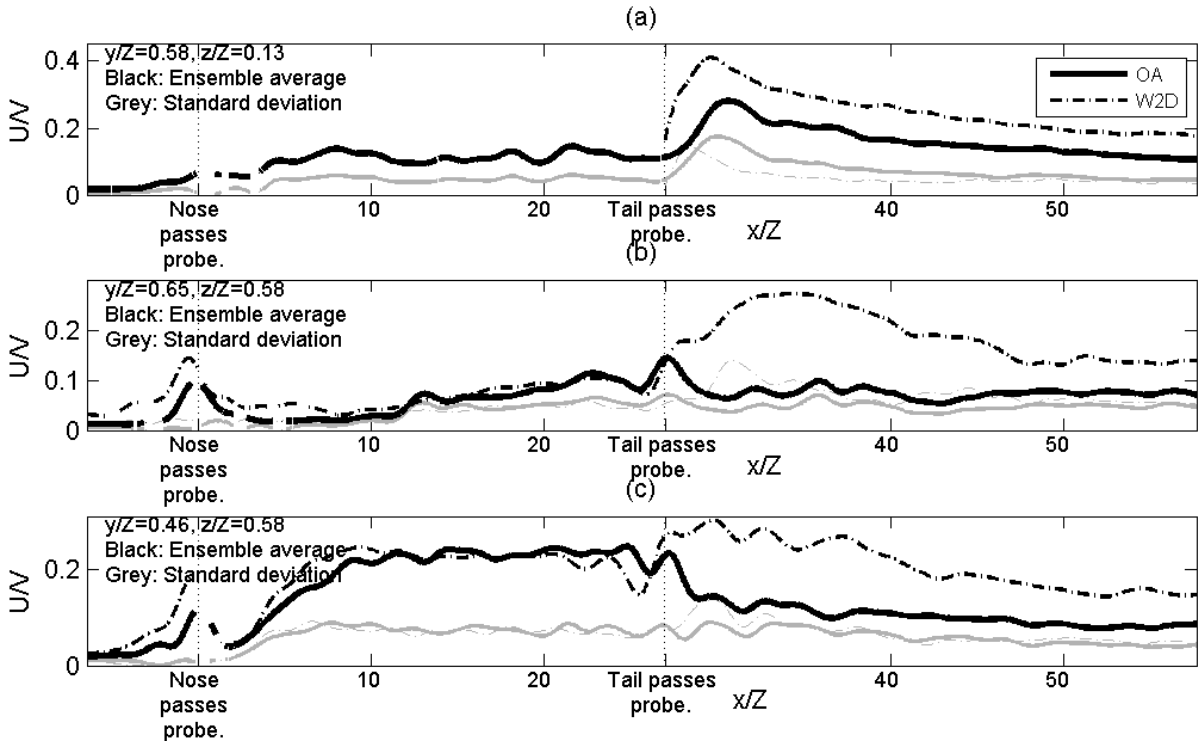

Figure 5.8: Ensemble average resultant velocity time histories at three positions for the open air (OA), and wall cases (W2D).

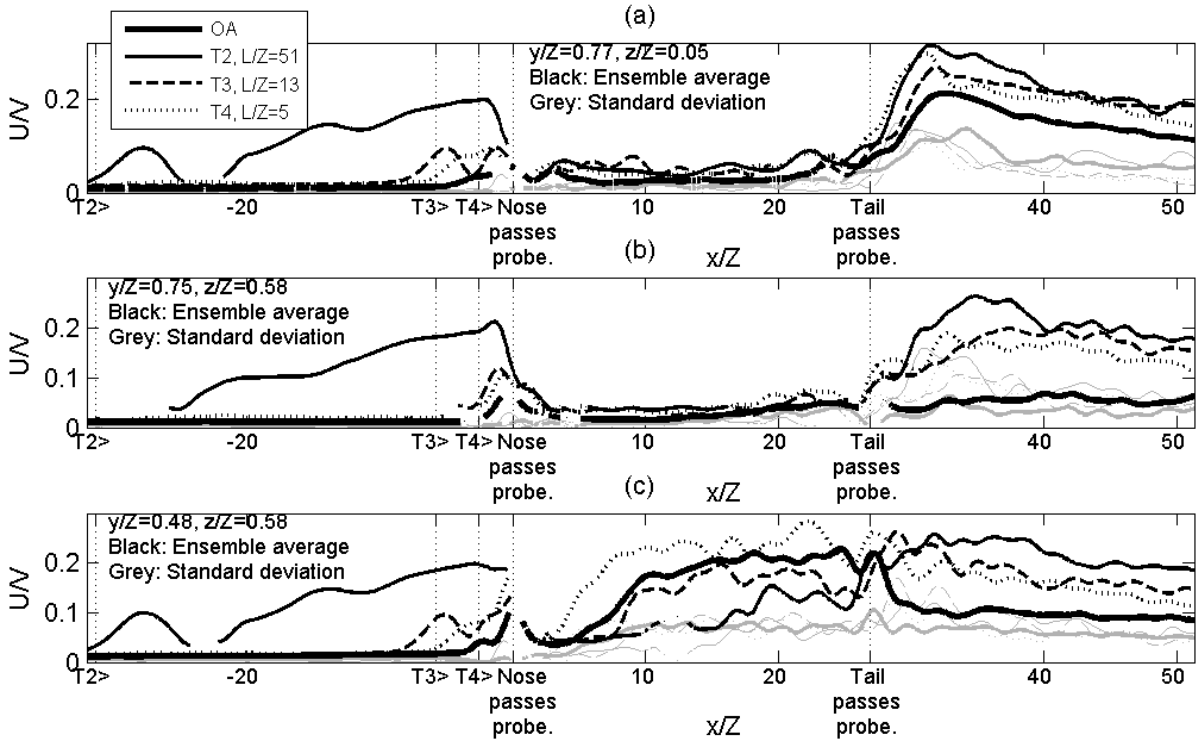

Figure 5.9: Ensemble average resultant velocity time histories at three positions for the open air (OA), and enclosed tunnels (α=0%, β=0.23) of three lengths: T2 (L/Z=51); T3 (L/Z=13); T4 (L/Z=5).

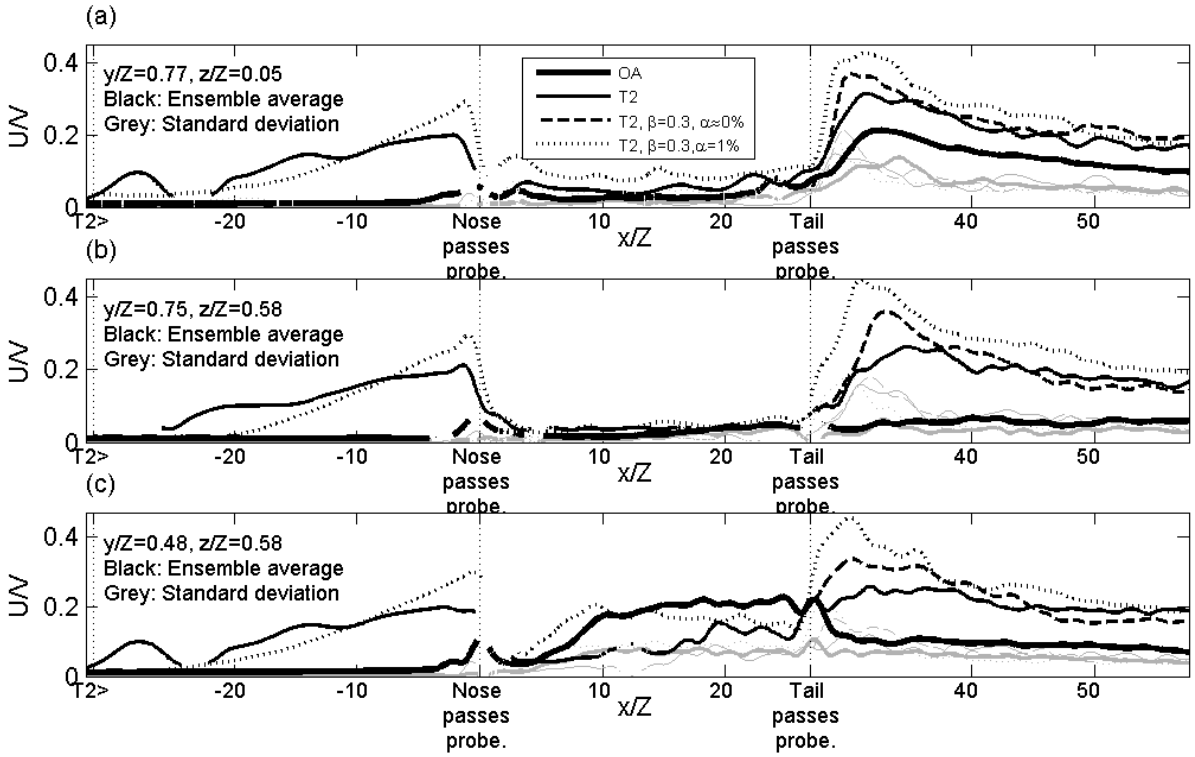

Figure 5.10: Ensemble average resultant velocity time histories at three positions for the open air (OA), and tunnels of length L/Z=51 (T2) with different values of opening ratio (α) and blockage ratio (β).

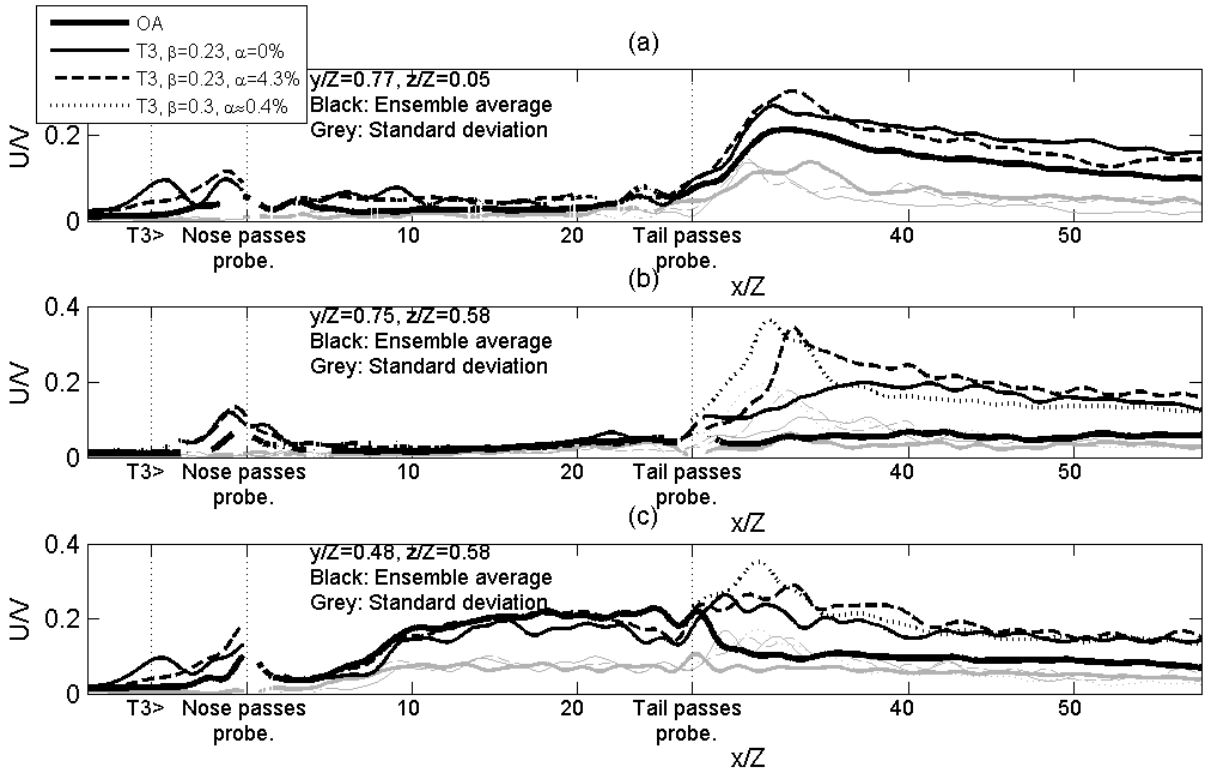

Figure 5.11: Ensemble average resultant velocity time histories at three positions for the open air (OA), and tunnels of length L/Z=13 (T3) with different values of opening ratio (α) and blockage ratio (β).

5.2.2 Upstream and nose region

In this section, the velocity in the upstream and nose region is analysed. Disclaimer - a reliability study reported in Appendix A4.2 has shown that the resultant air velocity measured by the Cobra probes in this region was unreliable when the open air experiments were repeated. Moreover, a comparison of the results with existing data in Section 5.1 revealed that the results around the train's nose differ from the existing datasets. Conclusions relating to this section cannot be guaranteed to be accurate.

The ensemble average velocities have been plotted in Figure 5.12 in a way which makes comparison between test cases and positions easier.

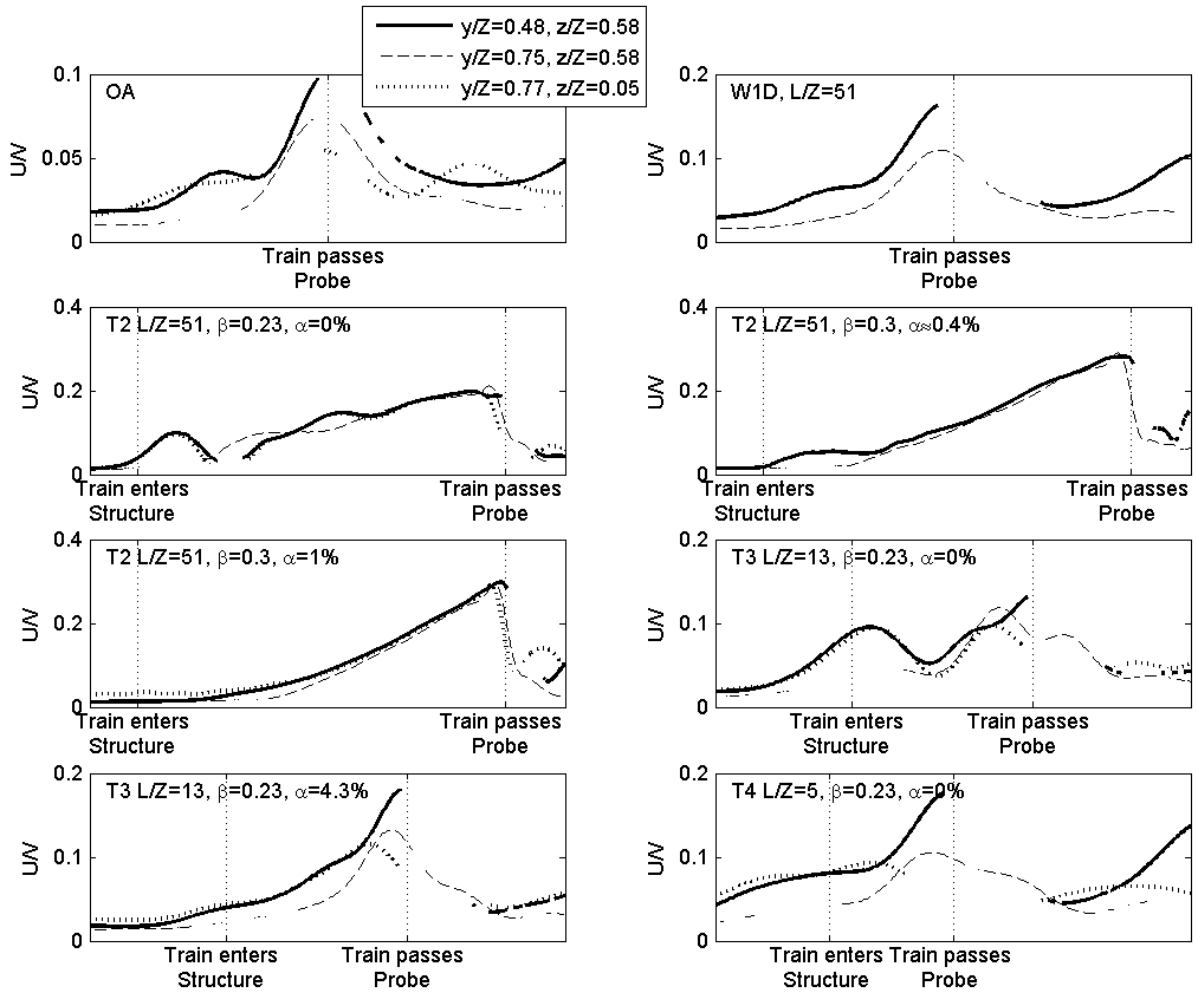

Figure 5.12: Ensemble average resultant velocity in the upstream and nose region. Each graph features data from one test case and three positions.

The results show that in all confined cases, the velocity begins to increase further upstream of the train's nose than in the open air case. The velocity in the tunnels and partially-enclosed tunnels increases between the points where the train's nose enters the tunnel and where it passes the sensor, due to the pressure-driven piston effect.

From the analysis in Chapter 4, the dominant pressure phenomenon in the upstream and nose region in the open air and wall cases is a positive peak followed by a suction peak around the train's nose. In tunnel and partially-enclosed tunnel cases, the positive and suction peaks are affected by nose-entry compression wave, and possibly the tail-entry expansion wave and nose-exit expansion wave. The peaks are also affected by pressure waves which superimpose

onto the underlying data. The difference in the pressure transient in tunnels may be generally attributed to the piston effect. A wind is induced by the piston effect, which is connected to the geometric parameters that affect pressure transients, such as: blockage ratio; opening ratio; tunnel length; and longitudinal sensor placement (Sections 4.2.3.1 and 4.2.4.1). The maximum velocities may be affected to some extent by the pressure results, via the wind induced by the piston effect ahead of the train's nose, and the peak-to-peak pressure fluctuation in the nose region. The relationships between maximum velocities and various measures of pressure changes are examined in Section 5.3.1.

In a paper which synthesised the findings from multiple studies, Baker (2010) remarked that the flow generally remains laminar up to the passage of the train's nose past the sensor. The standard deviation results in Section 5.2.1 show that σ_U/V is very low in the upstream region, which suggests that the flow is laminar.

In the open air, the results vary considerably between the three positions. This would be expected because Section 4.2.2 shows that the variation of the peak-to-peak pressure around the train's nose with y is also highest in the open air. In the wall case W1D, the variation between positions is similarly large despite the confining effect of the walls. The same occurs for the other double wall configurations. The confinement was expected to reduce the rate of decay and lead to more homogeneous results, because Section 4.2.2 also shows that the variation of the peak-to-peak pressure with y reduces in wall cases compared to the open air.

Moving on to the tunnels, the same maximum velocity is reached at all three Cobra probe positions in the tunnels of length L/Z=51, which shows a greater level of homogeneity. However, the ensemble average velocities initially differ between positions, only converging with each other just before reaching a maximum. For shorter tunnels (L/Z=13) the variation between positions is greater. This may be due to the shorter 'fetch' (x_P) which means that the

flow has not transitioned fully from the open air (i.e. highly three-dimensional) to that which would be expected in a tunnel with infinite fetch (i.e. near-one-dimensional). The static pressure for T2 and T3 in the nose region varies very little between positions.

In the partially-enclosed tunnel cases, the buildup of velocity ahead of the nose in T2 (L/Z=51, β=0.3, α=1%) shows the characteristics predicted by the analytical formula of Iida et al. (2005) illustrated in Figure 2.2(a): a smooth buildup of velocity following an exponential increase, followed by a sharp drop. By comparing the maximum velocity with that for α≈0.4%, it appears that the opening ratio has little effect on the maximum velocity around the train's nose. There is some evidence of pressure wave fluctuations at the lower opening ratio although they are highly damped.

The velocity directly around the train's nose is analysed. Figure 5.13 shows three components of the ensemble average velocity around the train's nose, at position (y/Z=0.75, z/Z=0.58), for three test cases. Note that some gaps (dropouts) in the data have been interpolated to improve readability.

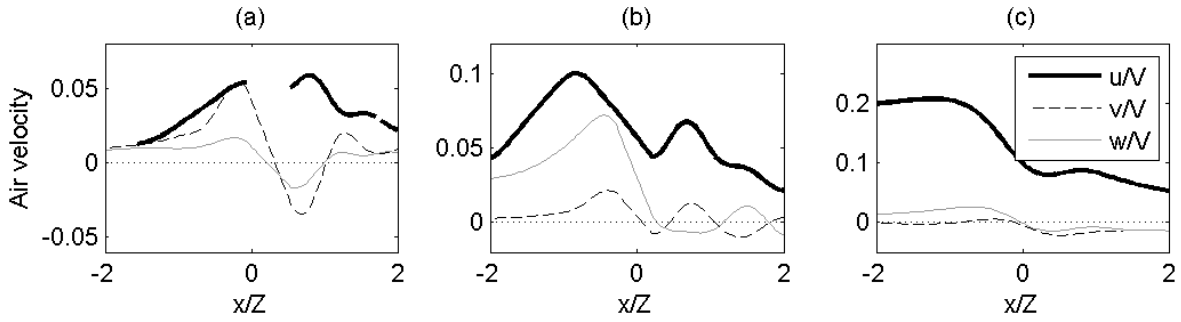

Figure 5.13: Ensemble averages of three velocity components in the nose region at position (y/Z=0.75, z/Z=0.58), for test cases: (a) OA; (b) W1D; (c) T2 (L/Z=51, β=0.23, α=0%).

The results show that confinement causes two significant and repeatable changes in this region relative to the open air. Firstly, the maximum lateral velocity is lower at the near-wall position, which is obviously due to the wall's blockage of wall-normal flow. The second and

most significant change occurs to the longitudinal velocity. The longitudinal velocity comprises a positive peak only, whilst the lateral velocity transitions from a positive to a negative peak. This was also found in a previous moving-model study focusing on the ICE2 in which Cobra probes were used (Del Valle, 2012). The shapes of the velocity fluctuations are consistent with the potential flow theory prediction of the transient longitudinal and lateral velocities caused by a passing Rankine half-body.

5.2.3 Boundary layer region

A boundary layer grows along the train's length. Therefore the velocity would be expected to be higher close to the train side than far from the train side. This is the case in the time history results (Section 5.2.1). At the far positions, the presence of a nearby wall decreases the velocity relative to the open air. This is probably due to the change of the velocity profile into a Couette-shape (Equation 2.28). Even at the near-train position, the velocity is lower than the open air in the longest enclosed and partially-enclosed tunnels (T2, L/Z=51). This is also probably due to the change in velocity profile. The velocity profiles are plotted in Section 5.2.3.2. Experiments reported in Sakuma et al. (2010) suggest that the boundary layer in a tunnel is thinner than in the open air.

The length of the tunnel and the distance of the sensors from the tunnel entrance appear to act as key variables determining the relative velocity magnitudes in the boundary layer region compared to the open air. When the opening ratio is increased, the boundary layer tends towards that in the open air and wall cases.

Four sub-sections will examine the structure of the boundary layer. The integral parameters (Section 5.2.3.1), velocity profile (Section 5.2.3.2), and turbulence level (Section 5.2.3.3) have been calculated and compared between test cases. The analysis of maximum velocities

in Section 5.3.2 will discuss the maximum velocities of individual runs occurring in the boundary layer region.

5.2.3.1 Integral parameters

Some boundary layer integral parameters have been calculated for the results at *z*/*Z*=0.58. The integral parameters defined in Section 2.3 have been normalised and modified to represent a trackside frame of reference:

$$\frac{\delta^*}{Y} = \frac{1}{VY}\int U\, dy \tag{5.1}$$

$$\frac{\theta}{Y} = \frac{1}{VY}\int U(1-U)\, dy \tag{5.2}$$

$$H = \frac{\delta^*}{\theta} \tag{5.3}$$

Figure 5.14 shows the boundary layer integral parameters, for five test cases in which a rake of at least three Cobra probes were positioned along the *y*-axis at *z*/*Z*=0.58. Unfortunately none of these test cases include fully-enclosed tunnels. The gradient of the static pressure, measured at position (*y*/*Z*=0.75, *z*/*Z*=0.58), is also shown.

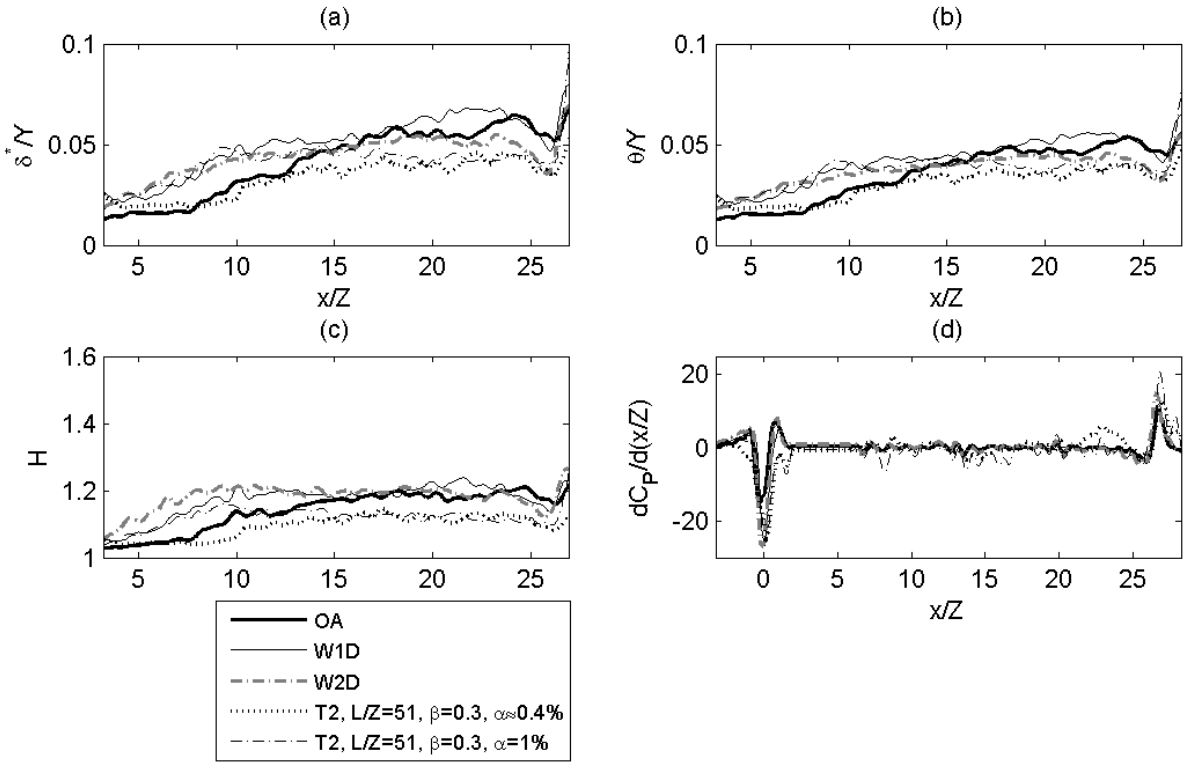

Figure 5.14: Normalised boundary layer integral parameters at height z/Z=0.58, including: (a) Displacement thickness; (b) Momentum thickness; (c) Shape factor; (d) Pressure gradient.

In the open air, the boundary layer appears to reach equilibrium by the start of the tail carriage. In Case W1D the boundary layer grows more rapidly than the open air due to the addition of walls, although the results converge with those from the open air close to the train's tail. Moreover, the boundary layer continues to grow along the train's length, and does not reach a constant thickness. The walls are therefore not sufficiently close to significantly alter boundary layer growth. When the walls are brought closer (case W2D), the boundary layer appears to reach a constant thickness along the tail carriage, implying that the closer walls constrain boundary layer growth.

In the partially-enclosed tunnels, the boundary layer reaches equilibrium beyond the second carriage, and remains thinner by the tail carriage than in the open air and wall cases. This is presumably also the case in enclosed tunnels. This may impact considerably on the flow

structures in the wake region. The relationships between boundary layer parameters and periodic flow structures in the wake region are examined in Section 5.2.4.2.

The pressure field around the train is very different from that in the wall cases, so analysing the pressure results may help to explain the observations. The nature of the pressure field can be assessed by examining the shape factor (*H*), and the pressure gradients in Figure 5.14(d). The shape factor provides an indication of the presence of pressure gradients in two-dimensional boundary layers. It has been used previously in Baker et al. (2001). A shape factor of H=1.3 is typical of a turbulent boundary layer along a flat plate with no pressure gradients. Lower values indicate boundary layers in adverse pressure gradients. The results show that H is around 1.2 in the open air and wall cases, which is close to that observed experimentally in Baker et al. (2001). In the partially-enclosed tunnels, H stabilises from the second carriage to the tail, reaching H=1.1. This is lower than the calculation for the open air and wall cases. The decrease indicates a boundary layer typical of a less favourable or adverse pressure gradient. This is contradicted by the results in Figure 5.14(d), which shows that the pressure gradients in the partially-enclosed tunnels are more favourable than in the open air and wall cases - an observation backed up by other studies such as Diedrichs et al. (2004). The shape factor may not even be valid due to the three-dimensionality of the flow, the lack of data, and the constraining effects of the walls on the boundary layer.

5.2.3.2 Velocity profile and skin friction coefficient

In this section, the nature of the velocity profile in the boundary layer is established. Many theoretical formulations have produced based on power law profiles (Section 2.3). A past study of the boundary layer of the ICE2 in the open air has revealed that a log-law velocity profile is obeyed (Baker et al., 2001).

For this study, power and log-law relationships were fitted to the mean ensemble average velocity profile along the third carriage of the train, using a least-squares fitting algorithm. The norm of the residuals was used to determine the best type of relationship to fit the data. The test cases included the open air, three wall cases, and a tunnel case. In all cases, a log-law relationship was found to fit the data slightly better than a power law. Figure 5.15 shows *y/Z* on a logarithmic axis plotted against 1-*U/V* (train reference frame), for six test cases in which data from at least three positions are available.

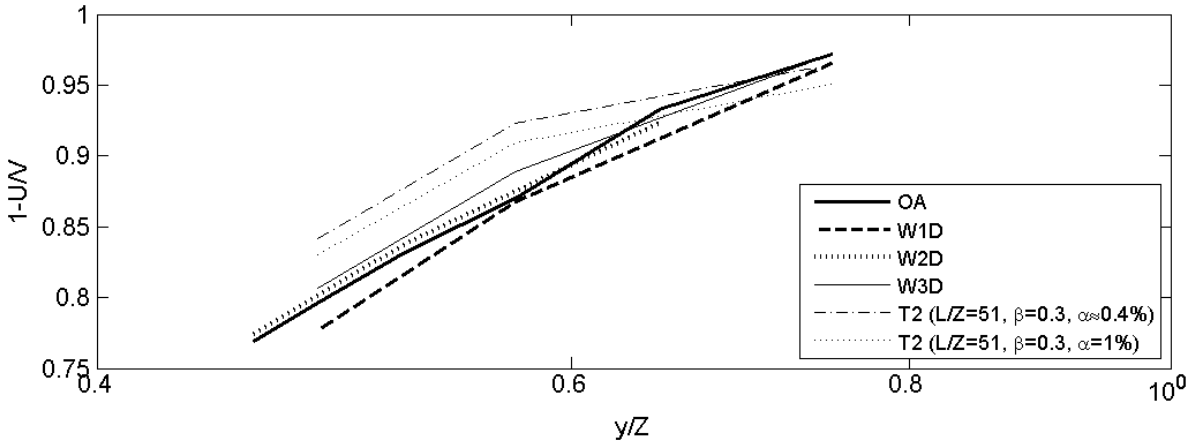

Figure 5.15: Logarithmic velocity profiles along the third carriage of the train, for six different test cases.

The results show that the velocity profiles in the three wall cases are similar to each other and the open air. The velocity profiles in the two tunnel cases are similar to each other, and the boundary layer is thinner than in the open air and wall cases. Experiments reported in Sakuma et al. (2010) also suggest that the boundary layer in a tunnel is thinner than in the open air.

The skin friction coefficient has been estimated from these results, in order to conduct a crude investigation into the effects of confinement on the boundary layer. There are too few measuring points to resolve the Couette-type velocity profile (defined in Section 2.3) which is expected in confined cases. Therefore rather than attempting to use the profile matching algorithm for the boundary layer flow in tunnels, presented in Barrow and Pope (1987) (and

discussed in Section 2.3), a log-law profile has been fitted to the data in order to estimate the skin friction coefficient. The log-law profile is as follows:

$$U = \frac{1}{\kappa}\sqrt{\frac{\tau_w}{\rho}}\ln\left(\frac{\sqrt{\frac{\tau_w}{\rho}}y}{\nu}\right) \quad 5.4$$

from which the skin friction coefficient C_f may be estimated:

$$C_f = \frac{\tau_w}{\frac{1}{2}\rho V^2} \quad 5.5$$

κ is the von-Kármán constant (κ=0.41), τ_w is the wall shear stress, and y is the distance from the side of the train (y=Y/2). A least-squares based fitting algorithm was used to fit Equation 5.4 to the data and calculate the skin friction coefficient. The results show that C_f=0.0042 in the open air, which is higher than the previous estimation of C_f=0.0029 made in Baker et al. (2001) from moving-model test results for the same train model. In the three wall cases, C_f=0.0042±0.0001, which represents no change. In the tunnel cases, C_f increases to 0.0044. This results from the steeper gradients of the velocity profiles which corresponds to higher wall shear stresses.

5.2.3.3 Turbulence level

The standard deviation (σ_U/V) is an approximate measure of turbulence, representing the run-to-run variation of the velocity. The time histories in Section 5.2.1 show that the standard deviation consistently increases along the train's length. In most cases the results are not much different from the open air. However, the initial rate of growth along the first carriages varies between test cases. At the mid-height position closest to the train side (y/Z=0.48, z/Z=0.58), the rate of growth is higher in W1D and W2D than the open air, whilst the rate of growth in W3D is not much different from the open air. The same trend occurs at y/Z=0.75.

The rate of growth is lower in T2 and T3 than the open air (both β=0.23, α≈0%). In T4, the rate of growth is similar to that seen in the wall test cases. Therefore, the length of a tunnel may be related to the rate of growth of σ, which decreases as the length of the tunnel increases. An increase of the blockage ratio from β=0.23 to 0.3 in tunnel T2 causes the rate of growth of the standard deviation to increase, showing that the tunnel blockage ratio may be related to the growth of the standard deviation. An increase in the opening ratio in tunnel T3 from α=0% to 4.3% causes the rate of growth of turbulence to increase, matching that found in the open air. An increase in the opening ratio from α≈0.4% to 1% in Case T2 has the same effect. Therefore, the growth rate of the standard deviation is increased by raising the opening ratio, for the positions closer to the train (y/Z=0.48). The opposite occurs for the positions which are further from the train and therefore closer to the wall (y/Z=0.75).

The analysis of maximum velocities from individual runs in Section 5.3.2 will show that in the open air and wall cases, a large proportion of the maximum velocities occur in the boundary layer region at the position close to the train's side (y/Z=0.48, z/Z=0.58). This is due to the higher turbulence level. However, in the tunnel and partially-enclosed tunnel cases, the peaks will predominantly occur in the wake region at all positions.

5.2.4 Wake region

The results in Section 5.2.1 have shown that the velocity in the wake region responds dramatically to the parametric changes studied. From the analysis in Chapter 4, the dominant pressure phenomenon in the wake region in the open air and wall cases is a suction peak followed by a positive peak around the train's tail. In tunnel and partially-enclosed tunnel cases, the suction and positive peaks are affected by tail-entry expansion wave, and possibly the tail-exit compression wave and nose-exit expansion wave. The peaks are also affected by pressure waves which superimpose onto the underlying data. The difference in the pressure

transient in tunnels may be generally attributed to the piston effect. A wind is induced by the piston effect, which is connected to the geometric parameters that affect pressure transients, such as: blockage ratio; opening ratio; tunnel length; and longitudinal sensor placement (Sections 4.2.3.1 and 4.2.4.1). The maximum wake velocities may be affected to some extent by the pressure results, via the wind induced by the piston effect behind the train's tail, and the peak-to-peak pressure fluctuation in the tail region. The relationships between maximum velocities and various measures of pressure changes are examined in Section 5.3.1.

In the open air, the ensemble average (U/V) and standard deviation (σ_U/V) at the low-height positions begin low, and then reach maximum values in the wake at around three train heights behind the tail. The velocity following the peak gradually decays. At the mid-height positions (z/Z=0.58), the maximum velocity occurs directly around the train's tail. The magnitude of the gust varies with the lateral separation of the position - the peak at the furthest mid-height position (y/Z=0.65-0.77) from the train is roughly half the magnitude of that at the closest position (y/Z=0.46-0.48) to the train. At the closest position, the velocity rapidly decays to $U/V \leq 0.1$ following the peak gust, after which it decays slowly. At the furthest position, the velocity remains constant and slightly higher than the ambient velocity a long distance into the wake.

The flow patterns change significantly when symmetrical walls are added (W1D, W2D). No other test case causes such an extensive change to all of the results. The ensemble averages in Figure 5.7 and Figure 5.8 show that at the low-height positions, the ensemble average peak magnitude increases by 15-60% relative to the open air due to the addition of symmetrical walls, whilst small to moderate increases in the peak of σ_U/V are observed at the same positions as the ensemble average peaks. The velocity remains high over a longer duration, leading to a gust duration approximately ten train-heights longer than in the open air. The rate

of decay appears to remain the same as in the open air. At the mid-height positions (z/Z=0.58), the time histories in the symmetrical wall cases appear very similar to each other at the near-train and near-wall positions. The addition of walls causes a 12-25% increase in resultant velocity on the open air for the near-train position, and 200-270% for the near-wall position. The peak magnitude and rate of decay are similar to those at low-height positions. Therefore, it is suspected that a near-one-dimensional flow structure is responsible for these observations, causing similar ensemble averages to occur at all positions. Analysis of the velocity components is carried out in Sections 5.2.4.1, and relationships are sought between pressure changes and maximum velocities in Section 5.3.1. From these sections, an understanding of the one-dimensionality of this flow structure will be gained.

When the wall opposite the Cobra probes was moved towards the train's side to form asymmetrical wall case W3D, the peak velocity magnitudes were expected to increase, as the paths of the wake vortices were expected to deflect towards the less constrained side (the side in which the wall was further from the train, where the Cobra probes were installed). However, the results in Figure 5.7 show that the peak ensemble average magnitude decreases at all three positions. A possible cause is identified in Section 5.2.4.2, related to periodic flow structures.

Fully enclosed tunnels (β=0.23), shown in Figure 5.9, cause the peak ensemble average velocity to increase beyond that measured in the wall cases. There are fewer differences between the results at the three positions in T2 than in W1D. At the low-height position, the peak ensemble average resultant velocity increases by 10-29% in T2 relative to W1D. At the mid-height positions, the increases are -9-27% for the position furthest from the train's side, and 0-10% for the closest position. Whilst this could be caused by a flow phenomenon specific to tunnels, conclusions cannot be drawn from ensemble averages alone - Gilbert and

Straathof (2013) discovered that a change in the spatial distribution of gust peaks may cause an apparent increase in the peak magnitude of an ensemble average. Section 5.3.2 accounts for the spatial distributions of gusts.

Figure 5.10 and Figure 5.11 show the effect of changing the opening ratio and blockage ratio on the results, for a constant tunnel length. When the blockage ratio of T2 (L/Z=51, α=0%) is increased from β=0.23 to 0.3, the peak ensemble average velocity at the three positions increases by between 18% and 36% to values which are nearly identical at all three positions. The results suggest that the flow is near-one-dimensional. The results for T3 (L/Z=13, α=0.4%) suggest the same. The opening ratio was increased to α=1% in Case T2 (L/Z=51, β=0.3), and to α=4.3% in Case T3 (L/Z=13, β=0.23). In the former case, the maximum velocity increases by 15-35%, whilst in the latter case, it increases by 10-73%. These increases are unexpected - the air leakage due to the opening was expected to reduce the maximum velocity by reducing the pressure gradients inside the tunnels. The increases occur consistently so this may be the result of flow structures specific to partially-enclosed tunnels which highly influence the peak ensemble average velocity, or it may be the result of an apparent increase in the ensemble average only caused by a tighter spatial distribution of gust peaks, such as that described above.

The analysis so far has focused on ensemble average results. The differences in the maximum velocity and rate of decay between the different test cases are of particular interest. In sub-section 5.2.4.1, the levels of contribution of the longitudinal, lateral and vertical velocities to the resultant peaks are examined. In sub-section 5.2.4.2, periodic effects are examined, as well as the relationship between the boundary layer properties and the maximum wake velocity. In sub-section 5.2.4.3, the flow in the far-wake region is examined. In Section 5.3, the maximum velocities of individual runs are examined further.

5.2.4.1 Flow components

This section explores the contribution of each velocity component to the resultant velocity peaks, by deconstructing the ensemble average velocity data presented in 5.2.1 into the longitudinal, lateral and vertical components. Figure 5.16 shows the ensemble average near-wake velocity measured at four positions at constant height *z/Z*=0.58, for the open air and close wall case W2D. The longitudinal, lateral and vertical velocity components are plotted separately.

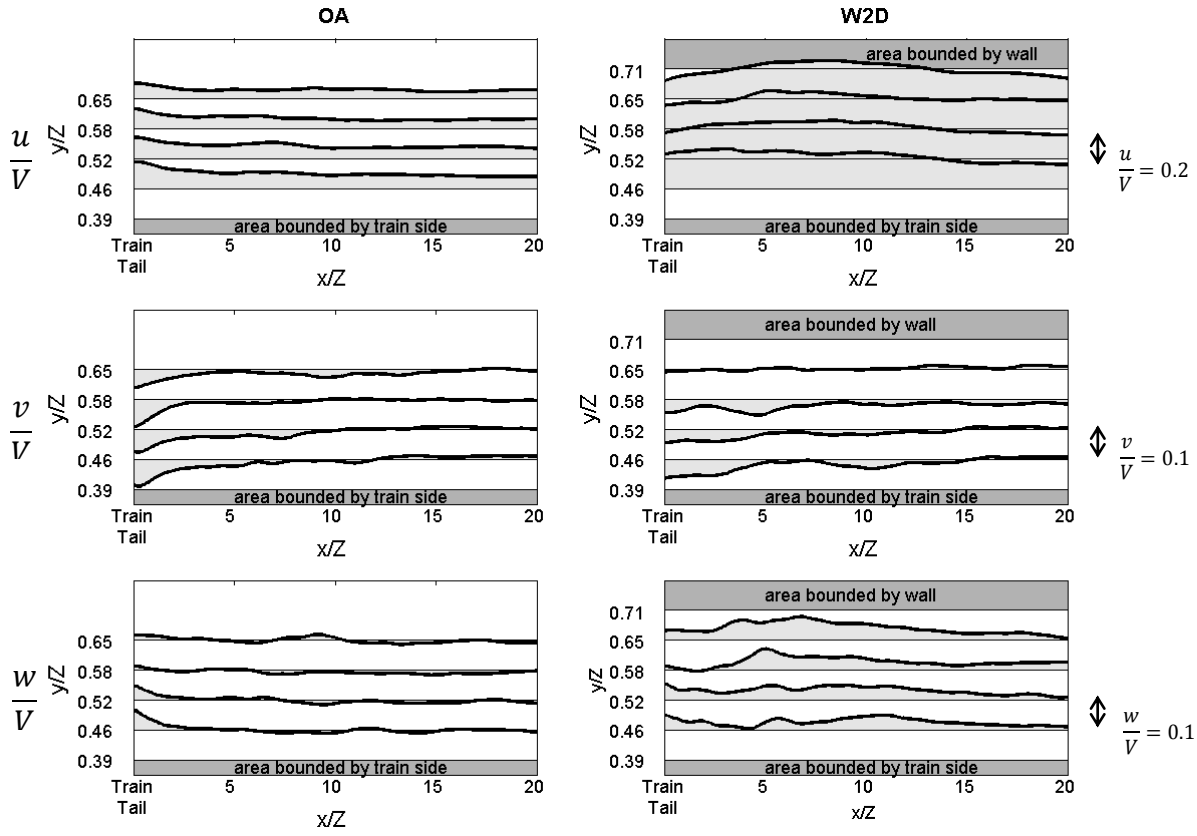

Figure 5.16: x-y plane views of the time histories of three ensemble average velocity components in the wake, for open air (OA) and wall (W2D) cases. Four lateral (*y*-axis) positions at height *z/Z*=0.58 are shown. Each *y/Z* interval corresponds to a fixed interval of velocity (specified on diagram), and the velocity abscissae are highlighted by shading the areas under the curves.

All of the results show that a fluctuation occurs directly around the train's tail. In the open air, a converging lateral flow occurs behind the tail, which is expected due to the wake pressure deficit. The results also show a vertical peak, which is presumed to be caused by the train's

tail geometry. The tail is reminiscent of an automotive ‘fastback’ shape with corner radii on the c-pillars (discussion relating research in the automotive sector to high-speed trains is included in Baker, 2001). A peak longitudinal velocity occurs around the train’s tail. The fluctuations are followed by rapid decay for all velocity components.

With the addition of walls, the converging lateral flow is constrained by the walls, so it is only detected close to the train’s side. The vertical peak directly around the tail is the same as that detected in the open air, but the decay is more gradual, and secondary peaks occur, some of which are higher than the initial peaks. Some aspects of the wake flow structures appear to have changed. The results for the lateral and vertical velocities suggest that rotational flow structures are detected at the mid-height positions. Regarding the wake structure in the open air, Baker (2010) states: ‘an unsteady helical vortex motion is more important close to the ground and other types of unsteadiness higher up the vehicle’. It seems that the helical vortex structure has been stretched vertically and squashed laterally by the walls, which leads to its detection at mid-height positions where its effects would not otherwise have been measured. Further analysis reveals that the same flow patterns occur in other confined cases. The next section (5.2.4.2) will show that the period of this vortex structure is related to the momentum thickness around the train’s tail carriage (which was shown in Section 5.2.3.1 to vary between test cases).

The results also show that the longitudinal velocity increases dramatically in the wake compared to the open air. It increases to a very similar magnitude at all positions, whereas the velocity measured in the open air at the furthest lateral position from the train’s side is significantly lower than that measured at the closest position. The changes to the longitudinal velocity seem to account for most of the overall increase in the resultant velocity (Figure 5.7).

Section 5.3.1 will show that the changes to the longitudinal velocity are linked to the pressure signature around the train's tail.

The effect of different types of test cases on the results will now be considered. Figure 5.17 shows the longitudinal, lateral and vertical velocity components measured at three positions, for test cases including tunnels and partially-enclosed tunnels. The effect of changing the tunnel length, opening ratio, and blockage ratio can be seen in the results.

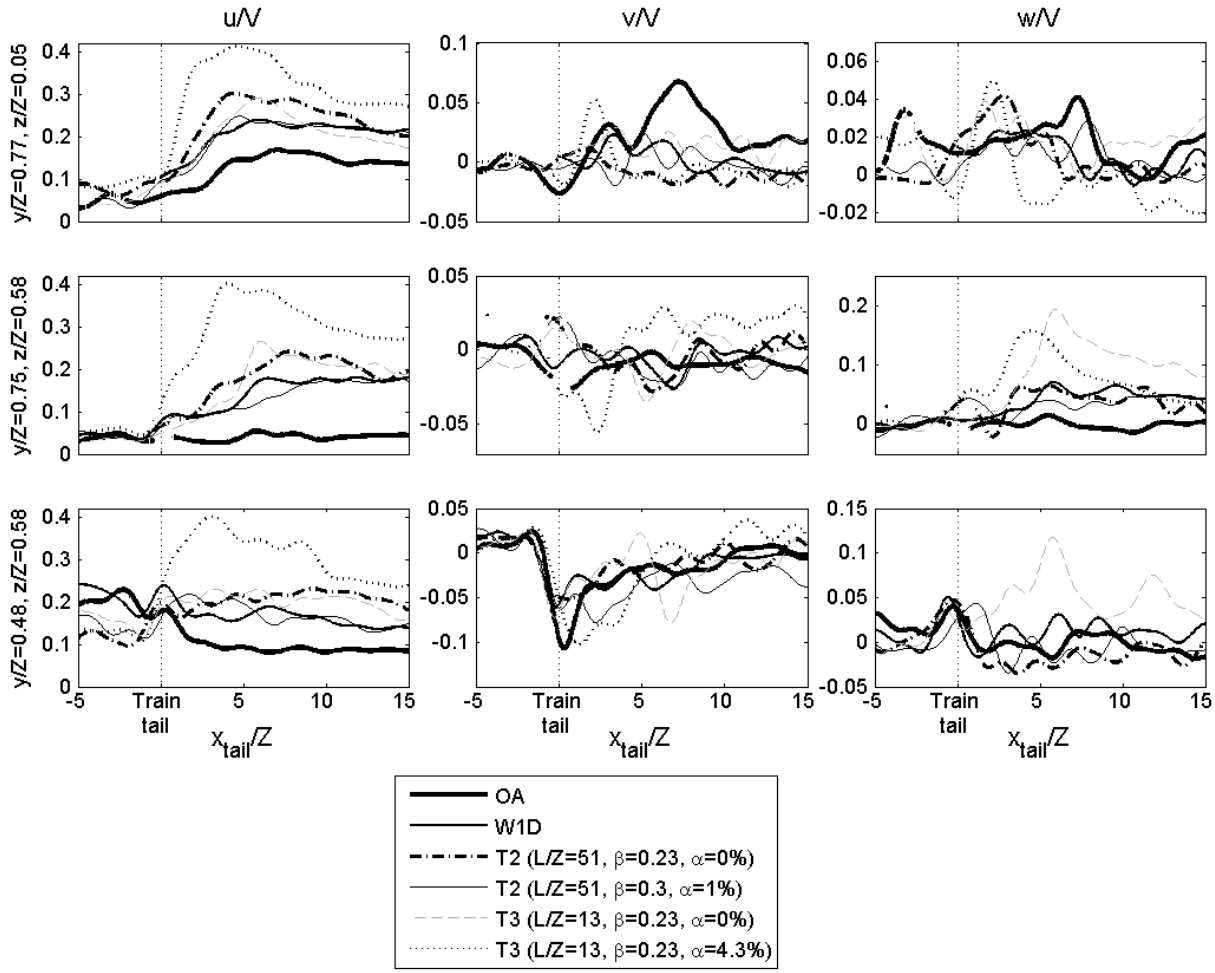

Figure 5.17: Time histories of three components of the ensemble average velocity in the near-wake region, for open air and tunnel cases, at three positions.

The results show that the longitudinal velocity in all of the confined cases is significantly higher than the open air. These results also show that the peak longitudinal velocity decreases and decays faster with reducing tunnel length. Section 5.3.1 will show that significant

correlations occur between the magnitudes and gradients of pressure changes and peak longitudinal velocities. A relationship between compressible effects such as pressure waves and the maximum longitudinal velocity is expected to relate to the finding for tunnels. Section 5.2.5 will explore whether pressure waves affect the maximum velocity.

If the opening ratio is increased, the maximum ensemble average longitudinal velocity increases relative to the enclosed tunnels. This is caused by a reduced spatial variation in the locations of the maximum velocities, perhaps due to a near-one-dimensional flow structure. The analytical method from Iida et al. (2005) presented in Sections 2.2 and 2.4 predicts that the pressure fluctuation around the train's tail tends towards an impulse as the opening ratio increases (Figure 2.2(a)), because the point at which the suction pressure region begins to grow (L-Δx_t) is inversely proportional to α (Equation 2.16). This increases the localised pressure gradients around the train's tail, which may relate to the increased peak longitudinal velocity. Section 5.3.1 seeks to identify relationships between pressure changes and peak longitudinal velocities.

When the opening ratio is increased, a large peak in the ensemble average vertical velocity occurs at the two mid-height positions shown in Figure 5.17. Both T2 and T3 show this behaviour, and it appears that this flow occurs for an opening ratio as low as α=1%. The flow peak is highest at positions close to the wall. This vertical flow appears to be a dominant factor in the very high resultant velocity peaks observed in Figure 5.10 and Figure 5.11, because the maximum vertical flow occurs at the same moment as peaks of longitudinal and lateral velocity components. There may be a relationship between the pressure loading pattern around the tail (Figure 4.5) and the higher maximum velocity in these structures. In Section 4.2.4.2 it was shown that the opening damps pressure discontinuities. A measurable flow should occur towards or away from the opening depending on the direction of the pressure

gradient. It is presumed that the peak vertical velocity (which affects the maximum resultant velocity magnitude) is further evidence of a flow travelling towards (and out of) the roof openings to dissipate differential pressures.

Further analysis shows that if the blockage ratio is increased by 30% to β=0.3, the peak longitudinal ensemble average velocity is approximately 30% higher for T2 (L/Z=51), and 50% higher for T3 (L/Z=13). The strength of the longitudinal flow in the tunnel is controlled by the piston effect which is highly dependent on the blockage ratio.

5.2.4.2 Periodic effects

Information about the gust peaks can be used to estimate the Strouhal number (*St*). In this section, a method from Sterling et al. (2008) has been used to estimate *St*. In this method, the frequency (f) corresponds to the train speed divided by the mean absolute deviation of the distances between gust peaks. The gust peaks have been calculated for both longitudinal and lateral velocity components. Figure 5.18 shows the estimated values of *St* for different test cases and positions.

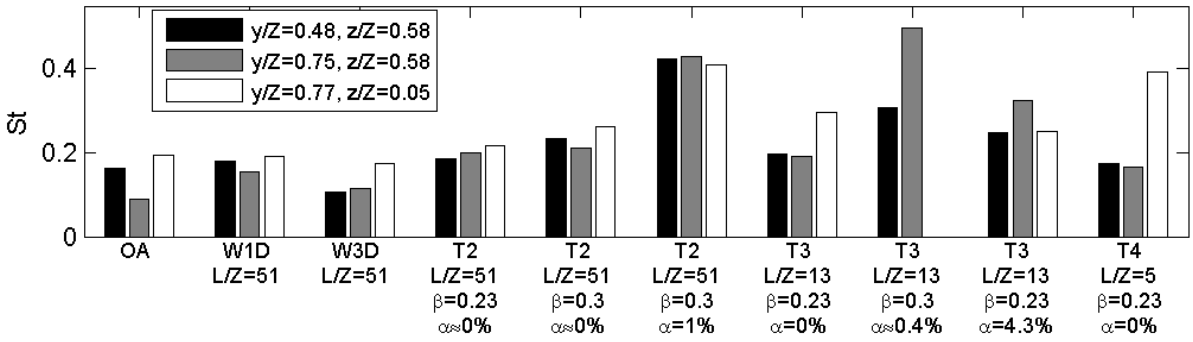

Figure 5.18: Strouhal numbers of flow structures in the near-wake, for different test cases and positions.

The results for the open air show that *St* is greatest at low-heights (y/Z=0.77, z/Z=0.05), and lowest far from the train's side. In the symmetrical wall case W1D, *St* increases slightly and is less changeable between the three plotted positions compared to the open air. This supports

the suggestion in Section 5.2.4.1 that the helical vortex structure is stretched vertically and squashed laterally by the walls, causing its detection at mid-height positions. In the asymmetrical wall case W3D, *St* is slightly lower than in symmetrical wall case W1D. This may result from the asymmetrical arrangement of the structures - perhaps it disrupts the formation of the trailing helical vortices. If this change is responsible for causing lower gust magnitudes, it may help to explain why the ensemble average peaks (Section 5.3) are lower than in the symmetrical configuration W1D.

St is significantly higher in all of the tunnel cases than the open air and wall cases. The length of the tunnel seems to have no effect on *St* at the mid-height positions, but *St* increases as tunnel length decreases at the low-height position. This could mean that the main low-height flow structure is disrupted significantly close to the tunnel entrance, and returns to stable behaviour a substantial distance into the tunnel. The flow structure is likely to be the helical vortex. This is supported by observations of CFD simulation results in Straathof (2013), of tunnel T2 (L/Z=51, β=0.3, $\alpha\approx$0%). Changing the blockage ratio has little effect on *St*. *St* is affected by the opening ratio: increasing the opening ratio in T2 (β=0.3) to α=1% causes a very large increase compared to $\alpha\approx$0%; and increasing the opening ratio to α=4.3% in T3 (β=0.23) causes a small increase compared to α=0%. High values of *St* means that the peak gusts are more tightly distributed spatially, which could mean that the effect of periodic oscillating flow structures on the peak gusts are overshadowed by a non-oscillatory (perhaps more one-dimensional) flow structure which causes *St* to rise by lowering the absolute deviation of the locations of the peak velocities. Section 5.3.2 examines the magnitudes and spatial distributions of maximum velocities from individual runs more closely.

The cause of the general trend of increasing Strouhal number with increasing confinement is investigated. The dominant flow structures causing velocity maxima must be different

between unconfined and confined cases in order to account for the substantial flow changes seen in Sections 5.2.1 and 5.2.4.1. Further analysis has been undertaken to test whether some of the changes in *St* are the result of changes to the boundary layer, which have been shown in Section 5.2.3.1 to be significantly different between open air and confined cases. Figure 5.19 compares *St* with the mean momentum thickness (θ/Y) calculated along the tail carriage (where it has reached its equilibrium value).

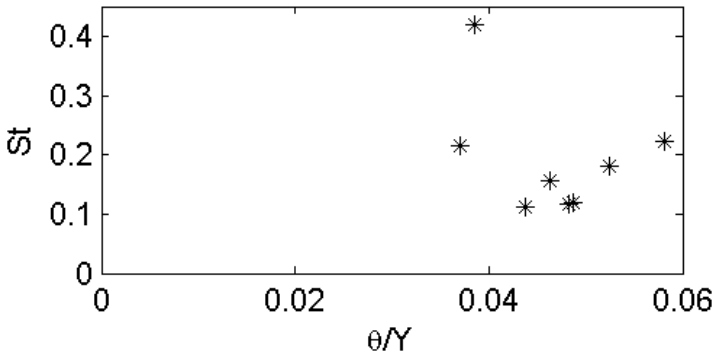

Figure 5.19: The relationship between Strouhal number and normalised momentum thickness, for eight test cases.

The results are scattered, but show a negative correlation of -37%. This agrees with the finding of Muld (2012). These results show that the variation occurs independently of Reynolds number. This behaviour has been derived previously in Rowe et al. (2000) for flow over a flat plate with a blunt trailing edge. In that study, trip wires were installed upstream of the trailing edge to control the momentum thickness. It was suggested that for thicker boundary layers, the circulation fed by the upstream boundary layer on one side of the plate takes longer to be carried across the wake in a sufficient concentration to initiate the formation of a vortex on the opposite side. This relationship may be a contributing factor towards the observations from these experiments relating to the helical vortex structure. Figure 5.14 has shown that the boundary layer thickness and momentum thickness decrease in confined spaces, whilst Figure 5.18 has shown that *St* increases correspondingly.

5.2.4.3 Far-wake region

This section examines the differences in the far-wake velocities between the test cases, based on functions which have been fitted to the velocity data starting from $10Z$ behind the tail. The ensemble average results in Section 5.2.1 have shown that in the wake region, velocity peaks occur a short distance behind the train's tail, which are then followed by gradual decay towards ambient conditions. In confined cases, the velocities at the ends of the time history graphs are consistently higher than in the open air. In all cases, the rate of decay appears to be exponential, as it tends towards - but does not reach - ambient conditions.

As described in Section 2.4, Baker et al. (2013a) determined that the decaying velocity in the far-wake most closely follows a power law relationship. A power law function (Equation 2.31) was fitted to data in order to compare the wakes of different vehicles. It has been modified for this study so that the variables retain their dimensionless forms without affecting the exponent a_2:

$$\frac{U}{V} = a_3 \left(\frac{x_{tail}}{Z}\right)^{a_2} \qquad 5.6$$

A new coefficient a_3 has been defined as its value differs to a_1 which was referred to in Equation 2.31. This is due to the modification of the variables. A least-squares-based fitting algorithm has been used to fit the function to the velocity data using the coefficients a_1 and a_2. Initial investigations were performed to determine appropriate upper limits for the x-axis. It was found that if the curve fitting range extends to a longer distance of 1600 train heights into the wake, the accuracy close to the train's tail is reduced. If the fitting range covers values of x_{tail} lower than $10Z$, accuracy for high values of x_{tail} is reduced. The fitting algorithm was therefore limited to between ten and 300 train heights behind the train's tail. The lower limit

is closer to the train's tail than in Baker et al. (2013a), where the power law-type decay was stated as beginning from 25 train heights into the wake.

Table 5.1 provides the coefficients a_3 and a_2 for the power law formula, for each test case and position. It also includes values of x_{tail}/Z which yield u/V=0.03, calculated as the average of three positions. A higher number indicates a slower rate of decay. u/V=0.03 is equivalent to 2.3m/s for a train operating at 280kph.

Table 5.1: Coefficients for a power law decay function describing the far-wake ensemble average longitudinal velocity.

Test case:	***y*/Z=0.77, *z*/Z=0.05**		***y*/Z=0.75, *z*/Z=0.58**		***y*/Z=0.48, *z*/Z=0.58**		**Mean x_{tail}/Z for u/V=0.03**
	a_3	a_2	a_3	a_2	a_3	a_2	
OA	0.59	-0.55	0.11	-0.25	0.26	-0.41	197
W1D, *L*/Z=51	0.84	-0.52	0.52	-0.43	0.39	-0.36	838
W3D, *L*/Z=51	0.64	-0.48	0.41	-0.41	0.37	-0.37	667
T2, *L*/Z=51, β=0.23, α=0%	0.83	-0.49	0.54	-0.38	0.53	-0.36	1994
T2, *L*/Z=51, β=0.3, $\alpha\approx$0%	0.68	-0.41	0.41	-0.28	0.37	-0.23	27150
T2, *L*/Z=51, β=0.3, α=1%	0.77	-0.42	0.69	-0.37	0.58	-0.32	5781
T3, *L*/Z=13, β=0.23, α=0%	1.05	-0.6	0.63	-0.49	0.52	-0.45	455
T3, *L*/Z=13, β=0.3, $\alpha\approx$0.4%	N/A	N/A	0.41	-0.37	0.49	-0.4	1093
T3, *L*/Z=13, β=0.23, α=4.3%	0.93	-0.58	1.06	-0.62	0.97	-0.62	311
T4, *L*/Z=5, β=0.23, α=0%	1.1	-0.66	0.58	-0.54	0.55	-0.54	228

For the low-height position (*y*/Z=0.77, *z*/Z=0.05), the power law exponent for the open air is -a_2=-0.55, which lies within the empirical range of a_2=-0.39 to -0.64 for different types of high-speed trains operating at full-scale (Baker et al., 2013a). The results show that using walls to confine the flow increases the time taken for the velocity to decay compared to the open air. Increasing the opening ratio reduces the decay time. This suggests that air leakage out of the opening may be responsible for reducing the airflow after the train has passed. It also appears that raising the blockage ratio decreases the rate of decay relative to lower blockage ratios. An increase of the blockage ratio by 30% in tunnel T2 increases the time taken for u/V to reach 0.03 by 1400%. It is likely that the increased longitudinal velocity is driven by the tail piston effect which moves the air column within the entire tunnel in the wake region. It was also found in Section 5.2.4.1 that the increased blockage ratio raises the

peak velocity significantly. Finally, the results suggest that reducing the tunnel length increases the rate of decay. These observations are consistent with findings in Section 5.2.4.1.

5.2.5 Velocity fluctuations caused by compressible effects

This section examines whether the piston effect and oscillatory pressure waves may be seen in the velocity data. These phenomena are visible in the pressure data (Section 4.2.1), and are due to compression of the air ahead of the train's nose, expansion behind the tail, and compression and expansion wavefronts which propagate inside the tunnel at the speed of sound. The bases for these phenomena are shown in Chapter 2.

If pressure waves are superimposed onto the experimental velocity data, they should stand out in the frequency domain as a band of high power with a constant period that is proportional to the tunnel's length. Figure 5.20 shows a time history and wavelet power spectrogram of the ensemble average static pressure and resultant velocity inside T3 (L/Z=13, β=0.23, α=0%). White contour lines have been added to the spectrograms to highlight regions in which the power spectrum at a particular time increment is significantly different (at the 5% probability level) from the background power spectrum. The background power spectrum in this case is the power averaged over all time increments. The power spectrum and significance contours for the static pressure show an oscillation in the frequency domain, visible as a band of high power with a period of 0.39s (2.56Hz). This corresponds to the expected frequency based on a sound wave reflecting inside the tunnel with a wavelength of $2L/c$, and it clearly describes the decaying sinusoid in the time history. However for the velocity, no increase in power is observed in this region, and no evidence is seen in the time history. Figure 5.21 shows the same approach used for T2 (L/Z=51, β=0.23, α=0%). The power spectrum and significance contours show a band of high power with a full-scale equivalent period of 1.2s (0.83Hz). In the velocity results, no increase is observed in this region.

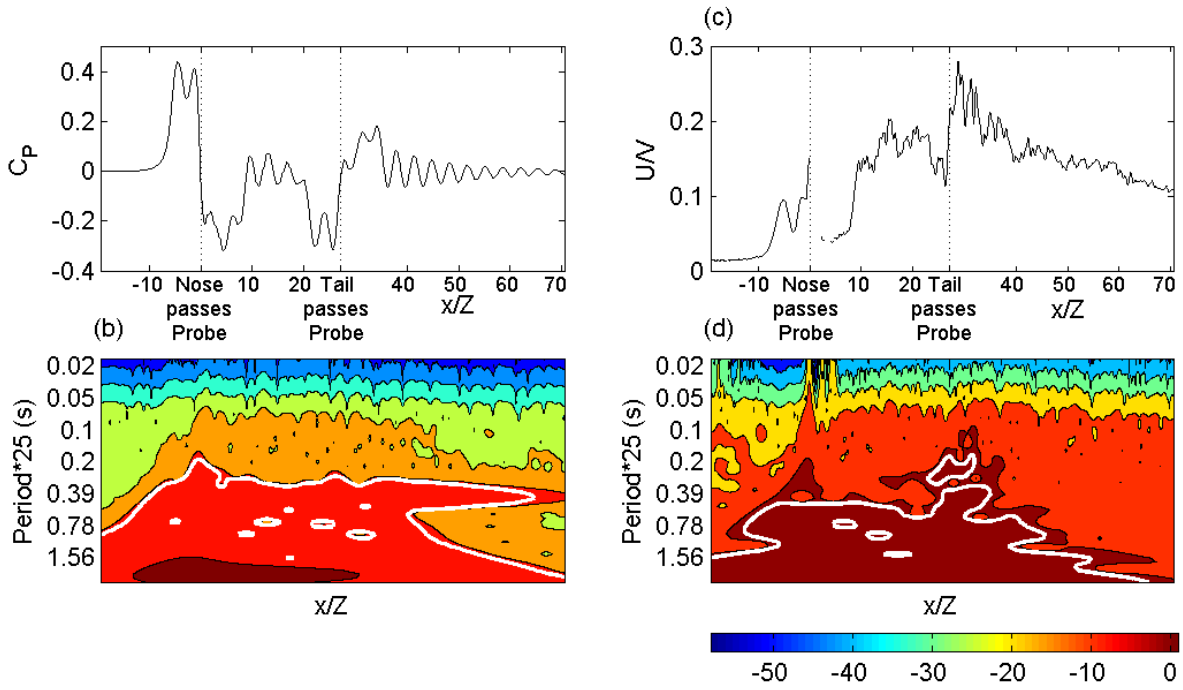

Figure 5.20: For tunnel T3 (L/Z=13, α=0%, β=0.23), ensemble average time histories and wavelet spectrograms of: (a-b) the static pressure on a wall surface tapping at z/Z=0.26; (c-d) resultant velocity at y/Z=0.48, z/Z=0.58.

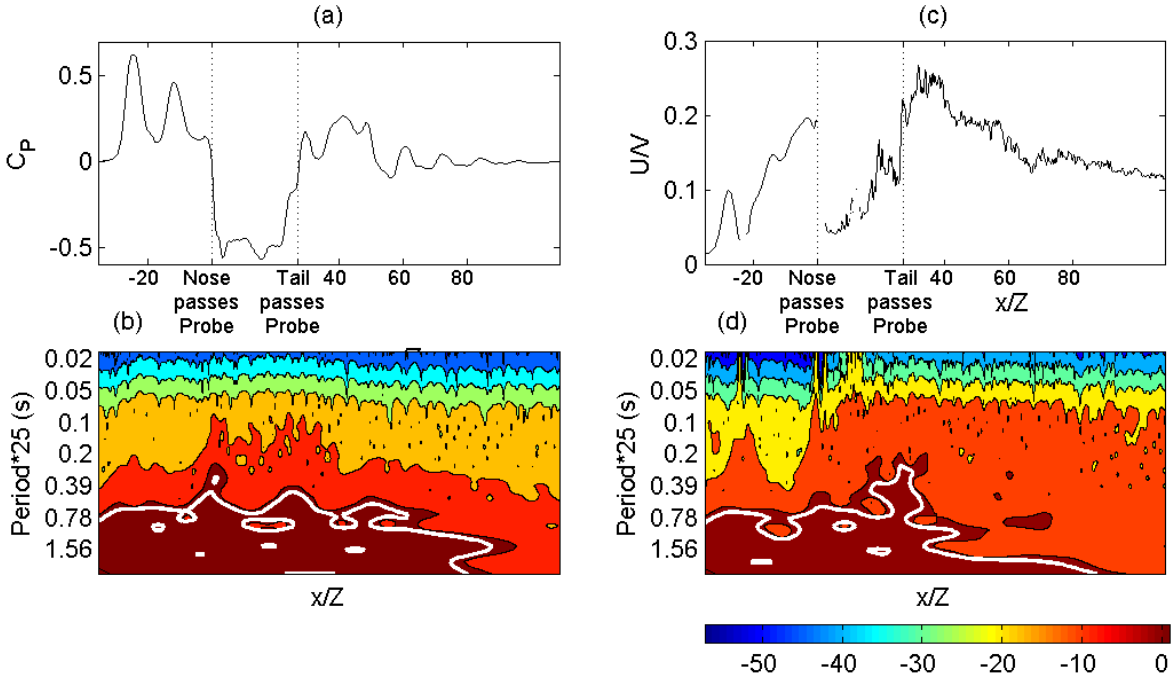

Figure 5.21: For tunnel T2 (L/Z=51, α=0%, β=0.23), ensemble average time histories and wavelet spectrograms of: (a-b) the static pressure on a wall tapping (Y_{wall}/Z=0.84, z/Z=0.26); (c-d) the resultant velocity at y/Z=0.48, z/Z=0.58.

These results suggest that the pressure waves do not affect the velocity time history results, apart from in the nose region where the velocity fluctuation induced by the first pressure wave fluctuation is approximately a quarter of the magnitude of the peak pressure. If this relationship between peak velocity and pressure fluctuations is assumed to apply to subsequent pressure wave fluctuations, the peak velocity should be no higher than U/V=0.025 because the highest pressure oscillations are of the order ΔC_P=0.1.

Gilbert and Straathof (2013) reported the results of CFD simulations which replicated two experiments on tunnel T2 (L/Z=51): (β=0.3, $\alpha\approx$0%); and (β=0.23, α=0%). The respective time history comparisons are shown in Figure 5.4 and Figure 5.5 (Section 5.1). Larger oscillations occurred in the simulated velocity time histories. It is not clear why these differences occur. It is possible that the wavelet power associated with the other turbulent velocity fluctuations is much higher than the power associated with the pressure wave-induced fluctuations, causing the latter to be masked. The turbulent fluctuations occur over a broad spectrum of frequencies, and some with the same or higher magnitudes. The solution would be to repeat the tests more times - Del Valle (2013) found that 80 moving-model train passes were necessary to reduce the residual turbulent fluctuations in the ensemble average to an acceptable level.

The influence of all of the compressible effects on the velocity was also studied using CFD simulations by Straathof (2013). The results for a tunnel are shown in Figure 5.22, in which 'Time (sec)' is multiplied to $V/25Z$ to get the standard x/Z axis. The train nose passes the sensor at 0 seconds, and the tail passes at 3.1 seconds.

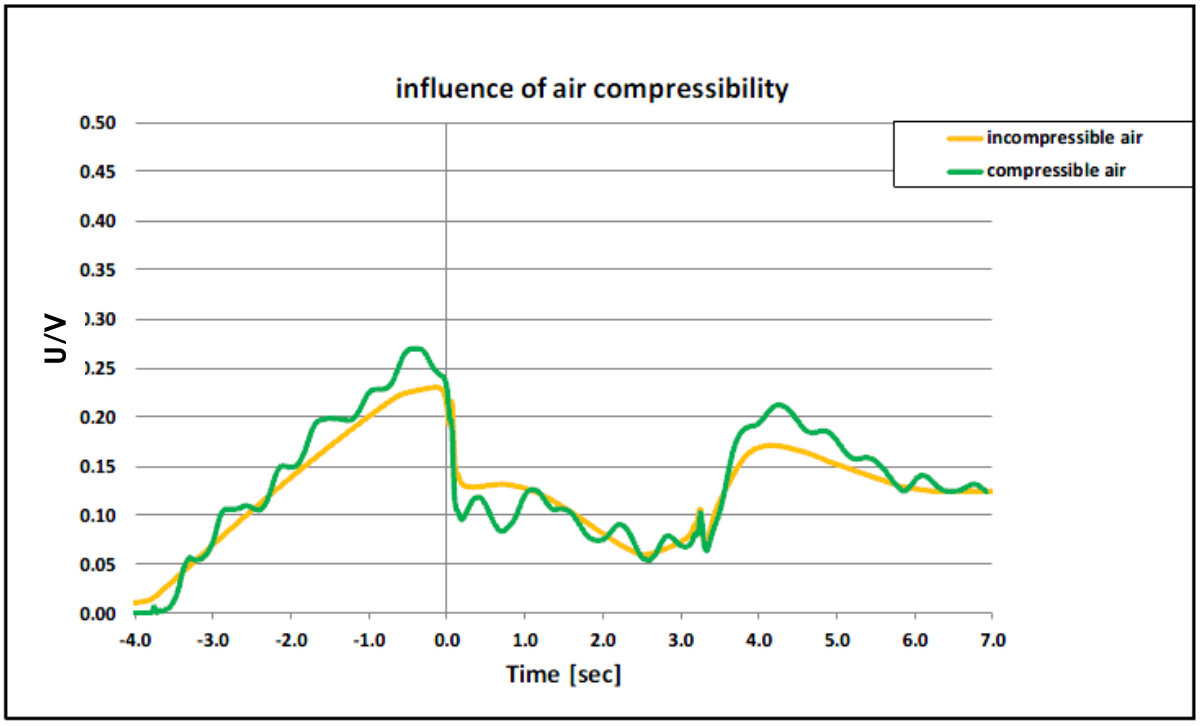

Figure 5.22: Compressible effects on the air velocity inside tunnels predicted by CFD (Straathof, 2013) - in this case T2 (L/Z=51, β=0.3, $\alpha\approx$0%) at y/Z=0.48, z/Z=0.58.

The results show that compressible effects cause a slight increase in the ensemble average velocity. This may be due to the piston effect, because the increases are localised to the upstream and wake regions adjacent to the train's nose and tail respectively. These regions were shown in Sections 2.2 and 2.4 to feature large regions of air compression and expansion respectively, caused by the piston effect. The results also show that pressure waves cause fluctuations to superimpose onto the velocity data with a period proportional to the length of the tunnel, affecting the maximum measured velocity. This suggests that although pressure waves were not detected in the experimental data, compressible effects are responsible for some of the increase in velocity.

5.3 Maximum velocities in individual runs

This section examines the maximum velocities reached in individual runs ('ensemble maxima') to try and establish which test cases cause the highest maximum velocities, and

what flow structures are most influential in causing the observations. Gusts occurring in individual runs are caused by one or more of a variety of different flow phenomena. Since most of the gusts occur sporadically, evidence of their existence is often smoothed by ensemble averaging. For this reason, a statistical analysis of peak gusts helps to reveal the true nature of the flow. Relationships are sought between pressure fluctuations and maximum velocities in sub-section 5.3.1. The statistical distributions of maximum velocities of individual runs are analysed in sub-section 5.3.2. In sub-section 5.3.3, some statistical gust analysis approaches are applied to the maximum velocity data within the framework of Objective 5.

As recommended in Appendix A5, the maximum velocities in T2 (L/Z=51, β=0.23) with an opening ratio of $\alpha\approx$0.4% have been merged with the maximum velocity data for α=0% in order to increase the ensemble size N. From the recommendations made, it is therefore presumed that $\alpha\approx$0%.

5.3.1 Relationships between the pressure signature and maximum velocity

Section 5.2.4.1 found that all confined cases caused a disproportionately high increase in the maximum longitudinal velocity in the wake region compared to the open air. In order to understand these increases, it is necessary to identify which flow structure is responsible. In this section, relationships are sought between the pressure loading pattern and the maximum longitudinal velocity ($max(u)/V$) in the wake region. All of the data have been filtered to a cutoff frequency of f_c=100Hz (calculated using Equation 3.22). This is a full-scale-equivalent duration of t_{fs}=0.25 seconds. Four pressure parameters have been calculated. The first two are the peak-to-peak pressure change for the whole time history (ΔC_P), and the train's tail ($\Delta C_{P,tail}$). The third and fourth parameters also relate to the fluctuation around the train's tail. These are the x-axis distance between the suction and positive pressure peaks ($dx(\Delta C_P)$), and

the peak pressure gradient ($max(dC_P/d(x/Z))$). These parameters are related to the rapidity of the pressure fluctuation. The reason for choosing the whole time history for the first parameter is to create a variable representative of the 'piston effect' and attempt to relate it to the maximum velocity. The reason for choosing the train's tail for the second parameter is because the same signature occurs in all test cases - a suction peak followed by a higher peak (usually positive). It is thought that this will correlate better with maximum velocity because the fluctuation can generally be isolated from other test case-specific pressure fluctuations (e.g. pressure waves) if the peak-to-peak pressure is measured within a suitably sized window. The highest correlation occurs when the window is $24 \leq x/Z \leq 31$ (three train heights upstream of the train's tail, and four downstream). This window contains a coherent fluctuation that is common to all test cases. Finally, an appropriate sensor position was chosen. This is (y/Z=0.75, z/Z=0.58) because the Cobra probe at this position was the only sensor which reliably measured the true pressure peaks without any dropouts hiding the peak pressures.

The data from all test cases have been added to scatter plots in Figure 5.23. Regressions and coefficients of determination (R^2) have been calculated for each plot.

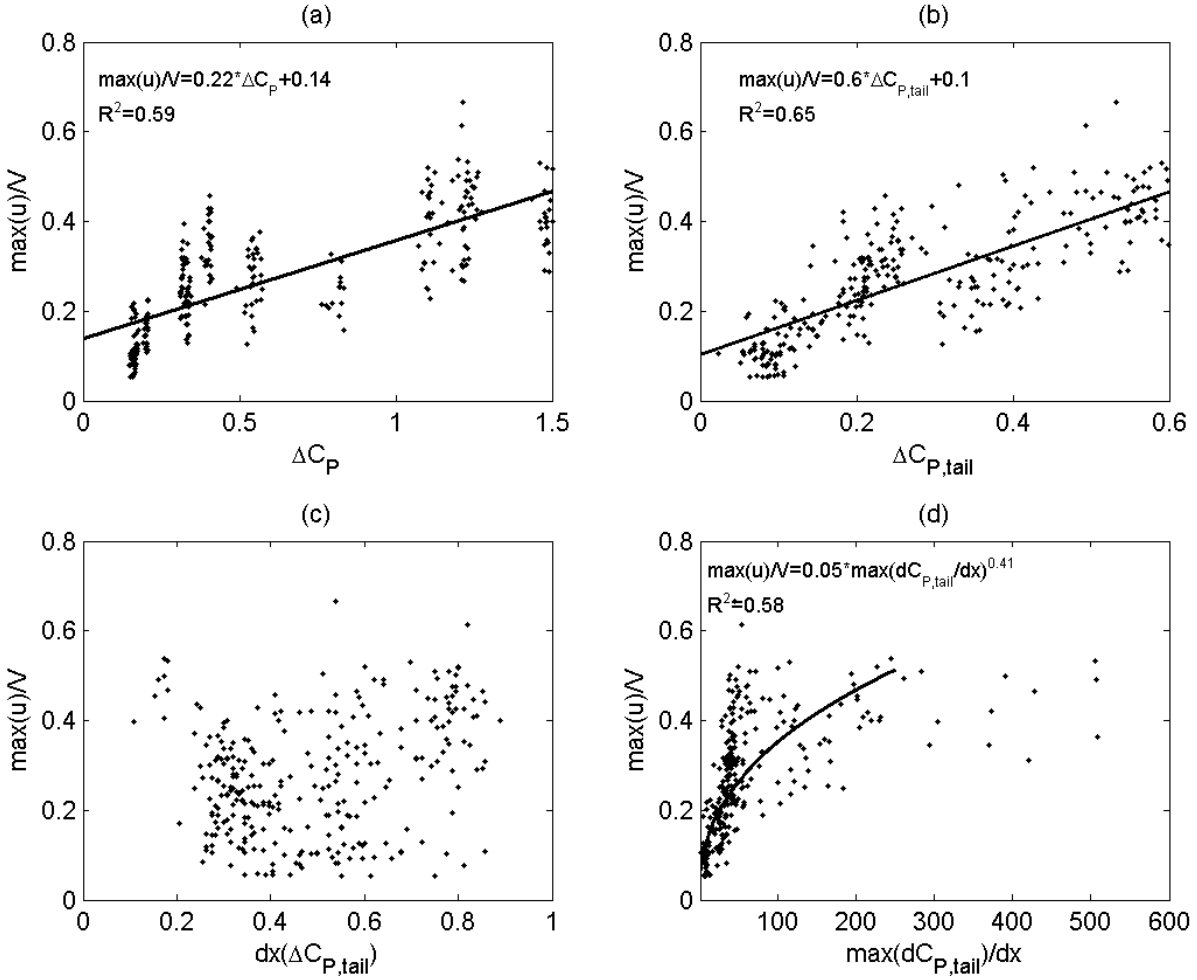

Figure 5.23: Relationships between four pressure variables and the maximum wake velocity, using the data from all test cases: (a) ΔC_P; (b) $dx(\Delta C_P)$; (c) $max(dC_P/dx)$.

The regressions are given by:

$$\frac{\max(u)}{V} = 0.22\Delta C_P + 0.14 \tag{5.7}$$

$$\frac{\max(u)}{V} = 0.6\Delta C_{P,tail} + 0.1 \tag{5.8}$$

$$\frac{\max(u)}{V} = 0.05 \max\left(\frac{dC_{P,tail}}{dx}\right)^{0.41} \tag{5.9}$$

The results show that the peak velocity is strongly positively correlated with ΔC_P, both for the whole time history (R^2=0.59, Equation 5.7), and for the tail pressure fluctuation (R^2=0.65, Equation 5.8). There is no correlation with $dx(\Delta C_{P,tail})$. The natural logarithm of the peak

velocity is strongly positively correlated with the natural logarithm of $max(dC_{P,tail}/dt)$ (R^2=0.58, Equation 5.9). Overall, it seems that the peak velocity is most closely correlated to the pressure fluctuation around the train's tail, as well as the peak-to-peak pressure within the entire structure. In the latter case, causality is difficult to establish as the causes of the pressure change and the velocity peak may differ.

The predicted maximum velocity has been compared with the pressure-velocity relationship in different test cases. Figure 5.24 shows the predictions of the three equations alongside one standard deviation of the mean of the maximum longitudinal wake velocity for each test case, measured at position y/Z=0.75 and z/Z=0.58.

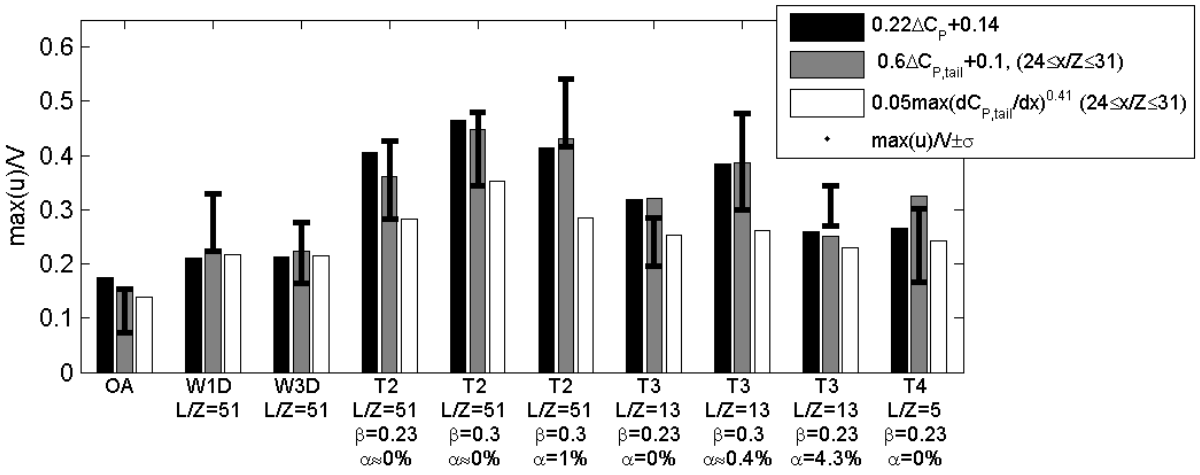

Figure 5.24: Predicted maximum velocity based on pressure fluctuations, compared with observation, for each test case, at position (y/Z=0.75, z/Z=0.58)

The means of the three equations: over-predict the maximum velocity in the open air; under-predict the maximum velocity in the wall cases and partially-enclosed tunnels; accurately predict the maximum velocity in the longer enclosed tunnels; and slightly over-predict the maximum velocity in the shorter enclosed tunnels. Equation 5.8 (the peak-to-peak pressure around the tail) shows the best agreement with the measured results, and Equation 5.9 (the maximum gradient around the tail) shows the poorest agreement.

In all wall cases, the pressure loading pattern (highlighted in Figure 4.3) shows that the relationship between the nose pressure change and the maximum wake velocity (Equation 5.7) cannot be causal, because the ΔC_P term captures the pressure change around the nose of the train only; the pressure decays to $\Delta C_P \approx 0$ between the nose and tail. However, the relationships in equations 5.8 and 5.9 could be causal as they represent the pressure fluctuations around the train tail. Figure 5.24 shows that wall case W1D causes the peak-to-peak pressure change and maximum pressure gradient around the train's tail to increase relative to the open air. These could be important factors in explaining the large increase in the longitudinal velocity. The equations under-predict the observed maximum velocity in W1D. This could be due to the types of trendlines used or due to other unexplored relationships.

The enclosed tunnels are discussed. When transitioning from walls to tunnels by adding a ceiling, a small further increase occurs in the longitudinal velocity above that caused by the walls, due to compressible effects (Section 5.2.5) which affect the peak pressure magnitudes and durations and the maximum pressure gradient around the train's nose and tail. Compressible effects are characterised by an increase in ensemble average velocity, and fluctuations due to pressure waves, although evidence of the latter is only seen in CFD simulations. Compressible effects depend on the train speed, x-axis position of the sensor, length of the tunnel, and blockage ratio (Section 4.2.3.1).

Figure 5.24 shows that the equations describing the magnitudes of the peak-to-peak pressures for the whole time history and for the tail region both predict the maximum velocity for T2 (L/Z=51, β=0.23, α=0%) closely. It is therefore likely that the difference in the peak longitudinal velocity between tunnels and walls is accounted for by its relationship with the pressure fluctuation. The dependency of the pressure results on the combined tunnel length

and x-axis sensor position (Equation 4.2 and Figure 4.12) means that the velocity results should not be associated with tunnel length, but rather the (inseparable) combination of these two variables: x_P/L.

Partially-enclosed tunnels are discussed. All three equations under-predict the maximum velocity compared to observation. In Section 5.2.4.1 it was stated that in these cases the ensemble average longitudinal velocity increases relative to the enclosed tunnels, and that a strong pressure gradient may be responsible. By comparing the predictions and observations in Figure 5.24, equation C appears to show the poorest agreement with observation. Therefore, the increased velocity appears to relate more closely to the magnitude of the peak-to-peak pressure (Equations 5.7 and 5.8), than the maximum gradient. The rest of the difference may be due to a variable that cannot be determined in this thesis.

Outside of the scope of this thesis, there is potential for these equations to be developed for use in predicting slipstream velocities from observed pressure transients.

5.3.2 Statistical distributions of maximum velocities

This section presents the mean and standard deviation of the ensemble maxima, using data from all test cases and from three positions. All of the data have been filtered to a cutoff frequency of f_c=100Hz. This is a full-scale-equivalent duration of 0.25 seconds. Figure 5.25 and Figure 5.26 show the means (bars) and standard deviations (lines) of the ensemble maxima ($max(U)/V$) and the x-axis locations at which they occur ($x_{max(U)}/Z$). It is presumed that the ensemble maxima and locations fit Gaussian distributions, based on the findings of Baker et al. (2013b). Dotted lines extend from the upper and lower limits of the open air results, representing the first standard deviation of the mean of the open air maximum velocity. This may be used as a basis on which to compare the confined results.

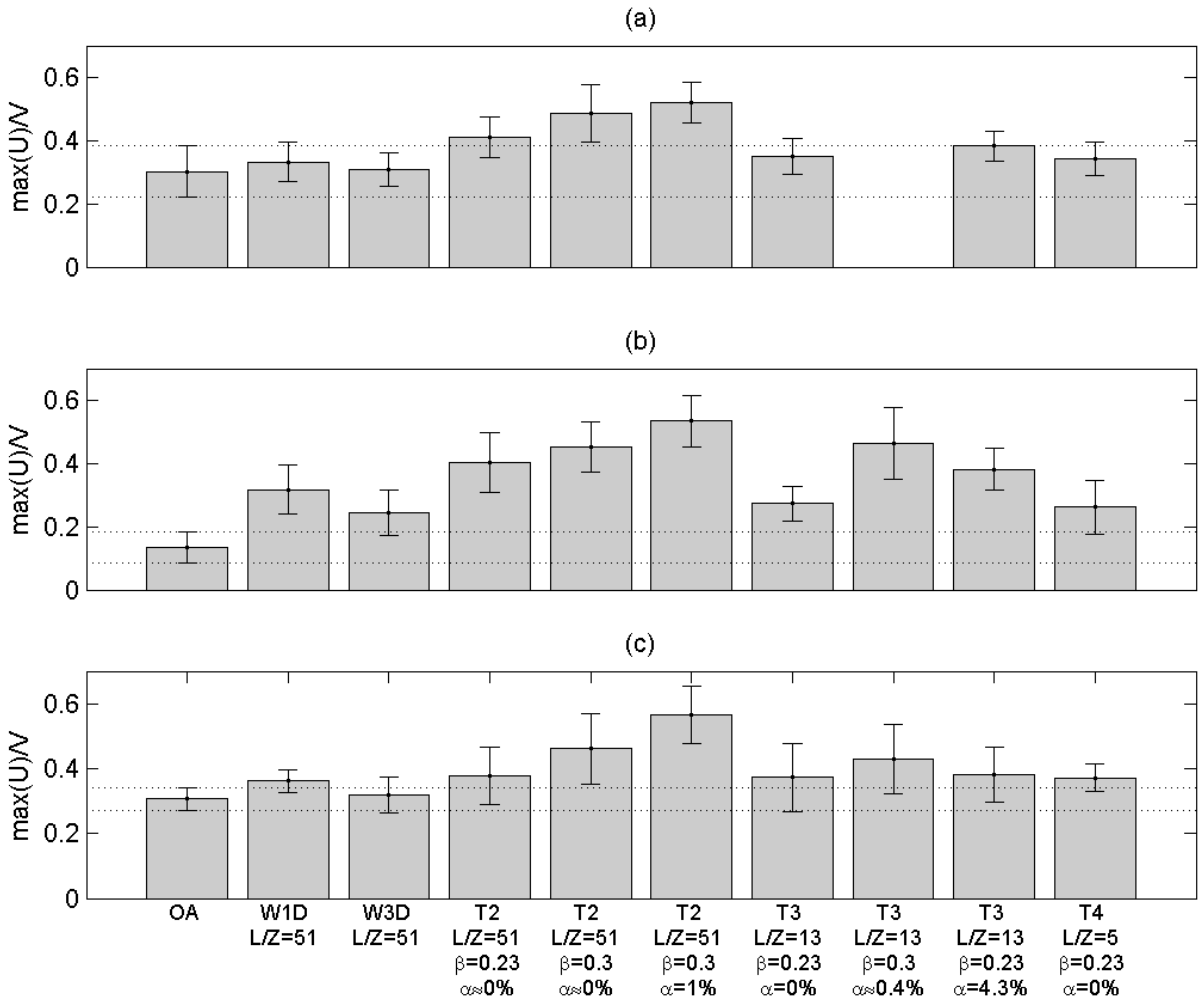

Figure 5.25: Means (shaded bars) and standard deviations (lines) of maximum velocities for different test cases. Positions: (a) *y*/Z=0.77, *z*/Z=0.05; (b) *y*/Z=0.75, *z*/Z=0.58; (c) *y*/Z=0.48, *z*/Z=0.58.

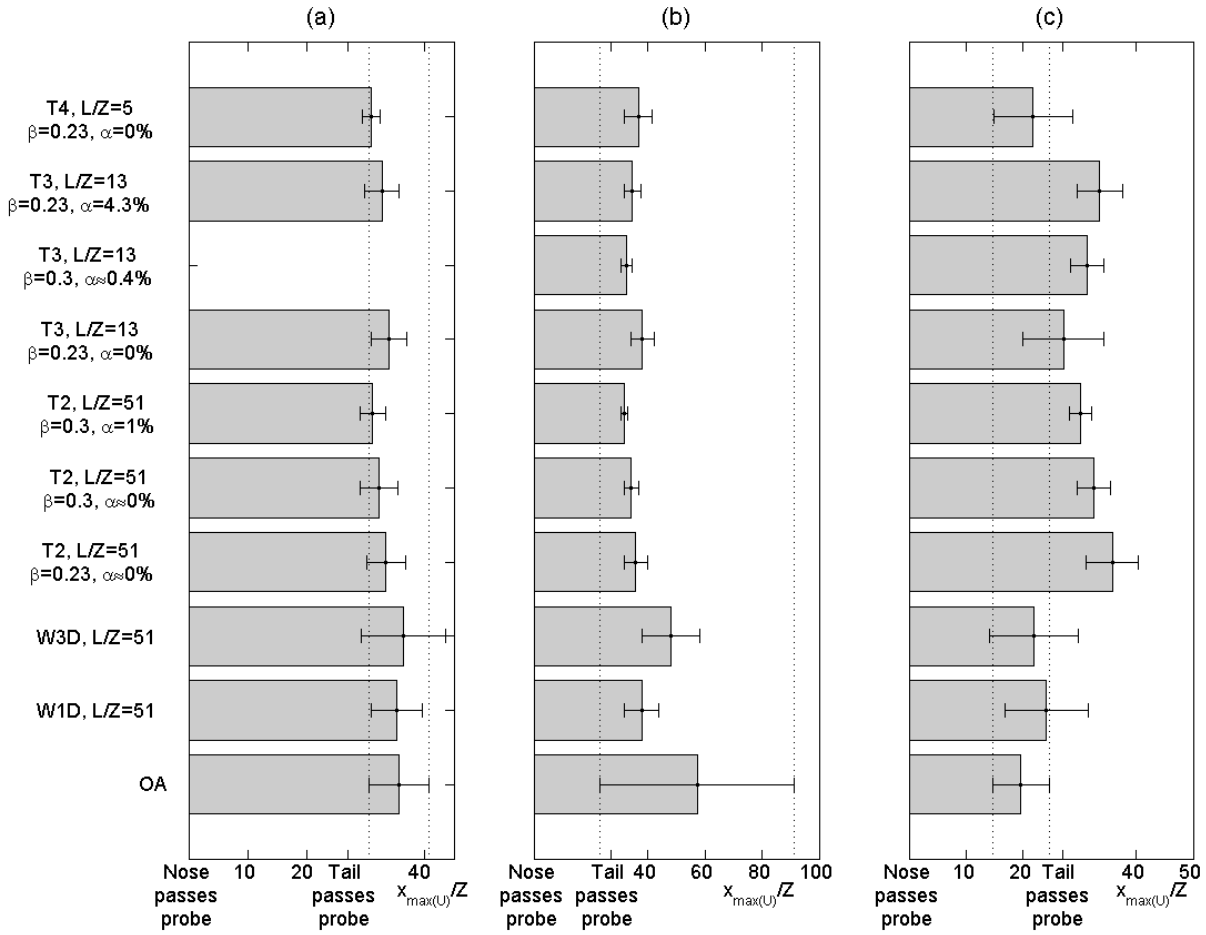

Figure 5.26: Means (shaded bars) and standard deviations (lines) of the *x*-axis positions of maximum velocities for different test cases. Positions: (a) *y*/*Z*=0.77, *z*/*Z*=0.05; (b) *y*/*Z*=0.75, *z*/*Z*=0.58; (c) *y*/*Z*=0.48, *z*/*Z*=0.58.

The following observations are made regarding the **ensemble maxima** from Figure 5.25, but only when the results from **all three positions** agree (this helps to isolate the effects of the largest and most influential flow structures):

1. **All of the confined cases cause higher means than the open air.** Most of these maxima occur in the wake. Section 5.2.4.1 suggests that these increases are driven by a strong longitudinal velocity, which Section 5.3.1 has found to correlate strongly with the increased magnitude of the peak-to-peak pressure around the train's tail and for the whole time history.

2. **If all of the test cases are ranked in order of mean, their rankings are identical at all three positions.** As with point one, this suggests that a more one-dimensional flow structure (and dominant longitudinal velocity) influences the results at all three positions in all confined spaces. Section 5.2.4.1 also suggested that the helical vortex structure around the tail is laterally squashed and vertically stretched by the walls, inducing similar velocities at all positions for all confined cases.

3. **The tunnels with higher blockage ratios cause higher means than the tunnels with lower blockage ratios.** The blockage ratio is responsible for a 'piston effect' which is a compressible phenomenon. It was found in Section 5.2.5 that the compressible effects increase the maximum ensemble average velocity, compared to cases in which compressible effects may be ignored. Discussion throughout Section 5.2.4 has found that the longitudinal velocity component is most significantly affected by changes in blockage ratio.

4. **The partially-enclosed tunnels cause higher means than their fully-enclosed variants, whilst the standard deviation reduces or stays the same.** The findings in Section 5.2.4.1 suggest that these increases are driven by two phenomena: increasing longitudinal velocity, which is most significantly affected by a distinctive pressure fluctuation around the train's tail (Section 5.3.1); and an increased vertical velocity peak, which corresponds to flow exiting the tunnel. The latter observation causes lower standard deviations due to the highly localised nature of the pressure-driven flow leaving the tunnel.

5. **The wall case W1D causes the same or higher means and standard deviations compared to the shortest tunnel T4.** This suggests that the required length of tunnel

beyond which peak gusts are higher than those found in wall cases lies within the range $5 \leq L/Z \leq 13$ (where $L/Z=13$ is the next shortest tunnel).

6. **Shorter tunnels cause the same or lower means than longer tunnels with the same blockage ratio.** The findings in Section 5.3.1 suggest that the difference in the peak longitudinal velocity between tunnels and walls, and tunnels of different lengths, is accounted for by the strong correlations found with the peak-to-peak pressure which was calculated for the whole time history and also around the train's tail. The findings in Section 5.2.5 suggest that an expansion wave related to the tail piston effect increases the velocity.

7. **The asymmetrical wall case W3D causes lower means and standard deviations than the symmetrical case W1D.** The findings in Section 5.2.4.2 suggest that the shedding frequency of the dominant wake structure is significantly disrupted by the asymmetrical wall configuration, causing lower magnitude gusts at all positions.

The following observations are made regarding the **ensemble maxima** from Figure 5.25, but only when the results from **two positions** at either constant heights or lateral separations agree:

8. **At height $z/Z=0.58$, the standard deviations are significantly higher in all confined cases than the open air.** Section 5.2.4.1 found that in confined spaces the results at all three positions are influenced by similar wake structures, possibly due to a change in the shape of the vortex structure which causes consistently higher standard deviations than the open air at this height.

The following observations are made regarding the ***x*-axis locations of the ensemble maximum velocities** presented in Figure 5.26, but only when the results from **all three**

positions agree. This helps to isolate the effects of the largest and most influential flow structures.

9. **In all confined cases the locations of the ensemble maxima vary less between the sensor positions than in the open air.** In the confined cases, the mean locations are within 20 train heights of the train's tail, whereas in the open air the mean locations vary from the boundary layer region to the far-wake region depending on the position of the sensor. The discussion throughout Section 5.2.1 suggests that the most significant confinement-related increases occur in the wake region.

10. **The standard deviations are lower in partially-enclosed tunnels than in their enclosed variants.** This artificially increases the peak ensemble averages. This was speculated in Section 5.2.4.1 as a possible reason for the increases in longitudinal ensemble average maximum velocities. This also supports the finding in point four; the low standard deviation is indicative of a different flow structure which is highly localised in the time history - a pressure-driven vertical flow at a fixed position behind the train's tail which influences the ensemble maxima.

11. **The standard deviations are lower in tunnels with higher blockage ratios than those with lower blockage ratios.** This is likely to be because the increased blockage ratio most affects the magnitudes of the pressures - other aspects of the loading pattern remain the same. Consequently, velocities induced by high local pressure gradients occurring at a very narrow range of locations are more influential on the ensemble maxima, and the standard deviation therefore decreases.

12. **The standard deviations in the tunnels and partially-enclosed tunnels are the same or lower than in any of the wall cases.** Based on the analysis in Section 5.3.1, it is likely that the lower standard deviations are the result of a greater influence of the

tail pressure fluctuation, which is significantly altered by confinement. These fluctuations typically occur over a narrow range of locations, and accordingly reduce the standard deviations of maximum velocities.

13. **The standard deviation of the asymmetrical wall case W3D is higher than that of the symmetrical wall case W1D.** Based on the analysis in Section 5.2.4.2, the shedding frequency of the dominant wake flow structure is significantly disrupted by the asymmetrical wall configuration. It appears that this has caused the gusts to occur over a higher range of positions.

14. **The variation in standard deviations between the three measurement positions is less in the confined cases than in the open air.** This suggests that whilst the flow structure causing velocity maxima in the open air may differ significantly between positions, one common flow structure influences the observations at all three positions in the confined cases. This supports observations in Point 2 and Section 5.2.4 - the flow structures causing the maxima in confined cases are substantially one-dimensional.

The following observations are made regarding the ***x*-axis locations of the ensemble maximum velocities** presented in Figure 5.26, for **individual positions**:

15. **At *y/Z*=0.75, *z/Z*=0.58, the mean in the open air is higher than the mean plus one standard deviation of all of the confined cases.** The analysis in Section 5.2.4 found that the maximum velocities at this measurement position increase the most compared to the open air, and this observation confirms that the dominant causes of the velocity maxima at this position have changed most significantly compared to the open air. The mean *x*-axis location in the confined cases is closer to the train's tail than in the open air. This supports the observation in Points 9 and 10 that the maximum velocities shift

into a similar position in the wake region in all confined spaces. This has been deemed to be largely due to the tail pressure fluctuation, and reasons for this are discussed from point nine onwards.

5.3.3 TSI velocity analysis and the effect of gust duration

In this section, statistical gust analysis methodologies are applied to the near-wake data. The lack of a methodology in codes of practice for assessing gusts in tunnels provides an opportunity to try different approaches, three of which are used in this section. These approaches are used to analyse the results for position at y/Z=0.77 and z/Z=0.05, which is equivalent to the 'TSI position' (y=3m, z=0.2m at full-scale) required in the TSI (2008) code of practice. Results for two cases which used the position at y/Z=0.58 and z/Z=0.13 instead of the TSI position are also included in the analysis. The methods are as follows:

1. The '1s method', based on the requirement in TSI (2008), relied on a t_{fs}=1 second window moving-average filter to smooth each individual run, and followed the TSI methodology requirements as closely as possible. The TSI requirements are taken out of context in this research as the main requirements are for experiments to be carried out at full-scale, and for the test speeds to be close to full-operational speeds. Section 3.11 describes the extent to which the methodology conforms to the code of practice. The 1 second window represents a full-scale-equivalent gust of 1 second duration, calculated by Equation 3.22.

2. The '0.1 second method' relied on a fifth order Butterworth low-pass filter with a cutoff frequency of f_c=250Hz, which corresponds to t_{fs}=0.1 seconds at full-scale according to Equation 3.22. It was used in a similar analysis in Gilbert et al. (2013b). This method was used to account for the inherent problem of over-smoothing in the

TSI method, which is an effect discussed in Baker et al. (2013b). 0.1 seconds is recommended in Sterling et al. (2008) as the minimum filter window size for risk assessing slipstream gust loads, so over-smoothing should not be an issue.

3. The '0.375 second method' relied on a first order Butterworth low-pass filter with a cutoff frequency of f_c=67Hz, which corresponds to t_{fs}=0.375 seconds at full-scale according to Equation 3.22. It was used in a similar analysis in Gilbert and Straathof (2013). This cutoff frequency is based on the recommendation in Jordan et al. (2009) for risk assessing loading on trackside workers. Research in wind tunnels found that a transient gust of this duration could cause a 'muscle response' (loss of balance). The filter was first order, and featured a shallower frequency roll off than in the second method in acknowledgement that the critical gust duration varies considerably between humans, based on their stance and clothing.

All three methods relied on calculating the mean $\bar{u}$ and standard deviation σ of the filtered maximum velocities from individual runs, of which there were N for each test case. The 95% confidence limit, $U_{2\sigma}/V$, is represented by the earlier-defined Equation 3.21:

$$\frac{U_{2\sigma}}{\mathrm{V}} = \frac{\overline{\max(U)} + 2\sigma_{\max(U)}}{\mathrm{V}}$$

Discussion in Baker et al. (2013b) reveals that this statistical approach is valid based on analysis of full-scale open air experimental data, which found that gusts are normally distributed about their mean values. Therefore $U_{2\sigma}/V$ may be interpreted as the maximum velocity at the 5% probability level. Table 5.2 shows the mean, standard deviation and 5% probability of the maximum velocity. Extra columns show the return period ('R.P' = 1/probability) of exceedence of the TSI gust limit of $U_{2\sigma}$=22m/s. The gust limit is U/V=0.283 for a train speed of 280kph, or V=77.77m/s). The return period is recommended in Gilbert et

al. (2013b) as a superior method for assessing risks based on limit-exceedence. This involves calculating the regularity of exceedence of the gust limit from the statistical gust distributions.

Table 5.2: Maximum velocities at low-height positions, at the 5% probability level.

Test case	Runs, N	1s method (TSI)				0.1s method				0.375s method			
		$\bar{u}/V$	σ/V	$U_{2\sigma}/V$	R.P.	$\bar{u}/V$	σ/V	$U_{2\sigma}/V$	R.P.	$\bar{u}/V$	σ/V	$U_{2\sigma}/V$	R.P.
TSI position: y/Z=0.77, z/Z=0.05													
OA	62	0.21	0.04	0.28	39.8	0.32	0.08	0.49	1.47	0.28	0.07	0.42	2.03
W1D	50	0.25	0.03	0.3	10.2	0.35	0.07	0.49	1.18	0.31	0.05	0.41	1.43
W3D	50	0.22	0.03	0.29	35.1	0.33	0.06	0.46	1.31	0.29	0.05	0.39	1.91
T2, L/Z=51, β=0.23, α≈0%	40	0.3	0.04	0.38	1.4	0.44	0.07	0.58	1.01	0.38	0.06	0.5	1.04
T2, L/Z=51, β=0.3, α≈0%	25	0.32	0.04	0.4	1.3	0.53	0.09	0.71	1.01	0.44	0.07	0.59	1.02
T2, L/Z=51, β=0.3, α=1%	25	0.37	0.02	0.41	1	0.55	0.06	0.67	1	0.47	0.05	0.57	1
T3, L/Z=13, β=0.23, α=0%	16	0.25	0.02	0.29	15.9	0.37	0.07	0.5	1.1	0.32	0.05	0.42	1.25
T3, L/Z=13, β=0.23, α=4.3%	15	0.26	0.03	0.31	4.9	0.42	0.05	0.51	1	0.35	0.04	0.43	1.05
T4, L/Z=5, β=0.23, α=0%	15	0.24	0.03	0.3	10.2	0.37	0.06	0.49	1.09	0.32	0.05	0.41	1.33
y/Z=0.58, z/Z=0.13													
OA	46	0.24	0.05	0.34	5	0.39	0.12	0.63	1.23	0.33	0.09	0.51	1.47
W2D	50	0.34	0.03	0.4	1	0.53	0.09	0.7	1	0.44	0.06	0.56	1

The results for the three methods differ considerably. In the 0.1s and 0.375s methods, $U_{2\sigma}/V$ is 65% and 40% higher on average than that calculated using the TSI method respectively. The return period reveals that when the 0.1s and 0.375s methods are used, the probability of limit exceedence is between 50% and 100% in all cases including the open air. The differences in the results between the three methods are due to the relationship between the filter width and the length scale of the gust causing the maximum velocity, which affects the attenuation of the maximum velocity. Filter width is an important consideration in designing a risk assessment methodology for confined flows, both in terms of the predicted gust magnitude and the relative changes between test cases. The probability of limit exceedence is more capable than $U_{2\sigma}/V$ for distinguishing risks in different confined spaces.

The results show that the highest values of $U_{2\sigma}/V$ occur in the longest tunnels (L/Z=51). The shorter tunnels produce similar $U_{2\sigma}/V$ values to the open air, but the return period shows that $U_{2\sigma}/V$ exceeds the gust limit two to four times more regularly than the open air, even in the

shortest tunnel T4. When the blockage ratio in enclosed tunnel T2 is changed from β=0.23 to 0.3, $U_{2\sigma}/V$ is very similar, but the return period shows that the limit is exceeded three times more regularly. When the opening ratio in T2 and T3 is increased, $U_{2\sigma}/V$ hardly changes but the return period shows that the limit is exceeded more regularly.

5.4 Concluding remarks

The following conclusions can be drawn from the analysis carried out in this chapter:

(a) The open air velocity has been compared with measurements from past studies. The flow patterns are similar in the boundary layer region and the wake region, but not the nose region. Data for an enclosed tunnel has been compared with a CFD simulation. The flow patterns are similar in the nose region. They are dissimilar in the wake region but this is probably a consequence of the limitations of the turbulence model.

(b) Vertical walls were added to both sides of the tracks in a symmetrical arrangement, and the changes relative to the open air have been assessed for two wall separations. The maximum velocity around the train's nose increases, although the measurements around the nose may not be reliable. The boundary layer grows at a faster rate but reaches the same thickness. The velocity profile remains logarithmic. In the wake region, the helical vortex structure appears to be laterally squashed and vertically stretched by the wall, causing higher velocities to be detected, and at higher positions. Most of the maximum velocities occur in the wake region, and they are higher at all positions. The longitudinal velocity increases more than the lateral and vertical velocities due to the increased peak-to-peak pressure and pressure load duration around the train's tail. The lateral velocity decays close to the wall due to its obstruction. The velocity in the far-wake decays more slowly, often causing the gust

duration to be extended. The rate of decay may be most accurately modelled using a power law function.

(c) When the vertical wall opposite the sensors is moved close to the train's side (an asymmetrical configuration), the ensemble average and maximum velocities decrease relative to the symmetrical configuration. A reduction in the Strouhal number suggests that the helical vortex flow structure is disrupted by the asymmetry, which may explain the decrease in maximum velocity.

(d) Ceilings have been added to vertical walls to create tunnels, and the differences compared to the walls have been assessed. The nose-entry compression wave causes a small fluctuation in the velocity time history. The longitudinal velocity increases upstream of the train's nose due to the 'piston effect' - the compression of air ahead of the train's nose which induces a flow towards the tunnel's exit. The magnitude of the peak piston-induced velocity is dependent on the tunnel's length and cross-sectional area. The piston effect also increases the longitudinal velocity in the near-wake, and therefore the maximum gust magnitudes, due to expansion of air behind the train's tail. It also reduces the rate of decay of the velocity, which extends the durations of the maximum gusts as well as the time taken for the air to return to ambient conditions, affecting the ventilation characteristics of tunnels. The sinusoidal pressure oscillations caused by 'pressure waves' - compression and expansion waves travelling along the longitudinal axis at the speed of sound and reflecting from the tunnel's entrance and exit portals - do not cause detectable velocity fluctuations over the same frequency range. In tunnels the boundary layer follows a logarithmic profile as with wall cases, but it is thinner. This may be due to pressure gradients around the train's nose and tail

which resist its growth and reduce its thickness around the first and last carriages respectively.

(e) The length of a tunnel has been changed. As the length decreases, all of the results tend towards those of the vertical wall cases, due mostly to a change in the longitudinal velocity which is strongly correlated with the piston effect around the train's tail, which is related to the combined tunnel length and position of the sensor. The results should be associated with sensor position divided by the tunnel length.

(f) The blockage ratio of the tunnel has been increased for some of the tunnel cases. A pressure-driven piston effect induces a steady wind in the tunnel, which is dependent on blockage ratio. The steady wind superimposes with the velocity fluctuation upstream of the train's nose and downstream of the tail. The latter superimposition causes the maximum wake velocity to increase relative to lower blockage ratio tunnels.

(g) Small openings have been made in tunnels to create partially-enclosed tunnels, and the results have been compared with those for enclosed tunnels. The maximum velocity increases at all sensor positions. The peak longitudinal velocity increases compared to enclosed tunnels. High velocities also occur in the direction of the opening in the wake region when the pressure rises inside the structure. In the wake region a pressure fluctuation around the train's tail induces a vertical velocity peak (caused by flow exiting through the opening). The peak vertical flow superimposes with the peak wake velocity, thereby increasing the maximum velocity relative to enclosed tunnels.

(h) As the above points have shown, there are some common flow changes seen in all confined cases relative to the open air. A near-one-dimensional velocity peak has been identified as correlating strongly with various measures of pressure fluctuations,

particularly the peak-to-peak pressure directly around the train's tail. Relationships have been derived from which it is possible to predict the maximum velocity, generally based on pressure measurements alone. The helical wake vortex structure is laterally squashed and vertically stretched by walls. The helical vortex shedding frequency is dependent on the momentum thickness around the tail carriage, which in turn varies between test cases. In asymmetrical wall cases a lower Strouhal number is associated with a lower maximum velocity due to the changes to the helical vortex structure.

(i) Three different methodologies have been used for calculating a characteristic gust comparing the maximum velocities in different confined spaces. Each methodology may be used for assessing risks caused by gust loads. One of the methodologies follows requirements in the 'TSI' codes of practice as closely as possible. Due to the different levels of peak gust attenuation which are caused by the low-pass filters inherent to the methodologies, the characteristic gust magnitude varies significantly. Filter design is therefore a crucial consideration when carrying out such assessments. Moreover, for some test cases the characteristic gusts are very similar, but a 'return period' parameter based on the regularity of limit exceedence has revealed significant differences between them.

Chapter 6

Conclusions and further work

The main aim of this research was to describe how changing the geometry of confining structures affects the flow patterns and engineering loads caused by transient velocity and pressure changes induced by passing high-speed trains. This section includes an explanation of what has been done to address the aim and each objective stated in Section 1.4, and recommends further work.

6.1 Conclusions

Objective 1: Develop a test methodology for undertaking TRAIN Rig moving model experiments and measuring the slipstream velocity and static pressure. The methodology should conform to codes of practice where their requirements do not inhibit the ability of the study to meet the other objectives.

The Methodology is described in Chapter 3. A combination of well-established and novel approaches were adopted in order to accurately and reliably measure the slipstream velocity and static pressure transient in a way which might reflect the true aerodynamic behaviour of a high-speed train operating at full-scale:

- A 1/25 scale train model was commissioned (Section 3.2), in the shape of an ICE2. The essential geometric features of the ICE2 train were included in the model. The

model also matched geometries adopted in past studies so that a reliable comparison study could be undertaken.

- Airflow measurement sensors were selected which met the following requirements: the ability to measure three components of slipstream velocity and the static pressure in the air around the train (TFI Cobra probes, Section 3.4.1), and static pressure on structure surfaces (pressure tappings and Sensortechnics HCLA-series pressure transducers, Section 3.4.2); a sufficiently high frequency response to capture the essential flow structures; a form which caused negligible disruption to the flow; and a low level of measurement uncertainty which was quantifiable (Appendix A2).
- An appropriate test speed of 32m/s was selected (Section 3.7). The factors which were accounted for included: the Reynolds number, which needed to be sufficiently high to ensure that the flow structures were representative of the full-scale ICE2 in operation; the sensors, which measured a finite number of data points at their maximum frequency as they were passed by the train; the number of possible tests, which reduced as the speed increased due to wear on the TRAIN rig; and finally the speed chosen in past studies so that a reliable comparison study could be undertaken.
- A speed measurement system was installed (Section 3.4.3) which was capable of measuring the train speed past the sensors to a high level of accuracy, and enabling the assessment of the speed measurement uncertainty. It featured light gates stationed at the beginning and end of the test section.
- The tests were repeated a suitable number of times (Section 3.8), in order to measure the ‘ensemble average’ slipstream velocity accurately, and the ensemble average static pressure accurately. The uncertainty of the ensemble average was quantified in Appendix A2.4.

- The data processing technique used a combination of well-established methods from past literature, and original solutions, to solve issues related to the chosen sensors and test method. Ensemble analysis was undertaken in order to obtain time histories of the ensemble average velocity, pressure, and the turbulent component of velocity (Section 3.8). An additional algorithm was created in order to ensure that the time history data from different test repeats were aligned to each other. The chosen low-pass filters (Section 3.9) ensured that the data time histories were presented as smoothly as possible without causing excessive attenuation of important flow peaks. This meant introducing a peak scaling factor.

- The level of conformance of the methodology to requirements in codes of practice was assessed (Section 3.11). Most of the requirements in EN 14067-4 and EN 14067-5 (BSI, 2005; BSI, 2006) were met, but some important requirements in TSI (2008) could not be met, due to its insistence on the use of full-scale tests.

Objective 2: Undertake moving-model experiments in the open air, in order to validate the results against existing data, check the reliability of the methodology, and provide open air reference data against which to compare data for confined spaces.

The first part of this objective requires that the results are compared with existing data to validate the methodology. The findings were as follows:

- Static pressure: Section 4.1 concluded that because the open air peak-to-peak pressure matches full-scale measurements, the methodology for static pressure measurement is acceptable in relation to previous accepted methodologies for open air operation. However, it could not be proven that the results in confined spaces were analogous to results from full-scale tests. Moreover, the superimposition effect of pressure waves in tunnels on the maximum pressures meant that the results were not scalable because the

essential Mach number parameter did not match the full-scale operational value. This was taken into account throughout the discussion of static pressure results in Chapter 4. The findings of the comparison study were not deemed to hinder the ability of the thesis to meet the aim and objectives 4 and 5; the discussion focused on comparative rather than quantitative debate. The flow physics captured in the experiments are likely to be correct based on a comparison of pressure loading patterns.

- Slipstream velocity: From a study in Section 5.1, the level of accuracy of the velocity results from this study at low-height positions is deemed to be acceptable for the upstream and nose region and the boundary layer region, but inconclusive in the wake region. The level of accuracy for mid-height positions is deemed to be acceptable for the boundary layer and wake regions, and also in the upstream and nose region in certain cases. The level of accuracy is acceptable for the aim and objectives 4 and 5 to be met (they focus on comparative rather than quantitative debate), as the flow physics captured in the experiments are likely to be correct.

The second part of the objective requires that the reliability of the methodology is assured. This was done in Appendix A4. Open air experiments were repeated once, and difference between the results was found to be insignificant. Double measurements were taken of the flow in a single open air experiment, and the difference between the results was also found to be insignificant.

The third part of the objective requires that open air data is used as a reference case against which to compare the results for confined cases. The open air dataset has been used for this purpose. It has also been proven above to be accurate and reliable to an acceptable degree.

Objective 3: Undertake moving-model experiments on a variety of structures including single and double vertical walls, partially-enclosed tunnels, and single-track tunnels.

Moving-model tests were undertaken on many different structures. The rationale behind the geometric parameters and the positions of sensors are described in Sections 3.5 and 3.6. The bases of the test cases are explained:

- The least confined case was the open air (OA), which was designed to meet the requirement of Objective 2;
- A vertical wall was installed with a height of z/Z=1.79 and a length of L/Z=51. The lateral separation of the 'Single Wall' from the tracks was changed, so that Y_{wall}/Z=0.84 (W1S), Y_{wall}/Z=0.71 (W2S), and Y_{wall}/Z=0.58 (W3S);
- An additional wall was placed on the opposite side of the track to form a 'Double wall' case. The separations of the 'Double Walls' from the tracks were changed (W1D, W2D, W3D). The right wall positions matched those of the single walls. The left wall positions matched those of the single walls in cases W1D and W2D, making these two cases symmetrical about the z-axis. However case W3D was asymmetrical because the left wall was placed further away at Y_{wall}/Z=0.84 while the right wall was placed at Y_{wall}/Z=0.58.
- An enclosed 'tunnel' was created by placing a ceiling over 'Double Walls' case W1D (T2, T3, T4). Tunnel T2 was the same length as the wall cases (L/Z=51). Tunnel T3 was shorter at L/Z=13, and T4 was the shortest at L/Z=5. A longer tunnel was tested (T1) with L/Z=147, and its cross-section was circular because it was an existing structure at the TRAIN Rig. The blockage ratio was β=0.23 in all cases.
- 'Partially-enclosed tunnels' were formed by one or more openings which ran along the lengths of various tunnels. The widths of the openings were changed to control the opening ratio (α). For T2 (β=0.3), the opening ratios are $\alpha\approx$0.4% and α=1%. For T3

(β=0.23), the opening ratios are α=0.2%, 0.4%, 1.4% and 4.3%. For T2 (β=0.23), the opening ratio is α≈0.4%.

- The tunnel ceiling was lowered to Z_{ceil}/Z=1.36 in order to raise the blockage ratio, for T2 (α≈0.4%) and T3 (α≈0.4%).

Up to six TFI Cobra probes were installed in the air around the train for each test case. Up to eleven pressure tappings were installed on the surfaces of structures. The effect of varying the positions of the sensors in three dimensions was tested. The positions of the sensors in each test case are described in Section 3.6.

Objective 4: Describe how changing the structure geometry, including the surfaces of the confined spaces and the positions of sensors, affects the flow patterns, maximum gusts and pressure fluctuations.

The static pressure results were presented in Chapter 4. The main conclusions are:

(a) Three loading pattern types have been considered. The first type is characterised by two fluctuations occurring around the train's nose and tail. These are respectively a positive followed by a suction peak, and then a suction followed by a positive peak. This is assumed in the literature to occur in the open air and on surfaces such as walls. The second type is characterised by: increased peak pressure magnitudes and durations caused by compression and expansion waves propagating from the tunnel entrance and exit portals; a region of suction or zero-pressure between the train's nose and tail; and an oscillatory 'pressure wave' pattern superimposed onto the underlying data which also affects peak load magnitudes and durations. This is assumed in the literature to occur in tunnels (longer than 20m at full-scale). The third type is characterised only by a positive peak around the train's nose, and a suction peak around the train's tail. This is assumed in the literature to occur in partially-enclosed tunnels.

(b) The tunnel loading pattern is altered in a number of ways by geometric parameters. The loading pattern is most strongly affected by: the position of the sensor; the tunnel's length; and the train speed. All of these factors control the time taken for the compression and expansion waves to reach the sensor from the entrance and exit portals, as well as the frequency of the oscillatory pressure wave pattern. The peak suction pressure decays towards atmospheric conditions between the train's nose and tail if the tunnel is shorter than the train.

(c) It is possible to transition between all three loading pattern types by varying the opening ratio in partially-enclosed tunnels. The opening ratio describes a continuous opening in a tunnel that allows pressure discontinuities to dissipate at a rate controlled by the size of the opening. As the opening ratio increases from α=0% to 0.4%, the oscillatory 'pressure wave' pattern disappears due to dissipation. As the opening ratio increases further to 4.3%, the loading pattern transitions from its second to its third state. The position of the sensor and the length of the tunnel have less of an effect on the results as the opening ratio increases. Further increases of the opening ratio cause the loading pattern to transition to the first state. The relationship between the maximum pressure and opening ratio depends on both the opening ratio and blockage ratio (β) - this is supported by an analytical prediction model.

(d) In-flow pressure measurements were made by Cobra probes positioned in the air gap between the train and a vertical wall. The peak-to-peak pressure decays according to a power law with an exponent of -1.2 in the open air, and -0.6 in wall cases. The wall surface pressure is twice that which would be experienced at the equivalent position in the open air. Moreover, the wall surface pressure measurements fit the decay relationships closely. However, significant differences occur between in-flow and

surface pressure measurements in tunnels and partially-enclosed tunnels. These differences increase with growing tunnel length and distance of the sensor from the entrance portal, and also with reducing opening ratio.

(e) Peak-to-peak pressure loads over characteristic durations have been calculated in order to test the effects that the different structure types and geometric variations have on engineering fatigue loads. Three characteristic durations between 0.2s and 1s (full-scale equivalent) have been tested using moving windows with widths corresponding to the required durations. Some of the tunnels and partially-enclosed tunnels which previously caused the highest peak-to-peak pressures are found to cause very low loads over short characteristic durations. This is because the size of the window is smaller than that required to envelop both the positive and suction peaks, so the worst case pressure change is missed. By contrast, the worst-case pressure changes lie within the envelopes in wall cases.

The slipstream velocity results were presented in Chapter 5. The main conclusions are:

(a) Vertical walls were added to both sides of the tracks in a symmetrical arrangement, and the changes relative to the open air have been assessed for two wall separations. The maximum velocity around the train's nose increases, although the measurements around the nose may not be reliable. The boundary layer grows at a faster rate but reaches the same thickness. The velocity profile remains logarithmic. In the wake region, the helical vortex structure appears to be laterally squashed and vertically stretched by the wall, causing higher velocities to be detected, and at higher positions. Most of the maximum velocities occur in the wake region, and they are higher at all positions. The longitudinal velocity increases more than the lateral and vertical velocities due to the increased peak-to-peak pressure and pressure load duration

around the train's tail. The lateral velocity decays close to the wall due to its obstruction. The velocity in the far-wake decays more slowly, often causing the gust duration to be extended. The rate of decay may be most accurately modelled using a power law function.

(b) When the vertical wall opposite the sensors is moved close to the train's side (an asymmetrical configuration), the ensemble average and maximum velocities decrease relative to the symmetrical configuration. A reduction in the Strouhal number suggests that the helical vortex flow structure is disrupted by the asymmetry, which may explain the decrease in maximum velocity.

(c) Ceilings have been added to vertical walls to create tunnels, and the differences compared to the walls have been assessed. The nose-entry compression wave causes a small fluctuation in the velocity time history. The longitudinal velocity increases upstream of the train's nose due to the 'piston effect' - the compression of air ahead of the train's nose which induces a flow towards the tunnel's exit. The magnitude of the peak piston-induced velocity is dependent on the tunnel's length and cross-sectional area. The piston effect also increases the longitudinal velocity in the near-wake, and therefore the maximum gust magnitudes, due to expansion of air behind the train's tail. It also reduces the rate of decay of the velocity, which extends the durations of the maximum gusts as well as the time taken for the air to return to ambient conditions, affecting the ventilation characteristics of tunnels. The sinusoidal pressure oscillations caused by 'pressure waves' - compression and expansion waves travelling along the longitudinal axis at the speed of sound and reflecting from the tunnel's entrance and exit portals - do not cause detectable velocity fluctuations over the same frequency range. In tunnels the boundary layer follows a logarithmic profile as with wall cases,

but it is thinner. This may be due to pressure gradients around the train's nose and tail which resist its growth and reduce its thickness around the first and last carriages respectively.

(d) The length of a tunnel has been changed. As the length decreases, all of the results tend towards those of the vertical wall cases, due mostly to a change in the longitudinal velocity which is strongly correlated with the piston effect around the train's tail, which is related to the combined tunnel length and position of the sensor. The results should be associated with sensor position divided by the tunnel length.

(e) The blockage ratio of the tunnel has been increased for some of the tunnel cases. A pressure-driven piston effect induces a steady wind in the tunnel, which is dependent on blockage ratio. The steady wind superimposes with the velocity fluctuation upstream of the train's nose and downstream of the tail. The latter superimposition causes the maximum wake velocity to increase relative to lower blockage ratio tunnels.

(f) Small openings have been made in tunnels to create partially-enclosed tunnels, and the results have been compared with those for enclosed tunnels. The maximum velocity increases at all sensor positions. The peak longitudinal velocity increases compared to enclosed tunnels. High velocities also occur in the direction of the opening in the wake region when the pressure rises inside the structure. In the wake region a pressure fluctuation around the train's tail induces a vertical velocity peak (caused by flow exiting through the opening). The peak vertical flow superimposes with the peak wake velocity, thereby increasing the maximum velocity relative to enclosed tunnels.

(g) As the above points have shown, there are some common flow changes seen in all confined cases relative to the open air. A near-one-dimensional velocity peak has been

identified as correlating strongly with various measures of pressure fluctuations, particularly the peak-to-peak pressure directly around the train's tail. Relationships have been derived from which it is possible to predict the maximum velocity, generally based on pressure measurements alone. The helical wake vortex structure is laterally squashed and vertically stretched by walls. The helical vortex shedding frequency is dependent on the momentum thickness around the tail carriage, which in turn varies between test cases. In asymmetrical wall cases a lower Strouhal number is associated with a lower maximum velocity due to the changes to the helical vortex structure.

Objective 5: Comment on how the observations in Objective 4 challenge the validity of the guidance in codes of practice.

Static pressure: When peak-to-peak pressure loads for some qualifying test cases were compared with predictive formulae from codes of practice, the results for single vertical walls and a short tunnel were found to be significantly lower than predictions. Even the loads for double wall configurations, which produced higher pressures than single walls, were lower than predictions. In the short tunnels, the method for calculating pressures failed to account for the increased load duration associated with the second loading pattern type. Had this been accounted for, the loads would be much higher and closer to the limits (and more relevant to operational conditions).

Velocity: Three different methodologies have been used for calculating a characteristic gust for comparing the maximum velocities in different confined spaces. Each methodology may be used for assessing risks caused by gust loads. One of the methodologies follows requirements in the 'TSI' codes of practice as closely as possible. Due to the different levels of peak gust attenuation which are caused by the low-pass filters inherent to the

methodologies, the characteristic gust magnitude varies significantly. Filter design is therefore a crucial consideration when carrying out such assessments. Moreover, for some test cases the characteristic gusts are very similar, but a 'return period' parameter based on the regularity of limit exceedence has revealed significant differences between them.

Objective 6: Provide a dataset of experimental data for third party use, which may for example be used as a benchmark for prediction models or CFD simulations.

A collection of electronic files is available which provides the experimental data, and a database for data searching. These are described in full in Appendix B.

In conclusion, the six main objectives have been fulfilled to a sufficient standard to meet the aim of this thesis.

6.2 Recommendations for further work

(a) This PhD research has focused on the effect of infrastructure changes on the aerodynamic characteristics of one type of high-speed train. Further work should be undertaken to test whether the same conclusions may be reached when trains with different aerodynamic shapes are tested, including more modern and streamlined rolling stock, and aerodynamically rough trains.

(b) More tests are needed in order to verify whether these conclusions are valid when geometric variables are changed beyond the ranges used in this study. In particular, no testing was undertaken for partially-enclosed tunnels over the range of opening ratios α=4.3% to 24% (wall case). Further testing would reveal at what point the maximum slipstream velocity stops increasing and begins to decrease towards the values seen in

the wall test cases, and how the pressure loading pattern will transition into the 'open air and walls' shape. It was not possible to assess the effect of changing the blockage ratio on the results without other variables affecting the results. However, the effect of changing blockage ratio on the maximum pressure is already well established in the literature. More work is needed in order to find out how changing the blockage ratio affects the variation of maximum pressure with opening ratio. Such work would potentially link this research with existing theoretical and experimental research into partially-enclosed tunnels and train stations. More work is also needed in order to verify whether the same flow patterns occur in tunnels with asymmetrical cross-sections, such as double-track tunnels, and tunnels with different cross-sectional shapes.

(c) In this work, the majority of the sensors were sited at the end of a long 'fetch', allowing flow structures to stabilise inside the structures. Work by Straathof (2013) and Gilbert and Straathof (2013) found that flow structures changed dramatically in proximity to the entrance and exit of a tunnel. For example, a back-flow occurs close to the tunnel entrance, and a 'galloping' of the wake occurs near the tunnel exit, which the former study identified as a factor causing unacceptable wind velocities in underground station platforms. The CFD technique was particularly useful in identifying the flow structures. More work is needed in which many sensors are sited close to the structure entrance and exit, in order to build a more complete understanding of how the flow phenomena evolve throughout a structure.

(d) The conclusions are based on entire ensembles of data (the ensemble average and the ensemble standard deviation), and statistical measures. There is an opportunity to

further test the validity of these conclusions by visually inspecting individual ensemble runs.

(e) Further work is needed in order to establish whether revisions are needed to codes of practice in light of the findings in this study. This study has drawn some conclusions regarding the ability of codes of practice to predict aerodynamic effects in test structures which fall within their remit. Therefore, further work could examine the potential for codes of practice to extend the range of geometric variables which fall within their scope.

References

Adami, S. and Kaltenbach, H.J. (2008). Sensitivity of the wave-steepening in railway tunnels with respect to the friction model. BBAA VI International colloquium on Bluff bodies aerodynamics and applications, Milan, Italy, 20-24 July.

Arup (2012). High Speed 2 London to West Midlands: Chilterns Long Tunnel Options Review. Retrieved July 6, 2012, from http://bit.ly/15jRpgm.

Arup (2010). Route Engineering Study Final Report: A Report for HS2 (Report reference HS2-ARP-00-RP-CX-00003-ISSUE-2-FEBRUARY 26.2010).

Baker, C., Quinn, A., Sima, M., Hoefener, L. and Licciardello, R. (2013a). Full-scale measurement and analysis of train slipstreams and wakes: Part 1 Ensemble averages. Proceedings of the Institution of Mechanical Engineers Part F: Journal of Rail and Rapid Transit. Advance online publication. doi: 10.1177/0954409713485944.

Baker, C., Quinn, A., Sima, M., Hoefener, L. and Licciardello, R. (2013b). Full-scale measurement and analysis of train slipstreams and wakes: Part 2 Gust analysis. Proceedings of the Institution of Mechanical Engineers Part F: Journal of Rail and Rapid Transit. Advance online publication. doi: 10.1177/0954409713488098.

Baker, C., Jordan, S., Gilbert, T., Quinn, A., Sterling, M. Johnson, T. and Lane, J. (2012). Transient aerodynamic pressures and forces on trackside and overhead structures due to passing trains. Part 1 model scale experiments Part 2 standards applications. Proceedings of the Institution of Mechanical Engineers Part F: Journal of Rail and Rapid Transit. Advance online publication. doi: 10.1177/0954409712464859.

Baker, C.J. (2010). The flow around high speed trains. Journal of Wind Engineering and Industrial Aerodynamics, 98, 277-298.

Baker, C. (2001). Flow and dispersion in ground vehicle wakes. Journal of Fluids and Structures, 15, 1031-1060.

Baker, C.J., Dalley, S.J., Johnson, T., Quinn, A. and Wright, N.G. (2001). The slipstream and wake of a high-speed train. Proceedings of the Institution of Mechanical Engineers Part F: Journal of Rail and Rapid Transit, 215, 83-99.

Barrow, H. and Pope, C.W. (1987). A simple analysis of flow and heat transfer in railway tunnels. International Journal of Heat and Fluid Flow, 8(2), 119-123.

Bell, J. Burton, D., Thompson, M., Sheridan, J. and Herbst, A. (2013). Wind tunnel analysis of the slipstream of high-speed trains. International Workshop on Train Aerodynamics, Birmingham, UK, April 8-10.

Brockie, N.J.W. and Baker, C.J. (1990). The aerodynamic drag of high speed trains. Journal of Wind Engineering and Industrial Aerodynamics, 34, 273-290.

BSI (2006). BS EN 14067-5-2006 +A1:2010. Railway applications - Aerodynamics - Part 1: Requirements and test procedures for aerodynamics in tunnels.

BSI (2005). BS EN 14067-4:2005 +A1:2009. Railway applications - Aerodynamics - Part 4: Requirements and test procedures for aerodynamics on open track.

BSI (2003). BS EN 14067-3:2003. Railway applications - Aerodynamics - Part 3: Aerodynamics in tunnels.

Busslinger, A., Hagenah, B., Reinke, P. and Rudin, C. (2009). Aerodynamics and climate in the Loetschberg base tunnel - prediction and findings. ITA-AITES World Tunnelling Congress, Budapest, Hungary, 23-28 May.

Del Valle, N. (2012). Measurement and analysis of slipstreams for passenger trains. Doctoral thesis, University of Birmingham, Birmingham.

Department for Transport (2012). High Speed Rail: Investing in Britain's Future - Decisions and Next Steps (Cm 8247). London: The Stationery Office.

Deutsche Bahn (2003). Eisenbahntunnel planen, bauen und instand halten. Regelwerk D853, August 2003.

Diedrichs, B., Berg, M. and Krajnovic, S. (2004). Large eddy simulations of a typical European high-speed train inside tunnels. SAE Technical Paper 2004-01-0229.

Dorigatti, F. (2013). Rail vehicles in crosswinds: analysis of steady and unsteady aerodynamic effects through static and moving-model tests. Doctoral thesis, University of Birmingham, Birmingham.

ERRI (1994). Loading due to dynamic pressure and suction from railway traffic. Effect of the slipstreams of passing trains adjacent to the track. Report ERRI D189/RP1.

EUK (1999). GUV-V D 33: Arbeiten im Bereich von Gleisen.

Friedl, H., Kari, H., Reiterer, M. and Handel, C. (2011). Fatigue tests on noise barrier walls. Rail Technology Review, 2, 2-7.

Gawthorpe, R. (1978). Aerodynamics of trains in the open air. Railway Engineering International, 3(3), 7-20.

Gilbert, T., Baker, C. and Quinn, A. (2013a). Aerodynamic pressures around high-speed trains: the transition from unconfined to enclosed spaces. Proceedings of the Institution of Mechanical Engineers Part F: Journal of Rail and Rapid Transit. Advance online publication. doi: 10.1177/0954409713494947.

Gilbert, T., Baker, C. and Quinn, A. (2013b). Gusts caused by high-speed trains in confined spaces and tunnels. Journal of Wind Engineering and Industrial Aerodynamics, 121, 39-48.

Gilbert, T., Baker, C. and Quinn, A. (2013c). Aerodynamic effects of high speed trains in confined spaces. International Workshop on Train Aerodynamics, Birmingham, UK, April 8-10.

Gilbert, T. and Straathof, J. (2013). The effects of confinement on high-speed train wakes. Sixth European and African Conference on Wind Engineering, Nottingham, UK, 7-9 July.

Gilbert, T. (2012). The flow around high-speed trains in partially-enclosed spaces. 10th UK Conference on Wind Engineering, Southampton, UK, 10-12 September.

Gilbert, T., Baker, C., Quinn, A and Sterling, M. (2012). Aerodynamics of high-speed trains in confined spaces. 7th International Colloquium on Bluff Body Aerodynamics and Applications (BBAA7), Shanghai, China, 2-6 September.

Greisinger Electronic (2011). GPB3300 Product Information. Retrieved July 11, 2012, from http://bit.ly/1dMzIIz.

Hemida, H., Baker, C. and Gao, G. (2012) The calculation of train slipstreams using Large-Eddy Simulation. Proceedings of the Institution of Mechanical Engineers Part F: Journal of Rail and Rapid Transit. Advance online publication. doi: 10.1177/0954409712460982.

Hemida, H., Gil, N. and Baker, C. (2010). LES of the slipstream of a rotating train. Journal of Fluids Engineering, 132, 051103, 1-9.

Howe, M.S., Iida, M., Fukuda, T. and Maeda, T. (2000). Theoretical and experimental investigation of the compression wave generated by a train entering a tunnel with a flared portal. Journal of Fluid Mechanics, 425, 111-132.

Howe, M.S. (1998). The compression wave produced by a high-speed train entering a tunnel. Proceedings of the Royal Society of London A, 454, 1523-1534.

Iida, M. Kikuchi, K., Takei, Y. and Izumi, Y. (2005). Steady pressure field around a train running in a vented tube (in Japanese). Collection of papers, Fluids Engineering Division, the Japan Society of Mechanical Engineers.

Johnson, T. (2012). Micro-pressure waves. RSSB Aerodynamics position paper. Issue 2: 10 September 2012.

Johnson, T. and Dalley, S. (2002). 1/25th scale moving model tests for the TRANSAERO project. Notes on Numerical Fluid Mechanics 79 (pp. 123-135). Berlin: Springer-Verlag.

Jordan, S., Sterling, M. and Baker, C. (2009). Modelling the response of a standing person to the slipstream generated by a passenger train. Proceedings of the Institution of Mechanical Engineers Part F: Journal of Rail and Rapid Transit, 223, 567-579.

Muld, T. (2012). Slipstream and flow structures in the near-wake of high-speed trains. Doctoral thesis, Royal Institute of Technology, Sweden.

Muraki, K., Iwasaki, K., Hoshikawa, T., Oikawa, J., Haraguchi, K. and Hayashi, A. (2010). Effect of train draft on platforms and in station houses. JR East Technical Review, 16, 39-42.

Oregon Scientific (2009). Manual for WMR200 Professional Weather Station. Retrieved August 7, 2012, from http://bit.ly/16OBGUV.

Quinn, A. Baker, C., Sterling, M., Sima, M., Weise, M., Hoefener, L. and Eisenlauer, M. (2011). The effect of crosswinds on the slipstreams of high speed trains. 11th International Conference on Wind Engineering, Amsterdam, The Netherlands, July 10-15.

Quinn, A., Baker, C.J., and Wright, N.G. (2001). Wind and vehicle induced forces on flat plates - Part 2: vehicle induced force. Journal of Wind Engineering and Industrial Aerodynamics, 89, 831-847.

Raghunathan, R., Kim, H.-D. and Setoguchi, T. (2002). Aerodynamics of high-speed railway train. Progress in Aerospace Sciences, 38, 469-514.

Reiterer, M. and Altay, O. (2009). Austrian approach for dynamical analysis of noise barriers. PowerPoint presentation, RED Bernard, Arsenal Research and OBB. Version 04.09.2009.

Rowe, A., Fry, A.L.A., and Motallebi, F. (2000). Influence of boundary layer thickness on base pressure and vortex shedding frequency. AIAA Journal, 39(4), 754-756.

RSSB (2011). Handbook 1: General duties and track safety for track workers. GE/RT8000/HB1 Issue 2.

Sakuma, Y., Suzuki, M., Ido, A. and Kajiyama, H., (2010). Measurement of air velocity and pressure distributions around high-speed trains on board and on the ground. Journal of Mechanical Systems for Transportation and Logistics, 3(1), 110-118.

Sanz-Andrés, A., Santiago-Prowald, J., Baker, C.J. and Quinn, A. (2003). Vehicle-induced loads on traffic sign panels. Journal of Wind Engineering and Industrial Aerodynamics, 91(7), 925-942.

Schlichting, H. (1979). Boundary layer theory. 7th Ed. Translated from German by Dr. J. Kestin. London: McGraw Hill.

Schultz, M. (1990). Experimentelle und rechnerische Ermittlung von Druckwellenausbreitungsvorgängen bei der Fahrt eines Zuges durch einen kurzen Tunnel. Unterschung des Einflusses der instationären Wandreibung auf die Wellendämpfung. Doctoral thesis, Vienna University of Technology, Vienna.

Schultz, M. and Sockel, H. (1991). Pressure transients in short tunnels. In: Proceedings of the 7th International Symposium on the Aerodynamics and Ventilation of Vehicle Tunnels, Brighton, UK, 221-237.

Sensortechnics (2013a). HCLA. Retrieved January 3, 2013, from http://bit.ly/19KZUAw.

Sensortechnics (2013b). Glossary 'Pressure sensing'. Retrieved January 3, 2013, from http://bit.ly/15ufW0P.

Sensortechnics (2010). PDF datasheet: HCLA Series Miniature amplified low pressure sensors. Retrieved July 4, 2011, from http://bit.ly/15ufZtD.

Sima, M., Grappein, E., Weise, M., Paradot, N., Hieke, M., Baker, C., Licciardello, R. and Couturier, M. (2011). Presentation of the EU FP7 AeroTRAIN project and first results. 9th World Congress on Railway Research, Lille, France, May 22-26.

Sockel, H. (2003). Formulae for the calculation of pressure effects in railway tunnels. Proceedings of the 11th International Symposium on the Aerodynamics and Ventilation of Vehicle Tunnels, Luzern, Switzerland, 7-9 July.

Sterling, M., Baker, C.J., Jordan, S.C. and Johnson, T. (2008). A study of the slipstreams of high-speed passenger trains and freight trains. Proceedings of the Institution of Mechanical Engineers Part F: Journal of Rail and Rapid Transit, 222, 177-193.

Straathof, J. (2013). Wind comfort at underground railroad platforms. Master's thesis, Eindhoven University of Technology, Eindhoven.

Suzuki, M., Ido, A., Sakuma, Y. and Kajiyama, H. (2008). Full-scale measurement and numerical simulation of flow around high-speed train in tunnel. Journal of Mechanical Systems for Transportation and Logistics, 1(3), 281-292.

Takei, Y., Izumi, Y., Yamada, S., Iida, M. and Kikuchi K. (2008). Evaluation method for air pressure variation and station facility member deterioration caused by high-speed train passage in stations. QR of RTRI 2008, 49(2), 89-95.

Temple, J. and Dalley, S. (2001). RAPIDE Project: Analysis of the slipstream data (AEA Technology Rail Report number AEATR-T&S-2001-197).

TFI (2007). Cobra probe. Retrieved May 1, 2011, from http://bit.ly/17d6uBk.

TFI (n.d.). Cobra probe. Retrieved February 3, 2013, from http://bit.ly/1dMBcCw.

TSI Incorporated (2013). Manual Velocity Calibrator with Pressure Transducer 1128. Retrieved August 8, 2013, from http://bit.ly/182i0fn.

TSI (2008). 2008/232/EC: EU Technical Specification for Interoperability Relating to the 'Rolling Stock' Sub-System of the Trans-European High-Speed Rail System.

Vardy (1996). Aerodynamic drag on trains in tunnels. Part 2: prediction and validation. Proceedings of the Institution of Mechanical Engineers Part F: Journal of Rail and Rapid Transit, 210(1), 39-49.

Appendix A

Uncertainty analysis

Contents

A1. Introduction

This uncertainty analysis report is divided into five sections. In Section A2, the quantifiable uncertainty is assessed. In Section A3, some erroneous data is analysed, and its deletion is justified where appropriate. In Section A4, the decision on whether to merge datasets from repeated experiments is discussed. In Section 0, the decision on whether to merge datasets from similarly positioned sensors is discussed. In Section 0, the decision on whether to merge datasets from similar test cases is discussed.

A2. Estimating uncertainty

A2.1. Uncertainty of train speed measurement

The train's speed past sensors was interpolated from the readings of two interface units. The units processed data from light gates installed at the entrance and exit of the test section. The 'indicated speed' provided by the interface units was unreliable, because the interface units intermittently (and erroneously) indicated that the train was accelerating. The light gate data was recorded to a data logger for use in uncertainty analysis.

To estimate the uncertainty, the speed has been calculated manually for every run in the dataset (294 runs), and compared with the speeds given by the interface units ($V_{0,run}$). In order to manually calculate the speed, the sample numbers of rising or falling edges in the light gate time histories must be known (n_a, n_b), as well as the corresponding separation distance (l_{ab}) and measuring frequency (f). Figure A - 1 shows an example time history, with rising and falling edges represented as 'on' and 'off' events.

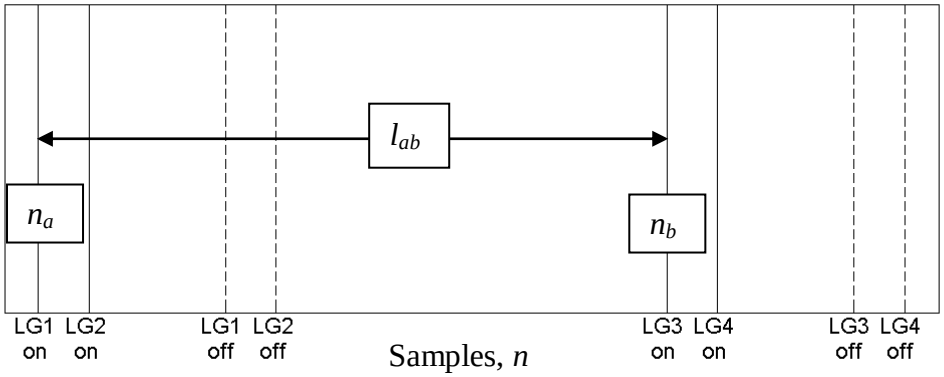

Figure A - 1: Time history of light gate states.

An uncertainty term has been calculated for each run ($V_{e,run}$) by dividing the manually calculated speed with the indicated speed:

$$V_{e,run} = \left(\frac{l_{ab} f}{(n_b - n_a)} \Big/ V_{0,run} \right) - 1$$

$V_{e,run}$ should ideally equal zero for there to be no systematic error. The mean ($\overline{V_e}$) and the standard deviation $\sigma(V_e)$ of $V_{e,run}$ for all runs are calculated.

$$\overline{V_e} = \frac{1}{294} \sum_{run=1}^{294} V_{e,run}\,, \qquad \sigma(\mathrm{V_e}) = \sqrt{\frac{1}{294} \sum_{run=1}^{294} \left(V_{e,run} - \overline{V_{e,run}}\right)^2}$$

Twelve different methods have been considered for combining two ‘on’ (rising edge) or two ‘off’ (falling edge) events, one of which is demonstrated in Figure A - 1. Table A - 1 shows the uncertainty parameters for twelve manual speed estimation methods, and their overall mean values.

Table A - 1: List of methods for assessing train speed measurement uncertanty.

Method	1st light gate	2nd light gate	On/off	l_{ab} (mm)	Train speed	$\bar{v}_e$ (%)	$\sigma(V_e)$(%)	Skewness
1	LG1	LG2	On	1000	$V_{0,lg1lg2}$	-0.02	0.10	-1.95
2	LG1	LG2	Off	1000	$V_{0,lg1lg2}$	-1.78	1.39	-0.10
3	LG1	LG3	On	9125	$\frac{V_{0,lg1lg2}+V_{0,lg3lg4}}{2}$	-0.35	0.47	-0.90
4	LG1	LG3	Off	9125	$\frac{V_{0,lg1lg2}+V_{0,lg3lg4}}{2}$	-0.87	0.55	-0.69
5	LG1	LG4	On	10125	$\frac{V_{0,lg1lg2}+V_{0,lg3lg4}}{2}$	-0.44	0.47	-0.89
6	LG1	LG4	Off	10125	$\frac{V_{0,lg1lg2}+V_{0,lg3lg4}}{2}$	-1.00	0.51	-0.76
7	LG2	LG3	On	8125	$\frac{V_{0,lg1lg2}+V_{0,lg3lg4}}{2}$	-0.53	0.57	-0.70
8	LG2	LG3	Off	8125	$\frac{V_{0,lg1lg2}+V_{0,lg3lg4}}{2}$	-0.90	0.50	-0.83
9	LG2	LG4	On	9125	$\frac{V_{0,lg1lg2}+V_{0,lg3lg4}}{2}$	-0.61	0.56	-0.71
10	LG2	LG4	Off	9125	$\frac{V_{0,lg1lg2}+V_{0,lg3lg4}}{2}$	-1.04	0.47	-0.90
11	LG3	LG4	On	1000	$V_{0,lg3lg4}$	-0.10	0.28	-1.99
12	LG3	LG4	Off	1000	$V_{0,lg3lg4}$	-1.07	0.38	-1.35
Mean:						**-0.7**	**0.53**	**-1**

The results show that the skewness is negative in most cases, suggesting that the speed interface unit was more likely to under-estimate the train speed. The systematic error is -0.7%, suggesting that an indicated speed of V_0=32m/s may be an over-prediction of around 0.22m/s. However, the systematic error cannot be taken into account, as it is impossible to find which of the indicated or manually calculated speeds is more accurate. Instead, the mean of the standard deviation ($\bar{\sigma_{V,e}}$=0.53%) will be used to quantify error. Propagation of error analysis must be used as two speed readings were used in order to calculate the interpolated train speed V_0 (Section 3.7 in main thesis):

$$V_{0,e} = \sqrt{0.0053^2 + 0.0053^2} = 0.71\%$$

A2.2. Uncertainty of the air velocity

The estimated uncertainty of the air velocity measured by the Cobra probes is estimated in this section. The manufacturer's stated uncertainty of 0.3m/s (TFI, 2007). Figure A - 2(a) shows the relationship between the resultant air velocity and the stated uncertainty. A method has been devised for obtaining a representative single value of uncertainty, by calculating the uncertainty of the maximum resultant air velocity for every run. Figure A - 2(b) is a histogram showing the statistical distribution of the uncertainties of maximum air velocities from all time histories. The reason for selecting the maximum air velocity is because only one type of analysis in the thesis is governed by rules concerning uncertainty - the analysis of maximum velocity gusts meeting some of the requirements of relevant codes of practice (TSI, 2008; BSI, 2005).

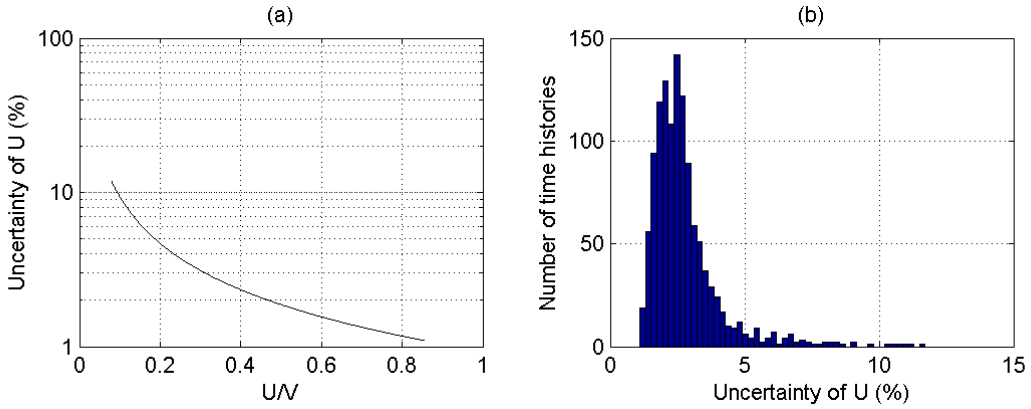

Figure A - 2: (a) Uncertainty of the air velocity; (b) Histogram of the uncertainties of the maximum velocities from all time histories.

95% of the uncertainties are less than 5.2%. This is taken to represent the uncertainty of the air velocity. Since the results are divided by train speed, the actual uncertainty is calculated using propagation of error analysis:

$$\left(\frac{U_e}{V_{0,e}}\right)_e = \sqrt{0.052^2 + 0.0071^2} = 5.2\%$$

The manufacturer states that Cobra probes cannot accurately measure velocities less than U=2m/s (TFI, 2007). The accuracy of the air velocity data below this limit has been assessed by replicating an experiment in which hot-wire anemometers were used (Baker et al., 2001), and comparing the results. The hot-wire anemometers would have been calibrated to a lower velocity limit of between 0.05m/s and 0.5m/s, depending on the type of embedded transducer that was used in the 'TSI 1128b' air jet calibrator (TSI Incorporated, 2013). The comparison is shown in Figure A - 3.

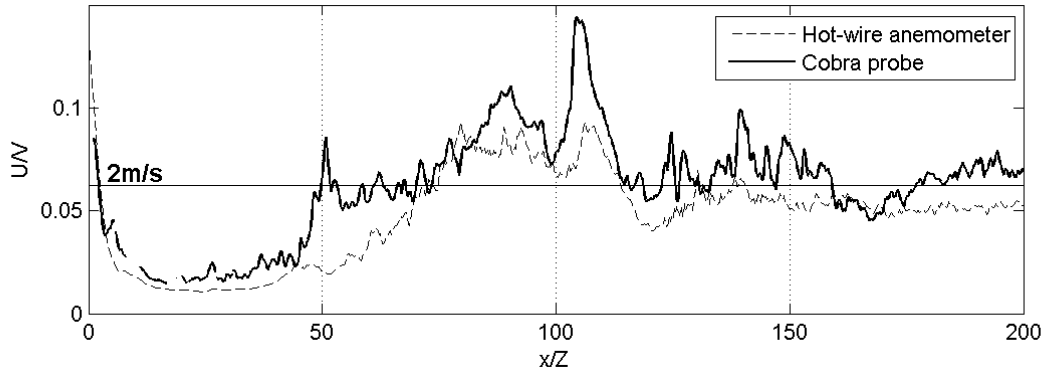

Figure A - 3: Cobra probe and hot-wire anemometer measurements of the resultant velocity close to the lower limit of the Cobra probe's accuracy.

The results show that the Cobra probe detects higher velocities than the hot-wire anemometer, although this is also the case above 2m/s. The general patterns in the data closely correspond with each other. In conclusion, the results below the limit do not need to be discarded, but they should be treated with caution.

A2.3. Uncertainty of the static pressure

Static pressure was measured by Cobra probes and pressure transducers mounted behind surface pressure tappings. The uncertainty of the static pressure is calculated in this section for each sensor. The uncertainty of the static pressure measured by the Cobra probes is unknown because manufacturer's uncertainties have not been provided. The smallest possible

error is ±0.05Pa, which corresponds to the discretisation uncertainty. However, the true uncertainty is likely to be higher than this.

The pressure transducers were calibrated extensively during the experiments reported in Dorigatti (2013), which occurred in the middle of the test program for this research. The calibration involved fitting a third degree polynomial to the data. The uncertainty can be estimated from the residuals which are shown in Figure A - 4. One value of uncertainty has been calculated for all the transducers.

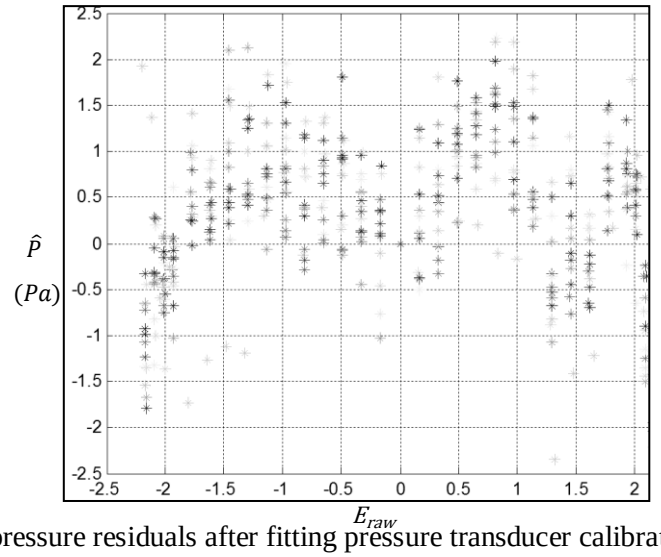

Figure A - 4: Static pressure residuals after fitting pressure transducer calibration data to a third degree polynomial function.

The standard deviation of the residuals is $\sigma(\hat{P})$=±0.75Pa. This is used as an uncertainty estimate. A method has been devised for obtaining a representative single value of uncertainty, by calculating the uncertainty of the peak-to-peak static pressure coefficient for every run. The reason for selecting this variable is because only one type of analysis in the thesis is governed by rules concerning uncertainty - the analysis of peak-to-peak static pressure coefficients in accordance with codes of practice (BSI, 2005). The uncertainty of the peak-to-peak static pressure (ΔP) is calculated using propagation of errors analysis:

$$\Delta P_e = \sqrt{0.75^2 + 0.75^2} = 1.1\text{Pa}$$

Figure A - 5(a) shows the relationship between ΔP and the uncertainty, for every run, transducer, and test case. The uncertainty of each ΔP value has been calculated and is shown in Figure A - 5(b).

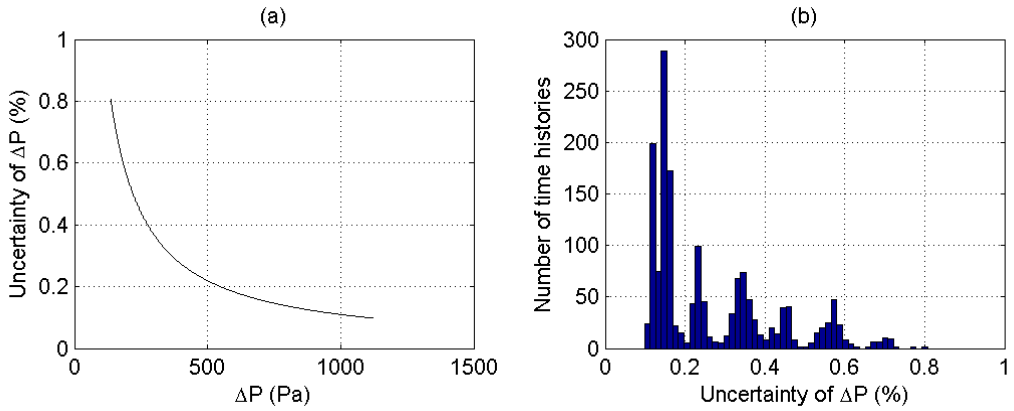

Figure A - 5: (a) Uncertainty of the peak-to-peak pressure; (b) Histogram of the uncertainty of the peak-to-peak pressure from all time histories.

95% of the uncertainties are less than 0.6%. This is taken to represent the uncertainty of ΔP. The uncertainty of the static pressure coefficient ΔC_P is obtained by dividing the static pressure by $0.5\rho_e V_{0,e}^2$. ρ_e is the uncertainty of the air density, which was calculated from the uncertainty of environmental pressure ($P_{atm,e}$) and temperature (T_e) readings. The environmental pressure was measured using a 'Greisinger Electronic GPB 3300', with a manufacturer's accuracy of 200Pa (Greisinger Electronic, 2012). This is approximately 0.2% of atmospheric pressure. The temperature was measured using an 'Oregon Scientific BAR208HG' weather station. The temperature accuracy is not stated, although other devices made by the same manufacturer, such as the WMR200 (Oregon Scientific, 2009), have accuracies of 1K. Presuming that this is the device's accuracy, the temperature uncertainty is 0.35% for a temperature of 280K. The rounded estimated uncertainty in the density is calculated using propagation of errors analysis:

$$\rho_e = \frac{P_{atm,e}}{T_e} = \sqrt{0.0035^2 + 0.002^2} = 0.4\%$$

The uncertainty of the peak-to-peak static pressure coefficient is calculated using propagation of errors analysis:

$$\Delta C_{P,e} = \left(\frac{\Delta P_e}{\rho_e V_{0,e}^2}\right)_e = \sqrt{0.006^2 + (2 \times 0.0071)^2 + 0.004^2} = 1.6\%$$

A2.4. Uncertainty of the ensemble peaks and ensemble average

The uncertainties of the ensemble peaks and ensemble averages are discussed in this section. In Section 3.8 of the main thesis, the ensemble averaging technique was defined as the averaging of flow measurements for repeated train passes. This may be either time history data or single values from each run (such as peaks). If more repeats are conducted, the true mean and variance become increasingly independent of each other and tend towards the time average mean and variance. A single value of uncertainty for the ensemble average would be practically meaningless, as it depends on the run-to-run variation of the flow variable which differs greatly at different points relative to the train in different test cases. However, a single value of uncertainty may be attributed at a specified probability level to the maximum resultant air velocity (*max(U)*) calculated by the Cobra probes, as well as the peak-to-peak static pressure coefficient (ΔC_P) measured on the surface pressure tappings by the pressure transducers.

A measure has been used to reduce the uncertainty of the ensemble average. Its uncertainty for measurements carried out by Cobra probes is increased by dropouts (defined in Section 3.4.1 of the main thesis), as they reduce the ensemble size at locations in the time histories where flow angles exceed the measuring capabilities of the Cobra probes. The ensemble size of usable data at these locations is small, making the uncertainty of the ensemble average very high. In order to reduce the uncertainty, the Cobra probe data has only been ensemble averaged at sample increments in which the number of usable data points is greater than a

specified threshold. For the air velocity the threshold is set to $N \geq 5$ points, and for the static pressure the threshold is reduced to $N \geq 3$ points, because the run-to-run variability of the static pressure coefficient is lower.

In order to estimate the uncertainty of the ensemble, the standard error of the mean has been calculated for the maximum resultant air velocity *max(U)* and peak-to-peak static pressure coefficient ΔC_P. The standard error of the mean has been calculated by dividing a standard deviation parameter $\sigma(max(U)$ or $\sigma(\Delta C_P)$ by the square root of the ensemble size (number of runs, N). The standard deviation of the maximum resultant air velocities is $\sigma(max(U))$, and the standard deviation of the peak-to-peak static pressure coefficient is $\sigma(\Delta C_P)$.

$$\left(\frac{\sigma(\max(U))}{\sqrt{N}}\right)\left(\frac{\sigma(\Delta C_P)}{\sqrt{N}}\right)$$

A Monte Carlo simulation has been undertaken on some representative data (wall case W1D) to show the dependence of the ensemble size on the standard error of the mean. A representative ensemble size of N=25 runs was selected from the data for each sensor in wall case W1D. Smaller subsets of varying ensemble sizes were formed using 500 random run combinations. The combinations were almost certainly unique for ensemble sizes of $3 \leq N \leq 47$. The uncertainty (standard deviation of the mean) was calculated for each combination. The uncertainty for each ensemble size was the average of all 500 run combinations. A curve was created which linked the ensemble size to the uncertainty for each sensor. To simplify the assessment further, the first standard deviation above the mean of the sensor-curves was calculated for the two types of data - the peak-to-peak static pressure coefficient on surface tappings measured by pressure transducers, and the maximum resultant air velocity measured by Cobra probes. This produced single curves which are shown in Figure A - 6.

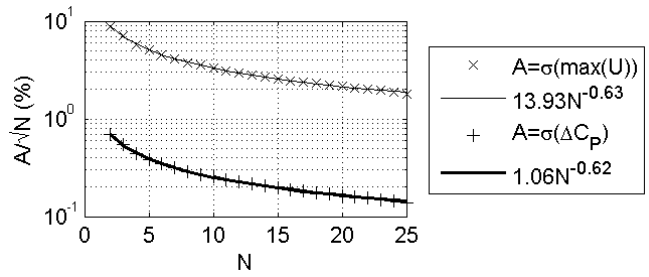

Figure A - 6: Relationship between the standard error of the mean and the number of runs, for the maximum resultant air velocity and the peak-to-peak static pressure coefficient.

The uncertainty follows an inverse-power relationship with the number of runs. The values of the coefficients and exponents of the curves have been derived, and are shown in the legend. The curves show that the uncertainty of the static pressure coefficient is an order of magnitude lower than the maximum resultant velocity, due to its much lower standard deviation. The uncertainty of every tested ensemble average has been calculated and is shown in Figure A - 7.

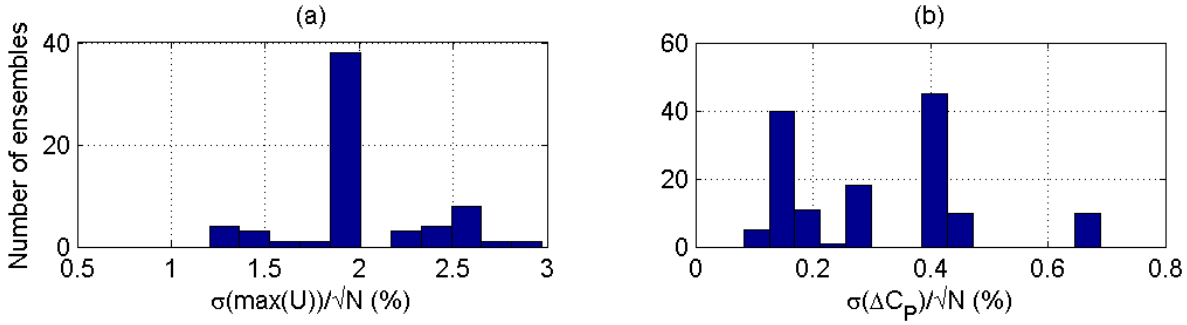

Figure A - 7: Histograms showing the standard error of the mean for all experimental ensembles: (a) the maximum resultant air velocity; (b) the peak-to-peak static pressure coefficient.

Five percent of the maximum velocity ensemble averages exceed an uncertainty of 2.6%. This is taken to represent the uncertainty of the maximum velocity. Five percent of the peak-to-peak static pressure coefficients exceed an uncertainty of 0.7%.

A2.5. Uncertainty of the 5% probability maximum gust

In this section, the uncertainty of the maximum gust at the 5% probability level is assessed in relation to the number of test repeats. A gust of this nature is calculated by adding two

standard deviations to the mean of the resultant velocity ensemble maxima. Since only one maximum value occurs in each test repeat, many repeats are needed in order to obtain reliable estimates of the maximum gust. In Baker et al. (2013b) the uncertainty of the 5% probability level gust ('TSI velocity') was assessed from a very large ensemble of N=366 maximum velocities. The ensemble was collected at full-scale by trackside ultrasonic anemometers which were passed by Velaro S-103 high-speed trains. A relationship describing the uncertainty of the TSI velocity was derived. This relationship is shown in Figure A - 8, and it demonstrates a connection between the uncertainty of the TSI velocity, the size of the ensemble, and the ratio of the ensemble standard deviation to the mean.

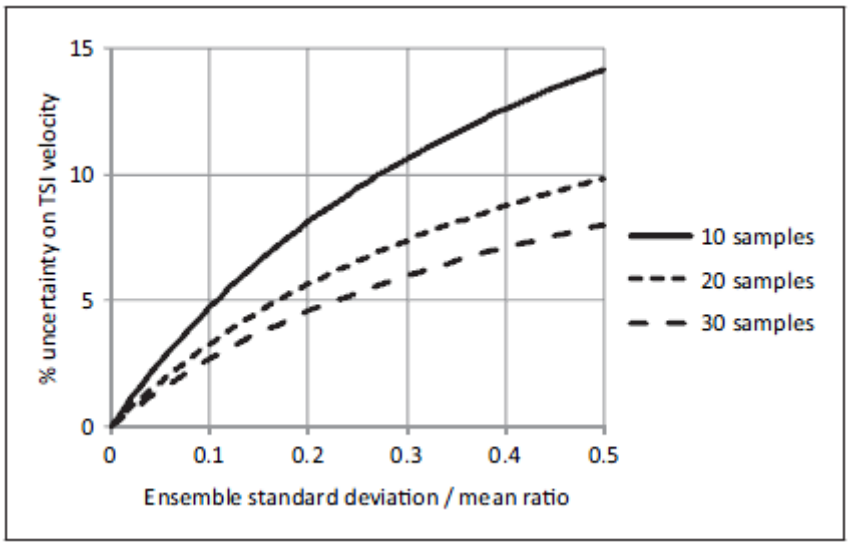

Figure A - 8: Variation of the uncertainty of the 5% probability maximum gust with the number of runs (Baker et al. 2013b).

The highest uncertainty occurs with the combination of the highest standard deviation to mean ratio and the lowest number of runs. Further analysis of the maximum gusts reported in Section 5.3.3 of the main thesis reveals that T3 (L/Z=13, β=0.23, α=0%) produces the highest uncertainty. The number of runs was 16, and the standard deviation to mean ratio was as high as 19%. According to Figure A - 8 this produces an uncertainty of approximately 7%.

Therefore it may be concluded that all of the 5% probability maximum gusts have uncertainties below this.

A2.6. Uncertainty of turbulent air velocity components

The uncertainty of the turbulent components of the air velocity has already been studied comprehensively by Del Valle (2012). The study referred to data for a moving-model ICE2-shaped 1/50 scale train model mounted on a circular spinning track, passing stationary trackside Cobra probes. The average root-mean-square of the slipstream velocity - taken to represent turbulent fluctuations - was repeatable to within 5.3% for 20 repeats, and 0.75% for 80 repeats, based on multiple experiments.

A2.7. Uncertainty of the distance axis and ensemble alignment

The data was aligned to the train nose by combining an automatic alignment algorithm with manual iterations. The train nose was aligned to the zero-crossing point of the lateral and vertical air velocity. The accuracy of the alignment is x/Z=0.3. The precise location of the nose-crossing point is unknown, so the uncertainty is estimated as one train nose length (x/Z=0.156).

A2.8. Confidence intervals

By using the estimated uncertainties of the measured variables, confidence intervals have been calculated for the resultant air velocity measured by Cobra probes, and the static pressure coefficient on surface tappings measured by pressure transducers. Figure A - 9 shows time histories of the individual runs which have been found to produce the widest confidence intervals. These include the resultant velocity in the open air, and the surface static pressure in case W1D. Note that where there are gaps in the data, there are no breaks in the shaded

confidence intervals, as the data needed to be interpolated in order for the shaded regions to be produced.

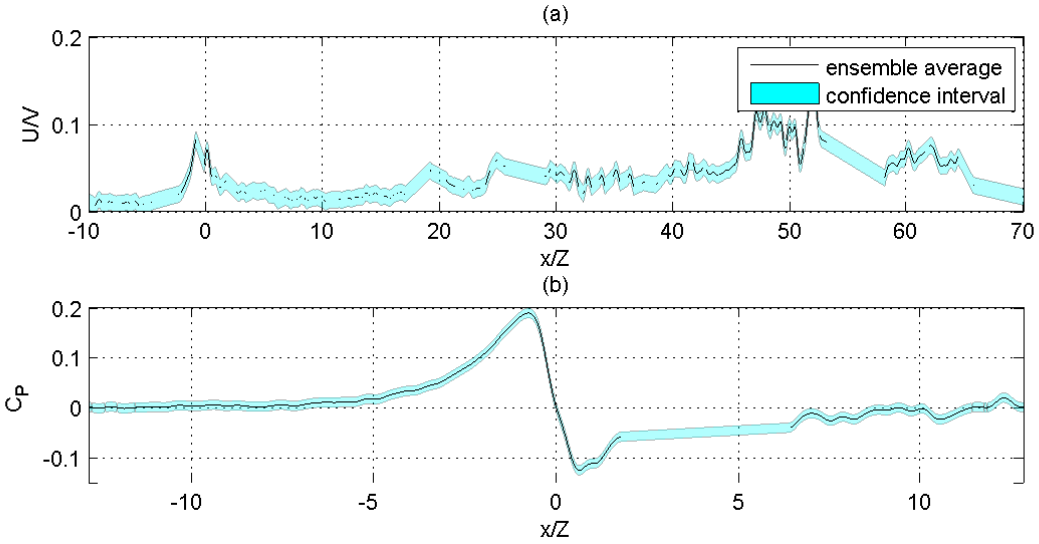

Figure A - 9: Confidence intervals for an individual run, of the: (a) Resultant velocity in the open air measured by a Cobra probe; (b) Static pressure coefficient in case W1D measured on a tapping.

A3. Deleted data

A3.1. Vibrations

During early experimental testing, some of the Cobra probes were mounted on stands which were anchored on the trackside rather than on the floor. This would not normally be a cause for concern, but it emerged that mechanical vibrations transferred from the track bed and via the stands to the Cobra probes, which caused the Cobra probes to record inaccurate data. This was proven in Section 3.9.3 of the main thesis. From the moment the train was fired, a significant longitudinal velocity was detected, as well as an offset in lateral velocity and lower peak static pressures, even while the train was still 20m upstream from the probes. Figure A - 10 shows the time histories of four flow variables measured by a Cobra probe at y/Z=0.77, z/Z=0.05, and compares the effect of different stand-anchoring locations on the flow.

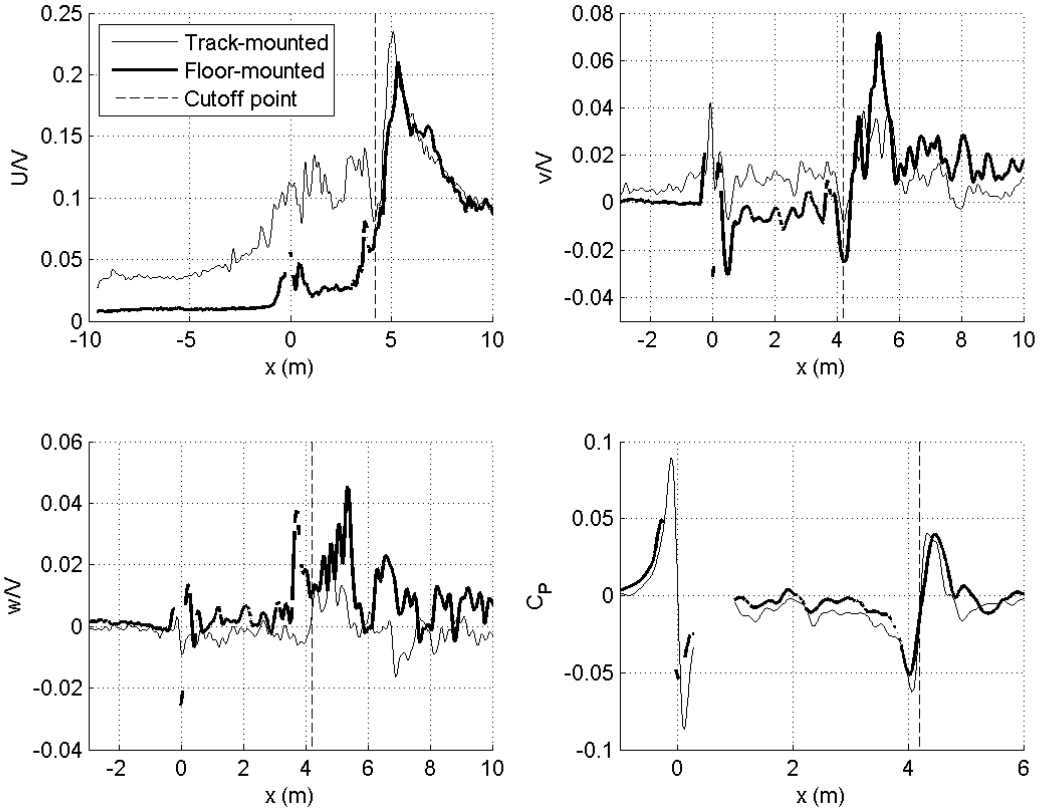

Figure A - 10: The effect of mechanical vibrations in the TRAIN Rig on the air velocity and static pressure coefficient measured by a trackside Cobra probe.

The results show a clear difference in results between the two anchoring locations. To confirm that the data for the track-mounted stand is incorrect, a comparison study reported in Sections 4.1 and 5.1 of the main thesis has revealed that the data collected using a floor-mounted stand closely corresponds to past measurements.

The results also show that the results in the wake region agree more closely. It appears that the errors caused by vibrations decrease with growing distance from the train's nose. A two-sample t-test has been used to test whether the 'ensemble' maximum resultant velocity differs between the anchoring locations to a statistical significance level of $p \leq 0.05$. The test has revealed that $p=0.70$, which suggests that the difference between the anchoring locations is not statistically significant when considering the maximum resultant velocity.

Clearly only the data in the wake should be retained if possible. The effect of the anchoring location on the ensemble average velocity is assessed. Figure A - 11 shows the results of a two-sample t-test applied to the ensemble data at every time increment measured from two Cobra probe positions. The ensemble averages are shown with the significant regions ($p \leq 0.05$) highlighted using thick lines.

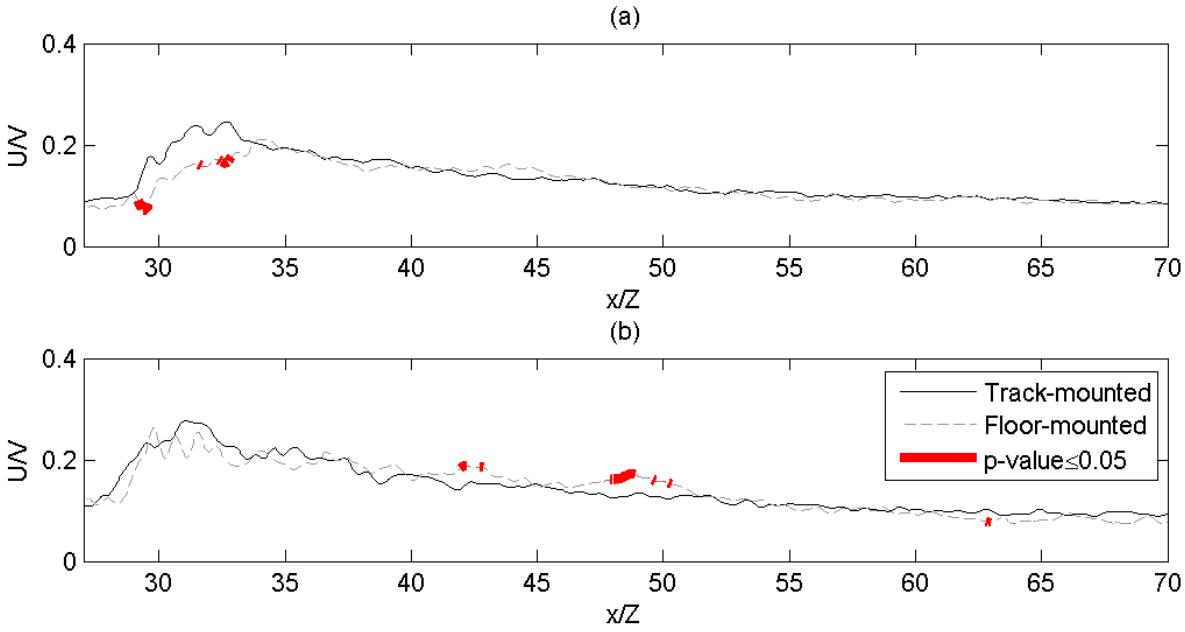

Figure A - 11: Effect of mechanical vibrations in the TRAIN Rig on the ensemble average resultant velocity, with significant differences from t-tests highlighted, for four positions: (a) y/Z=0.77, z/Z=0.05; (b) y/Z=0.58, z/Z=0.13.

Very little of the data is highlighted as significantly different. Overall, t-tests have indicated that it is acceptable to use the ensemble averages and maximum gusts of the data collected by Cobra probes on track-mounted stands, provided that the data up to the beginning of the wake region ($x/Z \leq 27$) has been deleted.

A3.2. Secondary peaks in the negative static pressure

An unusual pressure fluctuation was detected by low-height Cobra probes and low-height pressure tappings. The results are compared with static pressure measurements around a full-scale ICE2 train travelling in the open air at high speed, undertaken for the AeroTRAIN

project (Sima et al., 2011). Figure A - 12 shows the results from both sets of data, measured at a lateral distance of y/Z=0.64 and two heights of z/Z=0.38 and 0.85.

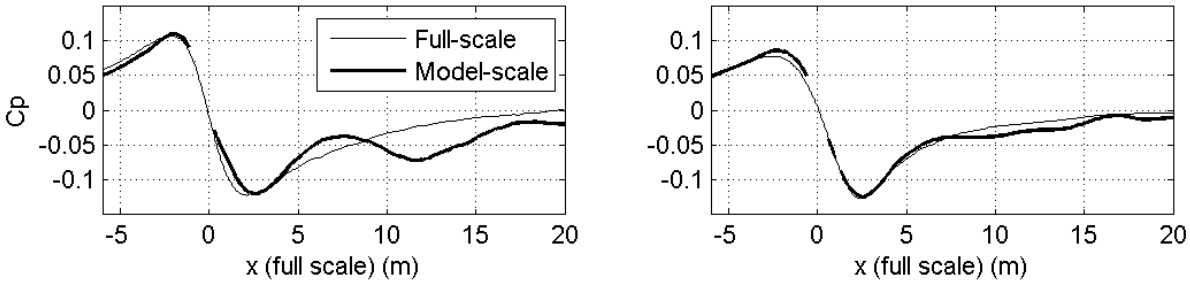

Figure A - 12: Comparison of static pressure coefficient around the train's nose in the open air with full-scale data, highlighting an erroneous peak in the model-scale data. Measurements were made at two heights: a) z/Z=0.38; b) z/Z=0.85.

The results show that a second negative pressure peak occurs at the lower position. No significant fluctuations occur at the higher probe position. Further analysis has found that the same fluctuation has been measured by Cobra probes and pressure transducers, which were connected to independent circuits during the experiments. The probable cause of the fluctuation is a piece of equipment which needed to be attached to the lower portion of the train in order to carry out the experiments. This is because its position relative to the train nose corresponds to the location of the fluctuation relative to the train nose in the time history. The fluctuation has been removed from the data. The equipment is highlighted in Figure A - 13.

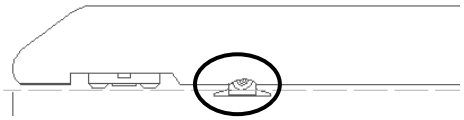

Figure A - 13: A side elevation of the ICE2 model. A piece of underbody equipment (circled) caused a peak in negative static pressure.

A4. Reliability study

A4.1. Reliability of the ensemble average

Figure A - 14 shows the ensemble averages and twice the standard error of the mean of the resultant velocity measured by a Cobra probe in the open air, and the surface static pressure coefficient measured by a pressure transducer. The test cases and sensor positions are identical to those shown in Figure A - 9. Doubling the standard error gives the approximate 95% confidence limit. Note that where there are gaps in the data, there are no breaks in the shaded confidence intervals, as the data needed to be interpolated in order for the shaded regions to be produced.

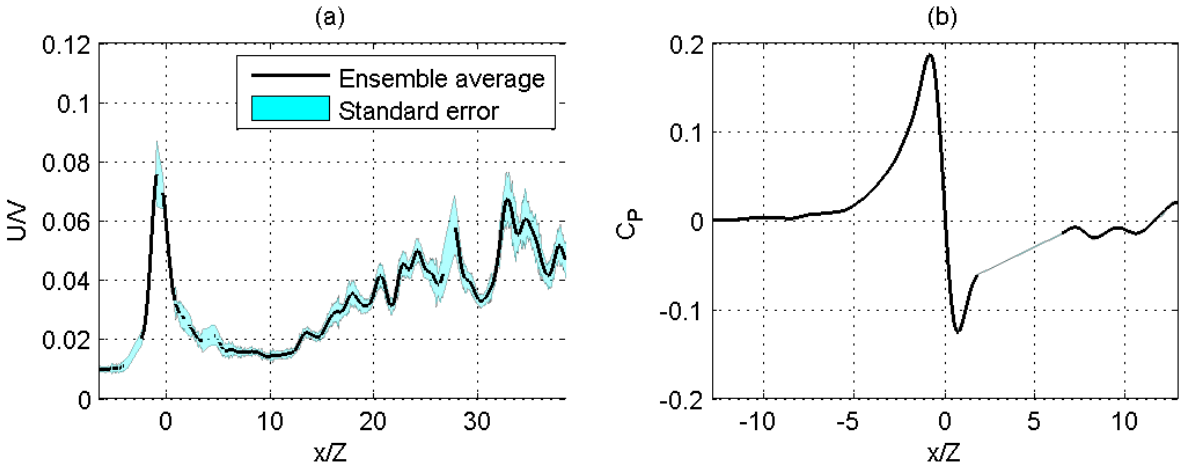

Figure A - 14: Confidence intervals of two ensemble averages: (a) Resultant velocity in the open air measured by a Cobra probe; (b) Static pressure coefficient in a tunnel case measured on a tapping.

A4.2. Repeated experiments

In this section, the reliability of the air velocity measurements is investigated. The open air tests were repeated once, so statistical tests have been applied to the ensemble averages and ensemble peaks of the resultant velocity to investigate whether differences between the repeats are significant at the $p \leq 0.05$ level. This probability level is commonly used in codes of practice, e.g. TSI (2008) and BSI (2005), for assessing maximum aerodynamic loads. Figure

A - 15 shows the results of a two-sample t-test applied to the ensemble data at every time increment, for four Cobra probes. The ensemble averages are shown with the significant regions highlighted using thick lines.

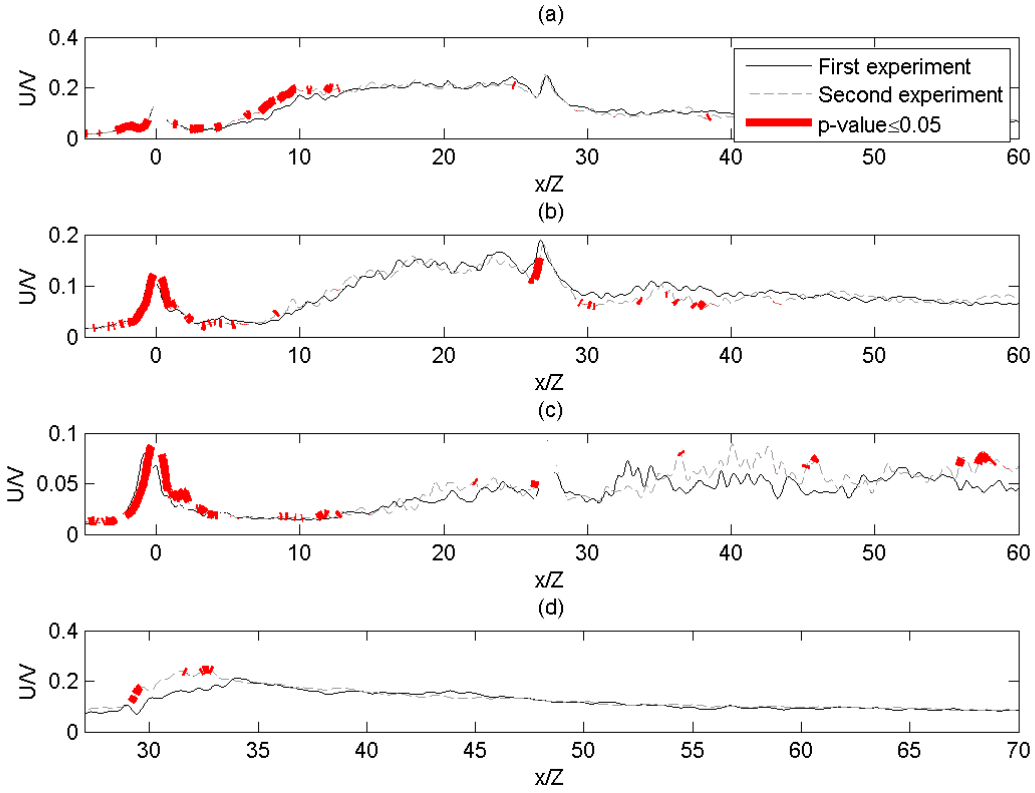

Figure A - 15: Effect of repeated open air experiments on ensemble average resultant velocity, with significant differences from t-tests highlighted, for four positions: (a) *y*/*Z*=0.48, *z*/*Z*=0.58; (b) *y*/*Z*=0.57, *z*/*Z*=0.58; (c) *y*/*Z*=0.75, *z*/*Z*=0.58; (d) *y*/*Z*=0.77, *z*/*Z*=0.05.

The results show that the difference between the data is insignificant at most locations. The flow around the train nose is an exception, as it is consistently highlighted as a region where the results differ significantly. A disclaimer has been added to the section of the main thesis in which the velocity around the train's nose is discussed (Section 5.2.2).

Table A - 2 shows the results of a two-sample t-test which has been applied to the maximum velocities in order to investigate whether the differences between the repeats are significant. The results show that the differences are insignificant at all four positions. Therefore, the

maximum velocities from the repeated open air experiment may be merged with the original experiment, and the maximum velocities may be considered as one large ensemble.

Table A - 2: Effect of repeated open air experiments on maximum resultant velocity, with significant differences from t-tests highlighted, for four positions.

y/Z	***z/Z***	***p*-value**
0.48	0.58	0.36
0.57	0.58	0.29
0.75	0.58	0.13
0.77	0.05	0.55

A4.3. Repeated measurements

In some experiments, two Cobra probes were placed in longitudinally staggered positions to collect extra data, which could be merged to create larger ensembles. This is particularly beneficial for the analysis of maximum velocities, as the uncertainty reduces rapidly with increasing ensemble size. This section explores whether the results for staggered probes can be merged. t-tests have been applied to the ensemble averages and ensemble peaks of the resultant velocity to investigate whether differences between the data are significant at the $p \leq 0.05$ level. Figure A - 16 shows the results of a two-sample t-test applied to the ensemble data at every time increment, for three test cases. The ensemble averages are shown, with the significant regions highlighted using thick lines.

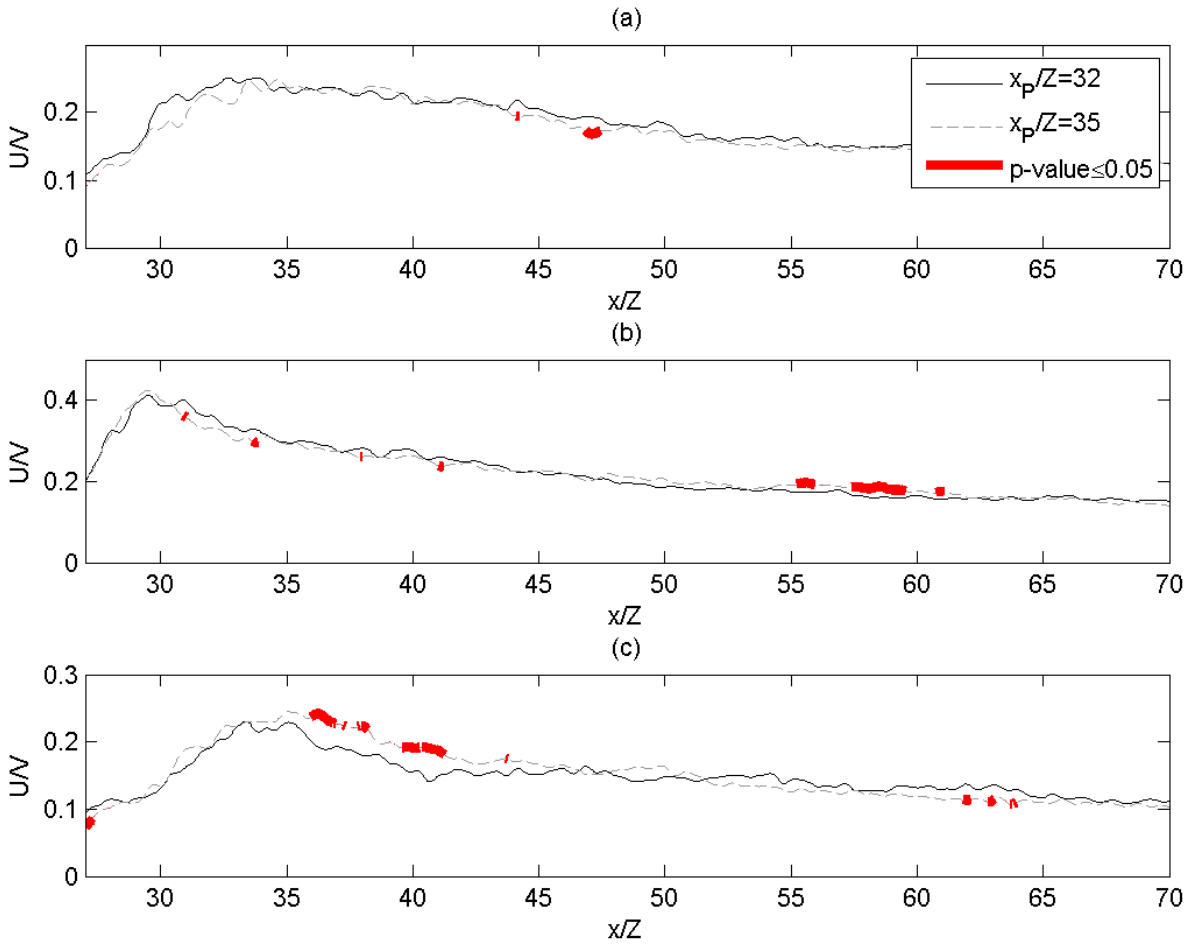

Figure A - 16: Effect of repeated measurements on ensemble average resultant velocity, with significant differences from t-tests highlighted, for three test cases and positions: (a) W1D, *y*/*Z*=0.77, *z*/*Z*=0.05; (b) W2D, *y*/*Z*=0.58, *z*/*Z*=0.13; (c) W3D, *y*/*Z*=0.77, *z*/*Z*=0.05.

The results show that the difference between the data is insignificant at most locations. Table A - 3 shows the results of a two-sample t-test applied to the maximum resultant velocity, to investigate whether the differences between the repeats are significant at the $p \leq 0.05$ level. The results show that the differences are insignificant. Therefore, the maximum velocities from the repeated measurements may be merged and considered as a larger ensemble.

Table A - 3: Effect of repeated measurements on maximum resultant velocity for three test cases and positions.

Test case	*y/Z*	*z/Z*	*p*-value
W1D	0.77	0.05	0.25
W2D	0.58	0.13	0.36
W3D	0.77	0.05	0.37

A5. The effect of imperfect tunnel sealing on velocities and pressures

This section will reveal that imperfect sealing of three tunnel test cases (T2: β=0.23 and 0.3; T3: β=0.3) has led to anomalous results, and that steps have been taken to obtain some useful data. When anomalies were first discovered, one of the affected tunnels (T2, β=0.23) was re-tested with an improved seal. Imperfect sealing was suspected as visual inspection of the tunnels showed that gaps had opened up in the eaves during testing which measured up to 2mm in length. This corresponds to an opening ratio of α≈0.4%. Section 4.2.4.1 of the main thesis examines static pressure time histories for partially-enclosed tunnels, and explains that in T2 (α≈0.4%), 'dissipation caused by air leakage removes the sinusoidal pressure wave pattern [compared to α=0%], but does not appear to attenuate the "underlying" ensemble average'. This matches up with the results for T3 (α=0.4%), and does not match up with the lower value of α=0.2% where there is not enough pressure wave attenuation. It is therefore with confidence that the results for the imperfectly sealed tunnels are labelled α≈0.4%, to the nearest decimal place.

It was feared that the study of changing the blockage ratio would need to be omitted from the thesis if all of the results are moderated by the opening ratio. In what follows, statistical tests will be applied to investigate whether any of the data is independent of the opening ratio. If this is the case, then the label of α≈0% may be used for that data. As mentioned above, one experiment (T2, β=0.23) was repeated with a proper seal. Two-sample t-tests have been

applied to the ensemble averages and ensemble peaks of the resultant velocity in order to investigate whether differences between the data are significant at the $p \leq 0.05$ level. In the event of a null hypothesis, the results are likely to come from the same statistical distributions at this probability level. The limit probability level of $p=0.05$ is deemed suitable for making this conclusion, due to its value in relation to the high uncertainties associated with the small number of test repeats and the experimental variables (Section A2). Figure A - 17 shows the results of the test applied to the ensemble data at every time increment, for three differently positioned Cobra probes. The ensemble averages are shown, with the significant differences (true hypothesis) highlighted using thick lines.

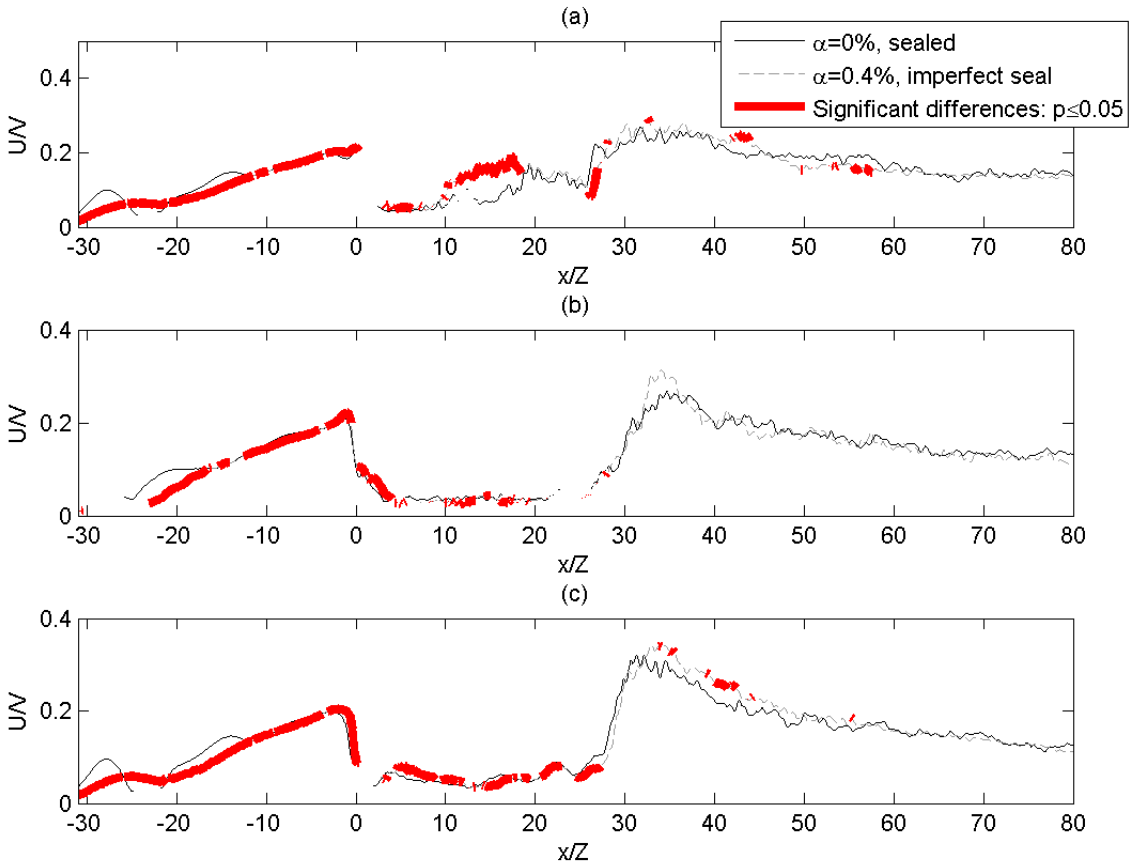

Figure A - 17: Effect of imperfect tunnel sealing on ensemble average resultant velocity in T2 (β=0.23), with significant differences from t-tests highlighted, at positions: (a) y/Z=0.48, z/Z=0.58; (b) y/Z=0.75, z/Z=0.58; and (c) y/Z=0.77, z/Z=0.05.

The results upstream of the train's tail differ significantly. The peak velocity in the wake is slightly higher when $\alpha \approx 0.4\%$, but the difference is not marked as significant due to the very high run-to-run variation of the velocity in the wake region. Therefore, the assumption of an opening ratio of $\alpha \approx 0\%$ may apply to the data in the wake region ($x/Z \geq 27$) for case T2 ($\beta = 0.23$). Therefore the maximum velocities in the 'slightly unsealed' and 'sealed' tunnels may be merged in order to improve the accuracy of the peak-value which is analysed in Section 5.3 of the main thesis. Presumably the same is true for the higher blockage ratio of $\beta = 0.3$. This is useful because the effect of changing blockage ratio may still be discussed in the part of the thesis which focuses on maximum velocities in the wake region (Section 5.3). The results in the shorter high-blockage-ratio tunnel (T3, $\beta = 0.3$) are different to those seen in Figure A - 17 due to its shorter length, so the assumption will not be made for that case.

Appendix B

Guide to the database of results

B1. Introduction

The database accompanying this thesis includes both raw and processed experimental data. It includes an interactive Excel database which can be used to look up information about data. It also includes photographs and videos from the tests. It also includes programs developed by the author for processing the raw data which can be modified to meet the end user's specifications. This document is split into two sections, providing instructions for how to handle processed data (Section B2) and raw data (Section B3) respectively.

B2. Processed data

To access processed data, please go through the following steps:

1. Open 'gilbert_phd_database_lookup.xlsx'.
2. Use the drop-down menus ('TESTCASE' and 'PROBE') to find the desired test case and instrument.
3. If MATLAB is used:
    a. Load the file 'gilbert_phd_database.mat', from the processed data directory, and locate the variable for the desired test case and instrument and flow component, with a name of 'TESTCASE_PROBE_ens' (ens=ensemble) or 'TESTCASE_PROBE_ea (ea=ensemble average).
4. Otherwise:

a. Starting from the processed data directory, navigate to the directory corresponding to the flow component (u, v, w, U or Cp for Cobra probes, or Cp_tappings for the pressure tappings). *Note: longitudinal velocity u is in the directory (u).*

b. The desired file is in this directory, with a filename of 'TESTCASE_PROBE.csv', and a comma-separated value format. It may be in a compressed rar archive. If so, use WinRAR to extract all files to the current directory.

c. In the data files, the first column is the variable x/Z. This is the x-axis, corresponding to the distance from the train nose (x=0 at the train nose). It is normalised by the train height, which is 156mm at model-scale (1:25 scale) or 3900mm at full-scale. The second column is the ensemble average. The remaining columns are the ensemble data. The number of remaining columns corresponds to the number of test repeats that were undertaken.

B3. Raw data

To access raw data, go through the following steps:

1. Open 'gilbert_phd_database_lookup.xlsx'.
2. Use the drop-down menus ('TESTCASE' and 'PROBE') to find the desired data.
3. In the 'Notes' section to the top right, note 2 will tell you the original name assigned to the test case, as referred to in 'Lab notes' and in the unprocessed data folders.

4. In the ‘Notes’ section, note 3 includes the original name assigned to the instrument, as referred to in ‘Lab notes’.
5. Check the ‘Comments’ in the ‘Lab Notes’ worksheet in ‘gilbert_phd_database_lookup.xlsx’. It includes which instruments failed and should not be taken into account, as well as other essential information.
6. To obtain the data for a particular instrument, follow the instructions below:
    a. In the raw data directory, navigate to the folder for the desired test case. Extract the data from the rar archive if necessary (using Winrar). The desired test case is obtained in Step 3 above.
    b. For Cobra probes:
        i. Navigate to the directory of the desired probe number. The desired probe number is obtained in Step 4 above.
        ii. The data within the file is self-explanatory. The longitudinal, lateral and vertical velocity is stored, as well as the static pressure.
    c. For pressure tappings:
        i. In the ‘Notes’ section, note 4 will tell you the column number (AI0#) assigned to the pressure tapping in the data file.
        ii. Go to the ‘Lab Notes’ worksheet.
        iii. Using the ‘Date’ and ‘Logger filename’ columns, make note of the dates and filenames that make up a particular test case.
        iv. Navigate to the directory of the desired date, then open the desired file of the form ‘log000##.csv’, to get the desired data (column AI0#).

v. The data is in units of Volts, and should be converted to Pascals using the calibration function defined in the main body of the thesis. Note 5 includes the name of the instrument.

d. Environmental readings may be obtained for calculating the air density and other useful information. These readings are obtained from the 'Lab Notes' worksheet in 'gilbert_phd_database_lookup.xlsx'.

e. Light gate data may be obtained from the pressure log files. The light gate data is at 0V when the beam is unbroken, and 5V when the beam is broken.

If the data is to be re-processed using a computer program, note that this is a complex process to do from scratch. Therefore, some m files (MATLAB files) are included with the database which will do the job. When viewed alongside the methodology and other appendices to the main thesis, it is possible to learn the process and edit it to meet different requirements. The files include:

- Path://firing_notes/Firing_notes.m: A copy of the lab notes in code form, which is used by the main routine to determine which data to download for each test case, and look up important information for processing the data.
- Path://processing_scripts/cobra_probe_script_ver5_thesis.m: The main program for obtaining processed Cobra probe data..
- Path://processing_scripts/launcher_cobraprobescript_thesis.m: Run this program in order to process the entire dataset at once (run the cobra_probe_script_ver5_thesis many times) and write the output to final_cobra_data/final_cobra_data_thesis.mat.
- Path://processing_scripts/pressure_transducer_script_ver3_thesis.m: The main program for obtaining processed pressure tapping data..

- Path://processing_scripts/launcher_pressuretransducerscript_thesis.m: Run this program in order to process the pressure dataset for all test cases (run the pressure_transducer_script_ver3_thesis many times) and write the output to final_cobra_data/final_transducer_data_thesis.mat.
- Path://processing_scripts/Remove_unwanted_data.m: A subroutine which removes unwanted data (e.g. duplicated data, temporary variables, sections of data etc).
- Path://processing_scripts/cobra_rearrange_rename.m: A subroutine used by the Cobra probe processing program to merge, rearrange and rename data into the desired syntax (the old syntax).
- Path for functions://buttertim.m: A low-pass butterworth filter.
- Path for functions://movavg.m: A moving-average filter.
- Path for functions://distalign.m: An algorithm for aligning data.
- Path for functions://interp0s.m: An algorithm for temporarily interpolating zeros in the data.
- Path for functions://interpnans.m: An algorithm for temporarily interpolating nans in the data.

Note that their output files and variables will use the old syntax for test case and instrument names - perhaps the user can modify the program to update the output file syntax, using Step 4 above as a lookup.

Note that the raw data is contained within rar archives and should be extracted first.

Table B - 1 shows the folder hierarchy required in order for the scripts to work straight away:

Table B - 1: Folder hierarchy required for running MATLAB scripts.

Base dir	Sub-dir	Sub-dir	Sub-dir
Main	Folder: firing_notes	File: firing_notes.m	~
Main	Folder: processing_scripts	File: cobra_probe_script_ver5_thesis.m File: pressure_transducer_script_ver3_thesis.m File: remove_unwanted_data.m File: cobra_rearrange_rename.m	~
Main	Folders: B1, B2, B3, B4, B4B, B5, B5NP, B6, OA1, OA2, OA3, V2, V5, V15, V47, W1, W2 ,W3 ,W4, W5, W6.	Folders: date yyyy-mm-dd	Files: Raw pressure tapping data - 'log000##.csv' where '##' is the file name.
		Folders: Cobra probe name: 1-8 Files: temporary variables created by the program to simplify the data processing ('TGWP1_##_RUN#.ap_pr#')	Files: Raw cobra probe data - 'TGWP1_## _ RUN# (Ve).ap' where '##' is the testcase of the directory (OA1, W2 etc) and '#' is the run number.
Main	Folder: final_cobra_data	File: final_cobra_data_thesis.mat File: final_transducer_data_thesis.mat	~
Functions	File: buttertim.m File: distalign.m File: movavg.m File: interp0s.m File: interpnans.m	~	~

Appendix C

Author’s publications

This Appendix contains the following journal articles and conference papers written and contributed to by the author:

Gilbert, T., Baker, C. and Quinn, A. (2013). Aerodynamic pressures around high-speed trains: the transition from unconfined to enclosed spaces. Proceedings of the Institution of Mechanical Engineers Part F: Journal of Rail and Rapid Transit. Advance online publication. doi: 10.1177/0954409713494947.

Gilbert, T., Baker, C. and Quinn, A. (2013). Gusts caused by high-speed trains in confined spaces and tunnels. Journal of Wind Engineering and Industrial Aerodynamics, 121, 39-48.

Gilbert, T. and Straathof, J. (2013). The effects of confinement on high-speed train wakes. Sixth European and African Conference on Wind Engineering, Nottingham, UK, 7-9 July.